

Dissertation

submitted to the

Combined Faculties for the Natural Sciences and for Mathematics

of the

Ruperto-Carola University of Heidelberg, Germany

for the degree of

Doctor of Natural Sciences

Put forward by

Dipl.-Phys. Andreas Hillert

born in *Breisach am Rhein, Germany*

Oral examination: 24 July 2014

GRASP

Development of an event reconstruction method using a
Gamma Ray Air Shower Parameterisation
and application to γ -ray sources with H.E.S.S.

Referees: Prof. Dr. Werner Hofmann
Prof. Dr. Stefan Wagner

Abstract

The H.E.S.S. experiment, with its high sensitivity and large field-of-view, is an ideal instrument to survey the Milky Way in VHE γ -rays. An accurate reconstruction of the γ -ray direction as well as a strong reduction of the hadronic background is essential for the analysis of the data. In this work a reconstruction algorithm is developed that applies a fit of pixel amplitudes to an expected image obtained from a Gamma Ray Air Shower Parameterisation (GRASP). This parameterisation was obtained using Monte Carlo air shower simulations by parameterising the angular Cherenkov photon distribution with suitable analytical functions. Furthermore, it provides new classifying variables to differentiate γ -ray induced air showers from hadronic ones. The reconstruction of air shower parameters is achieved by a maximum likelihood fit and improves the angular resolution by 20-30% with respect to traditional image moment analysis methods. In combination with a MVA-based background rejection method using these new classifying variables the sensitivity can be improved by about 70 %. An analysis of the Pulsar Wind Nebula MSH 15-5-2 and investigation of its morphology and spectral properties show an indication of energy dependent morphology in VHE γ -rays.

Kurzfassung

Das H.E.S.S. Experiment ist aufgrund seiner hohen Sensitivität und seinem großen Gesichtsfeld ein optimales Instrument zur Vermessung der Milchstraße in sehr hoch energetischer γ -Strahlung. Eine präzise Rekonstruktion der Richtung der γ -Strahlen sowie eine starke Reduktion des hadronischen Untergrunds ist notwendig in der Analyse der Daten. In dieser Arbeit wird ein Rekonstruktions-Algorithmus entwickelt, der einen Fit von Pixelamplituden auf ein von einer Gamma-Strahlen-Luftschauer-Parametrisierung vorhergesagtes Bild anwendet. Die Parametrisierung wird durch Monte-Carlo Luftschauer-Simulationen erlangt, in denen die Winkelverteilung von Cherenkov-Photonen durch geeignete analytische Funktionen parametrisiert wird. Weiterhin liefert sie neue klassifizierende Variablen zur Unterscheidung von Luftschauern ausgelöst durch γ - oder hadronische-Strahlung. Die Rekonstruktion von Luftschauerparametern wird erreicht durch einen Maximum-Likelihood Fit und verbessert die Winkelauflösung um 20-30% gegenüber einer herkömmlichen Analyse durch Bild-Momente. Kombiniert mit einer multivariaten Hintergrund-Unterdrückungsmethode, welche die neuen klassifizierenden Variablen verwendet, wird die Sensitivität um ungefähr 70% gesteigert. Eine neue Analyse von dem Pulsarwindnebel MSH 15-5-2 und eine Untersuchung seiner Morphologie und spektralen Eigenschaften zeigen einen Hinweis auf energieabhängige Morphologie in sehr hoch energetischer γ -Strahlung.

Contents

List of Figures	v
List of Tables	xi
1 Introduction	1
2 Theory of Air Showers	5
2.1 Electromagnetic Air Showers	5
2.1.1 Interaction mechanisms	5
2.1.2 Air Shower Cascade	7
2.1.3 Longitudinal Development	8
2.1.4 Transverse Particle Distribution Development	11
2.2 Hadronic Air Showers	12
2.2.1 Interaction Mechanisms	12
2.2.2 Air Shower Cascade	13
2.3 Atmospheric Cherenkov Radiation	16
3 H.E.S.S.	19
3.1 Introduction	19
3.2 H.E.S.S. Telescope Array	20
3.2.1 Telescopes	20
3.2.2 Cameras	22
3.2.3 Trigger	24
3.2.4 From Raw Data to DST	24
3.3 Data Calibration	25
3.3.1 Pedestal	27

CONTENTS

3.3.2	Gain	27
3.3.3	Flat Fielding	29
3.3.4	Optical Efficiency	29
3.3.5	NSB and Image Cleaning	29
3.4	Data Analysis	32
3.4.1	Hillas Reconstruction	32
3.4.2	Direction Reconstruction	36
3.4.3	Background Rejection	36
3.4.4	Multivariate Analysis Technique	39
3.4.5	Signal Extraction	41
4	GRASP - Gamma Ray Air Shower Parameterisation	45
4.1	Introduction	45
4.2	CORSIKA Air Shower Simulations	47
4.2.1	Parameters	47
4.2.2	Results	50
4.3	Gamma Ray Air Shower Parameterisation	62
4.3.1	Concept	62
4.3.2	Longitudinal and Transverse Profiles	63
4.3.2.1	Moyal Peak	65
4.3.2.2	Moyal Length	68
4.3.2.3	Moyal Norm	71
4.3.2.4	Lorentz Width	73
4.3.3	Parameterisation of the Shower Image	76
4.4	Reconstruction of Shower Parameters	76
4.4.1	Pixel Log-Likelihood	77
4.4.2	Shower Reconstruction	79
4.5	Example Fit of a MC simulated Event	82
4.6	γ -Hadron Separation	86
4.6.1	Fit Parameters	86
4.6.2	Multivariate analysis with BDTs	93
4.7	Performance	95
4.7.1	Accuracy of Direction and Energy Reconstruction	95

4.7.2	Test of Direction Reconstruction on a strong point-like Source . . .	101
4.7.3	Test of Background Rejection on a few Sources	102
4.7.4	Comparison of the Effective Area and Energy Spectrum	108
4.8	Galactic Plane Survey Map	111
5	CR Propagation and Pulsar Wind Nebulae	113
5.1	Introduction	113
5.2	Theory of Pulsars and Pulsar Wind Nebulae	116
5.2.1	Pulsars	116
5.2.2	PWN	120
5.2.3	Supernova Remnant	122
5.3	Anisotropic Diffusion	123
6	Complex Source MSH 15-5-2	125
6.1	Radio and X-ray Measurements	125
6.2	Previous γ -ray Measurements	128
6.3	Analysis using GRASP	130
6.3.1	Morphology of MSH 15-5-2	131
6.3.2	Energy Spectrum of MSH 15-5-2	144
6.3.3	Upper Limit on SNR Explosion Energy	148
6.4	Discussion	150
7	Summary and Conclusions	153
	References	157

CONTENTS

List of Figures

1.1	First design of an air Cherenkov counter	2
1.2	Cosmic Ray energy spectrum	3
1.3	TeVcat Skymap of discovered sources before the operation of H.E.S.S. . .	4
2.1	Mass attenuation coefficients for photons in air	6
2.2	Feynman graph for bremsstrahlung and pair production	7
2.3	Number of electrons as a function of the atmospheric depth - Greisen function	9
2.4	Particle density as a function of the radial distance - NKG function . . .	12
2.5	Sketch of an hadronic induced extensive air shower	15
2.6	Comparison of γ -ray and hadronic induced air shower	15
2.7	Sketch of the Cherenkov cone	16
2.8	Cherenkov ring radius as a function of the emission altitude	17
3.1	TeVcat Skymap of γ -ray sources discovered by H.E.S.S. (July 2013) . .	20
3.2	H.E.S.S. Telescope Array in Namibia	21
3.3	Sketch of depth of field (DOF)	22
3.4	H.E.S.S. Phase I camera	23
3.5	Sketch of the Calibration procedure	25
3.6	Electronic dark pedestal and pedestal shift as a function of NSB level .	27
3.7	Single p.e. ADC count distribution	28
3.8	Shower Image - RAW and Cleaned	31
3.9	Shower Image - Extended	31
3.10	Mapping of Cherenkov light	32
3.11	Imaging of Cherenkov light	33

LIST OF FIGURES

3.12	Sketch of Hillas reconstruction	34
3.13	Direction reconstruction via intersection of major axes	36
3.14	Hillas MSCW and MSCL distribution	37
3.15	Importance of TMVA parameters	41
3.16	Shows a sketch of the background estimation techniques	43
4.1	Sketch of the CORSIKA detector array	48
4.2	Atmosphere thickness vs height	51
4.3	Single and averaged Corsika Gamma Shower	52
4.4	Shower Slice Sketch	52
4.5	Corsika Gamma Shower - Longitudinal Distribution	54
4.6	Corsika Gamma Shower - Transversal Distribution	54
4.7	Corsika Gamma Shower - Longitudinal Distribution different d and h_t .	55
4.8	Corsika Gamma Shower - Transversal Distribution different d	56
4.9	Shower Longitudinal peak shift	57
4.10	Greisen function plus fit of a Moyal function	59
4.11	NKG function plus fit of a Lorentz function	59
4.12	Height of Production vs Transverse Direction	60
4.13	Lorentz width vs height and direction	61
4.14	Corsika Gamma Shower - Number of shower events in each d and h_t bin	63
4.15	Corsika Gamma Shower - Height of the first interaction distribution . .	64
4.16	Moyal peak p vs d and h_t	65
4.17	Moyal peak p vs d and h_t - Slices along h_t	66
4.18	Moyal peak p vs d and h_t - Slices along d	66
4.19	Moyal peak p vs d and h_t - Relative Deviation of the smoothed histogram to the original one	68
4.20	Moyal length l vs d and h_t	69
4.21	Moyal length l vs d and h_t - Slices along h_t	69
4.22	Moyal length l vs d and h_t - Slices along d	70
4.23	Moyal length l vs d and h_t - Relative Deviation of the smoothed his- togram to the original one	70
4.24	Moyal norm n vs d and h_t	71
4.25	Moyal normalisation n vs d and h_t - Slices along h_t	72

LIST OF FIGURES

4.26 Moyal normalisation n vs d and h_t - Slices along d	72
4.27 Moyal norm n vs d and h_t - Relative Deviation of the smoothed histogram to the original one	73
4.28 Lorentz width w vs d and u	74
4.29 Lorentz width w vs d and u - Slices along u	74
4.30 Lorentz width w vs d and u - Slices along d	75
4.31 Lorentz width w vs d and u - Relative Deviation of the smoothed his- togram to the original one	76
4.32 Shower Reconstruction Sketch	79
4.33 Duration of the shower reconstruction fit for 2 and 4 extended rows . . .	80
4.34 Simulated energy vs d and S for 50° zenith	82
4.35 MC simulated shower image for CT-1	84
4.36 Predicted GRASP shower image for CT-1	84
4.37 Residual shower image for CT-1	84
4.38 Two-dimensional projection of the likelihood surface for the direction . .	84
4.39 MC simulated shower image for CT-2	85
4.40 Predicted GRASP shower image for CT-2	85
4.41 Residual Image for CT-2	85
4.42 Two-dimensional projection of the likelihood surface for the core position	85
4.43 MSC Moyal peak and Moyal peak difference parameter distributions for MC γ and hadronic background at 20° zenith	88
4.44 MSC parameter distribution for MC γ and hadronic background at 20° zenith	89
4.45 Mean and RMS of the MSC parameter distributions as a function of energy for MC γ and hadronic background - first part	90
4.46 Mean and RMS of the MSC parameter distributions as a function of energy for MC γ and hadronic background - second part	91
4.47 Mean and RMS of the MSC parameter distributions as a function of the zenith angle for MC γ and hadronic background	92
4.48 GRASP BDT training - Relative importance of the top five most impor- tant variables vs. energy and zenith	93
4.49 θ^2 distribution for MC γ -ray simulations at 20° zenith	95

LIST OF FIGURES

4.50	Angular resolution as a function of MC simulated energy for 20° and 50° zenith	96
4.51	Angular resolution vs simulated energy for 50° zenith at two impact distance regimes	97
4.52	Angular resolution vs zenith for a MC simulated γ -ray point source	98
4.53	Energy Resolution and Bias vs simulated energy for 20° zenith	99
4.54	Energy Resolution and Bias vs simulated energy for 50° zenith	99
4.55	Height of the first interaction resolution and bias vs simulated energy	100
4.56	Correlation between shower maximum and the height of the first interaction	100
4.57	ThetaSquare distribution for PKS 2155-304 flare excess	101
4.58	Q factor vs zenith angle and energy	105
4.59	Sensitivity curve comparison	105
4.60	PSF std Hillas and std ζ GRASP for PKS 2155–304	107
4.61	Effective Area comparison between std ζ Hillas and std ζ GRASP	109
4.62	Energy spectrum of the Crab Nebula for std ζ GRASP	110
4.63	H.E.S.S. GPS significance map produced with std ζ GRASP	112
5.1	Electron energy spectrum and positron fraction measured by AMS-02	114
5.2	Hillas plot of potential cosmic accelerators	115
5.3	Sketch of the schematic model of a pulsar	118
5.4	Sketch of the sites and radiation mechanisms of nonthermal emission associated with rotation powered pulsars	121
6.1	View of MSH15-52 at radio (MOST) and X-ray (ROSAT) wavelengths	126
6.2	View of MSH 15-5-2 at X-ray wavelengths by Chandra	127
6.3	View of MSH 15-5-2 in the very high energy regime with H.E.S.S.	129
6.4	View of MSH 15-5-2 in the high energy regime with Fermi-LAT	129
6.5	MSH 15-5-2 reanalysis with std ζ GRASP smoothed excess map	130
6.6	Significance map of MSH 15-5-2 for std ζ GRASP and std ζ Hillas	131
6.7	MSH 15-5-2 model and residual map for a 2D Gaussian fit	132
6.8	MSH 15-5-2 model and residual map for two 2D Gaussian fit	134
6.9	MSH 15-5-2 model and residual map for two 2D Gaussians plus point-like model fit	136
6.10	MSH 15-5-2 model and residual map for three 2D Gaussian model fit	138

LIST OF FIGURES

6.11	Significance maps for MSH 15-5-2 in energy ranges	140
6.12	Energy dependent results of fit of one 2D Gaussians	141
6.13	Correlated excess map overlaid with a sketch of the slices	142
6.14	Projected excess for the other energy ranges of MSH 15-5-2	143
6.15	Energy spectrum of the Crab Nebula for std ζ GRASP	144
6.16	Correlated excess map overlaid with a sketch of the wedges	146
6.17	MSH 15-5-2 Spectral Index vs. radial distance	146
6.18	MSH 15-5-2 spatially resolved spectral analysis	147

LIST OF FIGURES

List of Tables

3.1	Trigger rates for various sources	24
3.2	Cut Configurations std, hard and loose	38
4.1	CORSIKA Simulations Parameters	48
4.2	Reconstruction results of Hillas and GRASP for one specific event . . .	83
4.3	Number of not converged events for MC simulated data and Off-Data .	87
4.4	Selection cuts for the ζ BDT analysis	102
4.5	Test analysis of the Crab Nebula	103
4.6	Test analysis of the starburst galaxy NGC253	103
4.7	Test analysis of the galactic centre region source HESS J1745-290	104
4.8	Required observation time for a source with 1% flux of the Crab Nebula	106
4.9	Test analysis of the AGN PKS 2155–304	106
4.10	Differential flux comparison for the Crab Nebula	110
6.1	Previous fit results for one two-dimensional Gaussian for MSH 15-5-2 . .	128
6.2	Fit results for one 2D Gaussian for MSH 15-5-2	133
6.3	Fit results for two 2D Gaussians for MSH 15-5-2	135
6.4	Fit results for two 2D Gaussians plus point-like model for MSH 15-5-2 .	135
6.5	Fit results for a three 2D Gaussians for MSH 15-5-2	137
6.6	Energy spectrum model comparison for MSH 15-5-2	145

GLOSSARY

Chapter 1

Introduction

High-energy γ -ray astronomy is defined as astronomy in the energy range from about 30 MeV to 100 GeV whereas the very high energy regime is for energies even greater than 100 GeV. The first starting point of the high energy γ -ray astronomy was the suggestion of Blackett that approximately 10^{-4} of the mean light of the night-sky background might originate from Cherenkov radiation produced in the atmosphere by cosmic radiation [Blackett, 1948]. His hypothesis might have inspired J.V. Jelley and W. Galbraith to look for flashes of light associated with extensive air showers using photomultipliers. They assembled what must be regarded as the first experiment to detect atmospheric Cherenkov radiation, comprising a 5 cm photomultiplier tube and 25 cm parabolic mirror which was coupled to an amplifier and an oscilloscope, see Fig. 1.1. They measured pulses by eye on the oscilloscope at a rate of about 1 per minute with the threshold set at three times that of the night sky noise and later also found an association of these light pulses with cosmic radiation, see [Galbraith and Jelley, 1953]. However, the source of these light pulses were only later attributed to Cherenkov radiation by further works of [Galbraith and Jelley, 1955]. In principle, however, the technique could be used to locate point sources of very high-energy gamma rays. What can be called the first γ -ray telescope was built in the Crimea mountains in the early 1960s but could only derive an upper limit on the flux of high energy gamma rays from observations of the Crab Nebula. Even the second gamma-ray telescope built in Glencullen, Ireland, could not find an excess of events from a variety of candidate sources. The major problem at this point was that there was no way of separating the γ -ray induced air showers from the hadronic cosmic ray (CR) background. Since the

1. INTRODUCTION

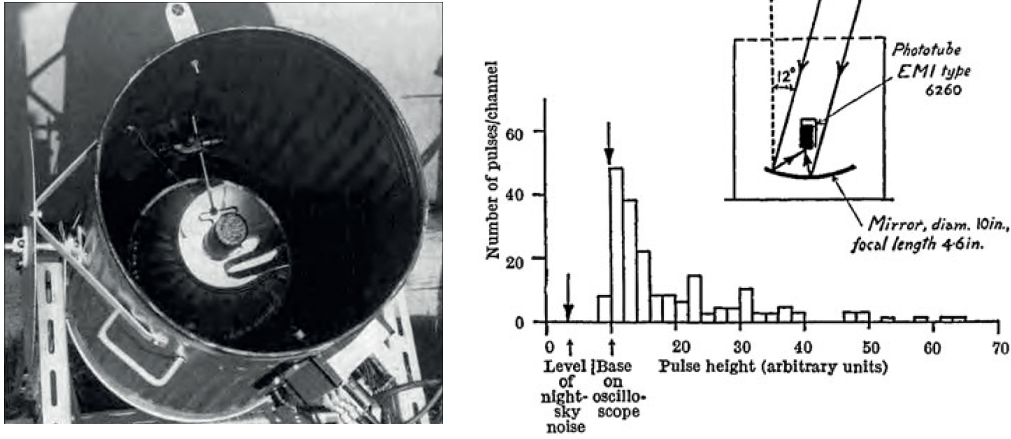


Figure 1.1: First design of an air Cherenkov counter in a garbage can used by Galbreith and Jelley in 1953, [Galbraith and Jelley, 1953]. Photograph taken from <http://cerncourier.com/cws/article/cern/50222>. Second figure on the left shows the results of the observations taken from the original article.

galactic magnetic fields scramble the directional history of the charged cosmic rays, no useful astrometric information can be derived from their detection. The composition of cosmic rays is dominated by hydrogen and helium but also includes heavier elements, up to iron. The intensity of primary nucleons in the energy range from several GeV to beyond 100 TeV is given approximately by the following power law:

$$\frac{dN}{dE} = N_0 \left(\frac{E}{E_0} \right)^{-\Gamma} \quad (1.1)$$

$$\approx 1.8 \times 10^4 \left(\frac{E}{1 \text{ GeV}} \right)^{-2.7} \frac{\text{nucleons}}{\text{m}^2 \text{ s GeV sr}} \quad (1.2)$$

Fig. 1.2 shows the almost featureless energy spectrum of the Cosmic Rays. One large step towards the goal of discriminating this background from the γ -rays was the construction of the Whipple 10m gamma-ray observatory on Mount Hopkins (Arizona, USA) in 1968. At first, only upper limits on the γ -ray photon flux were obtained on a few sources, including the Crab Nebula [Fazio et al., 1968]. However, after many years the first reliable detection of a source of very high energy γ -rays could finally be achieved in 1989 [Weekes et al., 1989]. Up until then all the γ -ray telescopes did not use an imaging technique, but the use of arrays of photomultiplier tubes (pixel) located at the focal plane allowed shower features to be resolved. This made it possible for the first

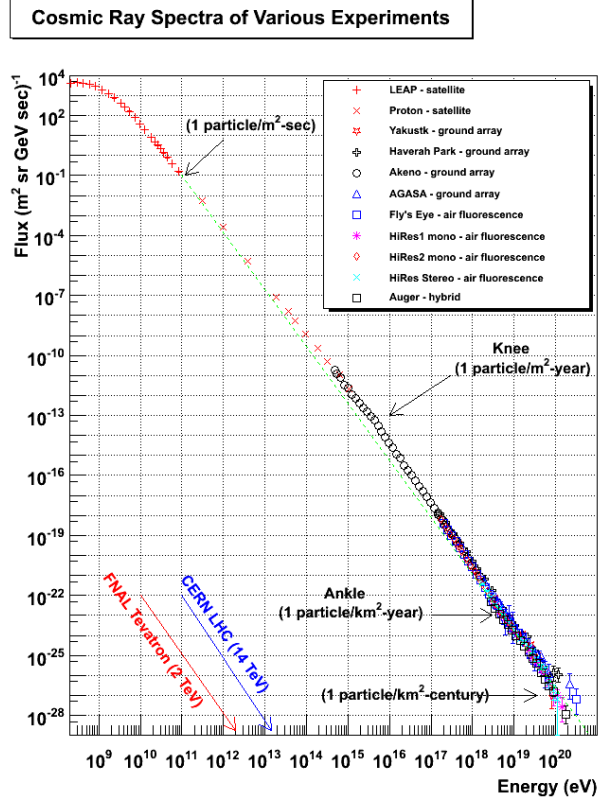


Figure 1.2: Cosmic Ray energy spectrum, taken from <http://www.physics.utah.edu/~whanlon/spectrum.html>

time to discriminate the γ -rays from the hadronic cosmic rays. Following the pioneering work of Whipple, a series of ground-based γ -ray astronomy projects commenced, with the intention of using this new technique to explore the universe in high energy γ -rays. These so called second generation γ -ray telescopes include Whipple [Lamb et al., 1990], Crimea [Vladimirsky et al., 1989], CAT [Barrau et al., 1998], HEGRA [Mirzoyan et al., 1994], among others. But even with these telescopes it was only possible to detect the brightest sources in high energy γ -rays which amounted to an order of 10, as shown in Fig. 1.3. The development of Imaging Atmospheric Cherenkov Telescopes (IACT) has culminated with the deployment of arrays consisting of several telescopes. These arrays of several large imaging Cherenkov telescopes, of which H.E.S.S. is one, are currently the most sensitive instruments for astronomy in the TeV (10^{12} eV) regime and are responsible for detecting the over 100 sources known today.

1. INTRODUCTION

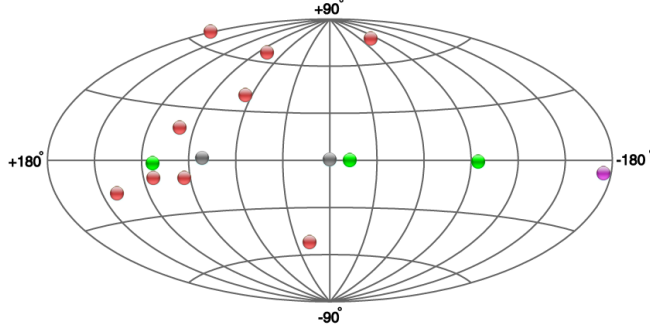


Figure 1.3: TeVCat sky map of discovered gamma ray sources before the operation of H.E.S.S.. The colors indicates the likely nature of sources: Supernova remnants (green), pulsar wind nebulae (violet), binaries (yellow), star cluster/star forming regions (blue), unidentified (grey), starburst galaxy (orange), active galactic nucleus (red). Taken from <http://tevcat.uchicago.edu/>

A detailed description of the H.E.S.S. telescope array is given in chapter 3. The key critical point in the detection of sources and physical information obtainable is the ability to discriminate the γ -rays from the cosmic ray background as well as the accurate reconstruction of their physical properties. The background discrimination technique dates back to when the Whipple observatory began using the imaging technique and when it was shown in the paper by [Hillas, 1985], that it should be indeed possible. This so called Hillas method of discrimination between γ -rays and hadronic background uses the width, length and orientation of the Cherenkov light image of the shower inside a camera, see section 3.4.1 and 3.4.3. The goal for this thesis was the development of an alternative method of reconstructing basic shower parameters as well as improving the background rejection efficiency. To that end the Gamma Ray Air Shower Parameterisation (GRASP) was developed and will be explained in chapter 4. The following chapter 2 will first give a short overview in basic air shower theory.

Chapter 2

Theory of Air Showers

Air showers (particle cascades) are produced when a high energetic cosmic ray or γ -ray enter the earth atmosphere. If the particles in the shower have a velocity greater than the speed of light in air, they produce Cherenkov radiation. This chapter will give an overview over the theoretical interaction mechanisms for electromagnetic and hadronic air showers in the first two sections. Furthermore, the basic principles of Cherenkov emission from particles in the air shower will be outlined in the last section.

2.1 Electromagnetic Air Showers

2.1.1 Interaction mechanisms

When a γ -ray traverses through the atmosphere there are three important ways it can interact with the surrounding medium. Depending on the energy, the photoelectric effect (low energies), the Compton effect (mid energies) or the pair production (high energies) dominates, see Fig. 2.1.

For very high energy (VHE, $E > 100$ GeV) γ -rays the pair production dominates with the threshold calculated by $E_{\text{threshold}} = 2m_e c^2 = 2 \times 511 \text{keV} = 1.02 \text{MeV}$.

For a charged particle traversing through matter the predominant energy losses are ionisation and bremsstrahlung. The cross-section for bremsstrahlung depends on the inverse square mass of the charged particle losing energy, which means that for electrons the main energy loss mechanism is bremsstrahlung, whereas heavier particles will predominantly lose their energy via ionisation. When radiative energy loss is dominant, it is useful to define a radiation length, X_0 , which is the thickness x of the material

2. THEORY OF AIR SHOWERS

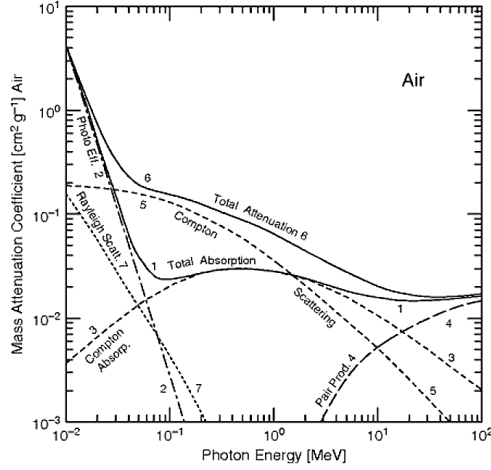


Figure 2.1: Mass attenuation coefficients for photons in air. Curve 1, labeled Total Absorption, is the sum of the linear coefficients for photoelectric absorption (curve 2), Compton absorption (curve 3) and pair production (curve 4). Other curves only shown for completeness. Specifics on the composition can be found in [Evans, 1955]

over which the charged particle energy is reduced by a factor of e .

$$E(x) = E_0 e^{-x/X_0} \quad (2.1)$$

The energy loss per unit radiation length due to bremsstrahlung can now be defined as:

$$-\left(\frac{dE}{dx}\right)_{\text{Bremsstrahlung}} = \frac{E}{X_0} \quad (2.2)$$

The critical energy E_c is the energy at which losses by ionisation are equal to losses by radiation, which for air at sea level is at about 83 MeV. This means that energy losses due to ionisation become dominant below this critical energy. At very high energies the most important processes for electrons and γ -rays traversing through the atmosphere are bremsstrahlung and pair production. Both processes depend on the same radiation length defined by [Tsai, 1974]:

$$\frac{1}{X_0} = \frac{4\alpha r_e^2 N_A Z^2}{A} \ln(183Z^{-1/3}) \quad [\text{g/cm}^2] \quad (2.3)$$

For the atmosphere the radiation length can be calculated to be $X_0 = 36.7 \text{ g/cm}^2$. By looking at the Feynman graphs of these two processes, see Fig. 2.2, it is clear that these are very similar processes. It turns out that the cross section of bremsstrahlung

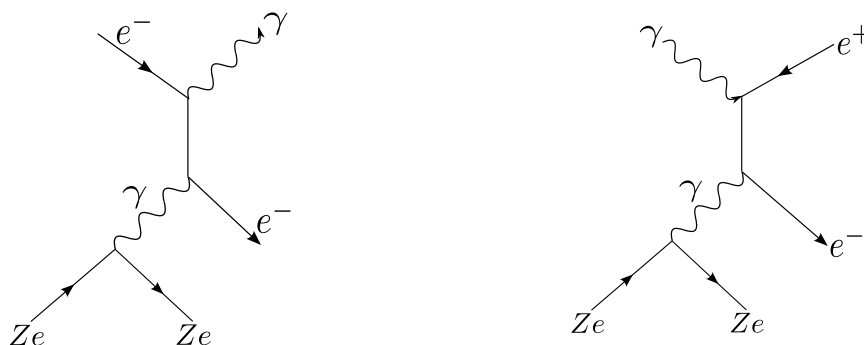


Figure 2.2: Left: Feynman graph for bremsstrahlung. Right: Feynman graph for pair production.

and pair production are related by a constant factor:

$$\sigma_{\text{pair}} = \frac{7}{9}\sigma_{\text{bremsstrahlung}} = \frac{7}{9} \left(\frac{A}{X_0 N_A} \right) \quad (2.4)$$

An electron or photon with very high energy traversing the atmosphere will therefore undergo multiple pair production and bremsstrahlung processes which will create a cascade of particles or an extensive atmospheric air shower.

2.1.2 Air Shower Cascade

As already mentioned the two fundamental processes for the growth of the air shower cascade are pair production by photons and bremsstrahlung by electrons. The scale on which pair production takes place can be defined by the radiation length X_0 . Under the assumption that after every radiation length the particle splits into two, [Heitler, 1954], the particle number or shower size N in a shower can be given by:

$$N = 2^t \quad (2.5)$$

where $t = \frac{x}{X_0}$ is the number of radiation length. The shower maximum is defined as the maximum number of particles which is reached at a depth X_{max} or in radiation length $t_{\text{max}} = X_{\text{max}}/X_0$. This can be defined by the following integral:

$$\int_0^{t_{\text{max}}} 2^t dt = \frac{E_0}{E_c} \quad (2.6)$$

The critical energy basically defines when the shower cascade stops developing. The above equation can be solved to yield:

$$t_{\text{max}} \approx \frac{\ln(E_0/E_c)}{\ln(2)} \quad (2.7)$$

2. THEORY OF AIR SHOWERS

At this depth in the atmosphere the particle number is:

$$2^{t_{\max}} \approx \frac{E_0}{E_c} \quad (2.8)$$

This means that the shower size N is proportional to the incident particle energy. After the shower maximum in this simplified picture it is assumed that the particle number is subject to exponential absorption.

2.1.3 Longitudinal Development

The electromagnetic (EM) cascade theory was originally developed by [Nishimura, 1967], [Kamata and Nishimura, 1958] and [Greisen, 1960], [Greisen, 1956]. In their theory they use two coupled integral-differential equations to describe a one dimensional cascade in the longitudinal direction. The solution to these equations is the shower structure function and is usually referred to as NKG-function. Furthermore Greisen developed an approximation for the number of particles in an electromagnetic shower around the shower maximum (Greisen equation):

$$N_e(X, E_0) = \frac{0.31}{\sqrt{\epsilon}} \exp\left(X \left(1 - \frac{3}{2} \ln(s)\right)\right) \quad (2.9)$$

where s is the shower age with $s = 1$ being the shower maximum and X is the atmospheric depth in g/cm^2 . The shower age s is here defined by:

$$s = \frac{3X}{X + 2\epsilon} \quad (2.10)$$

where $\epsilon = \ln(E_0/E_c)$ with E_c being the critical energy and E_0 the energy of the incident primary particle. For the height of shower maximum the following expression holds [Rossi, 1952]:

$$X_{\max} = 1.01 \left(\ln\left(\frac{E_0}{E_c}\right) - n \right) \quad (2.11)$$

where $n = 1$ if the primary is an electron and $n = 1/2$ if the primary is a photon. Combining eq. (2.11) and eq. (2.9) the number of particles at the shower maximum ($s = 1$) can be described by:

$$N(X_{\max}) \approx \frac{0.31}{\sqrt{\epsilon}} \frac{E_0}{E_c} \quad (2.12)$$

By comparing this with the simplified assumptions in the previous section almost the same dependency of the number of particles at the shower maximum with the energy of

the incident particle can be found. This approximation is based on an electromagnetic cascade theory which includes pair production, bremsstrahlung and ionisation losses but disregards Compton scattering.

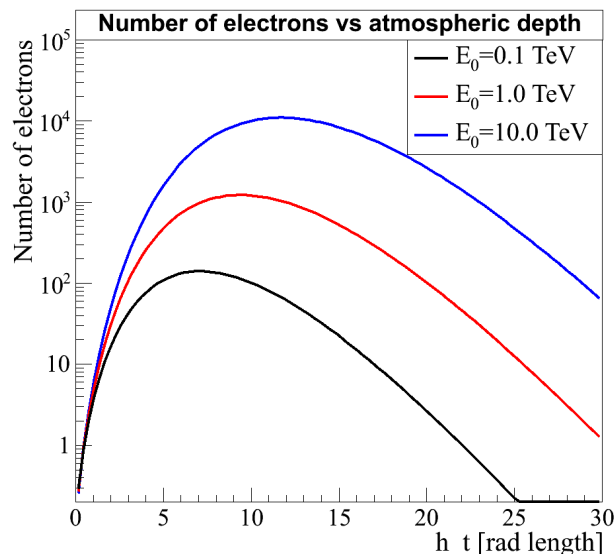


Figure 2.3: Number of electrons as a function of the atmospheric depth in units of the radiation length. Three different initial primary energies are shown. For a vertical shower the atmospheric depth at sea level is about 28 radiation length.

Fig. 2.3 shows the number of electrons as a function of the atmospheric thickness in units of the radiation length. The shower size N is also a function of the angle of incidence (zenith angle θ) and the height of first interaction in the atmosphere, which is the height an incident primary particle initiates an air shower. This is due to the fact that after traversing a column of air corresponding to one interaction mean free path along an inclined trajectory, the particle arrives at a higher altitude than when it traverses the same column density along a vertical direction. The same is of course true for all the secondary particles and hence for the height of the shower maximum. Due to the exponential altitude dependence of the density in the atmosphere, see Fig. 4.2 in section 4.2.1, an inclined trajectory of given column density is physically longer than a vertical trajectory of equal column density. The height of the first interaction of any particle initiating an air shower cascade fluctuates as a function of the interaction length. The extent of the fluctuation is determined by the radiation length in air and

2. THEORY OF AIR SHOWERS

therefore the depth of first interaction is proportional to e^{-x/X_0} . Furthermore fluctuations in the height of the first interaction lead to fluctuations in the height of the shower maximum. Fig. 2.3 illustrates the fact that the shower maximum which corresponds to the maximum number of produced particles shifts to a larger atmospheric depth for increasing primary energy. For example, the shower maximum for a vertical 1 TeV gamma-ray shower occurs at an average altitude of about 8 km. The shower axis is defined when the initial momentum vector of the primary cosmic ray is extended in the direction of the cascade propagation.

2.1.4 Transverse Particle Distribution Development

The lateral spread of particles is more or less symmetrical around the shower axis and is mostly governed by multiple coulomb scattering. In pair production the angle between the primary γ -ray and the resulting electron θ_{pair} is related via the expression $\theta_{\text{pair}} \sim \frac{m_e c^2}{E_e} = \frac{1}{\gamma}$, see [Bethe and Heitler, 1934]. This means at TeV or even GeV energies of the resulting electron or positron, the angle with respect to the incident photon is only a fractional amount of a degree which leads to a negligible transverse momentum transfer in the case of an electromagnetic shower. For multiple coulomb scattering the Moliere radius r_M characterises the lateral spread and a cylinder with this radius contains about 90 % of the total shower energy. It is defined by:

$$r_M = \frac{E_s \cdot X_0}{E_c} = \frac{\sqrt{4\pi/\alpha} m_e c^2 X_0}{E_c} \approx \frac{21 \text{ MeV} \cdot 36.7 \text{ g/cm}^2}{83 \text{ MeV}} \approx 9.3 \text{ g/cm}^2 \quad (2.13)$$

The Moliere radius can be converted to meters using the pressure and temperature at the altitude of interest. At sea level it corresponds to about $r_M \sim 79$ meters and it increases with altitude. One other important aspect of multiple coulomb scattering is the fact that the average deflection angle $\langle\theta\rangle$ is inversely proportional to the energy of the particle $\langle\theta\rangle \sim 1/E$. This means that shower particles of high energy remain concentrated in a narrow cone around the shower axis. The lateral spread of particles in the electromagnetic cascade theory can be described by the so called Nishimura-Kamata-Greisen (NKG) function. This NKG lateral distribution function is valid for an age parameter of $0.5 < s_N < 1.5$. The particle density in a pure electromagnetic shower can be described by:

$$\rho_e(r, s_N, N_e) = \left(\frac{N_e}{r_M^2}\right) \frac{\Gamma(4.5 - s_N)}{2\pi\Gamma(s_N)\Gamma(4.5 - 2s_N)} \left(\frac{r}{r_M}\right)^{s_N-2} \left(1 + \frac{r}{r_M}\right)^{s_N-4.5} \quad (2.14)$$

where

$$s_N = \frac{3}{1 + 2\ln(E/E_c)/t} \quad (2.15)$$

with t being the traversed atmospheric thickness in units of the radiation length X_0 . Fig. 2.4 shows an illustration of the NKG function for three different energies on the left. The number of electrons is calculated from the Greisen function in eq. (2.9). The atmospheric thickness t is calculated for an altitude of 8 km. The radial distance r is the perpendicular distance from the shower axis in meter at the specified altitude. The function is also mirrored by making the substitution $r \rightarrow |r|$.

2. THEORY OF AIR SHOWERS

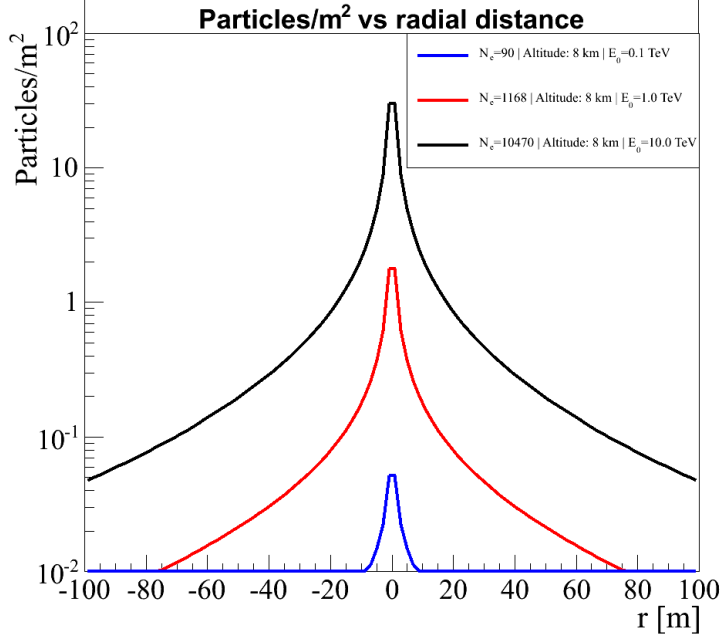


Figure 2.4: Particle density as a function of the radial distance from the shower axis. Three different initial primary energies are shown and the altitude is fixed at 8 km.

2.2 Hadronic Air Showers

2.2.1 Interaction Mechanisms

Since the bulk of the cosmic rays isotropically hitting the earth atmosphere are of hadronic origin (mainly protons) the most abundant air shower is a hadronic shower. In collisions with the atmospheric constituents (mainly nitrogen, oxygen, and argon) the cosmic rays create new or secondary particles which in turn propagate deeper in the atmosphere. The reaction can be seen as a proton-proton interaction which produces mostly pions:

$$p + p \longrightarrow \pi + X \quad (2.16)$$

where X represents any state reachable from the initial state. The cross section for proton-proton interaction at about 4 TeV is $\sigma_{\text{inel}} = 43 \pm 8$ mbarn and for proton-air interaction at the same energy it is $\sigma_{\text{inel}} = 272 \pm 22$ mbarn, see [Aielli et al., 2009]. The interaction mean free path can be defined by:

$$\lambda_{\text{int}} = \frac{A}{N_A \sigma_{\text{inel}}} [\text{g}/\text{cm}^2] \quad (2.17)$$

where A stands for the mass number of the target nucleus and N_A for the Avogadro's number. For nitrogen the interaction mean free path can be calculated to be $\lambda_{\text{int}} \approx 49$ g/cm². It should be noted, however, that the inelastic cross section for proton-proton interaction increases with energy.

2.2.2 Air Shower Cascade

In a hadronic interaction at high energies about 80% of the produced particles are pions with π^+ , π^- and π^0 in a ratio of 1:1:1. About 8% are kaons and neutrons/protons are produced with an overall probability of about 4-5%. The decay length of charged pions is about $c\tau = 7.8$ m and for neutral pions $c\tau = 25$ nm. This means neutral pions will almost immediately decay and feed the electromagnetic cascade via the reaction:

$$\pi^0 \longrightarrow \gamma + \gamma \quad (2.18)$$

Assuming the π^0 is moving with velocity β , the energy of the photons in the lab-frame is given by:

$$E = \gamma (E' + \beta p' \cos\alpha) \quad (2.19)$$

$$\Rightarrow E = \frac{E_{\pi^0}}{2} (1 + \beta \cos\alpha) \quad (2.20)$$

where α is the angle between the velocity of the pion and the emitted photon. The charged pions, however, will usually interact again before they decay into:

$$\pi^\pm \longrightarrow \mu^\pm + \nu_\mu / \bar{\nu}_\mu \quad (2.21)$$

The longlived secondary hadrons, meaning nucleons, charged pions, and kaons, make up the hadronic shower cascade. The muons in an air shower, of which about 90% are produced in the hadronic cascade due to the decay of pions and kaons, propagate through the atmosphere with small energy losses and reach the surface of the Earth almost unattenuated. The unstable mesons decay before making another interaction if their time-dilated decay length $\gamma\beta c\tau$ is shorter than their hadronic interaction length λ_{int} . From this a critical energy for pions can be calculated by:

$$\gamma_\pi \beta_\pi c\tau_\pi \stackrel{!}{=} \lambda_{\text{int}} \quad (2.22)$$

$$\rightarrow E_c = \frac{\lambda_{\text{int}}}{\beta_\pi c\tau_\pi} m_\pi c^2 \quad (2.23)$$

2. THEORY OF AIR SHOWERS

Using a few canonical values for the pions, $\beta_\pi \approx 0.9999$, $m_\pi c^2 \approx 140 \text{ MeV}/c^2$ and with a density of the order 10^{-4} g/cm^3 (at an altitude of 20 km) the critical energy can be calculated to be about $E_c \approx 88 \text{ GeV}$. This critical energy marks the energy at which most charged pions decay. Under the assumption that only pions are produced with the above defined ratio, about one-third of the energy will be transferred via the decay of π^0 particles to the EM shower component. After n generations the energies in the hadronic component is given by [Matthews, 2004]:

$$E_{\text{hadronic}} = \left(\frac{2}{3}\right)^n E_0 \quad (2.24)$$

and for the electromagnetic component:

$$E_{\text{em}} = \left(1 - \left(\frac{2}{3}\right)^n\right) E_0 \quad (2.25)$$

This means that after 6 generations approximately 90% of the initial shower energy is carried by EM particles. The shower maximum in this case is still determined from the electromagnetic component since its particles outnumber all other contributions. Assuming the EM subshower is produced in the first hadronic interaction:

$$X_{\text{max}}^{\text{had}} = \lambda_{\text{int}} + X_{\text{max}}^{\text{em}}(E_0/2n_{\text{tot}}) \quad (2.26)$$

where $X_{\text{max}}^{\text{em}}$ is defined in eq. (2.11) and n_{tot} is the number of new particles produced in a hadronic interaction. The number of electrons at the shower maximum of a hadronic shower corresponds to that of an electromagnetic shower with reduced energy, see eq. (2.25). Fig. 2.5 shows a sketch of the development of a hadronic induced air shower in the atmosphere. This cascade also spreads out laterally due to the transverse momentum of the secondaries and as a consequence of multiple scattering. Secondary hadrons are created on average with a transverse momentum $\langle p_\perp \rangle = 350 - 400 \text{ MeV}/c$. For a hadronic induced air shower the lateral spread of particles shown in Fig. 2.6 is very different from a pure electromagnetic shower. This is due to the fact that in a hadronic induced air shower a superposition of electromagnetic sub-cascades as well as that large transversal momentum transfer take place. This fact can be used to separate hadronic induced air showers from γ -ray induced ones, since the width of the hadronic shower should be wider, see also section 3.4.3.

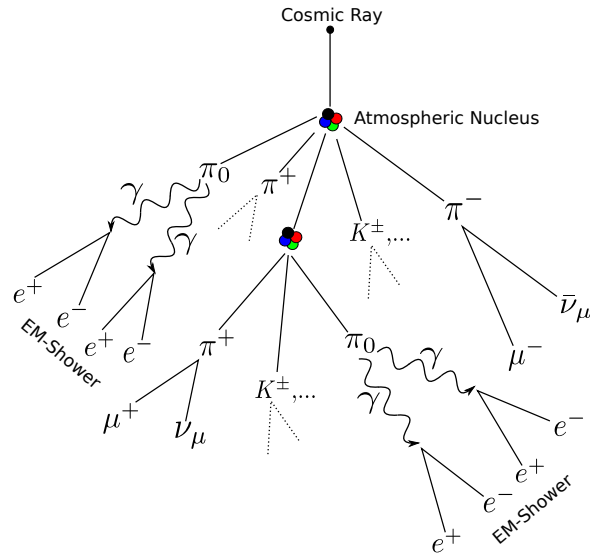


Figure 2.5: Sketch to illustrate the development of an hadronic induced extensive air shower.

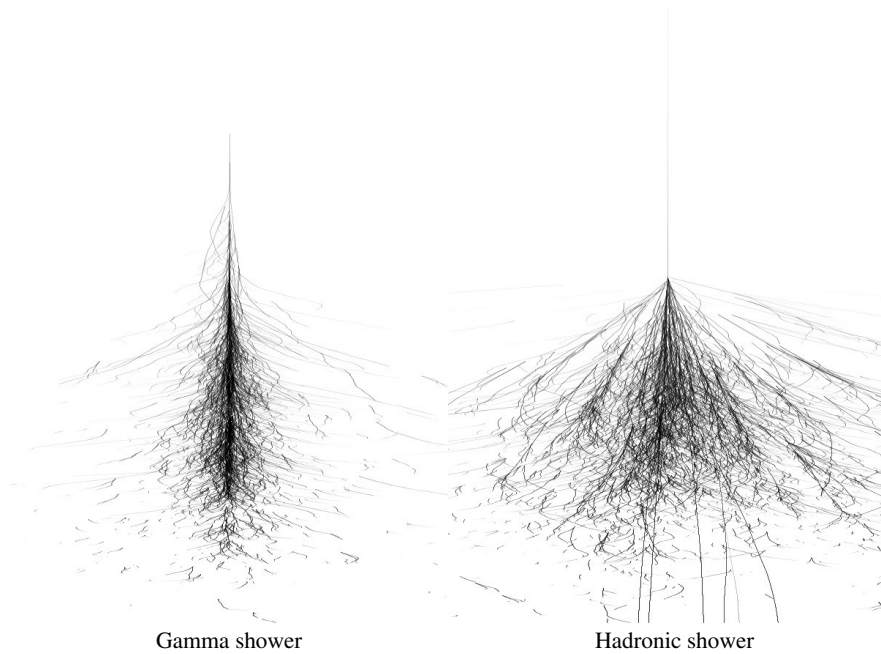


Figure 2.6: Comparison between a γ -ray induced air shower and a hadron induced one. Taken from Voelk and Bernloehr [2009]

2.3 Atmospheric Cherenkov Radiation

All charged particles moving through a dielectric medium cause a polarisation of this medium. Since the speed of light in a medium is reduced by the refractive index of that medium, it can happen that very high energetic particles are moving faster than the local speed of light. Along the particle track dipole fields are created that destructively interfere if the speed of the incoming particle is less than the local speed of light. If it is exceeded, however, the wavelets from all points on the particle track will be in phase with one another under the Cherenkov emission angle defined in eq. 2.28. According to Huygen's principle they will form wavefronts, which is illustrated in Fig. 2.7.

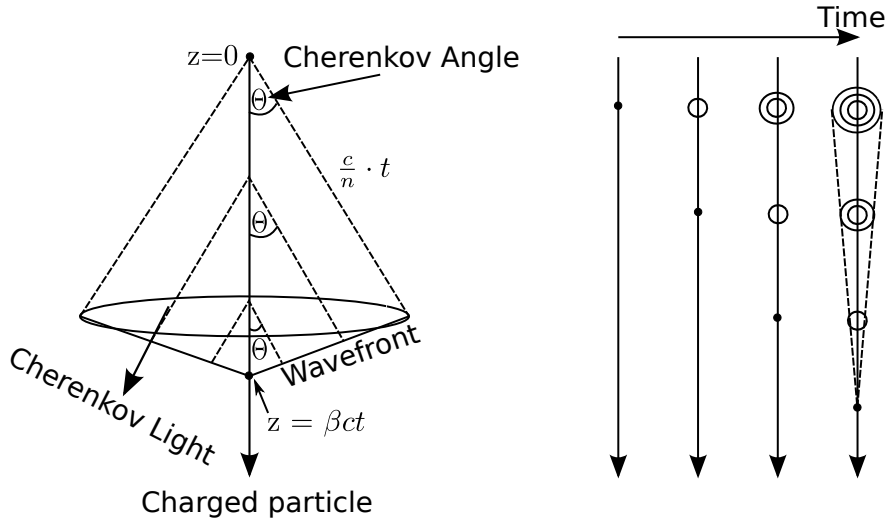


Figure 2.7: The right side shows that the moving particle creates an expanding spherical wavefront. At the time of the next crest, the particle has moved on and begun a new wavelet at that location. This continues, such that the wavefront, the direction of the ray and the particle's trajectory form the three sides of a right-angled triangle (left).

The threshold for Cherenkov radiation is:

$$v_{\text{particle}} > \frac{c}{n} \longrightarrow \beta > \frac{1}{n} \quad (2.27)$$

Looking also at the left sketch in this figure the Cherenkov angle can be calculated by:

$$\cos(\Theta) = \frac{c/n \cdot t}{\beta ct} = \frac{1}{\beta n} \quad (2.28)$$

In the ultra relativistic limit ($\beta = 1$) the maximum angle of emission is $\Theta_{\text{max}} = \arccos(1/n)$. Cherenkov emission will therefore be emitted for all wavelength λ for

2.3 Atmospheric Cherenkov Radiation

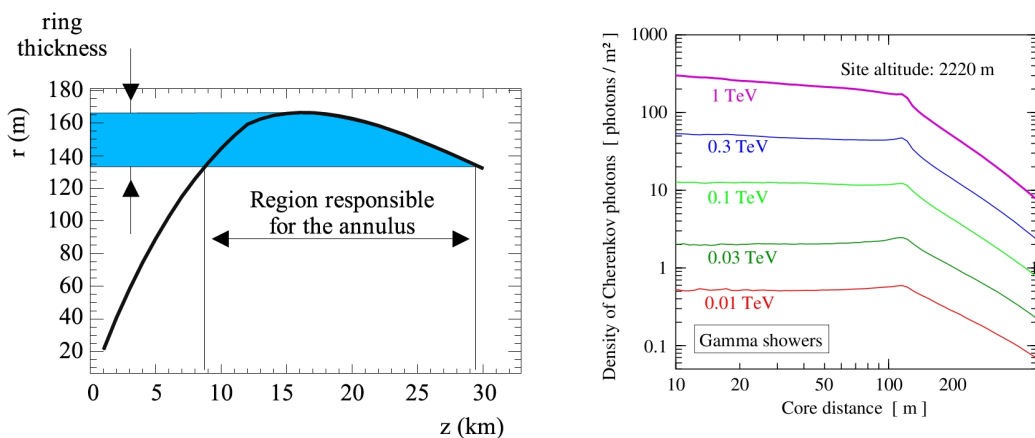


Figure 2.8: Cherenkov ring radius as a function of the emission altitude, taken from [de Naurois, 2006] on the left. On the right the lateral Cherenkov photon density at an altitude of 2220 m for different primary photon energies is shown, courtesy of Konrad Bernloehr

which the condition $\beta n > 1$ holds. The refractive index of air is a function of pressure, temperature and water vapour content. For 0° celsius at 1 atm it is $n \approx 1.000293$ which means that for $\beta = 1$ the Cherenkov angle is $\Theta \approx 1.38^\circ$. This angle decreases with the height in the atmosphere since the pressure and therefore the refractive index also decrease with increasing altitude. This implies that most of the Cherenkov radiation lands on the ground within a radius between 130-170 meters, see Fig. 2.8. The right side of this figure shows the lateral Cherenkov photon density as a function of the core distance. For example a primary photon at TeV energy produces only a few hundred photons per square metre on the ground at an observation level of about 2.2 km above sea level. The number of emitted photons per unit track dx and wavelength $d\lambda$ interval is given by the Frank-Tamm formula:

$$\frac{d^2 N_{\text{ph}}}{dx d\lambda} = 2\pi\alpha Z^2 \frac{\sin^2(\Theta)}{\lambda^2} = \frac{2\pi\alpha Z^2}{\lambda^2} \left(1 - \frac{1}{n(\lambda)^2 \beta^2} \right) \quad (2.29)$$

The dependance of λ^{-2} leads to the fact that most of the emission is in the UV region, for which the atmosphere is mostly opaque due to the ozone absorption. This means that most of the photons are emitted in the visible blue region. It has to be noted that the index of refraction $n(\lambda)$ is also a function of the wavelength but varies only by a few percent in the Cherenkov regime of typically 300 nm up to 600 nm. However, Cherenkov radiation does not necessarily reach the ground due to absorption processes

2. THEORY OF AIR SHOWERS

and scattering. The processes responsible are Mie scattering, Rayleigh scattering and absorption by ozone. Integration of eq. (2.29) between the two wavelengths λ_1 and λ_2 yields:

$$\frac{dN_{\text{ph}}}{dx} = 2\pi\alpha Z^2 \left(\frac{1}{\lambda_1} - \frac{1}{\lambda_2} \right) \cdot \sin^2(\Theta) \quad (2.30)$$

The total Cherenkov yield Q produced by an air shower through the atmosphere down to sea level, neglecting absorption, is given by:

$$Q = \int_{E_{\text{th}}(X)}^{E_0} \int_0^{X_{\text{s.l.}}} N_e(X, E, E_0) \frac{dN_{\text{ph}}(X)}{dx} \frac{dx}{dX} dX dE \quad (2.31)$$

where $N_e(X, E, E_0)$ is the number of electrons of energy E at atmospheric depth X in units of the radiation length. E_0 is the energy of the primary particle, $X_{\text{s.l.}}$ the atmospheric depth at sea level, $E_{\text{th}}(X)$ the threshold energy for Cherenkov radiation at depth X and dx/dX the radiation unit expressed in meters. The threshold energy can be given by $E_{\text{th}}(X) = m_0c^2/\sqrt{1-n(X)^{-2}}$. For electrons and positrons this results in $E_{\text{th}} \approx 20$ MeV at sea level and $E_{\text{th}} \approx 35$ MeV at an altitude of 10 km above sea level.

Assuming the energy spectrum of the electrons is independent of the total number of electrons one can use the approximation given in eq. (2.9). Furthermore, under the approximation that the total number of electrons is equal to the total number of electrons at the shower maximum the Cherenkov yield becomes roughly proportional to the energy of the incident primary particle, eq. (2.32).

$$Q \sim \frac{E_0}{\sqrt{\ln(E_0/E_c)}} \quad (2.32)$$

Fluctuations in the height of first interaction lead also to fluctuations in Cherenkov density at the observation level. This is due to the fact that a shower with a maximum at smaller altitudes result in a higher number of Cherenkov photons since the Cherenkov yield is an increasing function of the refractive index. Since the Cherenkov radiation is of low intensity and has a typical duration of a few nanoseconds, a large mirror area and a fast acquisition system is needed. See section 3.2 for details on both. For details on the mapping of Cherenkov photons onto a camera using the large mirror surface of the H.E.S.S. telescopes see section 3.4.1.

Chapter 3

H.E.S.S.

3.1 Introduction

H.E.S.S. stands for High Energy Spectroscopic System and pays homage to Victor Hess, who received the Nobel Prize in Physics in 1936 for his discovery of cosmic radiation. It is a system of five Imaging Atmospheric Cherenkov Telescopes. Four of them are smaller in size and are operating since 2003. A much larger fifth telescope was built and has been operational since July 2012. Since H.E.S.S. has been in operation it collected over 9400 hrs of data, observing in about equal parts the band of the milkyway and extragalactic space (latitude $> 10^\circ$)¹. Over 80 very high energy gamma ray sources were detected by H.E.S.S. alone, among them more than 60 galactic objects and 19 extragalactic sources². Fig 3.1 shows a TeVcat skymap with all sources discovered by H.E.S.S. by July 2013. The inner 60° around the center of the milkyway reveals that in this region most sources are either Supernova Remnants (SNRs), Pulsar Wind Nebulae (PWN) or unidentified, meaning only seen in VHE gamma-rays. Indeed the most abundant source type in our galaxy are PWN which are giant bubbles filled with electrons and positrons created by spinning neutron stars.

¹As of September 2012

²See also <http://tevcat.uchicago.edu/> for updates

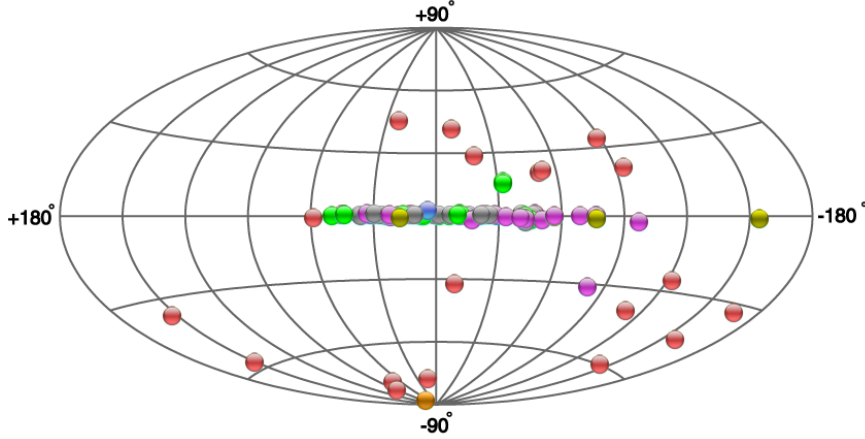


Figure 3.1: TeVCat sky map of γ -ray sources discovered by H.E.S.S. (July 2013). The colors indicates the likely nature of sources: Supernova Remnants (green), Pulsar Wind Nebulae (violet), Binaries (yellow), Star Cluster/Star forming regions (blue), Unidentified (grey), Starburst Galaxy (orange), Active Galactic Nucleus (red). Taken from <http://tevcat.uchicago.edu/>

3.2 H.E.S.S. Telescope Array

The H.E.S.S. Telescope Array is located in the Khomas Highlands near Gamsberg in Namibia. Each of the smaller four telescopes is identical in construction and they are arranged in a square of 120 m side length. This length was chosen in consideration of the fact that the Cherenkov light pool is approximately 250 m in diameter and to ensure a stereoscopic view of the same air shower. The much larger fifth telescope was added to the existing four and placed in the centre of the array with the goal to improve the sensitivity at lower energies. Fig. 3.2 shows a picture of the site.

3.2.1 Telescopes

All the telescopes use an alt-azimuth mount which is controlled electronically to point the telescopes at any given position in the sky. The telescope structure is made of steel and it has a steel dish with a diameter $D=13$ m supporting the mirrors which amounts to a total of 107 m^2 mirror surface for the smaller H.E.S.S. Phase I telescopes. With typically 100 Cherenkov photons per m^2 at 1 TeV at the height of the H.E.S.S. site, assuming a typical photodetector efficiency around 10 %, this mirror area will ensure images of the order of thousand detected photons. Since at least 50 to 100 detected



Figure 3.2: H.E.S.S. Telescope Array in Namibia. Photo by Mathieu de Naurois

photons are required to reconstruct a shower image, a threshold energy around 100 GeV can be expected [Bernloehr et al., 2003]. The mount rotates on a steel rail and achieves a maximum speed of 100° per minute. There are 380 individual mirrors on each dish with a size of 60 cm diameter each. The average reflectivity of the mirrors is $\approx 80\%$ ($\lambda > 330$ nm). Each mirror is made of aluminised glass with a quartz coating and all of them are arranged in a Davies-Cotton [Davies and Cotton, 1957] design. The total mirror area focuses the Cherenkov light with a focal length of $f = 15$ m. In order to focus the telescopes at the typical distance of the height of the shower maximum ($H \approx 8$ km), H.E.S.S. (Phase I) cameras are located at a distance of $f/(1 - f/H) \approx 15.03$ m. The pixel size of the cameras can be approximated by a circle with a diameter of about 0.042 m. To calculate the depth of field (DOF) for the telescopes, Fig. 3.3 is helpful. From similar triangles the following expressions can be derived.

$$\frac{v_N - v}{v_N} = \frac{c}{D} \Rightarrow v_N = \frac{v}{1 - c/D} \quad (3.1)$$

$$\frac{v - v_F}{v_F} = \frac{c}{D} \Rightarrow v_F = \frac{v}{1 + c/D} \quad (3.2)$$

3. H.E.S.S.

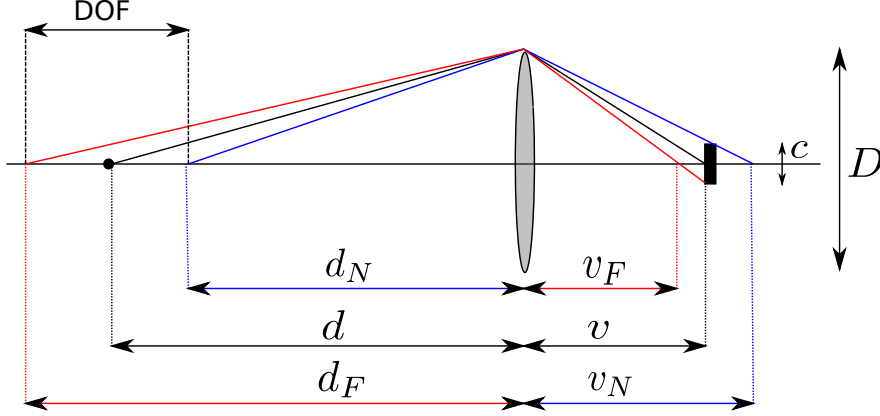


Figure 3.3: Sketch of depth of field (DOF) derivation.

Using the lens equation $\frac{1}{d} + \frac{1}{v} = \frac{1}{f}$ and the fact that $f \ll d$, the near and far depth of field can be calculated to be:

$$d_N = \frac{df^2}{f^2 + \frac{fc}{D}(d-f)} \approx \frac{d}{1 + cd/(fD)} \quad (3.3)$$

$$d_F = \frac{df^2}{f^2 - \frac{fc}{D}(d-f)} \approx \frac{d}{1 - cd/(fD)} \quad (3.4)$$

Assuming defocusing by half of a pixel diameter $2c = p \approx 0.021$ m is acceptable, and using $d = H \approx 8$ km it follows $d_N \approx 5.6$ km and $d_F \approx 14.1$ km.

The H.E.S.S. Phase II telescope structure follows the same principles but has a 28 m dish resulting in a mirror surface area of about 614 m^2 . This increase in mirror area allows for much higher sensitivities at lower energies of approximately 20 – 100 GeV, [Becherini and Punch, 2012].

3.2.2 Cameras

Each of the H.E.S.S. Phase I cameras are approximately octagonal in shape, fitting in a cylinder of 2 metres in length and 1.6 metres in diameter, see Fig. 3.4. It is comprised of 960 photo-multiplier tubes (PMTs) arranged in drawers of 16 PMT each, and weighs about 900 kg in total. In front of the PMTs are Winston Cones which serve the purpose of limiting the solid angle to reduce noise due to stray light. The H.E.S.S. Phase II camera offers better resolution than that of the H.E.S.S. Phase I cameras. First of all, the field of view (FoV) is a bit smaller than that of the H.E.S.S. Phase I cameras,

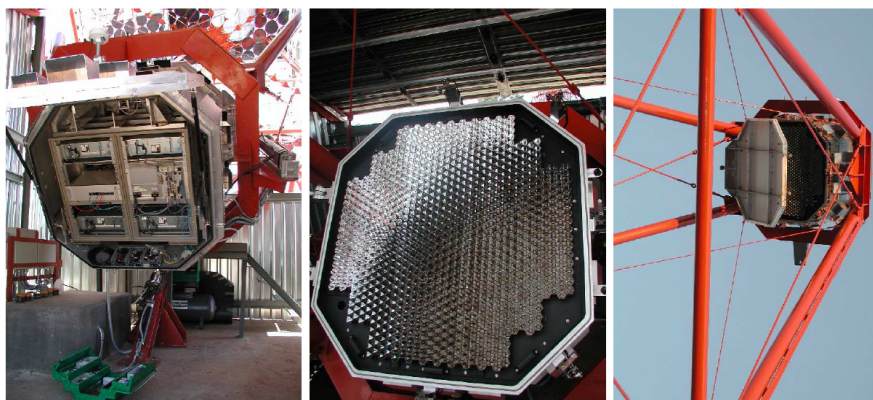


Figure 3.4: H.E.S.S. Phase I camera, taken from [Vincent et al., 2003]

3.5° instead of 5°. Additionally the H.E.S.S. Phase II camera has substantially more pixels (2048) than the H.E.S.S. Phase I cameras (960). The smaller FoV combined with the larger number of pixels lower the FoV seen by one pixel from 0.16° to 0.07°. Since in this thesis only data from the H.E.S.S. Phase I telescopes are used no more specifications for the Phase II telescope are given. Each pixel of the H.E.S.S. Phase I camera has three channels, one trigger channel and two acquisition channels. Those two acquisition channels have different gains. The high-gain (HG) channel is used to detect signal charges up to 200 photoelectrons (p.e.) whereas the low-gain (LG) channel is used to cover the range from 15 to 1600 p.e.. The analogue signal is then sampled in an Analogue Ring Sampler (ARS) initially developed for the ANTARES experiment [Vincent et al., 2003]. The signal from a triggered pixel is read from the analogue ring sampler memory in a window of 16 ns and then digitized with a 12-bit ADC and stored in an FPGA chip. This relatively short exposure time is needed due to the short time scales of Cherenkov light flashes (order of a few nanoseconds). Even at higher energies most of the Cherenkov light can be collected within a $\sim 15\text{-}20$ ns time window per pixel. However, the time spread for photons coming from a distant 10 TeV shower can be as large as 200 ns which means that either a large buffer section of the analogue ring sampler memory has to be readout or a significant amount of the signal is not recorded for those showers, see [Bernloehr et al., 2012]. With a fixed integration or readout window, the relative error on the integrated charge from the contribution of the night sky background is around a minimum of 16 ns.

3. H.E.S.S.

Source	Trigger Rate [Hz]
Hadronic Background	~ 200
Gamma-rays from the Crab Nebula	0.5

Table 3.1: Lists the mean system trigger rate of the telescope array for hadronic cosmic ray background and for γ -rays coming from the Crab Nebula at 40° zenith. The trigger requires a coincidence of 3 pixels in a trigger sector with more than 4 p.e. in each photo-multiplier of the telescope camera, taken from [Aharonian et al., 2006a]

3.2.3 Trigger

The Trigger-System of H.E.S.S. is split into two levels. The first is a camera level trigger for each telescope alone and the second level is basically a coincidence level trigger among all the telescopes in the array. Each camera is divided into 38 overlapping sectors, each containing 64 pixels. Within one sector the typical requirement for triggering the readout of a telescope is that a minimum number of pixels (2-4) exhibit a signal larger than a given threshold (around 4 p.e.) within a short time window (1.3 ns). The second level is called the central trigger system (CTS) and helps greatly in reducing random triggers from the night sky and hadronic CR background. Essentially the CTS requires a coincidence of at least two telescopes in a trigger window of about 80 ns. The Night Sky Background (NSB) consists of a number of different sources of light which are anthropogenous light, atmospheric nightglow, zodiacal light, starlight, diffuse galactic light and extragalactic light, see [Schlenker, 2001] for details. Table 3.1 summarizes the trigger rate for γ -rays coming from the Crab Nebula and hadronic cosmic rays (hadronic background). The trigger requires a coincidence of 3 pixels in a trigger sector with more than 4 p.e. in each photo-multiplier of the telescope camera.

3.2.4 From Raw Data to DST

Once the CTS has accepted the event, the collected charges from each pixel in each camera of the participating telescopes are readout and sent to a computer farm for further processing. The event information for the separate telescopes is merged and stored in the so called raw data format, meaning that no data calibration has been done yet. The event size from the H.E.S.S. Phase I cameras can be approximated:

$$200\text{Hz} \times 2.7\text{Telescopes} \times 960\text{Pixels} \times 2\text{Channels} \times 4\text{byte} \approx 4\text{MB/s}$$

In addition to this raw data, monitoring data is also produced by other subsystems and used in the analysis as a control of the instrument, i.e. various atmospheric parameters to assess the quality of the data in the analysis later on. The data acquisition system (DAQ) serves to collect data from the telescopes and acts as a monitoring interface between all subsystems of the instruments on site. Once collected, it is processed by the DAQ and a real time analysis is performed. See also [Balzer et al., 2014] One typical so called run of observation is 28 minutes long which then amounts to about 6.5 GB of data, which is usually compressed a bit further. The number of observation runs per night differs of course depending on the observational conditions. For each period of data taking of about 29 days, following the moon cycle, the entire data will be stored on tapes amounting to about 500-800 runs. Not all of them are observation runs, because a few calibration runs have to be taken every period. Later the tapes are sent to Heidelberg (Germany) and Lyon (France) where they are properly calibrated to ensure that the physical results are correct. Then they are made accessible for the rest of the collaboration.

3.3 Data Calibration

Since the amount of Cherenkov light is proportional to the primary energy of the particle initiating the air shower, see section 2.3, a careful conversion from the collected charge of the PMTs to the number of photons has to be deployed. The following Fig. 3.5 outlines the steps needed for this conversion. The electronic signal of the PMTs has

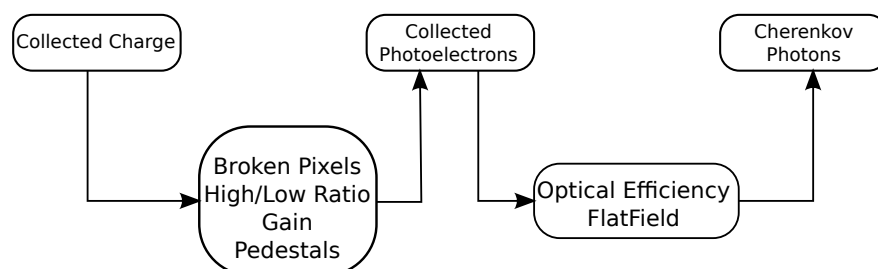


Figure 3.5: Sketch of the Calibration procedure

the units of analog-to-digital converter (ADC) counts. Which basically means that if a photon enters a PMT, the photo effect converts it into an electron, which is then

3. H.E.S.S.

multiplied by the dynodes, using high voltages and converted from an analog to a digital signal via an ADC.

The calibration steps in order to get the collected number of cherenkov photons are:

- Determine the electronic baseline or pedestal which basically defines zero p.e.
- Afterwards the gain calculation converts the ADC counts into p.e.
- The High to Low Gain ratio is used to calibrate the different channels relatively to each other
- Another important step is to check for broken pixels, i.e. Analogue Ring Sampler chip not synchronised, PMTs without signal or HV switched off because of bright stars
- The FlatField coefficient corrects different optical and quantum efficiencies between pixels within a camera.
- The last step is the conversion of detected p.e. into a number of Cherenkov photons using the optical transmission efficiency of the system. This can be obtained from the measurements of the signal generated by muons crossing the telescope

The ADC counts are measured in both channels. The calculation of the amplitude in p.e. received by every pixel is expressed as:

$$\begin{aligned} S_{HG} &= \frac{ADC_{HG} - P_{HG}}{\gamma_{HG}} \cdot FF \\ S_{LG} &= \frac{ADC_{LG} - P_{LG}}{\gamma_{HG}} \cdot \frac{HG}{LG} \cdot FF \end{aligned} \quad (3.5)$$

ADC_{HG} and ADC_{LG} are the measured charges for the high and low gain channels.

P_{HG} and P_{LG} are the ADC position of the baseline for both channels (pedestal positions).

FF is the FlatField coefficient and $\frac{HG}{LG}$ is the amplification ratio of the high gain to the low gain channel.

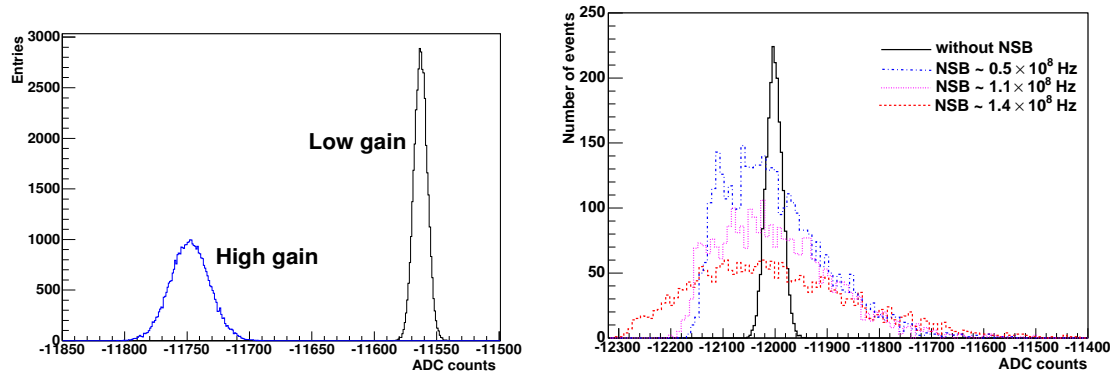


Figure 3.6: Left: Electronic dark pedestal for the low and high gain channel. Right: Pedestal variation versus the level of the Night Sky Background (NSB). Taken from [Aharonian et al., 2004a]

3.3.1 Pedestal

The dark or electronic pedestal position is defined in the absence of any Cherenkov light. Electronic noise creates a Gaussian ADC distribution whose mean is the pedestal position, see left side of Fig. 3.6. However, temperature variations have an impact on the pedestal position which therefore needs to be calculated for all channels regularly. Another effect which has an influence on the pedestal is the illumination by the Night Sky Background (NSB) photons, see right side of Fig 3.6. In normal operations, there is over 1 p.e. of NSB per readout window. See also [Aharonian et al., 2004a] for further details.

3.3.2 Gain

The gains of the PMTs are calibrated using a flashing LED without contamination by the NSB. It illuminates the camera with an intensity of about 1 p.e./pixel. This allows the measurement of the single photoelectron peak on the PMTs. For the gain calibration only the high gain channel is used, due to the fact that it has the higher resolution and the illumination is too faint to be seen in the low gain channel. This procedure is done in a special run called single photoelectron run.

3. H.E.S.S.

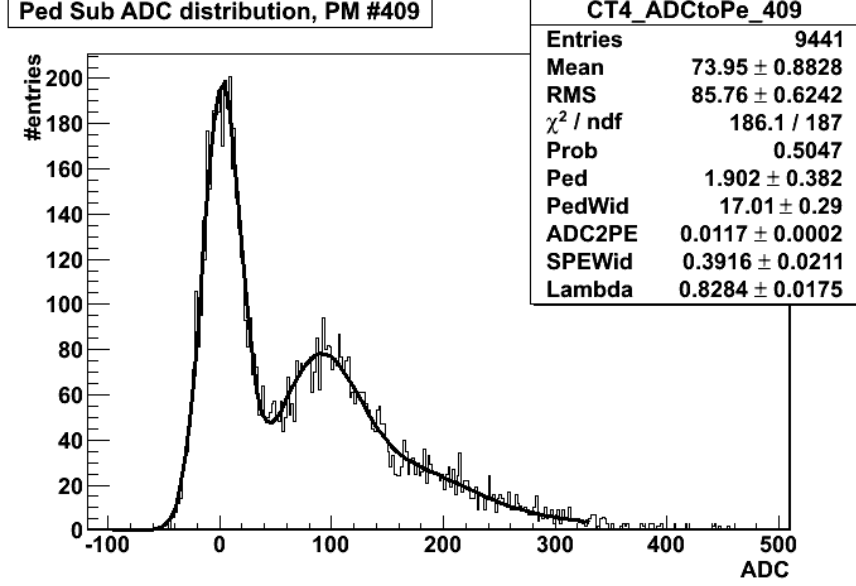


Figure 3.7: Example of an electronic pedestal corrected ADC count distribution for a single p.e. run. In this case the Gain γ_{HG} would be about 85 ADC per p.e. and corresponds to the distance from first to second peak.

The fit function is defined as follows:

$$\mathcal{G}(x) = N \times \left(\frac{e^{-\mu}}{\sqrt{2\pi}\sigma_P} \exp\left[-\frac{1}{2}\left(\frac{x - P_{HG}}{\sigma_P}\right)^2\right] + \kappa \sum_{n=1}^{m \gg 1} \frac{e^{-\mu}}{\sqrt{2\pi(\sigma_P^2 + n\sigma_{\gamma_e}^2)}} \frac{\mu^n}{n!} \exp\left[-\frac{1}{2}\frac{(x - (P_{HG} + n\gamma_{HG}))^2}{\sigma_P^2 + n\sigma_{\gamma_e}^2}\right] \right) \quad (3.6)$$

- The first term describes the electronic pedestal and is approximated by a Gaussian with a standard deviation σ_P and with a mean position in ADC counts of P_{HG} . This assumes that the electronic noise is smaller than the width of the single photoelectron distribution.
- The second term assumes that the photoelectrons follow a Poisson distribution. This is then convoluted with Gaussian of increasing width, representing the resolution of the PMT for a signal of n p.e..

Furthermore, N is the fixed total number of events in the run. σ_P is the pedestal and σ_{γ} the single photoelectron peak width. γ_{HG} is the gain and P_{HG} is the pedestal position in the high gain channel. μ corresponds to the average number of photoelectrons per

event and κ should be equal to 1 for a true Poissonian distribution. Fig. 3.7 shows an example of an ADC count distribution for a single photoelectron run (corrected for the shift of the electronic pedestal) for telescope 4 and pixel number 409. The gain in this case would be $1/\text{ADC2PE} = 1/0.0117 \approx 85$ ADC counts per p.e.. The resolution of the PMT of pixel 409 is also given to be $\text{SPEWid} \approx 39\%$ and is defined as the ratio of the single photoelectron width normalized to the gain. Average calibration coefficients can be calculated by averaging all single photoelectron runs over a period of observation.

3.3.3 Flat Fielding

As already mentioned the FlatField coefficient corrects different optical and quantum efficiencies between pixels within a camera. Its purpose is to calibrate a uniform response of all pixels inside the camera. This can essentially be done by homogeneously illuminating the camera with a UV-Laser or a flashing LED in front of a diffuser. There are dedicated runs to calculate the FlatField coefficient.

3.3.4 Optical Efficiency

Muons are created in great abundance from hadronic air showers via the decay of charged pions and kaons. They can easily penetrate deeply into the earth and produce Cherenkov light on their way through the atmosphere. If a muon passes directly through one of the telescope mirrors a ring-like image can be seen in the camera. These ring-shaped images can be easily distinguished from other air shower events. The amount of Cherenkov photons from such a muon event can be calculated from several geometrical parameters and can therefore be used to calculate the optical efficiency of the telescope:

$$\epsilon = \frac{N_{\text{p.e.}}}{N_{\gamma}} \quad (3.7)$$

This is simply the ratio of the number of measured p.e. inside the ring-shaped image to the calculated number of expected Cherenkov photons.

3.3.5 NSB and Image Cleaning

Before any reconstruction of shower parameters can be done each image in the camera needs to be cleaned to remove pixels containing only NSB noise. To that end the actual NSB rate in each pixel which is possibly influenced by a star in the field of view

3. H.E.S.S.

of that pixel needs to be known. There are two methods, the first estimates the NSB from the pedestal width, see Fig. 3.6, and the second one uses the total current drawn by each PMT from the HV supply (HVI). Both methods are described in detail in [Aharonian et al., 2004a]. In order to identify pixels corresponding to an air shower event the so called tail-cuts are deployed. This is done as follows. Pixels containing more photoelectrons than c_{high} with a neighbouring pixel above c_{low} are kept in the image. Also, pixels containing more photoelectrons than c_{low} but less than c_{high} with a neighbouring pixel above c_{high} are kept in the image. To remove any additional NSB noise only pixels with an intensity of more than 3σ of the pedestal RMS are kept. The tail-cuts are typically based on two threshold values $c_{high} = 10$ p.e. and $c_{low} = 5$ p.e.. The following Fig. 3.8 shows the comparison between an image with NSB and a cleaned image.

In this work, however, an extended cleaning method is used. The threshold for the cleaning is lowered to $c_{high} = 7$ p.e. and $c_{low} = 4$ p.e. and after that two additional rows of pixels around the cleaned image are added back to create a so called extended image, see Fig. 3.9. This is done in order to have information in the surroundings of the shower image needed later for the fit of a γ -ray air shower parameterisation image explained in chapter 4.

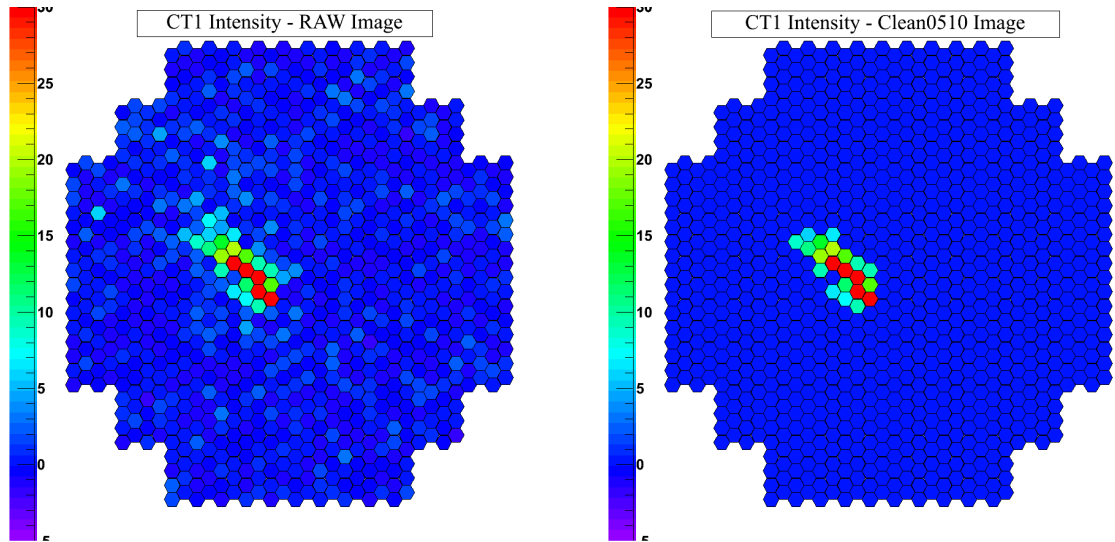


Figure 3.8: Raw image of a MC shower event with NSB noise in the entire camera on the left. The right shows the same shower after the cleaning procedure of the 5-10 p.e. tail-cuts which is used to calculate the Hillas parameters.

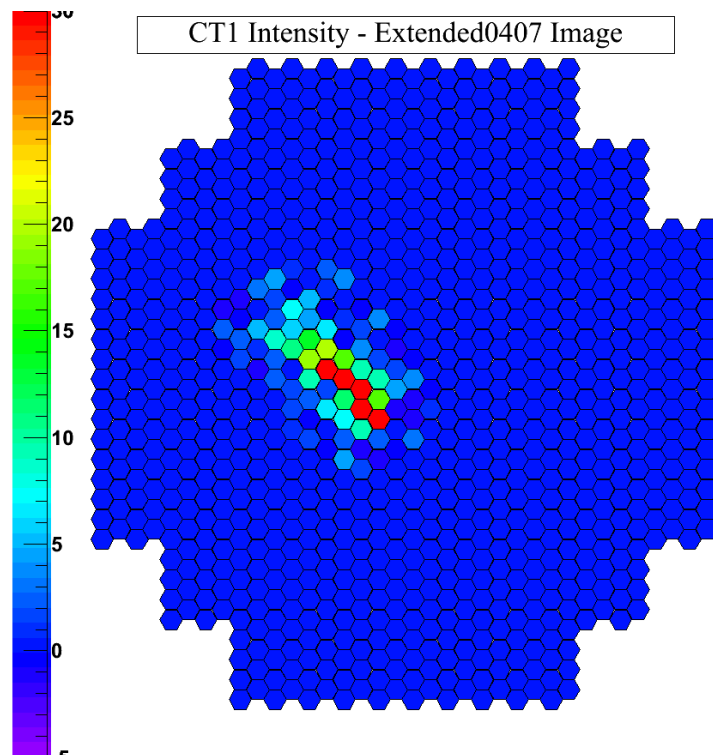


Figure 3.9: Extended cleaning used throughout this work which deploys 4-7 p.e. tail-cuts as well as an extension of the resulting image by two additional rows of pixels.

3.4 Data Analysis

The main goal of the data analysis is the reconstruction of shower parameters to obtain the direction of the incoming γ -ray, the height of first interaction, the impact point on the ground and also its energy. From a precise reconstruction of the height of first interaction it would be possible to separate γ -showers from electron-showers. An accurate determination of the γ -ray direction is important for the classification of sources and to resolve their structure. Furthermore the energy reconstruction is highly important for the determination of the energy spectrum of a given source.

3.4.1 Hillas Reconstruction

The mirrors mounted on each H.E.S.S. telescope map the Cherenkov light on a camera located at a distance which is about the focal length of the system, see section 3.2.1. The following Fig. 3.10 illustrates this mapping. An incident Cherenkov light ray with an opening angle of ϕ emitted at a position (x_1, z_1) will be reflected under the same angle onto a point (u_1, v_1) in the focal plane of the camera.

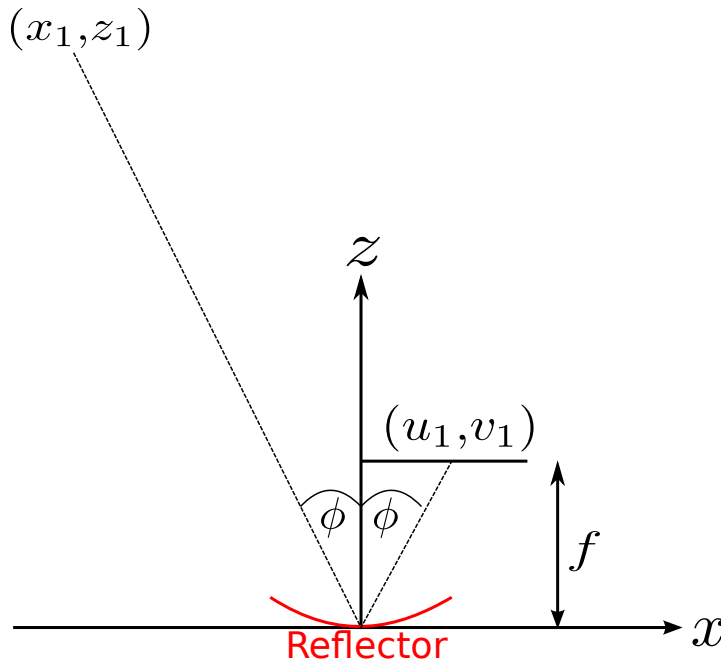


Figure 3.10: Principle of mapping Cherenkov light onto a distance approximately equal to the focal length of the telescope system.

The following equation describes this mapping, in which f is the focal length.

$$\tan(\phi) = \frac{x_1}{z_1} = -\frac{u_1}{f} \quad (3.8)$$

In general the relationship of the coordinates in the focal plane (u,v) to a point (x,y,z) in the atmosphere is defined by:

$$\begin{pmatrix} u \\ v \end{pmatrix} = -\frac{f}{z} \begin{pmatrix} x \\ y \end{pmatrix} \quad (3.9)$$

Since the units are in meter with this definition they are usually divided by the focal length yielding angles, which means this mapping measures the angular distribution of the emitted Cherenkov light.

The emission region of Cherenkov light in an air shower can be approximated by an ellipsoid. This ellipsoid will then be mapped onto the focal plane through the telescope mirrors. The principal imaging is illustrated in Fig. 3.11. The sketch on the left shows this ellipsoid in the plane spanned by the shower axis and the telescope z-axis. Cherenkov light with different emission height will be mapped on different points along the projected shower axis in the focal plane. The angular difference of these two points are defined as $\Delta\phi = \phi_1 - \phi_2$, which is basically the length of the shower image in the camera. Here, point A will be mapped closer to the center of the camera and point B farther away.

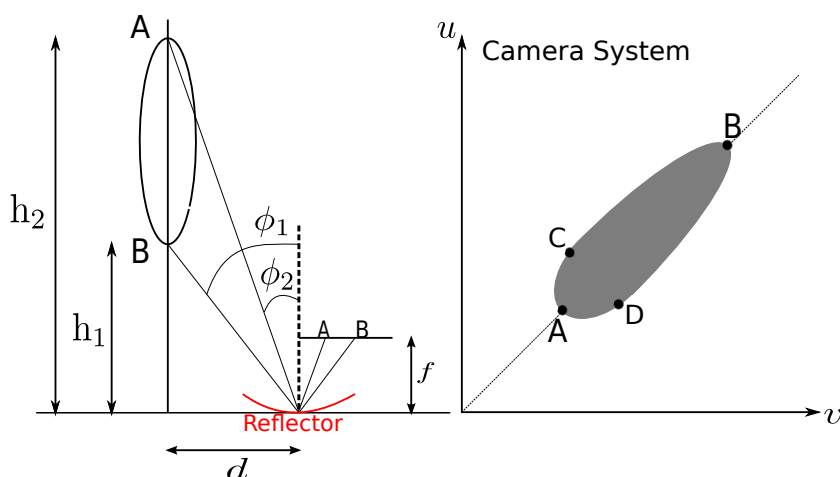


Figure 3.11: Principle of imaging the Cherenkov light of an air shower onto the camera of the telescopes.

3. H.E.S.S.

The shower impact distance d on the ground is usually, depending on the energy and the inclination of the shower, much smaller than the emission height and therefore eq. (3.8) can be approximated by $\phi \approx \frac{d}{h}$. This means that moving the same shower farther away from the telescope (increasing d) the shower image in the camera will be stretched proportionally to the distance between the shower impact point and the telescope. This in turn moves the shower image farther away from the camera center. One other important aspect of the imaging in eq. (3.9) is that the coordinates (u,v) in the camera are inversely proportional to the height of the emission. This has the effect that by going down in emission height the image points are extended to the outside of the camera (meaning the shower image becomes stretched). This effect is illustrated in Fig. 3.11 on the right side. The points C and D indicate the transversal width of the shower ellipsoid mapped symmetrically around the shower axis in the camera since they come from the same height. Even though the shape of the image in the camera is asymmetrical it can be approximated by an ellipse since the longitudinal extension is larger than the lateral extension of the shower.

This is the basic idea of the Hillas reconstruction which is described in [Hillas, 1985]. There are 6 different parameters, the Hillas Length L and Width W describe the length

- Length L and Width W
- Image Size
- Nominal Distance n_d
- Orientation Angle α

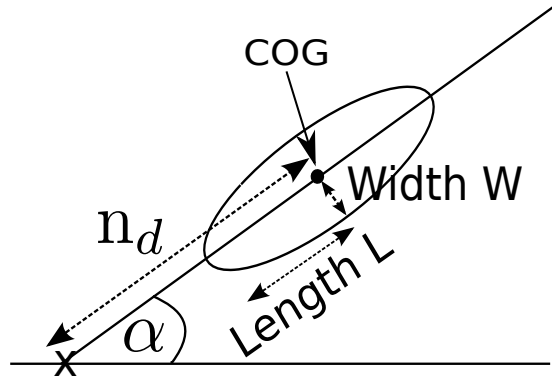


Figure 3.12: Sketch of the Hillas reconstruction parameters.

and width of the ellipse. The Image Size corresponds to the total image intensity in p.e., the Nominal Distance is the distance of the camera center from the Center Of Gravity (COG) and the Orientation Angle is the angle of the shower axis. The determination of all these parameters can be done by calculating first and second moments of the image.

Let $I(x, y)$ be the Intensity at a position (x, y) in the camera, the raw image moments can then be calculated as follows:

$$M_{ij} = \sum_x \sum_y x^i y^j I(x, y) \quad (3.10)$$

This yields for the first and second moments:

$$\langle x \rangle = \frac{M_{10}}{M_{00}} \text{ and } \langle y \rangle = \frac{M_{01}}{M_{00}} \quad (3.11)$$

$$\langle x^2 \rangle = \frac{M_{20}}{M_{00}}, \langle y^2 \rangle = \frac{M_{02}}{M_{00}} \text{ and } \langle xy \rangle = \frac{M_{11}}{M_{00}} \quad (3.12)$$

The variances and covariances read:

$$\sigma_{x^2} = \langle x^2 \rangle - \langle x \rangle^2, \sigma_{y^2} = \langle y^2 \rangle - \langle y \rangle^2 \text{ and } \sigma_{xy} = \langle xy \rangle - \langle x \rangle \langle y \rangle \quad (3.13)$$

By defining:

$$\alpha = \sigma_{x^2} - \sigma_{y^2} \quad (3.14)$$

$$\beta = \sqrt{\alpha^2 + 4\sigma_{xy}^2} \quad (3.15)$$

the Hillas Width and Length can then be calculated by:

$$L = \sqrt{\frac{\sigma_{x^2} + \sigma_{y^2} + \beta}{2}} \quad (3.16)$$

$$W = \sqrt{\frac{\sigma_{x^2} + \sigma_{y^2} - \beta}{2}} \quad (3.17)$$

The longitudinal extend of the shower (shower length) is related to the major axis of the ellipse which is the Hillas Length and the lateral extend is related to the Hillas Width. Another correlation is the distance n_d (distance of the camera centre from the COG of the ellipse) with the distance d (distance between the shower impact point on the ground and the telescope), which is called the impact parameter. The first major drawback of this approach is that it heavily depends on the image cleaning procedure since only pixels contributing to the shower image need to be taken into account. The second drawback is that this method is subject to biases from non-operational pixels or the camera border. An extra distance cut from the COG to the camera centre has to be deployed. This is done in order to get rid of truncated events due to the camera edges, which would otherwise lead to large uncertainties and misestimations in the reconstruction of the Hillas parameters.

3.4.2 Direction Reconstruction

The major axis of the ellipse points in the direction where the shower came from which means that the origin of the shower is located on this axis. If at least two telescopes observe the shower simultaneously, the shower direction can be calculated by intersecting the major axis of the ellipses from the different cameras. This means a stereoscopic approach is used which greatly improves the accuracy of the reconstructed direction. Fig. 3.13 illustrates the reconstruction of the shower direction. The impact point of the shower on the ground (core position) can be determined in a similar way.

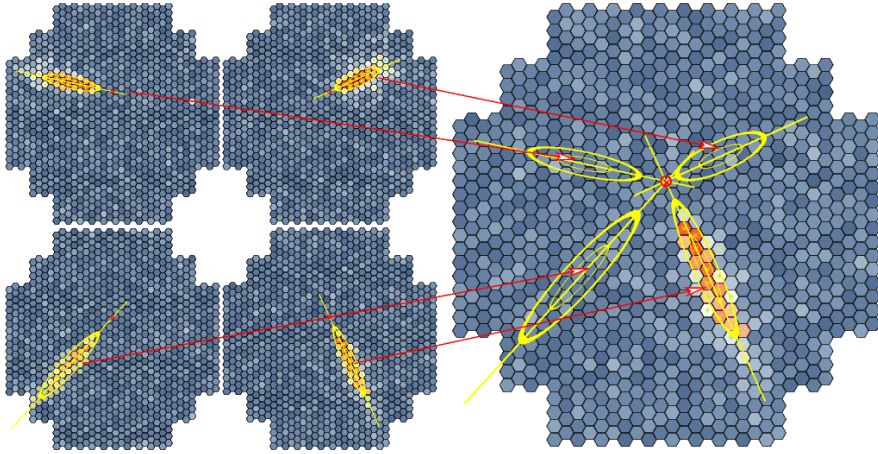


Figure 3.13: Illustrates the principle of the direction reconstruction by intersection of the major axes of the ellipses.

3.4.3 Background Rejection

Since the majority of recorded events result from hadronic cosmic-rays the goal of the background rejection is to significantly reduce its number while almost keeping all the events initiated from γ -rays. The Hillas parameters also provide some discrimination between γ -ray candidates and hadrons. This is done by calculating scaled variables for the Hillas Width (SCW_i) and Length (SCL_i), for each image (telescope i) with a given size and impact distance. Let σ_{W_i} and σ_{L_i} be the standard deviations of the Hillas Width (W_i) and Length (L_i).

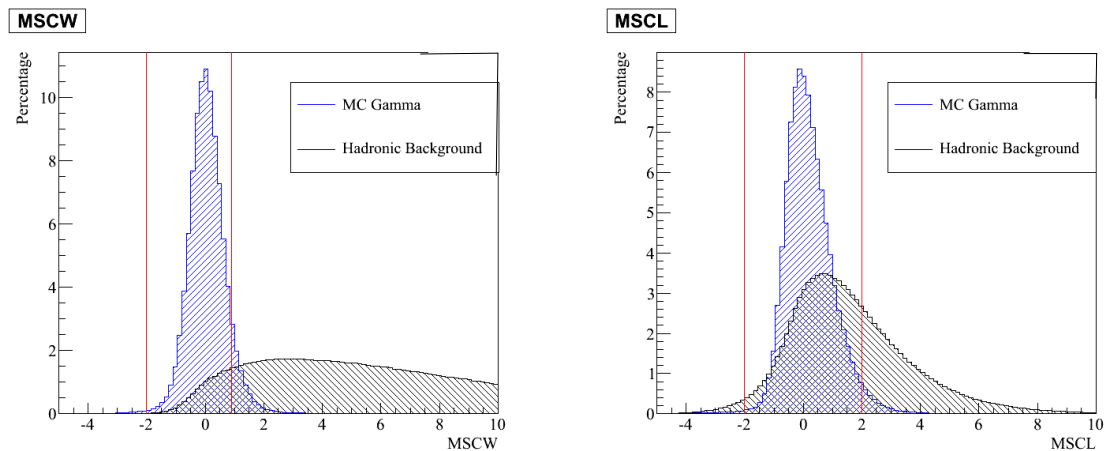


Figure 3.14: Hillas MSCW and MSCL distributions for MC γ -rays simulated at 0° zenith in blue and real hadronic background in black. The red vertical lines indicate the standard Hillas cuts. The distributions are normalized to the total integral.

With the expectation values, $\langle W_i \rangle$ and $\langle L_i \rangle$, obtained from γ -ray simulations the following expressions can be defined:

$$\begin{aligned} \text{SCW}_i &= (W_i - \langle W_i \rangle) / \sigma_{W_i} \\ \text{SCL}_i &= (L_i - \langle L_i \rangle) / \sigma_{L_i} \end{aligned} \quad (3.18)$$

By weighting SCW and SCL with $\omega_{W_i} = \frac{\langle W_i \rangle^2}{\sigma_{W_i}^2}$ and $\omega_{L_i} = \frac{\langle L_i \rangle^2}{\sigma_{L_i}^2}$ respectively and summing over all participating telescopes the mean reduced scaled parameters for Hillas Width can be defined by:

$$\text{MSCW} = \frac{\sum_{i=1}^{N_{tel}} \text{SCW}_i \times \omega_{W_i}}{\sum_{i=1}^{N_{tel}} \omega_{W_i}} \quad (3.19)$$

$$(3.20)$$

The mean reduced scaled length (MSCL) can be calculated analogously.

These so called shape parameters can be directly used as shape cuts to select γ -like events. Fig. 3.14 shows the distribution of the MSCW and MSCL for MC γ -rays and real hadronic background events. These shape cuts are optimised to maximise the detection significance for typical sources. Since they depend on the assumed γ -ray

3. H.E.S.S.

Config.	MSCL	MSCL	MSCW	MSCW	θ_{cut}^2	Image Size	Distance
	Min.	Max.	Min.	Max.	Max. (degrees ²)	Min. (p.e.)	Max. (°)
Standard	-2.0	2.0	-2.0	0.9	0.0125	80	2.0
Hard	-2.0	2.0	-2.0	0.7	0.01	200	2.0
Loose	-2.0	2.0	-2.0	1.2	0.04	40	2.0

Table 3.2: Lists the values for each cut parameter for the three different configurations

spectrum they are optimised for 3 different sets of spectrum classes or configurations (standard, hard and loose). The standard configuration is optimised to give the maximum detection significance for an integral flux being 10 % of the Crab Nebula above 200 GeV, with an energy distribution $dN/dE \propto E^{-\Gamma}$ with $\Gamma = 2.6$ being the spectral index, see also eq. (1.1). This means that this configuration is optimised for strong and steep spectrum sources. Hard cuts are optimised for an integrated flux of 1% of the Crab Nebula flux with $\Gamma = 2$, giving a higher significance for weak and hard spectrum sources, at the expense of a higher energy threshold. Finally the loose cuts are also optimised to give the maximum significance for a similar source to the Crab Nebula but with $\Gamma = 3$. This cut has the lowest image size cut and therefore the lowest energy threshold. All these configurations incorporate the following parameters:

- A set of shape cut parameters MSCW and MSCL
- A θ^2 cut which is calculated as the square of the angular difference between the reconstructed shower position and the source position. This cut defines the squared radius of the region encompassing the source. Especially for point sources this cut can strongly reduce the number of background events in the signal region.
- Image size, which is the sum of all pixel amplitudes for one shower image
- Distance, also called nominal distance, which is the distance between the camera center and the COG

Table 3.2 lists the values for the three different cut configurations. The local distance cut and the image size cut are called preselection cuts, which preselect a part of the events. Afterwards the shape parameters MSCW and MSCL as well as the θ^2 value are calculated in order to cut on them. These cuts are then called postselect cuts.

The events passing the application of all the shape cuts for one specific configuration are called γ -ray like events. This simply means that the events look like γ -rays in terms of the parameters used in the selected cut configuration. Due to fluctuations in the shower development of hadronic induced showers they can also pass the cuts, in particular if the shower has a large electromagnetic component. In order to estimate the contribution of the γ -ray like hadronic background that is still contained in the signal region, different estimation techniques can be used, see section 3.4.5.

3.4.4 Multivariate Analysis Technique

In order to improve on the Hillas background rejection by MSCW and MSCL alone, a new classification scheme using Boosted Decision Trees (BDT) was implemented, see [Ohm et al., 2009]. The BDT is a multivariate analysis method that combines the information of several classification parameters into one parameter ζ . Basically this parameter describes how likely it is that the event is of electromagnetic origin, so the goal is to divide events into signal and background. The principle behind the BDT method can be summarized as follows. Samples of MC γ -rays and real hadrons are used and divided into two parts. The first part is the training sample and is used to train the decision tree. The second part is the test sample which is used to test the final classifier after the training. For each event there are a number of parameters useful for distinguishing between signal and background. These parameters are the MSCW and MSCL but also include:

- MSCWO and MSCLO which are calculated as the weighted average difference between the measured Hillas Width/Length of an image of given size and corresponding impact distance and the expectation for a hadronic event, instead of a γ -ray as done for MSCW and MSCL
- X_{max} , which is the reconstructed shower maximum in radiation length since the radiation length of hadrons is on average larger compared to the radiation length of electrons and photons
- $\frac{\Delta E}{E}$ is the average spread in reconstructed energies over all participating telescopes and can provide additional γ -hadron separation potential

3. H.E.S.S.

This means that there are in total 6 parameters which are used in [Ohm et al., 2009] to classify γ -rays and hadrons.

The steps in the training of the decision tree are to pick one parameter and for each event value split the training sample into two parts, left and right, depending on the value of that parameter. The splitting parameter and value is chosen in a way that it gives the best separation into one side, containing mostly signal, and the other mostly background. Now there are two (left and right) samples called branches with the original sample called the node. This step is repeated for each branch and the splitting is done until a given number of final branches called leaves are obtained. The splitting is stopped if each leaf is pure signal or pure background or has too few events to continue in order to avoid overtraining due to statistically insignificant leaves. According to the majority of signal and background events, the leaves are assigned as signal or background. Single decision trees are sensitive to statistical fluctuations in the training sample and in order to circumvent that, a boosting procedure is applied which extends a single tree to a forest of trees. If a training event is misclassified, i.e. a signal event lands in a background leaf or a background event lands in a signal leaf, the weight of that event is increased (boosted). The second tree is built using the new weights and again misclassified events have their weights boosted and the procedure is repeated. The total number of trees in the forest was chosen to be 200 and the minimum number of events in the leaves was about 100-1000, where the splitting was stopped, see [Ohm et al., 2009] for further details.

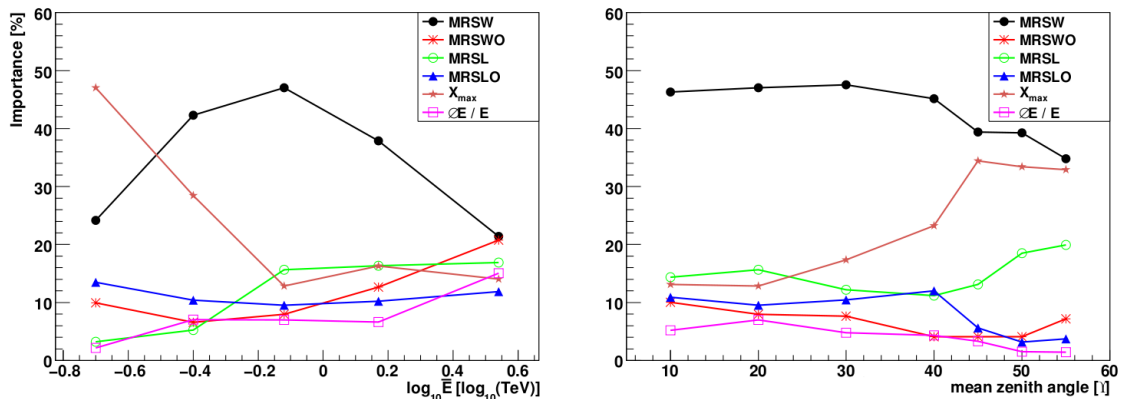


Figure 3.15: Importance of the training parameters as a function of the mean reconstructed energy in the $15^\circ - 25^\circ$ zenith angle band (left) and as a function of mean zenith angle for reconstructed energies between $(0.5 - 1.0)$ TeV (right), taken from [Ohm et al., 2009]

Using the rate of occurrence of a splitting variable during the training procedure, weighted by the squared separation gain and the number of events in the corresponding nodes an importance factor can be calculated [Breiman et al., 1984]. Fig. 3.15 demonstrates this relative importance of the training parameters and shows the dependence on the energy and zenith angle.

3.4.5 Signal Extraction

In general the reconstruction techniques provide discriminating parameters, that more or less allow to separate the γ -ray candidates from the background events. In order to classify what corresponds to signal and background one can have a look at Fig. 3.14 again. The MSCW distribution of γ -rays and hadronic background clearly shows some overlap in the region of the standard cut configuration. In general, however, for real data most events falling in the signal region of the distribution are of hadronic origin. The background region are events falling i.e. in a band ranging from a MSCW value of 4 to 8. The range in between is not used in the analysis since the instrument response to them is particularly difficult to establish. By looking at the sky one can define a so called ON-region which encompasses the source of interest and an OFF-region which is selected to presumably only contain background events made up from hadronic induced air shower events. The ON-region consists of a number N_{on} of γ -ray induced events

3. H.E.S.S.

plus a certain number of background events N_{off} due to the fact stated above. In order to get an estimate of the number of background events that are contained in the signal region, the events from the OFF-region are used. Due to the fact that the instrument response is not the same for the two different regions an additional factor α has to be taken into account. Therefore αN_{off} should be an estimate of the expected number of background events in the ON-region and a number of excess events N_γ above the background level can be calculated. The ON-region is usually defined as a circular region with a radius given by a θ -cut. The excess N_γ can then be estimated by:

$$N_\gamma = N_{\text{on}} - \alpha N_{\text{off}} \quad (3.21)$$

The normalisation factor α accounts for the fact that the solid angle and/or the exposure time t may differ for the number of ON-OFF events. Additionally, the acceptance for γ -ray like events varies within the field of view of the system, with zenith angle, exposure time t and the energy. In fact, the acceptance drops rapidly towards the edge of the camera or field of view. This effect has to be corrected for, if different regions in the field of view are used for the determination of N_{on} and N_{off} .

The significance S_γ of a signal above the background can be determined by the Li-Ma-Formula, see [Li and Ma, 1983]:

$$S_\gamma = \sqrt{2} \left(N_{\text{on}} \ln \left(\frac{(1 + \alpha) N_{\text{on}}}{\alpha (N_{\text{on}} + N_{\text{off}})} \right) + N_{\text{off}} \ln \left(\frac{(1 + \alpha) N_{\text{off}}}{N_{\text{on}} + N_{\text{off}}} \right) \right)^{1/2} \quad (3.22)$$

For each position in a region of the sky a two-dimensional excess and significance map can be calculated by determining N_{on} , α and N_{off} . There are several different background estimation techniques that determine the number of OFF events N_{off} still contained inside the ON-region. Each of them are appropriate for different purposes, for a detailed description of all the methods, see [Berge et al., 2007]. For the purpose of source detection the Ring background method is predominantly used. It has the advantage that any linear gradient in the acceptance is averaged out, but its major drawback is that an acceptance correction has to be done because the ring covers many offsets from the centre of the camera, see left side of Fig. 3.16. Since the radial acceptance depends also on the energy this method is disfavoured for the reconstruction of the energy spectra. For this purpose the Reflected background method is used. This method does not need any acceptance correction since the ON-region and all the OFF-regions are placed at the same offset from the observation position in the camera field of

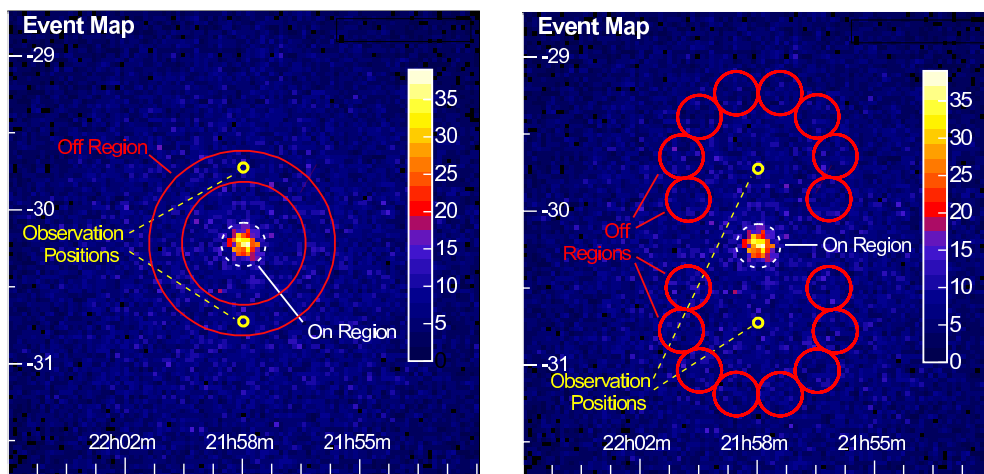


Figure 3.16: This illustrates the Ring (left) and Reflected (right) background method. In both cases it is a count map of γ -ray like events from five hours H.E.S.S. observations of the blazar-type Active Galactic Nuclei (AGN) PKS 2155–304. The ON-region is indicated as the dashed white circle, the OFF-regions as the solid red circles and the observation position as the small yellow circles. There are two observation positions at an offset of $\pm 0.5^\circ$ in declination from the target position. This is also known as the Wobble mode of observation [Berge et al., 2007]

view, see right side of Fig. 3.16. The factor α is just $1/n_{\text{off}}$ with n_{off} being the number of OFF-regions. The major drawback of this method is that with many different γ -ray sources in the FoV it becomes increasingly difficult to find suitable OFF-regions. This is because known γ -ray sources are excluded through the use of predefined exclusion regions in order to not estimate the background from a region which clearly contains a γ -ray signal.

3. H.E.S.S.

Chapter 4

GRASP - Gamma Ray Air Shower Parameterisation

4.1 Introduction

The CR proton flux is in general three orders of magnitude higher than the γ -ray flux (see table 3.1). It is needed to discriminate this hadronic background from the γ -ray signal. The higher the efficiency at which this background rejection works the faster one can detect a source at a predetermined significance level. The so called standard Hillas Reconstruction is described in the previous section (3.4.1). As already mentioned it suffers from a number of drawbacks.

- It is evident from eq. (3.9) that the coordinates in the camera are inversely proportional to the height of the emission. This has the effect that by going down in emission height the strongly fluctuating tail is expanded whereas the head of the shower at higher altitudes is compressed. This leads to a significant uncertainty in the determination of the image axis and therefore the shower direction.
- Effects of broken pixels (see section 3.3) add to the uncertainty in the determination of all the Hillas parameters.
- Looking at the transverse photon intensity distribution (see section 2.1.4) it can be very well represented by $\rho(y) \propto \frac{1}{w^2 + v^2}$ and consequently the second moment of such a function is described by:

$$\text{Var}(\rho) = \int_{-r}^r v^2 \rho(v) dv = 2r - 2w \cdot \arctan(r/w)$$

4. GRASP - GAMMA RAY AIR SHOWER PARAMETERISATION

This shows that the second moments depend on the actual value of r which corresponds to the tail cuts used in the cleaning of the image, see also section 3.3.5.

This chapter will introduce an alternative reconstruction algorithm that applies a fit of pixel amplitudes to an expected image obtained from a Gamma Ray Air Shower Parameterisation (GRASP). This parameterisation was obtained using Monte Carlo air shower simulations, from the CORSIKA software, by parameterising the angular Cherenkov photon distribution with suitable analytical functions.

4.2 CORSIKA Air Shower Simulations

CORSIKA (COsmic Ray Simulations for KAScade) is a detailed Monte Carlo program to study the evolution and properties of extensive air showers in the atmosphere. It was developed to perform simulations for the KASCADE¹ experiment at Karlsruhe [Heck et al., 1998]. All simulations done in this work use the version 6.980 from April 7, 2011. The purpose of these simulations is to obtain the angular distribution of Cherenkov light and parameterise the shower image shape through suitable analytical functions. In turn those functions depend on air shower parameters like the impact distance or the height of the first interaction in the atmosphere.

4.2.1 Parameters

Simulations were done using a $N_x \times N_y$ detector array with $N_x = N_y = 11$ displayed in Fig. 4.1. Looking at the coordinate system used in CORSIKA the angle θ defines the zenith angle and ϕ the azimuth angle of the observation. Detectors are spaced $d_{x,y} = 50$ m apart in each dimension. The detector size in the y direction is $l_y = 10$ m and in the x direction $l_x = \frac{10 \text{ m}}{\cos(\theta)}$ since the area of the detector dish must stay the same when viewing the shower under different zenith angles. Table 4.1 summarizes the parameters and values used in the simulations. The photon that produces an extensive air shower was simulated at seven fixed energies ranging from 0.1 TeV to 10 TeV. The number of simulated showers is adjusted at the higher energies to avoid too large simulation times. In total 121 detectors are used to view an individual shower from many angles and as a result each detector has a different impact distance to the shower impact point on the ground. It should be noted that the impact distance is calculated in a system where the shower axis and the detector plane are perpendicular to each other. The observation level, magnetic field and atmospheric profile are set to the local H.E.S.S. site values.

¹http://www-ik.fzk.de/KASCADE_home.html/

4. GRASP - GAMMA RAY AIR SHOWER PARAMETERISATION

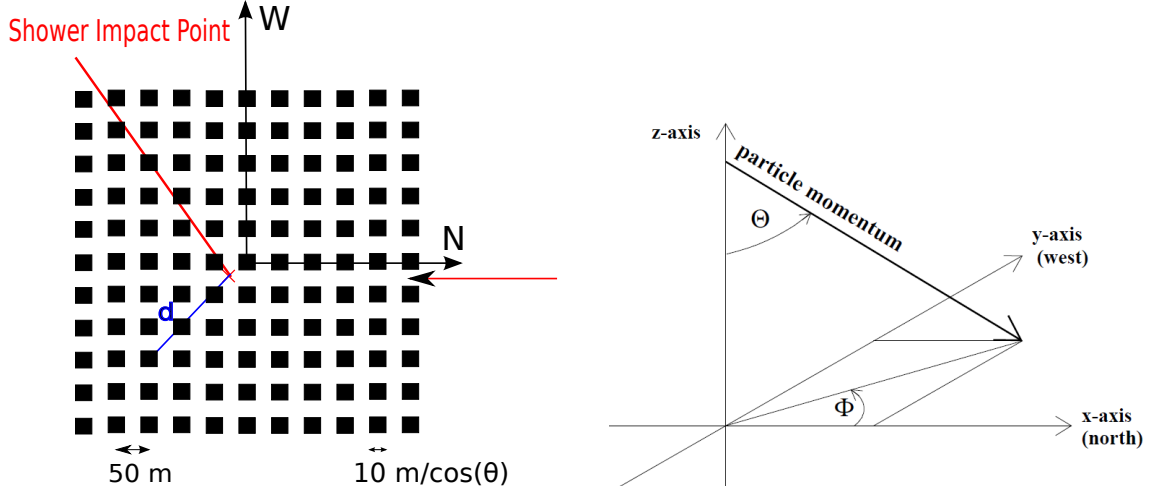


Figure 4.1: Sketch of the CORSIKA detector array used in the simulations on the left. Each black square represents a detector. Showers were simulated coming from the North and transversing to the South. The CORSIKA coordinate system is shown on the right.

θ [$^{\circ}$]	ϕ [$^{\circ}$]	Photon Energy E [TeV]	Number of simulated showers $\times 10^3$
0	0	(0.1, 0.3, 0.5, 1, 2, 5, 10)	(20, 17, 15, 12, 10, 5, 5)
10	180	(0.1, 0.3, 0.5, 1, 2, 5, 10)	(20, 17, 15, 12, 10, 5, 5)
20	180	(0.1, 0.3, 0.5, 1, 2, 5, 10)	(20, 17, 15, 12, 10, 5, 5)
30	180	(0.1, 0.3, 0.5, 1, 2, 5, 10)	(40, 40, 35, 25, 10, 5, 5)
40	180	(0.1, 0.3, 0.5, 1, 2, 5, 10)	(40, 40, 35, 25, 10, 5, 5)
45	180	(0.1, 0.3, 0.5, 1, 2, 5, 10)	(40, 40, 35, 25, 10, 5, 5)
50	180	(0.1, 0.3, 0.5, 1, 2, 5, 10)	(50, 50, 45, 35, 10, 5, 5)
55	180	(0.1, 0.3, 0.5, 1, 2, 5, 10)	(50, 50, 45, 35, 10, 5, 5)

Table 4.1: Lists the values for the CORSIKA simulations parameters.

The output of the CORSIKA simulations can be summarised as follows:

- Core position of the event C_x and C_y in meters
- Height of the first interaction h_t in the atmosphere in meters and converted to radiation length
- Photon positions x_p and y_p of the event on the ground in meters
- Photon direction angles u and v with respect to the x and y axis, respectively in degrees
- Photon time t defined as the time the photons need after production to reach the observation level and counted since the first interaction in ns

Furthermore the shower impact point (core position) on the ground and the height of the first interaction as well as the parameters (θ , ϕ , and E) described in Table 4.1 are stored in the so called event header for each shower event. The detector array parameters are stored there too. Combining all this information a shower image can be created from the mapping of the angles (u, v) . The focus height is chosen to be about 8000 m, which is about the average height of the shower maximum for a shower at zenith with an energy of 1 TeV. Since the depth of field for the H.E.S.S. telescopes is large (see section 3.2.1) the focusing height does not significantly change the results in the following chapters, provided it lies somewhere in this range.

In order to figure out which detector was hit the following equations are used:

$$x' = C_x - x_p + \frac{1}{2}(N_x - 1) \cdot d_x + \frac{l_x}{2} \quad (4.1)$$

$$y' = C_y - y_p + \frac{1}{2}(N_y - 1) \cdot d_y + \frac{l_y}{2} \quad (4.2)$$

$$n_x = \lfloor \frac{x'}{d_x} \rfloor + 1 \quad (4.3)$$

$$n_y = \lfloor \frac{y'}{d_y} \rfloor + 1 \quad (4.4)$$

where n_x and n_y are the detector numbers in the array and then the detector position can be calculated by:

$$T_x = -\frac{1}{2}(N_x - 1) \cdot d_x + (n_x - 1) \cdot d_x \quad (4.5)$$

$$T_y = -\frac{1}{2}(N_y - 1) \cdot d_y + (n_y - 1) \cdot d_y \quad (4.6)$$

4. GRASP - GAMMA RAY AIR SHOWER PARAMETERISATION

With the following definition the impact distance of each detector to the shower can be calculated from the distance of a point in space (detector position) to a line (shower direction). Let a line in three dimensions be specified by two points $\vec{\mathbf{x}}_1 = (x_1, y_1, z_1)$ and $\vec{\mathbf{x}}_2 = (x_2, y_2, z_2)$ lying on it. The distance between a point on the line and a point $\vec{\mathbf{x}}_0 = (x_0, y_0, z_0)$ is in general given by:

$$d = \frac{|(\vec{\mathbf{x}}_1 - \vec{\mathbf{x}}_0) \times (\vec{\mathbf{x}}_2 - \vec{\mathbf{x}}_1)|}{|\vec{\mathbf{x}}_2 - \vec{\mathbf{x}}_1|} \quad (4.7)$$

where $\vec{\mathbf{x}}_2 - \vec{\mathbf{x}}_1$ can be expressed by direction cosines of the shower direction:

$$\vec{\mathbf{x}}_2 - \vec{\mathbf{x}}_1 = \begin{pmatrix} x_2 - x_1 \\ y_2 - y_1 \\ z_2 - z_1 \end{pmatrix} = \begin{pmatrix} \alpha \\ \beta \\ \gamma \end{pmatrix} = \begin{pmatrix} \sin(\theta) \cos(\phi) \\ -\sin(\theta) \sin(\phi) \\ \cos(\theta) \end{pmatrix} \quad (4.8)$$

The impact distance d is then given by setting $\vec{\mathbf{x}}_1 = (C_x \ C_y \ 0)$ and $\vec{\mathbf{x}}_0 = (T_x \ T_y \ 0)$. The height of the first interaction is available in meters and is converted to a number of radiation length depending on the traversed thickness in the atmosphere. A list of thickness as a function of the height in the atmosphere is used and corrected for the zenith angle of the observation. Fig. 4.2 shows the atmospheric thickness as a function of height for the local H.E.S.S. site in Namibia. The height of the first interaction in the atmosphere can then be calculated in units of the radiation length in air $X_0 = 36.7 \text{ gcm}^{-2}$ by interpolation:

$$\begin{aligned} \bar{h}_t &= \ln(th_1) + (\ln(th_2) - \ln(th_1)) \frac{h - h_1}{h_2 - h_1} \\ h_t &= \frac{\exp(\bar{h}_t)}{X_0 \cdot \cos(\theta)} \end{aligned} \quad (4.9)$$

where θ is the zenith angle of the observation.

4.2.2 Results

By simply creating a two dimensional histogram of the angular distribution of photons Fig. 4.3 is obtained. It shows a simulation of a 1 TeV gamma-ray air shower from CORSIKA simulations. The impact distance of this event is 200 m and the height of the first interaction is 1 X_0 . The left figure shows a single shower event, whereas the right shows an average of 50 showers. By looking at Fig. 4.3 it becomes clear that a parameterisation of this shower event by an ellipse might not result in the best description due to the asymmetric shape. Furthermore, from this illustration the basic

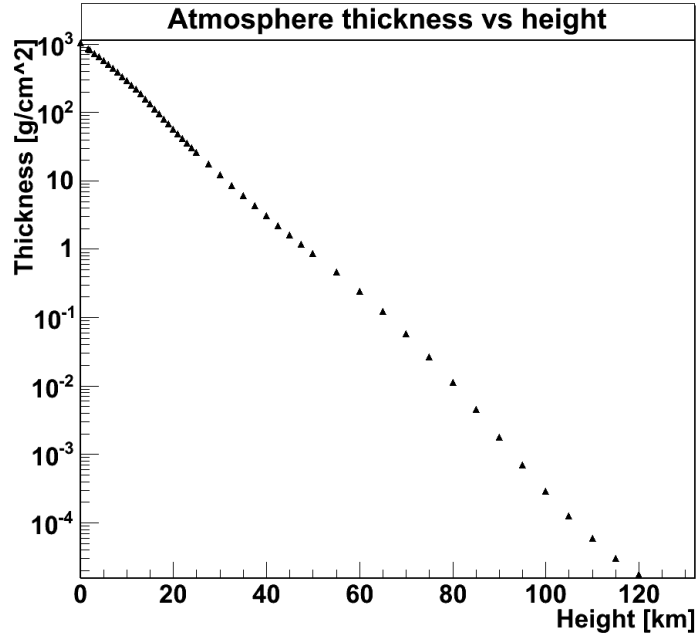


Figure 4.2: Atmospheric thickness as a function of height for the local H.E.S.S. site in Namibia.

properties of a better parameterisation can be inferred by looking at the longitudinal and transverse part of the shower image. In order to extract the longitudinal and transversal angular distribution of photons, slices in u and v are made. A sketch of this procedure is shown in Fig. 4.4. For the transverse part slices of one bin width of about 0.1° are made whereas for the longitudinal slice the dimension of the H.E.S.S. pixel width of 0.16° is used. As an example the shower event displayed in Fig. 4.3 is taken and a slice along the u -axis is made. From the resulting distributions corresponding to the longitudinal and transverse slice of the image, suitable analytical functions need to be found in order to model the shower image.

4. GRASP - GAMMA RAY AIR SHOWER PARAMETERISATION

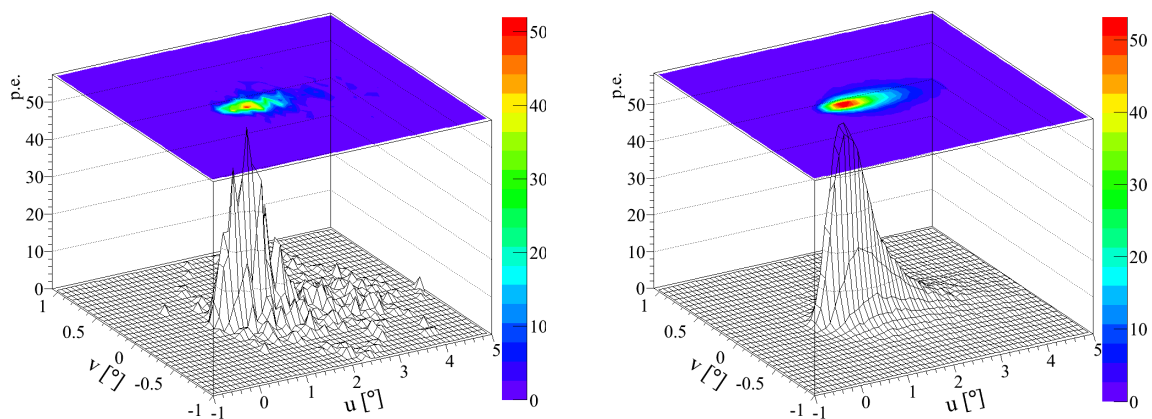


Figure 4.3: Both figures show the angular distribution of photons converted to photoelectrons for a 1 TeV γ -ray air shower obtained from CORSIKA. On the left a single shower event is shown for an impact distance from the telescope of 200 m and an height of first interaction of $t=1 X_0$. On the right the same shower averaged over 50 shower events is shown.

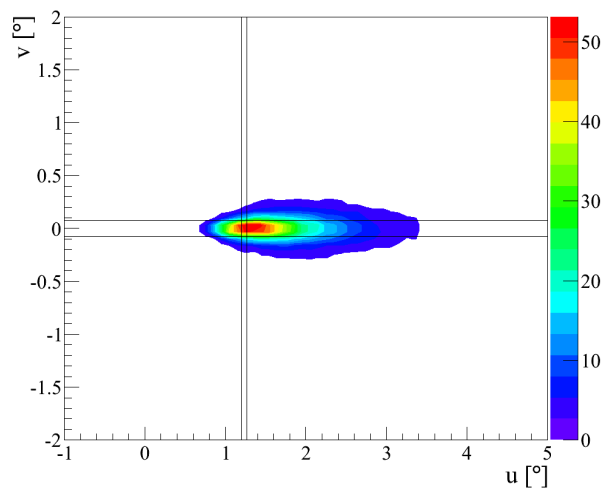


Figure 4.4: Illustrates the slices that are used in determining the longitudinal and transverse distribution of the shower image.

The result is shown in Fig. 4.5 and illustrates on the left a single shower event slice and on the right an average of 50 showers. The black line corresponds to a fit of a Moyal function of the form:

$$L_{\text{Moyal}}(\lambda, n, l) = \frac{n}{l \cdot \sqrt{2\pi}} \cdot \exp\left(-\frac{1}{2}(\lambda + \exp(-\lambda))\right) \quad (4.10)$$

with $\lambda = \frac{u-p}{l}$. Here, n describes the normalisation, p the peak and l the length of the Moyal function. It can be seen that this function describes the single and average shower quite well. In the case of the average shower, the peak is at roughly $p \approx 1.4^\circ$ and the length is about $l \approx 0.3^\circ$.

For the transverse part of the shower a slice at $u = 1.25^\circ$ is made and shown in Fig. 4.6. It shows a symmetric distribution around zero and can be well described by a Lorentz function defined by:

$$T_{\text{Lorentz}} = a \frac{w}{\pi(w^2 + v^2)} \quad (4.11)$$

where a is the normalisation and w is the width of the function. In this example the normalisation a was fixed to the integral of the distribution and the offset was set to zero. A fit of this Lorentz function is also shown in Fig. 4.6 as the black curve and the width of the average shower is obtained to be about $w \approx 0.06^\circ$.

As already mentioned in section 3.4.1 the same shower should move further away from the camera centre and be stretched by increasing the impact distance to the telescope. This effect can be seen in Fig. 4.7. On the left side the shower event has a fixed height of the first interaction of $h_t = 1 X_0$ at three different impact distances of $d=100\text{m}$, $d=200\text{m}$ and $d=300\text{m}$. The image on the right side displays the shower event with a fixed impact distance to the telescope of $d=200\text{m}$ but for two different heights of first interactions $h_t = 1 X_0$ and $3 X_0$. This clearly shows that a parameterisation that should describe the longitudinal distribution of the shower depends on the impact distance as well as the height of the first interaction in the atmosphere. For the transverse part, by looking at Fig. 4.3 or Fig. 4.4, it is evident that the width of the shower depends on where the slice is made or in other words the longitudinal position u . This is due to the air shower broadening while developing down in the atmosphere, which is also explained in detail in section 2.1.4. Furthermore, the width also depends on the impact distance illustrated in Fig. 4.8.

4. GRASP - GAMMA RAY AIR SHOWER PARAMETERISATION

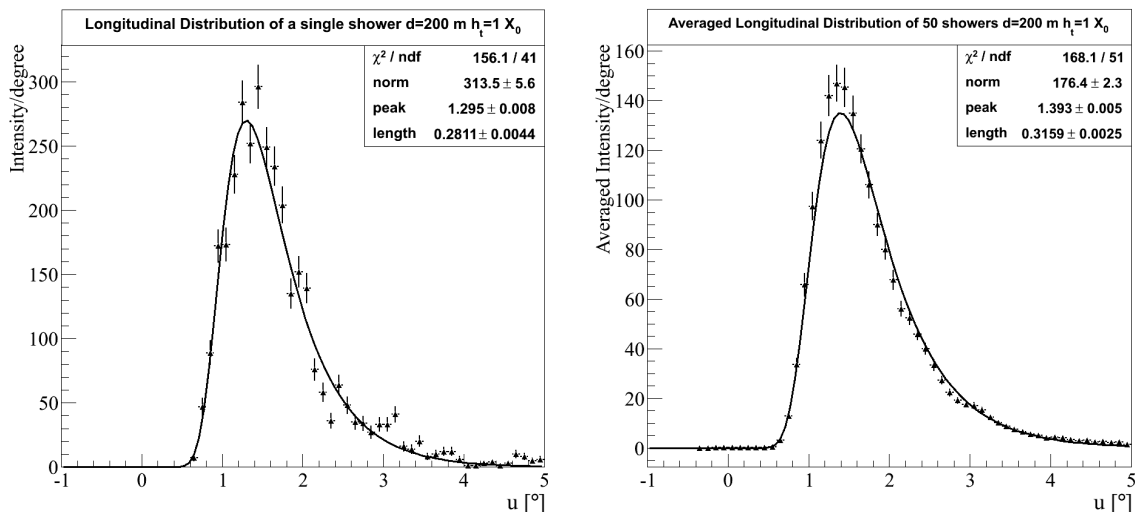


Figure 4.5: Longitudinal distribution of photons converted to photoelectrons for the same shower as in Fig. 4.3 for a slice along the u -axis in the range of $-0.08^\circ < v < 0.08^\circ$. The black line corresponds to a fit of a Moyal function.

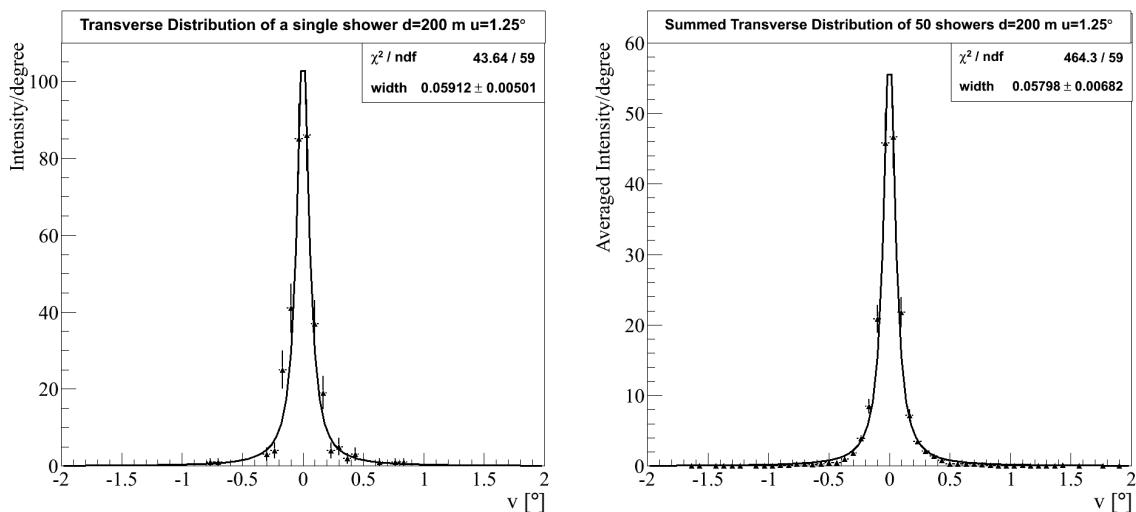


Figure 4.6: Transversal distribution of photons converted to photoelectrons for the same shower as in Fig. 4.3 for a slice along the v -axis at $u = 1.25^\circ$

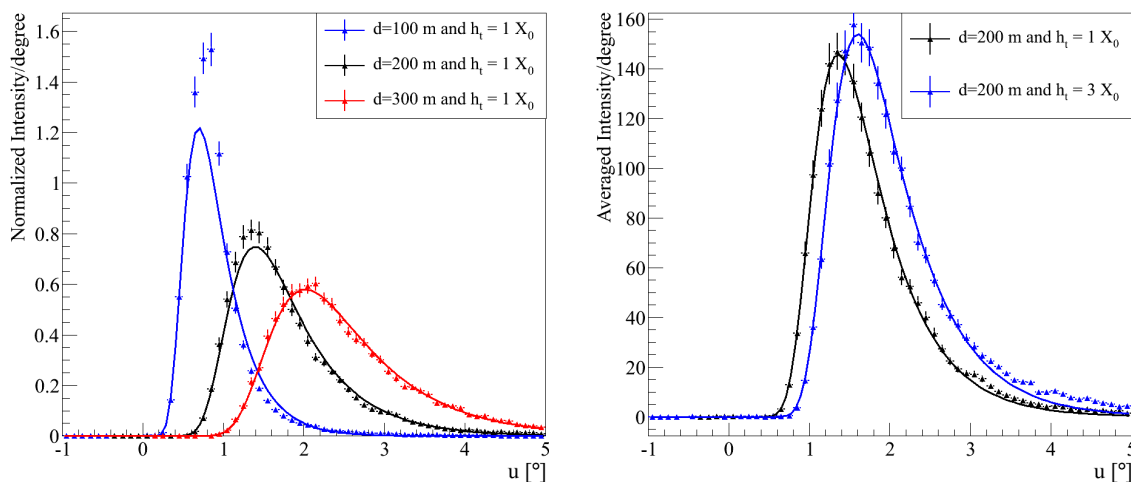


Figure 4.7: On the left the longitudinal distribution of photons converted to photoelectrons is shown for the same $h_t = 1 X_0$ but different impact distances of $d=100\text{m}$, $t=200\text{m}$ and $d=300\text{m}$. On the right the impact distance is fixed at $d=200\text{m}$ but $h_t = 1 X_0$ and $3 X_0$

All of these informations describing the shape of the shower image can be summarized as follows:

Longitudinal profile:

- Moyal function with the parameters peak p , length l and normalisation n
- All of these parameters depend on the impact distance d and the height of the first interaction h_t

Transverse profile:

- Lorentz function with the parameter width w
- Parameter depends on the impact distance d and the longitudinal direction u

It can be seen that the height of emission of Cherenkov photons is correlated with the emission angle by the approximation $\phi \approx d/h$ with d being the impact distance and h the height of emission of the Cherenkov photons, see section 3.4.1 and eq.(3.8). The following Fig. 4.9 illustrates this dependance. It shows an average shower event (50 events) for a 1 TeV γ -ray induced air shower at 0° zenith, on the left for an impact

4. GRASP - GAMMA RAY AIR SHOWER PARAMETERISATION

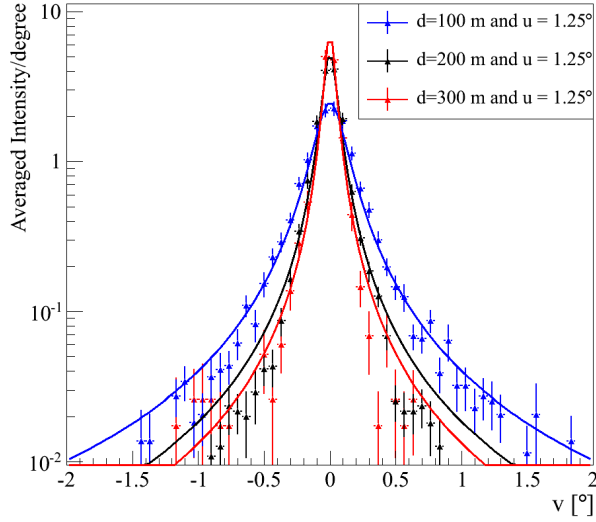


Figure 4.8: Transversal distribution of photons at three different impact distances of $d=100\text{m}$, $d=200\text{m}$ and $d=300\text{m}$.

distance of 100 m and on the right for 300 m. Both have a height of the first interaction of 1 radiation length. The peak of the longitudinal projection of Cherenkov photons corresponds to the maximum intensity from the height of the shower maximum h_{max} seen under the angle $\phi(h_{\text{max}}) = \phi_{\text{max}} \approx d/h_{\text{max}}$. As already mentioned, Fig. 4.9 shows an average shower event averaging over 50 events. The height of shower maximum is the same and the shift of ϕ_{max} comes from the different impact distances of the shower (100 m (left) and 300m (right)). On the other hand individual showers at the same impact distance can exhibit fluctuations in the depth of the shower around the average shower maximum in the atmosphere.

4.2 CORSIKA Air Shower Simulations

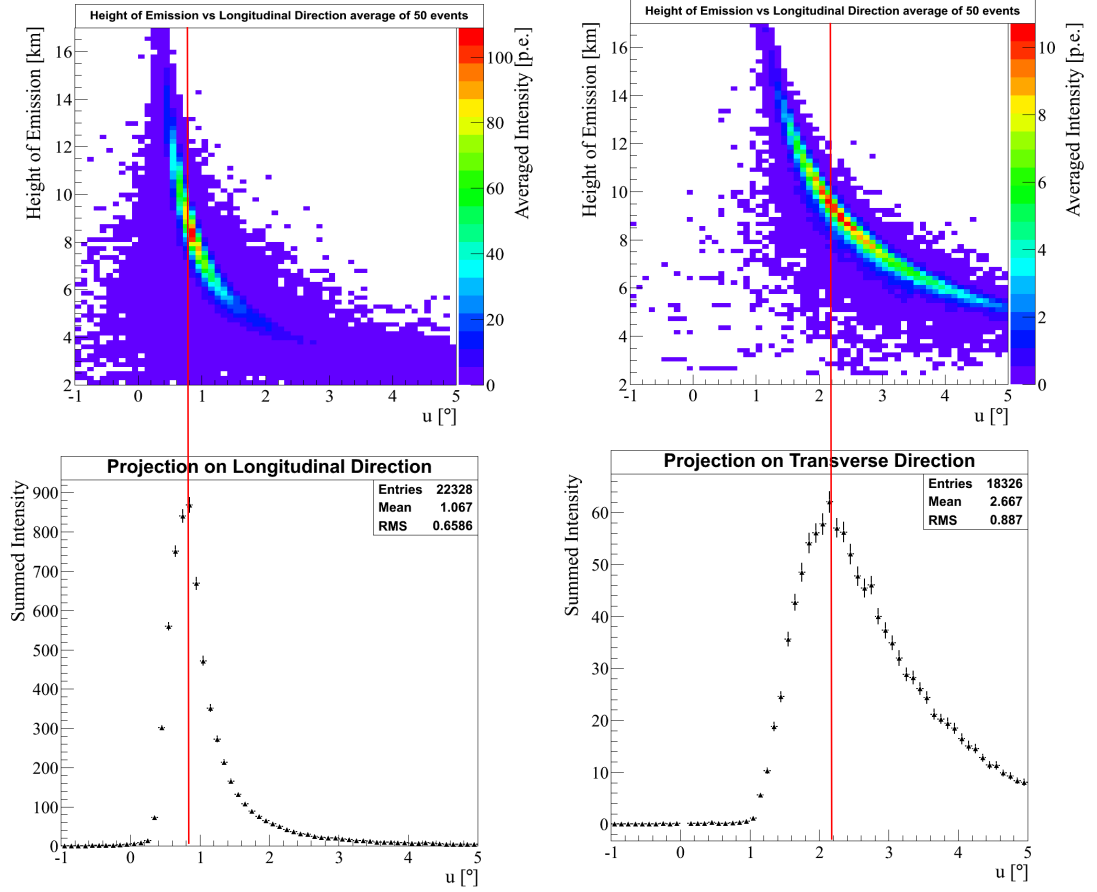


Figure 4.9: Height of Cherenkov photons production vs. longitudinal direction for 50 shower events with an energy of 1 TeV at 0° Zenith and for an impact distance d of 100 m (left) and 300 m (right) with a height of the first interaction of 1 radiation length.

This can be expressed by doing a Taylor series expansion around h_{\max} and neglecting higher orders:

$$\phi(h) \approx \phi_{\max} + \frac{d\phi}{dh}\bigg|_{h=h_{\max}}(h - h_{\max}) \quad (4.12)$$

$$= \phi_{\max} - \frac{d}{h_{\max}^2}(h - h_{\max}) \quad (4.13)$$

$$= \phi_{\max} \left(1 - \frac{h - h_{\max}}{h_{\max}}\right) \quad (4.14)$$

If h is defined as a new shower maximum $h = \bar{h}_{\max}$, then $\Delta h = \bar{h}_{\max} - h_{\max}$ describes

4. GRASP - GAMMA RAY AIR SHOWER PARAMETERISATION

the shift of the new shower maximum and the above equation can be rewritten to yield:

$$\bar{\phi}_{\max} \approx \phi_{\max} \left(1 - \frac{\Delta h}{h_{\max}} \right) \quad (4.15)$$

where $\bar{\phi}_{\max}$ is the angle under which the new shower maximum \bar{h}_{\max} is seen. This uncertainty in shower maximum from one shower event to another correlates to the uncertainty in the height of the first interaction of the incoming particle, see Fig. 4.56. In the reconstruction of shower parameters later described in section 4.4.2 this uncertainty can be compensated by leaving the height of the first interaction as a free parameter that will be determined by a fitting procedure. In order to further justify the parameterisation of the longitudinal part of the shower with a Moyal function, the Greisen function given in eq. (2.9) can be used to show the longitudinal angular distribution of electrons as well as photons in Fig. 4.10 on the right side as the red histogram. Here the thickness h_t is converted into an altitude or height using the atmospheric profile at the end of section 4.2.1 and shown in Fig. 4.2. By using the approximation defined above $u \approx d/h$ and assuming an impact distance of 200m the height is converted into a longitudinal angle u . The black line corresponds to a fit of a Moyal function defined in eq. (4.10). It should be noted that the Greisen function was derived using several approximations and does not fully agree with MC simulations, a circumstance which can be remedied by incorporation of a few more factors, see [Fenyves et al., 1988].

The same can be done for the transverse part of the shower using the NKG function and converting the radial distance into an angle via $v \approx r/h$. This is illustrated in Fig. 4.11 as the red histogram. Here, the black curve corresponds to a fit of a Lorentz function defined in eq. (4.11).

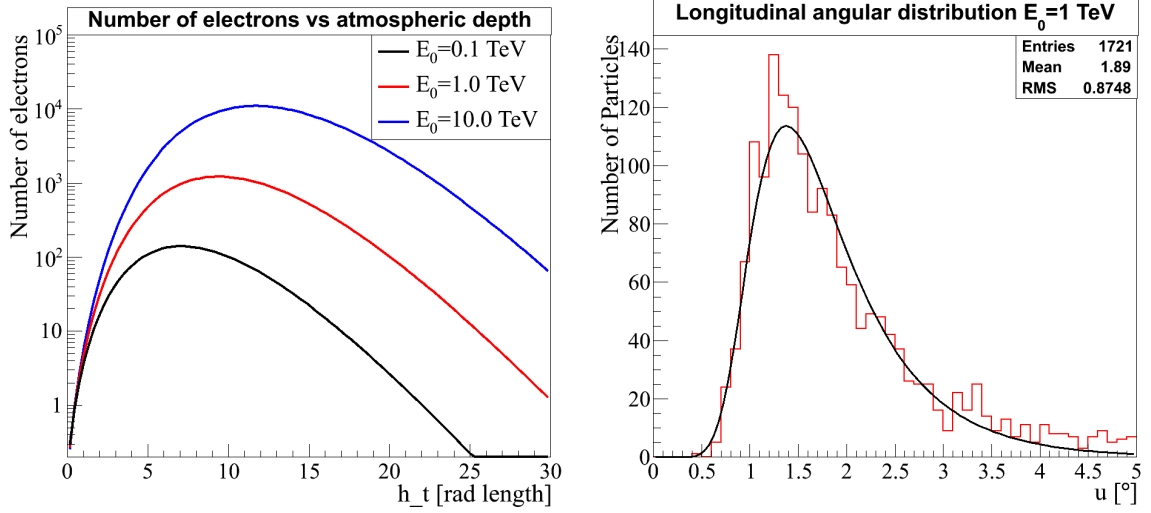


Figure 4.10: Left: Number of electrons as a function of the atmospheric depth in units of the radiation length. Three different initial primary energies are shown. Right: Longitudinal angular distribution following the Greisen function (red) as a function of the longitudinal direction angle defined in the text. The black curve corresponds to a fit of a Moyal function.

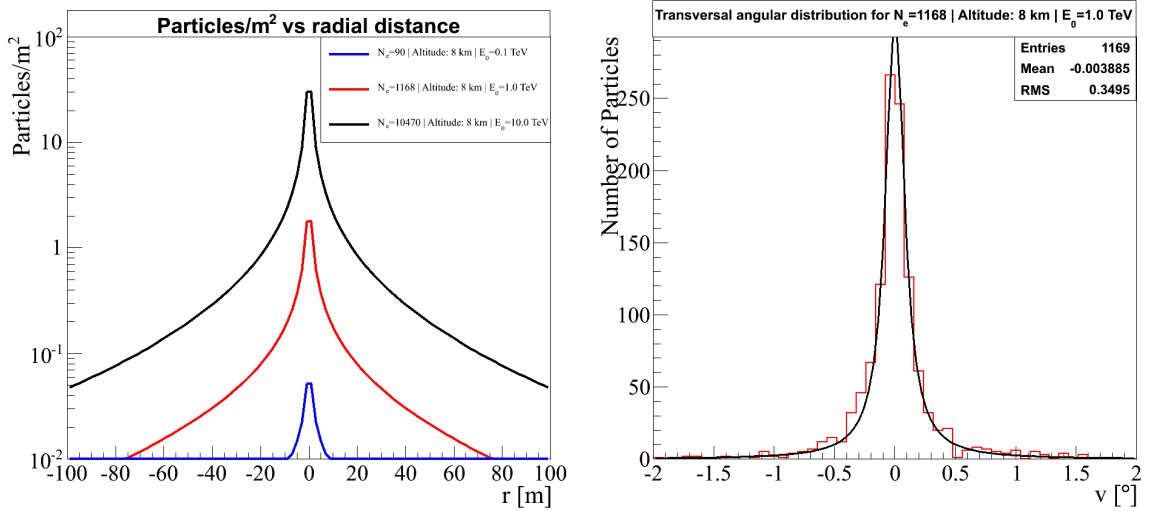


Figure 4.11: Particles per square metre as a function of the radial distance from the shower axis on the left side. Three different initial primary energies are shown and the altitude is fixed at 8 km. On the right side the transversal angular distribution following the NKG function (red) is shown as a function of the transversal direction angle defined in the text. The black curve corresponds to a fit of a Lorentz function.

4. GRASP - GAMMA RAY AIR SHOWER PARAMETERISATION

From all of this it can be seen that the longitudinal and transverse part of the shower can be well fitted by a Moyal and Lorentz function respectively. The lateral spread of the shower is increasing with decreasing altitude since v is inverse proportional to the emission height h ($v \approx r/h$), which is illustrated in Fig. 4.12. A projection onto the u -axis shows the transversal distribution and a projection onto the height of emission axis shows that the shower maximum is around 8 km.

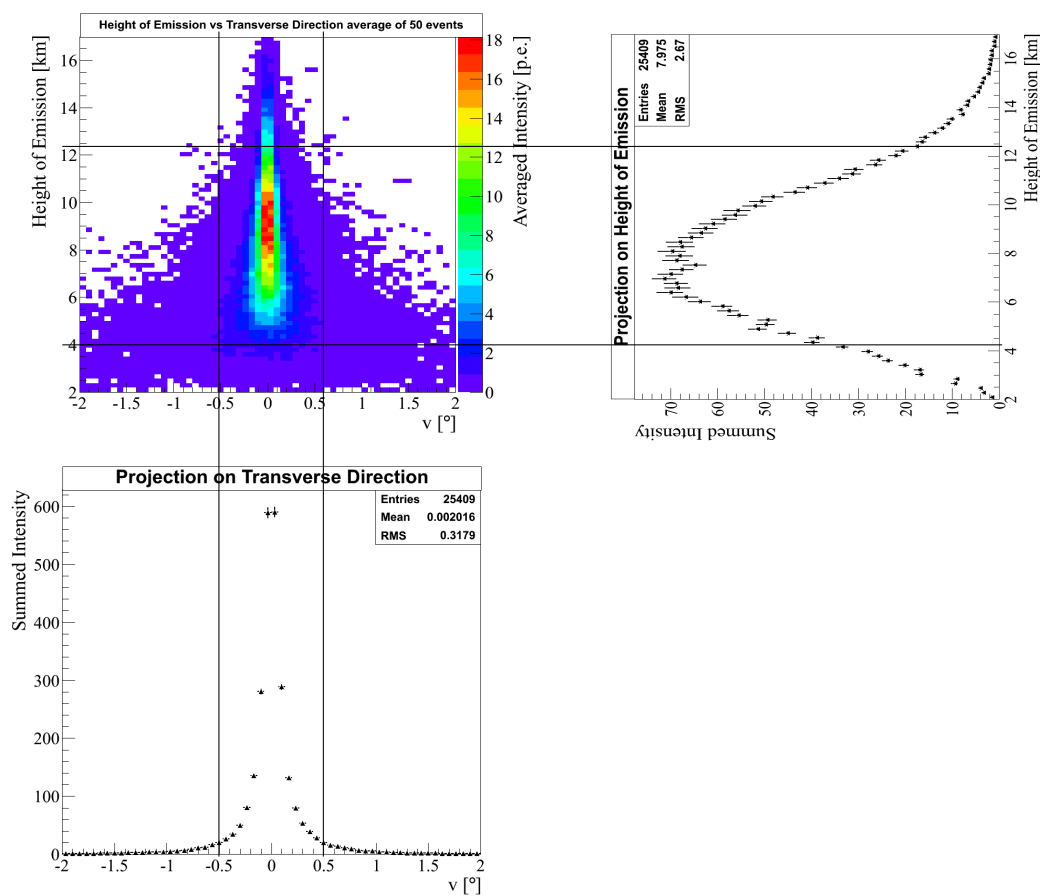


Figure 4.12: Height of Cherenkov photons emission vs. transverse direction for 50 shower events with an energy of 1 TeV at 0° zenith and for an impact distance d of 200 m and a height of the first interaction of 1 radiation length.

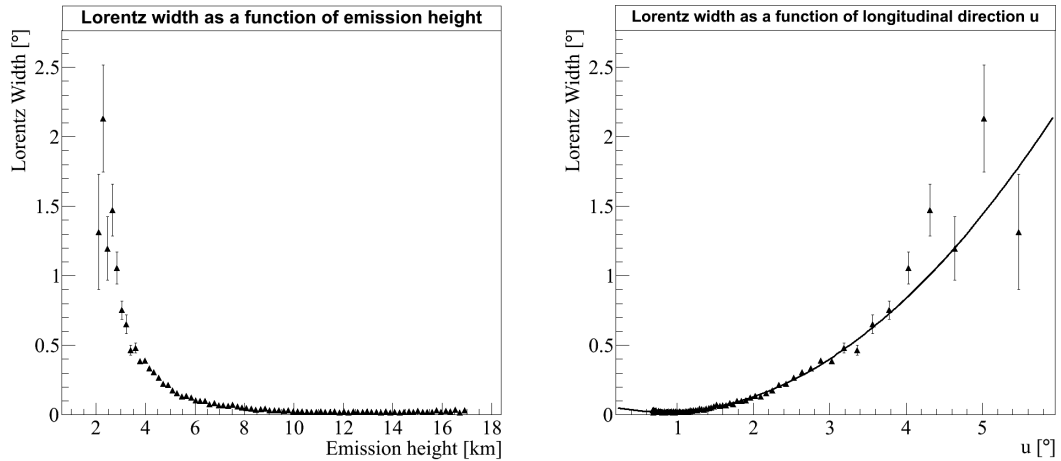


Figure 4.13: Lorentz Width as a function of the height of emission (left) and as a function of the longitudinal direction u (right). The right figure also shows a fit of a second order polynomial to the data which agrees well.

In order to investigate how the lateral spread changes with altitude the top left histogram in Fig. 4.12 was taken and slices were made in every bin of the height of emission axis. The resulting distribution was then fitted with a Lorentz function and the obtained width is shown in Fig. 4.13 as a function of the height of emission on the left and as a function of the longitudinal direction angle u on the right. Here, the same approximation as before is used $u \approx d/h$. The impact distance d was set to 200m again. From the left figure the expected behaviour of the Lorentz width w as a function of the impact distance can be seen too since the impact distance is proportional to the height of emission $d \sim h$. Furthermore, by looking at the right figure a fit of a second order polynomial fits the data quite well.

The next section combines all of this information to get an expected shower image given the shower impact point on the ground, the height of the first interaction as well as a first estimate of the shower energy.

4.3 Gamma Ray Air Shower Parameterisation

In the previous section the basic procedure in obtaining γ -ray air shower simulations from CORSIKA were described. It was also mentioned how the angular distribution of the shower photons can be separated in a longitudinal and transverse part. Furthermore, the effect of changing shower parameters like impact distance and height of the first interaction on the shower shape was investigated separately for these two parts.

4.3.1 Concept

There are two different approaches in obtaining a parameterisation of gamma ray air showers. In section 4.2.2 there are two ways in obtaining parameters like the peak, length and normalisation of the Moyal function as a function of the impact distance and height of the first interaction.

- First Approach: Fit every single shower with the two parameterisations for the longitudinal and transverse part of the shower separately. Afterwards every fitted parameter will be averaged in the corresponding impact distance and height of the first interaction bin
- Second Approach: Average these showers first that fall in the same impact distance and height of the first interaction bin and then apply only a single fit for the longitudinal and transverse part

The first approach unfortunately has the drawback that in the tail of the shower the photon statistics is low, especially for showers with a high impact distance, relatively low energy and at high zenith angles. This will result in a larger error i.e. for the shower parameter that describes the width w of the shower image and therefore the second approach will be used in this work. The basic idea is to fill four histograms:

- First- third histogram: Moyal peak p , length l and normalisation n as a function of the impact distance d and height of the first interaction h_t
- Fourth histogram: Lorentz width w as a function of the impact distance and longitudinal direction u

All of these histograms are filled for all the zenith angles and energies listed in the table 4.1.

4.3.2 Longitudinal and Transverse Profiles

After the CORSIKA simulations are performed the output is read, showers falling in the same impact distance and height of the first interaction bin are averaged and the longitudinal and transverse slices are fitted independently with a Moyal and a Lorentz function respectively. The impact distance d ranges from $0 \leq d \leq 700$ meters and is divided in 80 bins. The height of the first interaction is calculated as the logarithm of h_t defined in eq. (4.9) and ranges from $-6 \leq \ln(h_t) \leq 3$ and is also divided in 80 bins. For the transverse part the longitudinal direction u ranges from $-1^\circ \leq u \leq 5^\circ$ and is divided in 60 bins yielding a bin width of 0.1° . Shower events falling in the same impact distance and height of the first interaction bin are averaged.

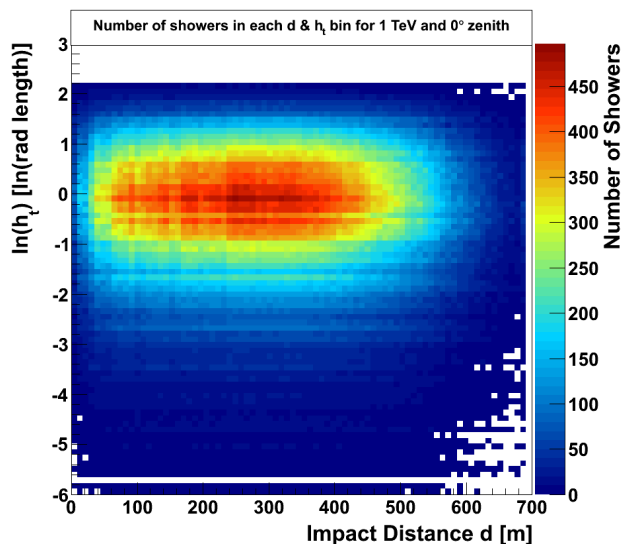


Figure 4.14: Number of shower events falling in each impact distance d and height of the first interaction $\log(h_t)$ bin for the CORSIKA shower simulations of 1 TeV at 0° zenith.

Fig. 4.14 illustrates the number of showers falling in each impact distance and height of the first interaction bin for the 1 TeV CORSIKA simulation at 0° zenith. It has to be noted that each shower event can be seen by more than one detector. This means that for one shower event all detectors see the same height of the first interaction but not all have the same impact distance. Furthermore, depending on where the shower impact point on the ground was, the same impact distance bin can be populated more than once for one shower event. From this figure it can be calculated

4. GRASP - GAMMA RAY AIR SHOWER PARAMETERISATION

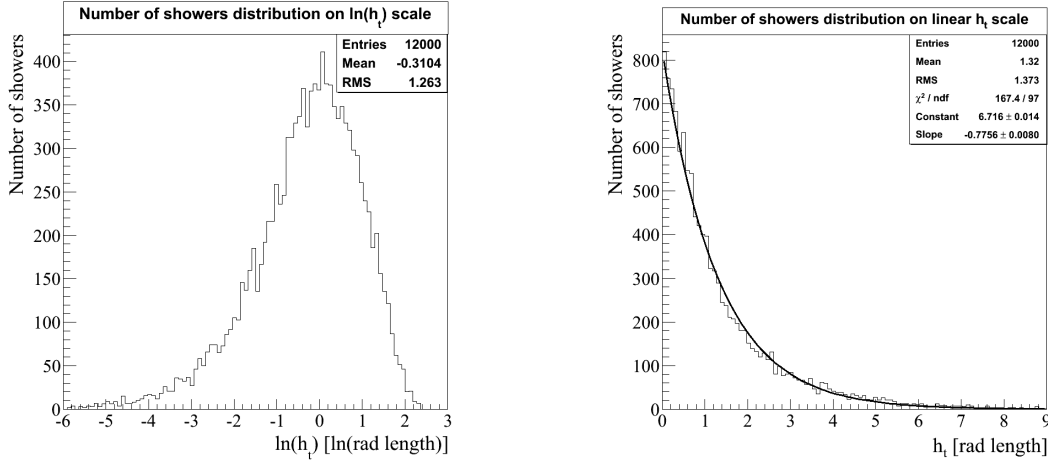


Figure 4.15: Height of the first interaction distribution for the 12000 shower events for the CORSIKA shower simulations of 1 TeV at 0° zenith. On the right the distribution of the height of the first interaction is shown and on the left the logarithm of the height of the first interaction. The right figure also shows a fit of an exponential to the distribution, which yields a slope of about (-0.78 ± 0.01) .

that about 90 % of all the simulated events is between $-2 \leq \ln(h_t) \leq 2$ or in linear scale $0.14X_0 \leq h_t \leq 7.39X_0$. Fig. 4.15 shows the height of the first interaction distribution for the 12000 showers that were simulated with CORSIKA for 1 TeV at 0° zenith. In order to fit the longitudinal and transverse part of the shower, slices are defined and are shown in Fig. 4.4. The longitudinal part is fitted with a Moyal function defined in eq. (4.10) which has the three parameters peak (p), length (l) and normalisation (n). For each of these parameters a histogram is filled as a function of impact distance d and height of first interaction h_t . The filling is performed as the logarithm of h_t , due to the fact that the CORSIKA simulations only go to about 9 radiation lengths ($\ln(9) \approx 2.2$), additionally it is easier to extrapolate towards roughly 20 radiation lengths ($\ln(20) \approx 3$) since this spans only a few bins. The transverse part is fitted with a Lorentz function defined in eq. (4.11) and has only one parameter which is the width w . For this parameter a histogram is filled as a function of impact distance d and longitudinal direction angle u . Since the photon statistics at larger impact distances or larger height of first interactions are severely reduced, all the histograms are first smoothed and then extended in order to have a complete description of showers inside the boundaries. This is especially important for a fitting procedure in order to not introduce artificial steps

4.3 Gamma Ray Air Shower Parameterisation

in the likelihood surface. The smoothing and extending is a threefold step:

- First: Histogram is smoothed with a median filter of 3x3 bins, meaning the median of each bin with its surrounding neighbours is calculated and this value replaces the old one.
- Second: The histogram is extended in the x and y direction by a fit of line, exponential or polynomial of second order to a number of bins before the value drops to zero.
- Third: Another smoothing procedure with an extended kernel (5x5 bins) is used to smooth out fluctuations at larger scales.

4.3.2.1 Moyal Peak

Fig. 4.16 shows the resulting histogram for the CORSIKA simulations at 1 TeV and a zenith angle of 0° for the Moyal peak (p) on the left. After smoothing and extending the histogram on the right side is obtained. The resulting smoothed and extended

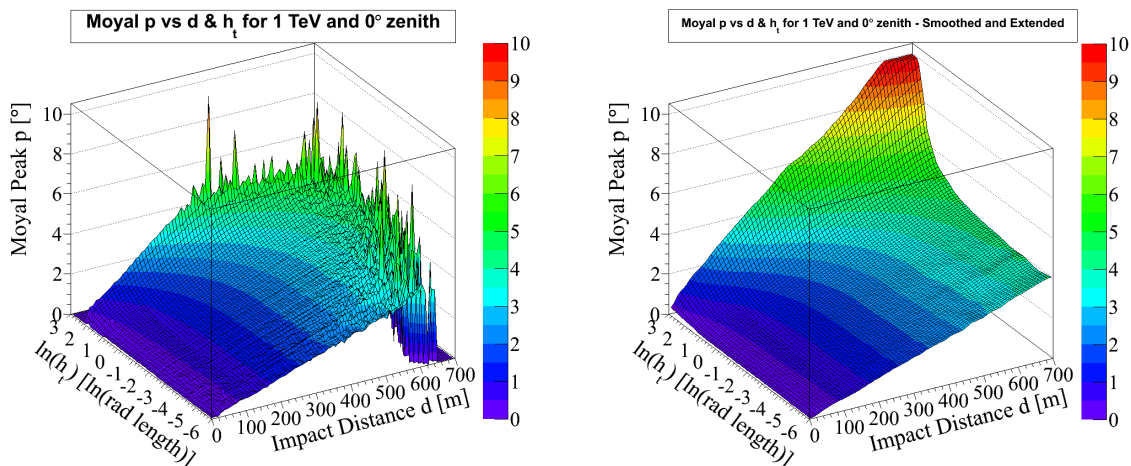


Figure 4.16: On the left is the original histogram filled from CORSIKA data and on the right is the histogram after a smoothing procedure. The histograms are filled in 80 bins in impact distance and height of the first interaction with the fitted Moyal peak p in degrees.

histogram can be compared to the original one in slices along both axis to look for large deviations and is shown as an example in Fig. 4.17 and Fig. 4.18 for two different slices. From Fig. 4.17 it can also be seen that the Moyal peak p linearly depend on

4. GRASP - GAMMA RAY AIR SHOWER PARAMETERISATION

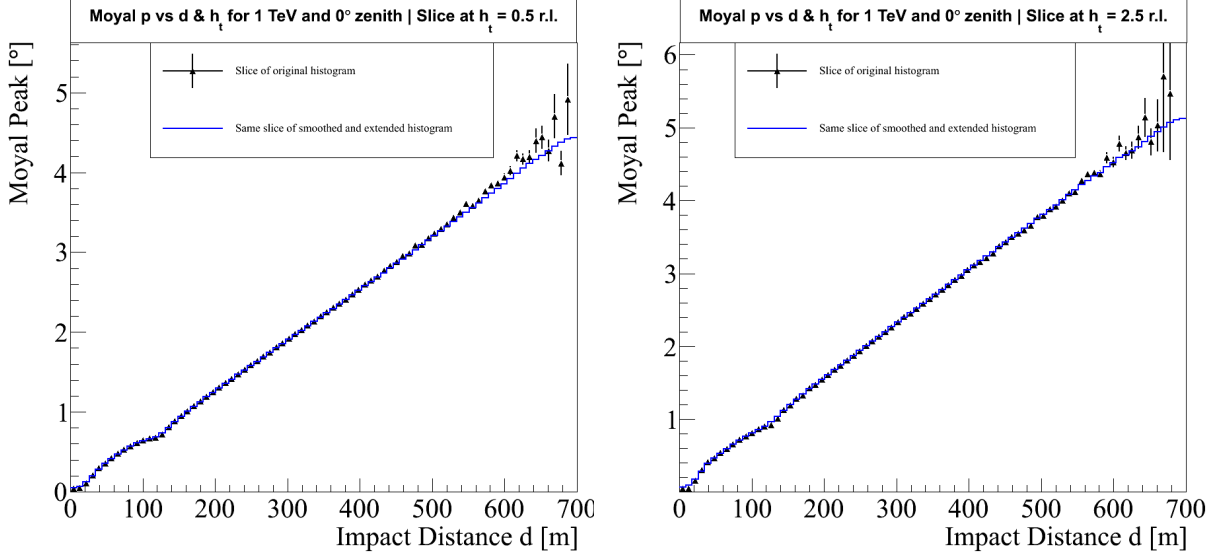


Figure 4.17: Slice of the original histogram of the Moyal peak vs. d and h_t in black as well as the smoothed one in blue for the same slice. It is shown for two different height of first interactions of $h_t = 0.5X_0$ (left) and $h_t = 2.5X_0$ (right).

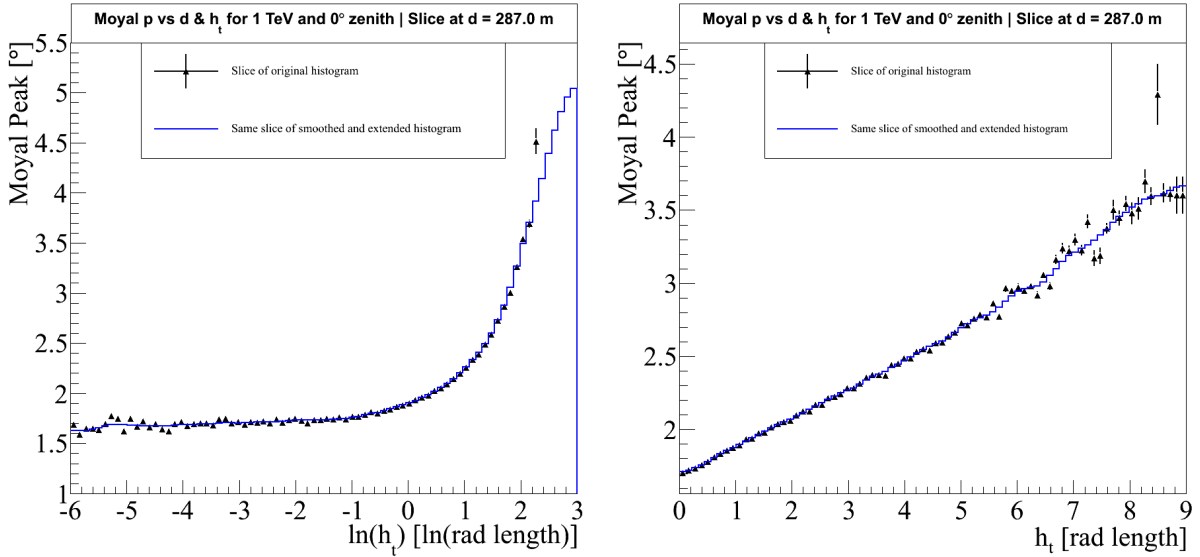


Figure 4.18: Slice of the original histogram of the Moyal peak vs. d and h_t in black as well as the smoothed one in blue for the same slice. It is shown for an impact distance of $d = 287$ m in $\ln(h_t)$ scale on the left and in linear scale on the right.

4.3 Gamma Ray Air Shower Parameterisation

the impact distance d as already expected from section 2.1.3. The plateau at about 130 m corresponds to the Cherenkov radius, see section 2.3. The atmospheric thickness as a function of altitude is given by the expression $X(h) = X_{s.l.} \exp(-h/h_0)$, where $X_{s.l.} \approx 1030 \text{ g/cm}^2$ is the thickness at sea level. Using this and following eq. (4.12) it can be written:

$$\phi(X) = \frac{d}{h_0 \ln(X/X_{s.l.})} \quad (4.16)$$

$$\begin{aligned} \phi(X) &\approx \phi(X_t) + \left. \frac{d\phi}{dX} \right|_{X=X_t} (X - X_t) \\ &= \phi(X_t) \left(1 - \frac{X - X_t}{X_t \ln(X_t/X_{s.l.})} \right) \\ \phi(X'_t) &\approx \phi(X_t) \left(1 - \frac{\Delta X}{X_t \ln(X_t/X_{s.l.})} \right) \end{aligned} \quad (4.17)$$

where $\Delta X = X'_t - X_t$ is the shift of height of the first interaction and relates to h_t via $X_t = h_t \cdot X_0$. The new and old emission angles are defined by $\phi(X'_t)$ and $\phi(X_t)$. They correspond to the angle under which Cherenkov emission is seen for the new and old height of the first interaction X'_t and X_t respectively. This means that the Moyal peak p is expected to shift proportionally with the height of the first interaction h_t and this behaviour can be seen in Fig. 4.18 on the right side. A more complete view of the relative deviation of the smoothed peak from the original peak, defined as $(p_{\text{orig}} - p_{\text{smoothed}})/p_{\text{orig}}$ in percent is shown in Fig. 4.19. The left side shows a two dimensional representation of the relative deviation as a function of impact distance d and height of the first interaction h_t . The left figure illustrates the distribution of the relative deviation which shows that for most of the bins the fluctuations are between $\pm 20\%$.

4. GRASP - GAMMA RAY AIR SHOWER PARAMETERISATION

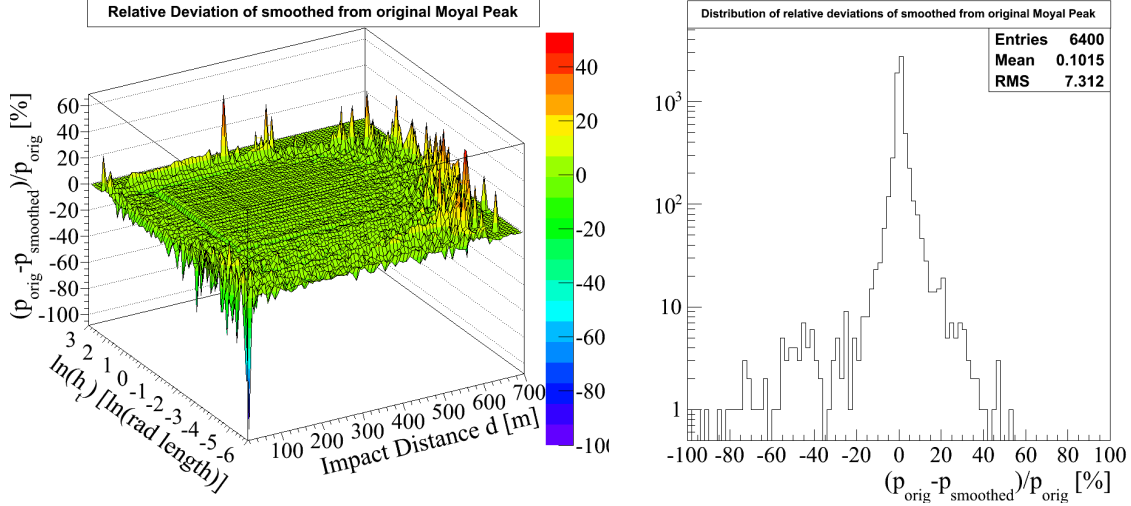


Figure 4.19: Left: Relative deviation of the smoothed Moyal peak p histogram to the original one. Right: Distribution of these relative deviations.

4.3.2.2 Moyal Length

The next parameter obtained from the longitudinal fit is the Moyal length and the original distribution is shown in Fig. 4.20 on the left and the smoothed extended distribution on the right. Following the argument from section 3.4.1 the length of the shower image is stretched proportionally to the impact distance d . This can very well be seen from Fig. 4.21. The relative deviation of the smoothed length from the original length, defined as $(l_{\text{orig}} - l_{\text{smoothed}})/l_{\text{orig}}$ in percent is shown in Fig. 4.23. The left side shows a two dimensional representation of the relative deviation as a function of impact distance d and height of the first interaction h_t . The right figure illustrates the distribution of the relative deviation which shows that for most of the bins the fluctuations are also between $\pm 20\%$.

4.3 Gamma Ray Air Shower Parameterisation

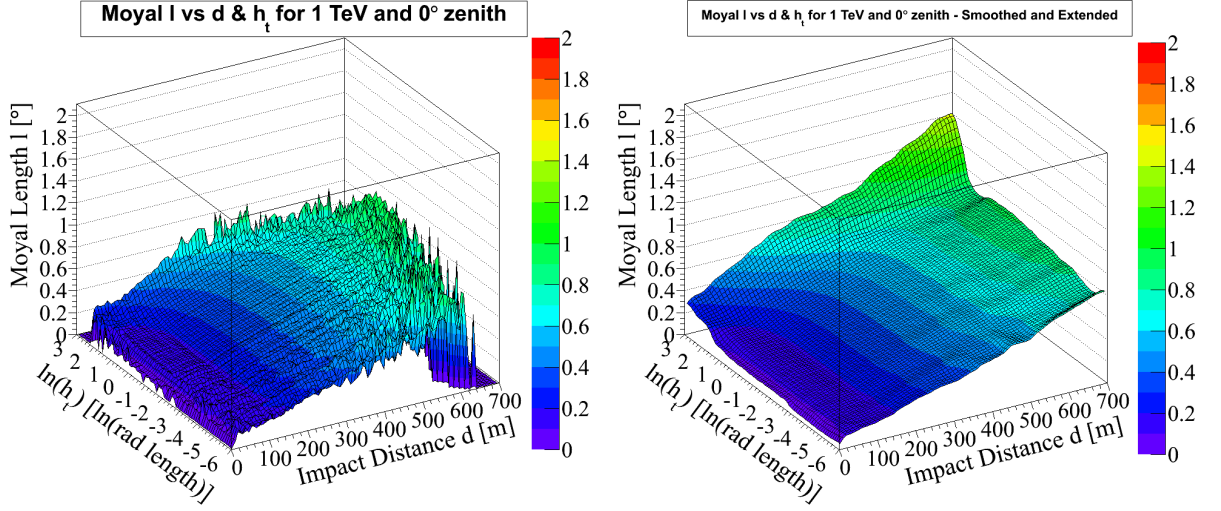


Figure 4.20: On the left is the original histogram filled from CORSIKA data and on the right is the histogram after a smoothing procedure. The histograms are filled in 80 bins in impact distance and height of the first interaction with the fitted Moyal length l in degrees.

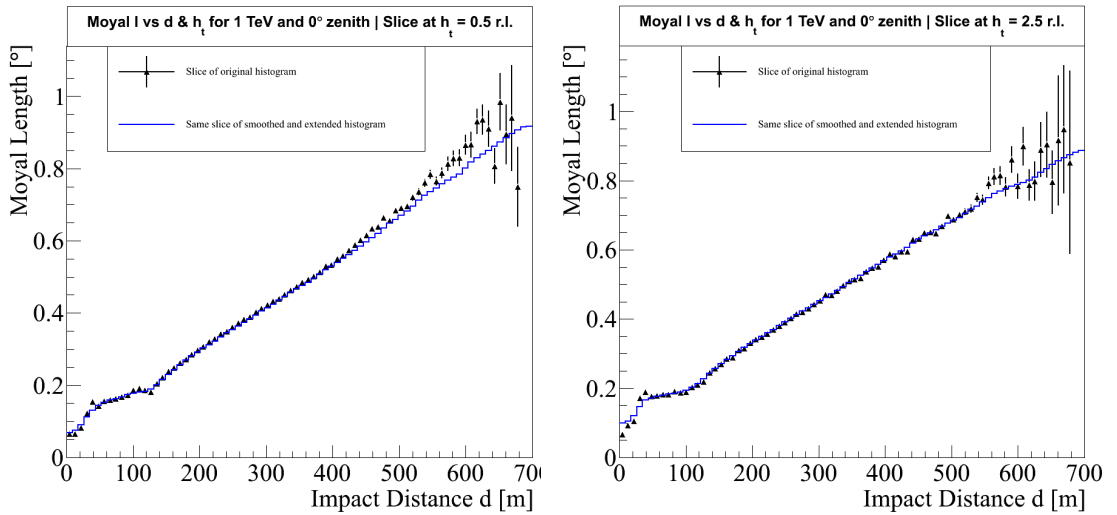


Figure 4.21: Slice of the original histogram of the Moyal length vs. d and h_t in black as well as the smoothed one in blue for the same slice. It is shown for two different height of first interactions of $h_t = 0.5X_0$ (left) and $h_t = 2.5X_0$ (right).

4. GRASP - GAMMA RAY AIR SHOWER PARAMETERISATION

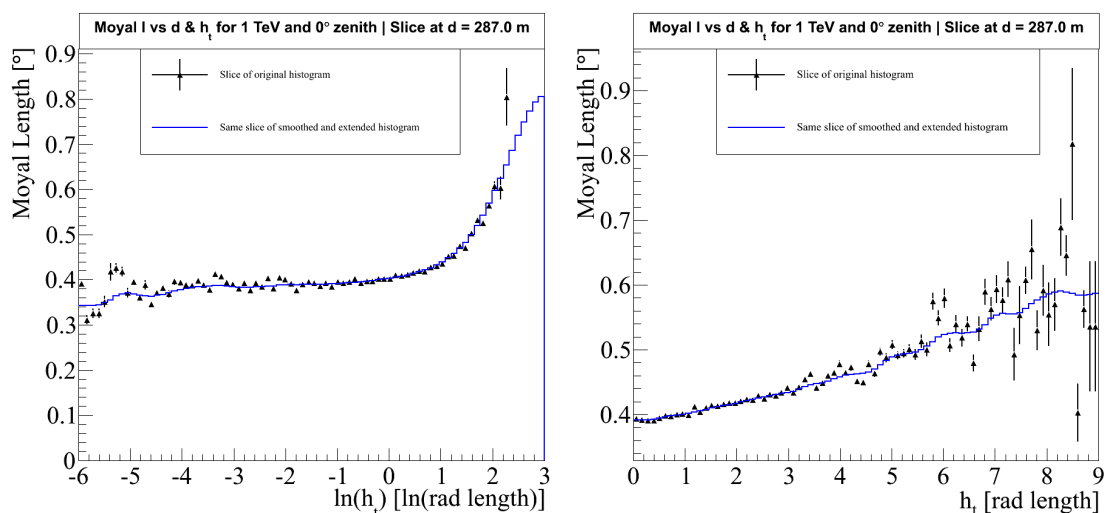


Figure 4.22: Slice of the original histogram of the Moyal length vs. d and h_t in black as well as the smoothed one in blue for the same slice. It is shown for an impact distance of $d = 287$ m in $\ln(h_t)$ scale on the left and in linear scale on the right.

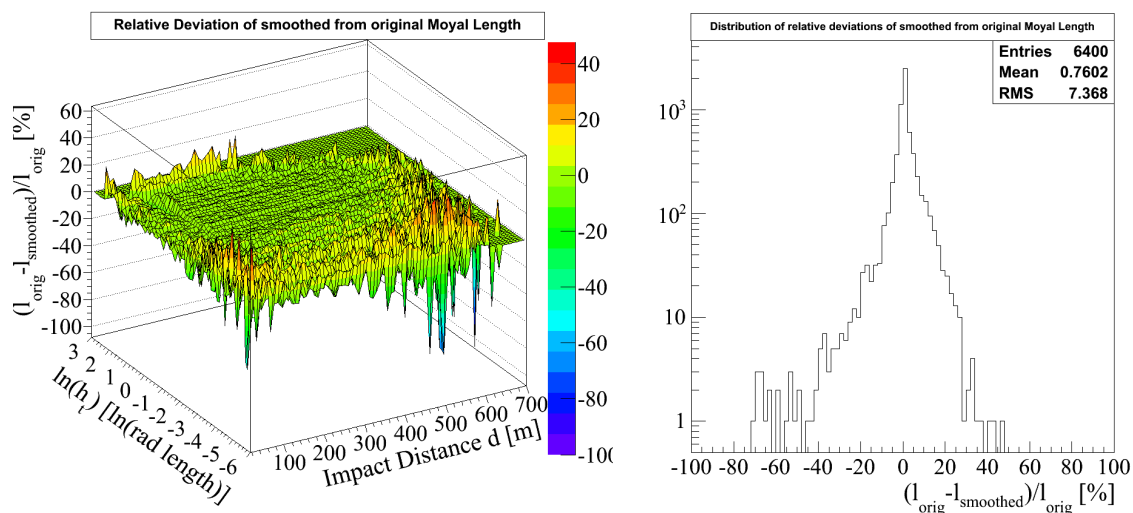


Figure 4.23: Left: Relative deviation of the smoothed Moyal length l histogram to the original one. Right: Distribution of these relative deviations.

4.3.2.3 Moyal Norm

The last parameter in the longitudinal fit is the Moyal normalisation n and is obtained by projecting the whole shower onto the shower direction and fitting the longitudinal distribution again. This means that unlike before the projection is done in the range of $-2^\circ < v < 2^\circ$. The following Fig. 4.24 shows the original distribution on the left and the smoothed and extended distribution on the right.

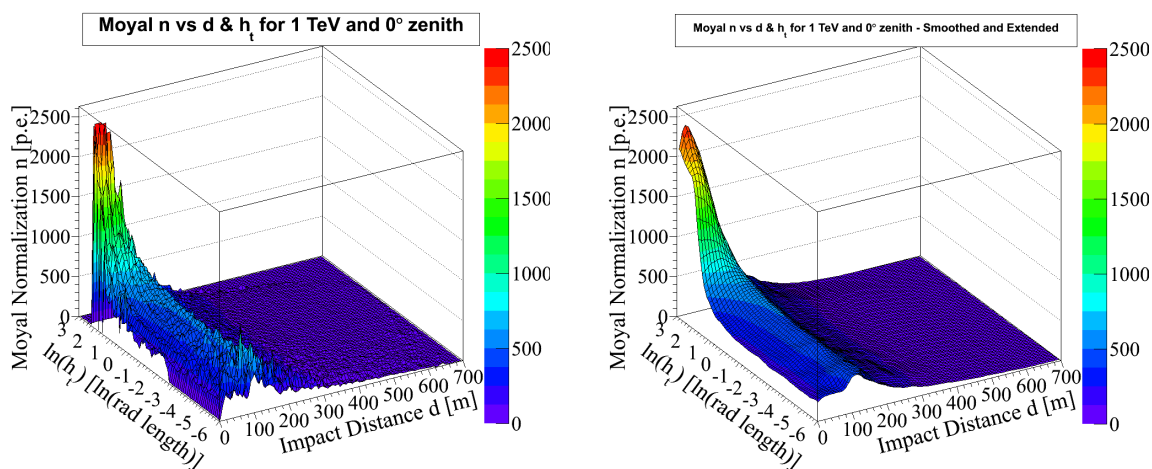


Figure 4.24: On the left is the original histogram filled from CORSIKA data and on the right is the histogram after a smoothing procedure. The histograms are filled in 80 bins in impact distance and height of the first interaction with the fitted Moyal normalisation n in p.e.

From the projection onto the impact distance d -axis in Fig. 4.25, it can be seen that inside the Cherenkov radius the normalisation or intensity of the Cherenkov emission rises and after the maximum declines exponentially due to multiple scattering. By looking at the projection onto the height of the first interaction it can be seen that the normalisation outside of the Cherenkov radius is basically constant. This means that outside the Cherenkov radius the normalisation is independent of the height of the first interaction. However, inside the Cherenkov radius it increases, since an increase in height of the first interaction leads to an increase in the shower maximum and the shower becomes similar to a higher energy shower, see eq. (2.11) and Fig. 2.8 in section 2.3. Furthermore, the refractive index is increased at the shower maximum since the shower reaches lower altitudes, which in turn leads to a higher number of produced Cherenkov photons, see eq. (2.29).

4. GRASP - GAMMA RAY AIR SHOWER PARAMETERISATION

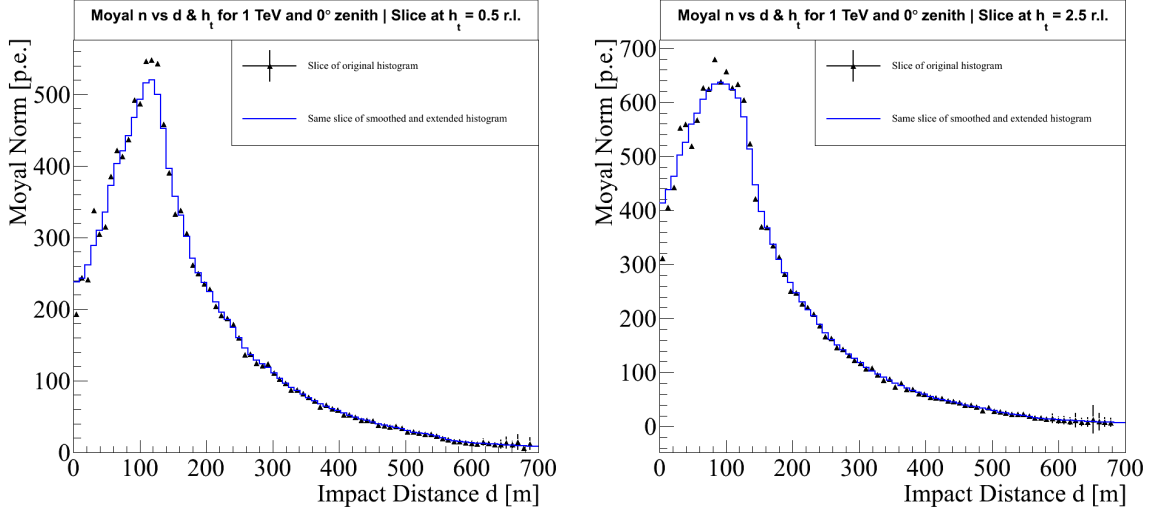


Figure 4.25: Slice of the original histogram of the Moyal normalisation vs. d and h_t in black as well as the smoothed one in blue for the same slice. It is shown for two different height of first interactions of $h_t = 0.5X_0$ (left) and $h_t = 2.5X_0$ (right).

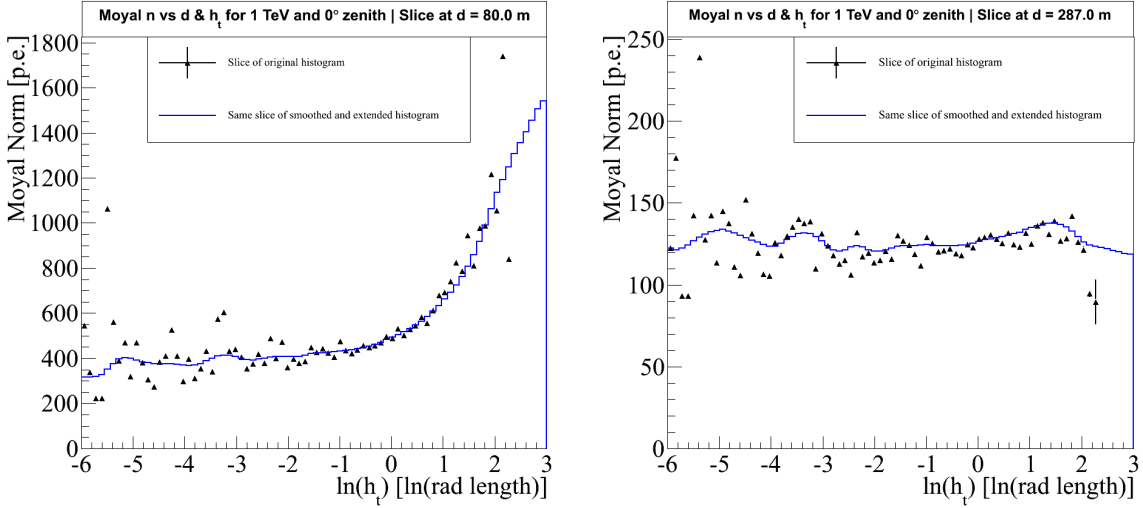


Figure 4.26: Slice of the original histogram of the Moyal normalisation vs. d and h_t in black as well as the smoothed one in blue for the same slice. It is shown for two different impact distances of $d = 80$ m (left) and $d = 287$ m (right).

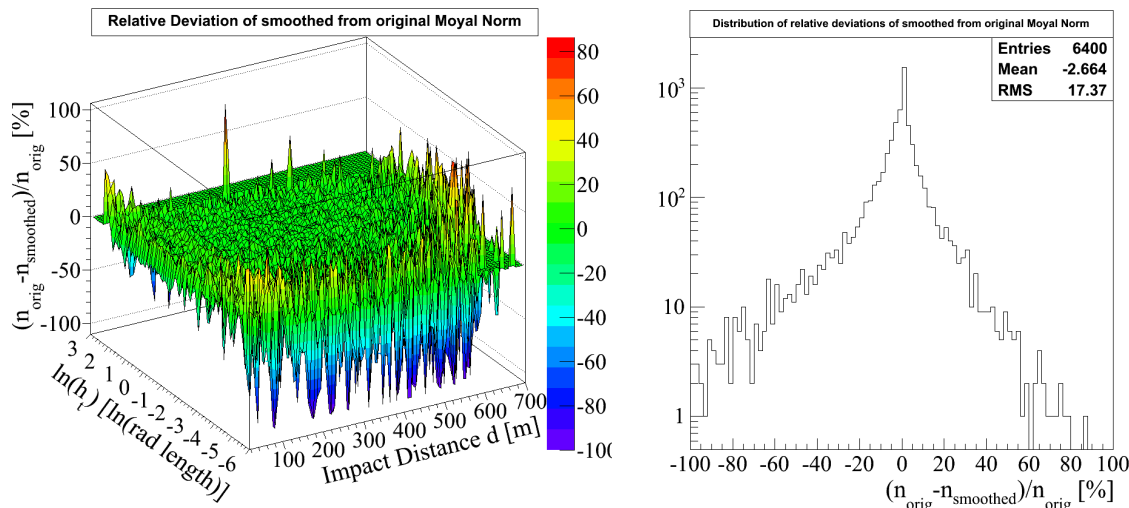


Figure 4.27: Left: Relative deviation of the smoothed Moyal normalisation n histogram to the original one. Right: Distribution of these relative deviations.

The relative deviation of the smoothed normalisation from the original normalisation, defined as $(n_{\text{orig}} - n_{\text{smoothed}})/n_{\text{orig}}$ in percent is shown in Fig. 4.27. The left side shows a two dimensional representation of the relative deviation as a function of impact distance d and height of the first interaction h_t . The right figure illustrates the distribution of the relative deviation which shows that for most of the bins the fluctuations are between $\pm 30\%$.

4.3.2.4 Lorentz Width

For the transverse part, slices along the longitudinal direction u with a bin width of 0.1° are made and a Lorentz function is fitted. There is only one parameter which is the Lorentz width w , since the normalisation is fixed to the total integral of the distribution. The original and smoothed histogram is shown in Fig. 4.28. Fig. 4.29 shows a slice along the longitudinal direction u at $d = 161$ m (left) and at $d = 287$ m (right). It shows that after the minimum the width of the shower rises with increasing emission angle or decreasing altitude. A fit of a polynomial of second order after the minimum fits the data quite well, see also right side of Fig. 4.13 in section 2.1.4. The larger error bars below some 0.5° are due to the fact that the photon statistics directly before the head of the shower image are poor. By looking at a slice along the impact

4. GRASP - GAMMA RAY AIR SHOWER PARAMETERISATION

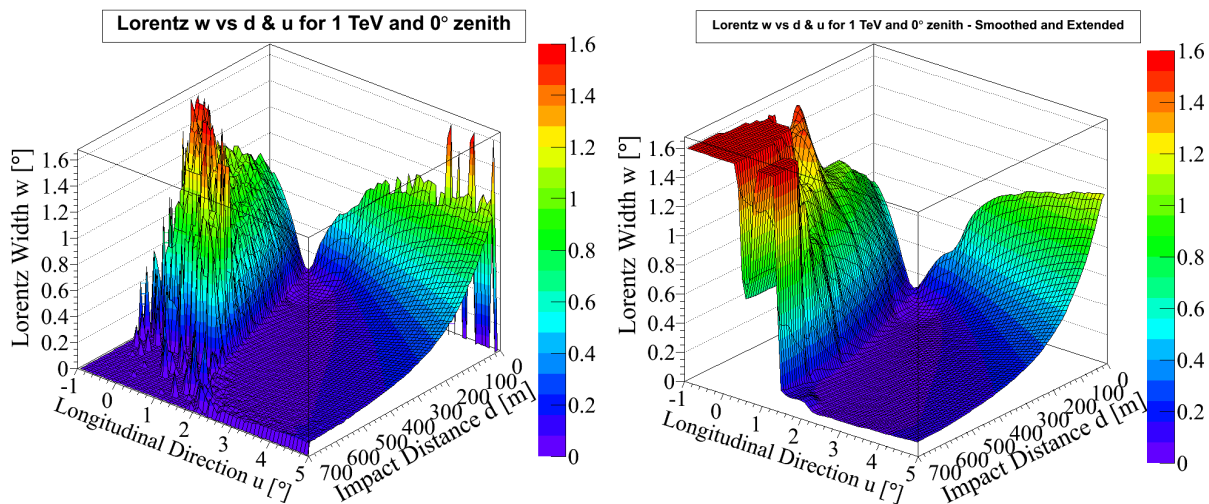


Figure 4.28: On the left is the original histogram filled from CORSIKA data and on the right is the histogram after a smoothing procedure. The histograms are filled in 80 bins in impact distance and the longitudinal direction in 60 bins with the fitted Lorentz width w in degrees.

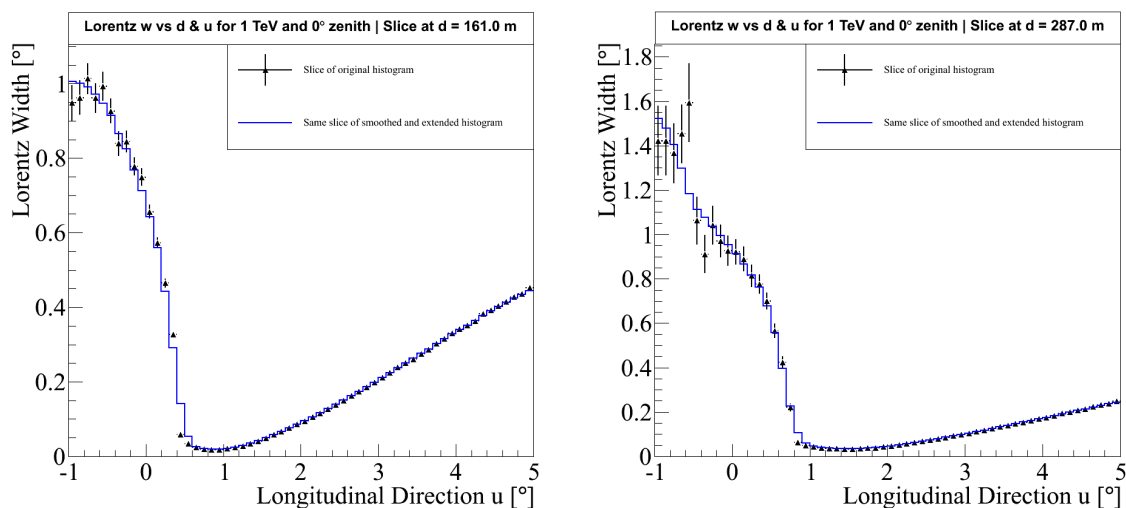


Figure 4.29: The left figure shows a slice along the longitudinal direction u at $d = 161$ m of the original histogram of the Lorentz width vs. u in black as well as the smoothed one in blue for the same slice. The right shows a slice at $d = 287$ m.

4.3 Gamma Ray Air Shower Parameterisation

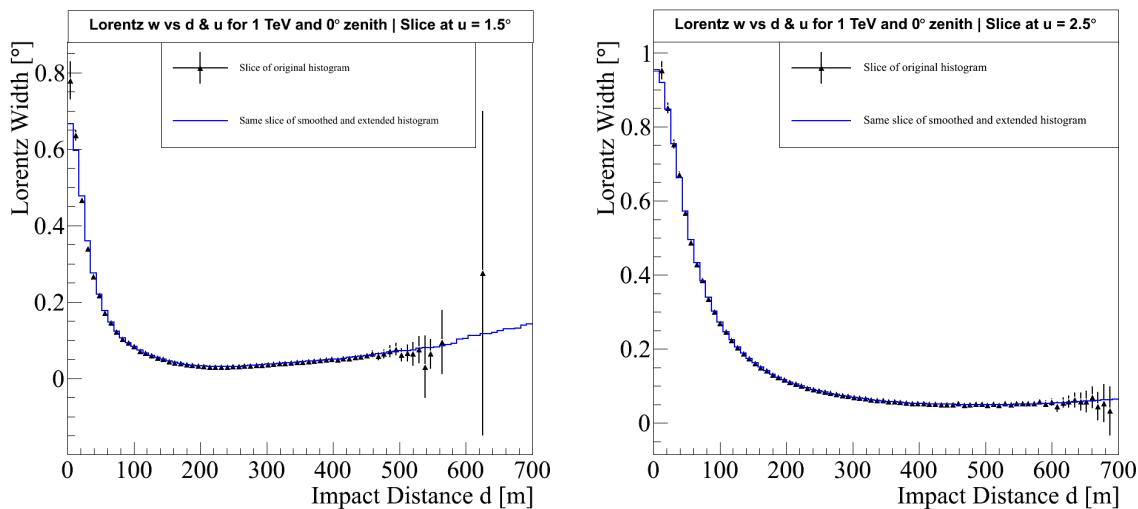


Figure 4.30: The left figure shows a slice along the impact distance axis at $u = 1.5^\circ$ of the original histogram of the Lorentz width vs. impact distance d in black as well as the smoothed one in blue for the same slice. The right shows a slice at $u = 2.5^\circ$.

distance axis at $u = 1.5^\circ$ and $u = 2.5^\circ$ in Fig. 4.30, it can be seen that the width rapidly declines with the impact distance and then varies only little, see also left side of Fig. 4.13 in section 2.1.4. The purpose of the slices was only to show that the smoothed and extended histogram quite nicely follows the original one.

The relative deviation of the smoothed Lorentz width from the original width, defined as $(w_{\text{orig}} - w_{\text{smoothed}})/w_{\text{orig}}$ in percent is shown in Fig. 4.31. The left side shows a two dimensional representation of the relative deviation as a function of impact distance d and longitudinal direction u . The right figure illustrates the distribution of the relative deviation which shows that for most of the bins the fluctuations are between $\pm 20\%$.

4. GRASP - GAMMA RAY AIR SHOWER PARAMETERISATION

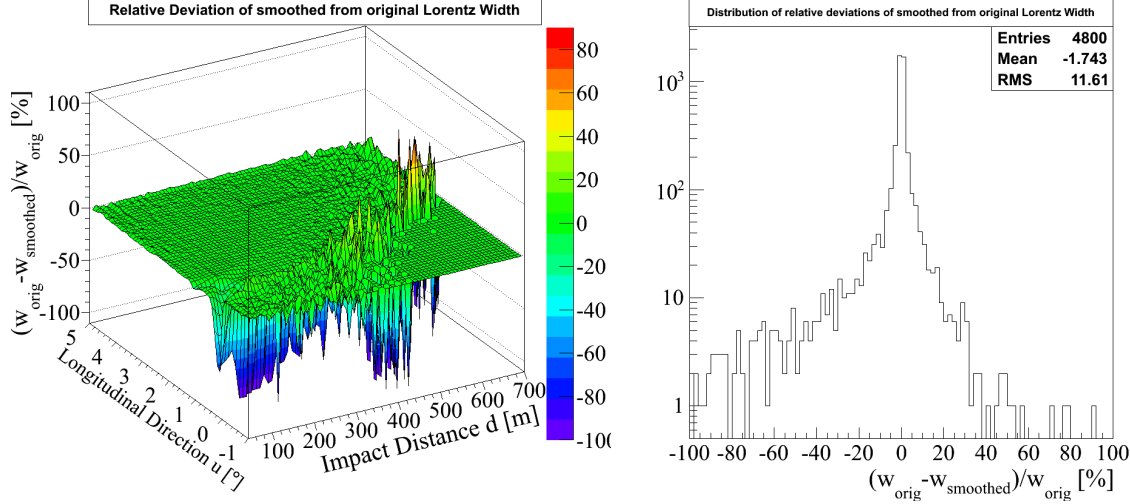


Figure 4.31: Left: Relative deviation of the smoothed Lorentz width w histogram to the original one. Right: Distribution of these relative deviations.

4.3.3 Parameterisation of the Shower Image

By combining the longitudinal and transverse part in eq. (4.10) and eq. (4.11) the total Cherenkov image due to a γ -ray induced air shower can be described by the following formula:

$$\frac{\rho(u, v)}{dudv} = L_{\text{Moyal}}(u; p, l, n) \times \frac{T_{\text{Lorentz}}(u, w)}{\pi(T_{\text{Lorentz}}(u, w)^2 + v^2)} \text{ [p.e./degrees}^2\text{]} \quad (4.18)$$

where $p = p(d, h_t)$, $l = l(d, h_t)$, $n = n(d, h_t)$ and $w = w(d, u)$ are obtained from the smoothed and extended histograms shown and described in section 4.3.2. It describes the angular distribution of Cherenkov photons inside the solid angle $dudv$. In order to get the total photoelectrons seen by one pixel of the camera this parameterisation has to be integrated over the pixel area. This will be the subject of the next section.

4.4 Reconstruction of Shower Parameters

With the parameterisation defined in the previous section a prediction of a shower image is given as a function of shower impact point of the incoming γ -ray candidate on the ground, its direction, height of the first interaction in the atmosphere and a normalisation scaling factor that relates to its energy. These predictions can then

be compared to actual shower images from the H.E.S.S. cameras and a minimisation procedure determines the shower parameters described above under the assumption of a γ -ray particle. The minimisation procedure compares the intensity of each pixel with the expected value of the shower image obtained from the parameterisation similar to [Le Bohec et al., 1998] and [de Naurois and Rolland, 2009]. To get the expected intensity the shower parameterisation is integrated over the pixel assuming a circular pixel with the same area as the hexagonal pixel in the H.E.S.S. camera. To that end the transverse part of eq. (4.18) is first partially integrated and then numerically with 8 integration points along the longitudinal direction. The number of integration steps was chosen to yield a precision in the order of $\sim 1\%$.

$$\begin{aligned}
 \bar{\rho}(u_c, v_c) &= \int_{u_c-r}^{u_c+r} du \int_{v_c-\sqrt{r^2-(u-u_c)^2}}^{v_c+\sqrt{r^2-(u-u_c)^2}} dv \rho(u, v) \\
 &= \int_{u_c-r}^{u_c+r} du L_{\text{Moyal}}(u; p, l, n) \times \left[\arctan \left(\frac{v}{T_{\text{Lorentz}}(u, w)} \right) \right]_{v_c-\sqrt{r^2-(u-u_c)^2}}^{v_c+\sqrt{r^2-(u-u_c)^2}} \\
 &\approx \sum_{i=1}^8 \Delta u_i L_{\text{Moyal}}(u_i; p, l, n) \times \left[\arctan \left(\frac{v}{T_{\text{Lorentz}}(u_i, w)} \right) \right]_{v_c-\sqrt{r^2-(u_i-u_c)^2}}^{v_c+\sqrt{r^2-(u_i-u_c)^2}}
 \end{aligned} \tag{4.19}$$

The centre of a pixel is defined as (u_c, v_c) and r is its radius. Furthermore u_i is defined as $u_i = (u_c - r) + i \cdot \Delta u_i$ with $i \in \{0, \dots, 8\}$ and $\Delta u_i = (2 \cdot r)/8$.

4.4.1 Pixel Log-Likelihood

The shower image resulting from the parameterisation in eq. (4.18) provides a number of photo electrons per degree squared and by integrating it over one pixel the expected intensity in photoelectrons can be calculated (see eq. (4.19)). By looking at eq. (3.6) in section 3.3.2 the basic form of the probability density function to observe a signal given an expected intensity leads to the following definition, see also [de Naurois and Rolland, 2009]:

$$P(s|\rho, \sigma_p, \sigma_\gamma) = \sum_n \frac{\rho^n e^{-\rho}}{n! \sqrt{2\pi(\sigma_p^2 + n\sigma_\gamma^2)}} \exp \left(-\frac{(s-n)^2}{2(\sigma_p^2 + n\sigma_\gamma^2)} \right) \tag{4.20}$$

This describes the probability density or likelihood to observe a signal of s in a pixel given an expected intensity of ρ , calculated from eq.(4.19), assuming the pedestal is

4. GRASP - GAMMA RAY AIR SHOWER PARAMETERISATION

at zero. It is given by the convolution of the Poisson distribution of the photoelectron number n with the photomultiplier resolution, which is represented by a Gaussian of width $\sqrt{\sigma_p^2 + n\sigma_\gamma^2}$. Here σ_p is the width of the pedestal and σ_γ the width of the single photoelectron peak, see also section 3.3.2 for details on both. The log-likelihood is then defined by:

$$\ln L = -2 \times \ln P(s|\rho, \sigma_p, \sigma_\gamma) \quad (4.21)$$

For high values of ρ the Poisson distribution can very well be approximated by a Gaussian of width $\sqrt{\rho}$ which simplifies the probability density function to a convolution of two Gaussians [de Naurois and Rolland, 2009]:

$$P(s|\rho \gg 0, \sigma_p, \sigma_\gamma) \approx \frac{1}{\sqrt{2\pi} (\sigma_p^2 + \rho(1 + \sigma_\gamma^2))} \exp\left(-\frac{(s - \rho)^2}{2 (\sigma_p^2 + \rho(1 + \sigma_\gamma^2))}\right)$$

The expectation value of the log-likelihood given the same shower expectation but different signal intensities due to Poisson noise can be calculated by:

$$\begin{aligned} \langle \ln L \rangle |_\rho &= \int ds \ln L(s|\rho, \sigma_p, \sigma_\gamma) \times P(s|\rho, \sigma_p, \sigma_\gamma) \\ &= 1 + \ln(2\pi) + \ln(\sigma_p^2 + \rho(1 + \sigma_\gamma^2)) \\ \sigma^2(\ln L) &= 2 \end{aligned} \quad (4.22)$$

For each telescope that participates in an air shower event the log-likelihood can be calculated by summing over all the pixels that were identified to belong to this event. See also section 3.3.5 for details on the identification of pixels for a shower event.

$$\ln L_{\text{tel}} = \sum_{\text{pixel } i} \ln L_i = \sum_{\text{pixel } i} -2 \ln P(s|\hat{\rho}, \sigma_p, \sigma_\gamma) \quad (4.23)$$

The total log-likelihood is defined as the sum of the log-likelihood over all the participating telescopes by:

$$\ln L_{\text{total}} = \sum_{\text{tel}} \ln L_{\text{tel}} \quad (4.24)$$

This total log-likelihood is then minimized using the MINUIT tool inside the ROOT software [Brun and Rademakers, 1997].

4.4.2 Shower Reconstruction

A sketch of the shower reconstruction is shown in Fig. 4.32 and illustrates how the parameterisation reflects data displayed as a shower image in the H.E.S.S. cameras.

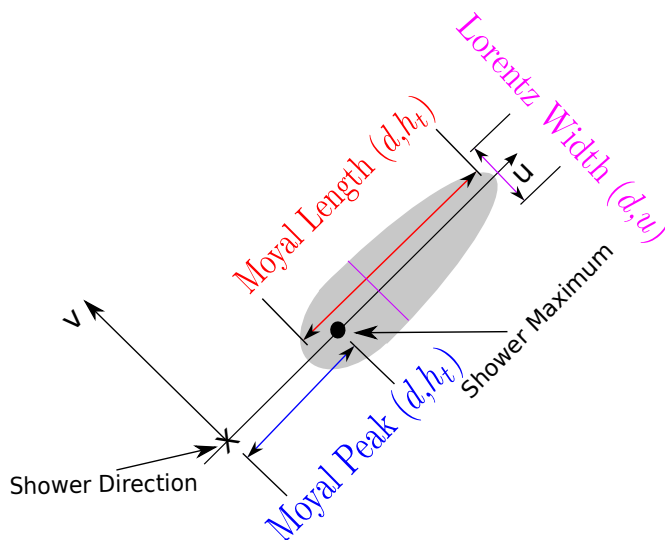


Figure 4.32: Sketch of the shower reconstruction.

First the shower direction marks the zero point of the coordinate system in the camera in which the parameterisation eq. (4.18) is calculated. Furthermore the Moyal peak p as a function of impact distance d and height of the first interaction h_t describes the distance between the shower direction and the shower maximum, which corresponds to the peak of the intensity distribution inside the shower image. The Moyal length l describes the length and the Lorentz width w the width of the shower image. It can already be seen that there is a degeneracy in the distance from the shower direction to the shower maximum. Looking at Fig. 4.32 it is clear that by moving the shower direction further out along the u -axis the same shower image can be obtained from a smaller Moyal peak p and therefore a smaller impact distance d . This degeneracy can be resolved when viewing the same shower from different sides, meaning with more than one telescope.

The predicted shower image, given a set of parameters, is compared to the actual shower image pixel by pixel and a total log-likelihood is then calculated by eq. (4.24).

4. GRASP - GAMMA RAY AIR SHOWER PARAMETERISATION

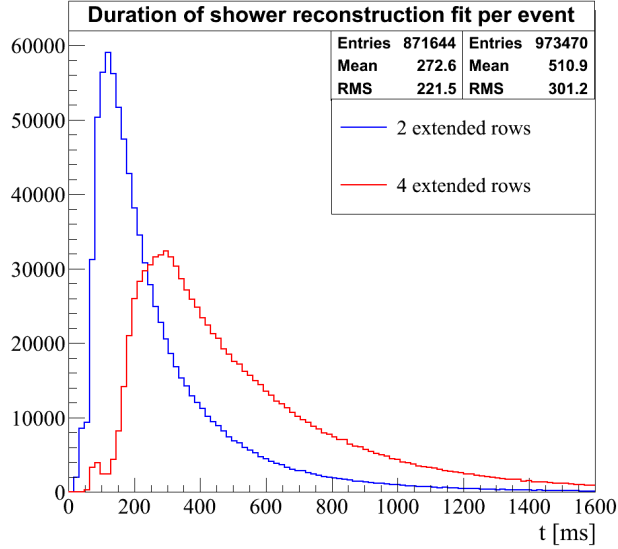


Figure 4.33: Duration of the shower reconstruction fit for 2 and 4 extended rows.

A minimisation algorithm reconstructs the best shower parameters:

- Shower Direction θ_u and θ_v
- Impact Point on the ground C_x and C_y
- Height of the first interaction h_t in the atmosphere in meters and converted to radiation length
- Scaling factor s that relates to the energy of the shower

In this minimisation procedure only pixels belonging to the extended cleaned images described in section 3.3.5 are used. The two additional extended rows are enough to yield a sufficient accuracy while maintaining a relatively short runtime of the fitting procedure.

From Fig. 4.33 it can be seen that the typical duration for this fit is on the order of 300 milliseconds which means that a whole MC γ -ray run with its typical 6000-10000 events will take about 30-50 minutes. For a whole observation run of about 28 minutes (see section 3.2.4) which only contains hadronic events (so called Off-run) there are about 500000 events before preselection cuts (see section 3.4.3) and about half pass the application of these cuts. This would take about 21 hours per run and would

4.4 Reconstruction of Shower Parameters

therefore take an unreasonable amount of time. To circumvent that, an additional loose preselection Hillas cut on MSCW and MSCL will be used. This cut retains about 99 % of the MC γ -ray events and reduces the number of hadronic events by about 70 %, severely reducing the runtime of the fitting procedure for one observation run. As starting points for the fitting procedure the Hillas based reconstruction is used. To that end the extended image is cleaned using the tail-cuts method described in section 3.3.5 using a few different threshold-pair combinations. After that the Hillas parameters are determined and the direction and impact point on the ground is calculated for each different cleaning. For all of those starting values the log-likelihood is determined and the ones which give the lowest log-likelihood will be used for the fit. Since the parameterisation is available at seven fixed energies of $E_{\text{lookup}} = \{0.1, 0.3, 0.5, 1, 2, 5, 10\}$ TeV the energy of the shower calculated from the Hillas reconstruction is used to determine the lookup for all the parameters of the shower image (Moyal peak p , length l , normalisation n and Lorentz width w). Unfortunately the CORSIKA simulations were done with different PMT quantum efficiencies and with different mirror reflectivities than the H.E.S.S. telescopes. This means an additional lookup had to be obtained that translates the scaling factor from the fit to the energy of the incident γ -ray. This is done in the following way, since there are seven different normalisation lookups that already relate to the energy of the incoming particle, the obtained scaling factor s is multiplied by the energy of the specific lookup that is used:

$$S = s \times E_{\text{lookup}} \quad (4.25)$$

In this way the logarithm of the new scaling factor S should linearly relate to the logarithm of the energy of the incident primary γ -ray. Using MC shower simulations for the H.E.S.S. telescope array produced with *sim_telarray* ([Bernloehr, 2008]) the obtained scaling factor S can be related to the true MC γ energy used in the simulations. These simulations incorporate the correct mirror reflectivities and quantum efficiencies for H.E.S.S.. This is shown in Fig. 4.34 where the simulated MC energy is shown as a function of the impact point d_A and the scaling factor S of the fit on the left side. Here the distance d_A is defined as the distance from the centre of the H.E.S.S. telescope array to the shower impact point on the ground. From this histogram the energy of the incident γ -ray can be obtained by looking up the impact distance d_A and the scaling factor S reconstructed from the fitting procedure.

4. GRASP - GAMMA RAY AIR SHOWER PARAMETERISATION

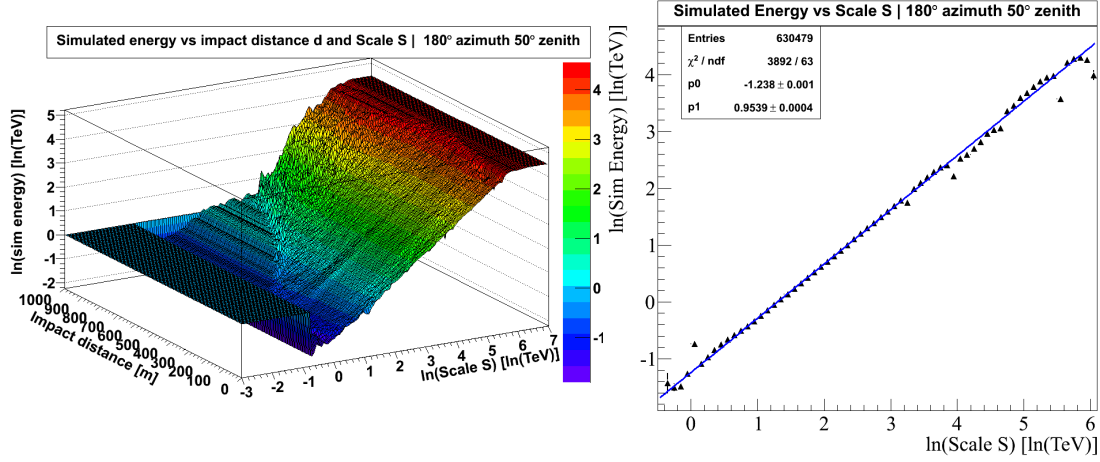


Figure 4.34: Logarithm of the simulated energy as a function of the impact distance d_A and the logarithm of the scale S for 180° azimuth and 50° zenith on the left and the same but only as a function of the scale S on the right.

On the right side of Fig. 4.34 the logarithm of the simulated MC energy as a function of the logarithm of the scale S is shown. The linear fit to the data shows a nice agreement with a slope close to unity. It has to be noted that the errors are computed as an error on the average of each bin, meaning e.g. two values close together still result in a small error bar.

4.5 Example Fit of a MC simulated Event

A first check of whether the parameterisation obtained is sensible can be done by fitting the parameterised shower image to a MC simulated γ -ray air shower event. In order to show that, one specific event was chosen at 0° zenith which triggered four telescopes. The following table 4.2 illustrates the Hillas based reconstruction shower parameters, the MC true simulated values as well as the reconstructed parameters from the GRASP method. The shower reconstruction fitting done by the GRASP method shows a nice agreement with the MC simulated values. It should be noted that this is of course a best case example. Fig. 4.35 shows the MC simulated air shower event inside the first H.E.S.S. camera CT-1. After the fitting procedure of the GRASP method Fig. 4.36 is obtained. A residual image can be obtained by subtracting the simulated MC shower event image from the predicted shower image of the GRASP method and is displayed in

4.5 Example Fit of a MC simulated Event

Shower parameter	Hillas	GRASP	MC simulated value
Direction in u (θ_u) [$^\circ$]	0.46	0.49 ± 0.01	0.5
Direction in v (θ_v) [$^\circ$]	0.01	-0.01 ± 0.01	0
Core position in x (C_x) [m]	33	26 ± 2	23
Core position in y (C_y) [m]	-35	-36 ± 2	-36
Height of the first interaction (h_t) [X_0]	/	-1.4 ± 0.2	0.14
Shower Energy (E) [TeV]	0.58	0.74 ± 0.11	0.75

Table 4.2: Comparison of one reconstructed air shower event for the different reconstruction methods with the true MC simulated values.

Fig. 4.37. Fig. 4.38 shows a two-dimensional projection of the likelihood surface with three position markers for the Hillas reconstructed direction (red triangle), the MC simulated direction (black circle) and the fitted GRASP direction (blue square). The same MC simulated air shower event inside the second H.E.S.S. camera CT-2 is shown in Fig. 4.39. After the fitting procedure of the GRASP method Fig. 4.40 is obtained. Again a residual image can be obtained by subtracting the simulated MC shower event image from the predicted shower image of the GRASP method and is displayed in Fig. 4.41. Fig. 4.42 shows a two dimensional projection of the likelihood surface for the core position. It shows three position markers for the Hillas reconstructed core position (red triangle), the MC simulated core position (black circle) and the fitted GRASP core position (blue square).

For air shower events with an impact distance to the telescope smaller than ≈ 50 m, the GRASP parameterisation might not adequately describe the shower image, since the air shower is not seen from the side. In such cases a Moyal function might not be a well suited function to describe the longitudinal angular Cherenkov photon distribution. The examples shown here and for the results in the following, the data was removed for telescopes which have an impact distance less than 50 m, from the fit. This could be subject for future improvements.

4. GRASP - GAMMA RAY AIR SHOWER PARAMETERISATION

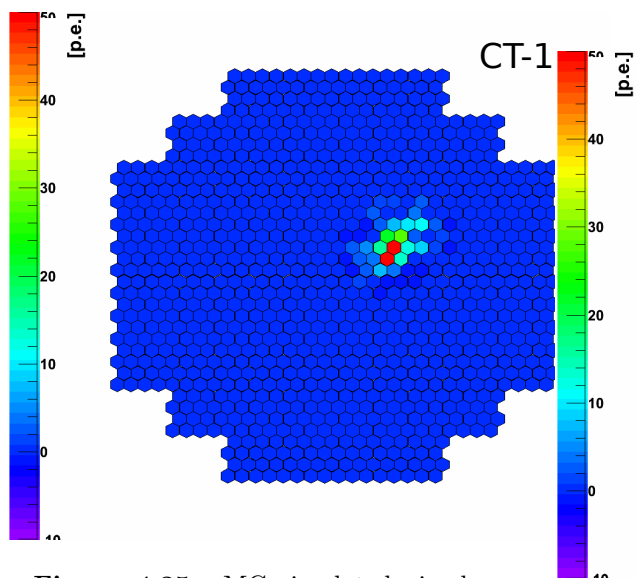


Figure 4.35: MC simulated air shower event inside the first H.E.S.S. camera CT-1.

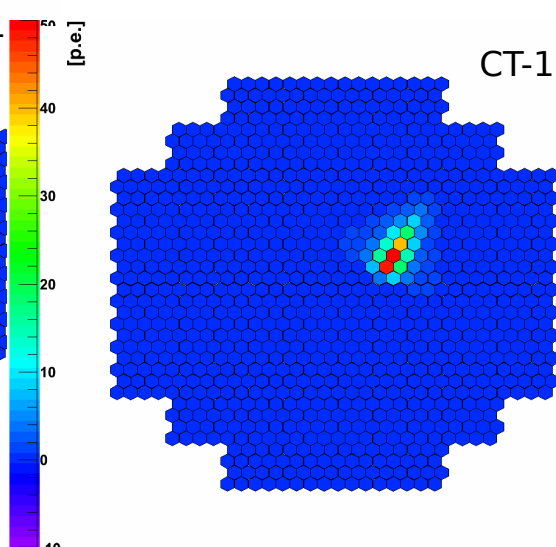


Figure 4.36: Predicted GRASP shower image after the fitting procedure for CT-1.

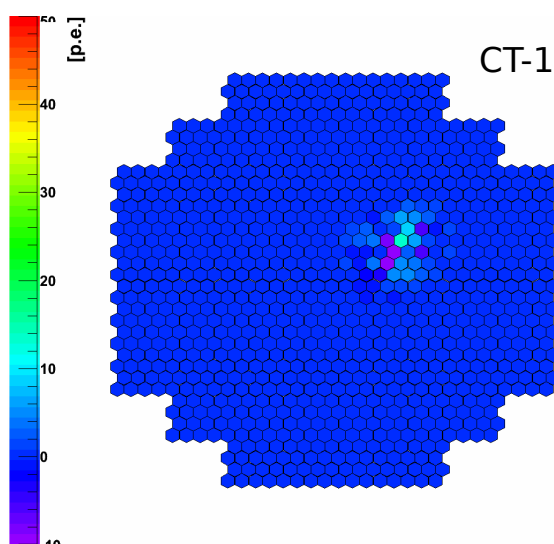


Figure 4.37: Residual image calculated by subtracting the simulated MC shower event image from the predicted shower image of the GRASP method.

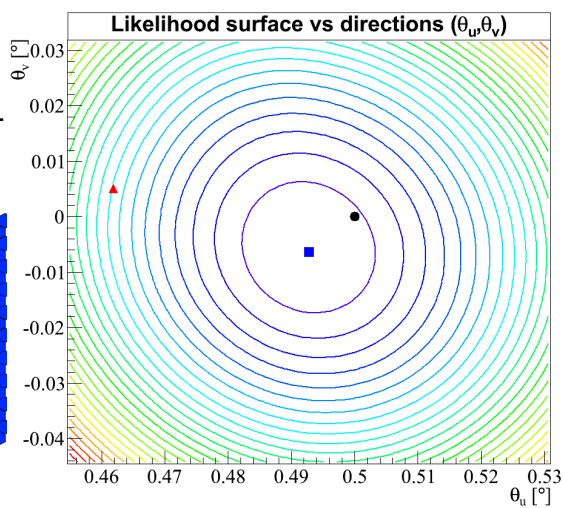


Figure 4.38: Two-dimensional projection of the likelihood surface with three position markers for the Hillas reconstructed direction (red triangle), the MC simulated direction (black circle) and the fitted GRASP direction (blue square).

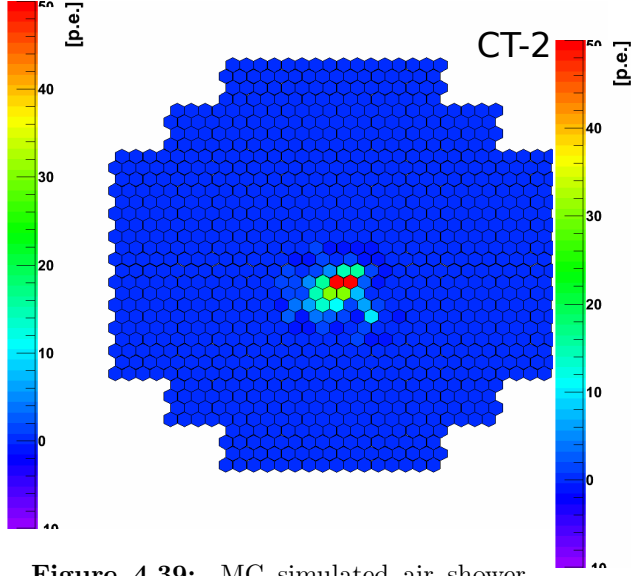


Figure 4.39: MC simulated air shower event inside the first H.E.S.S. camera CT-2.

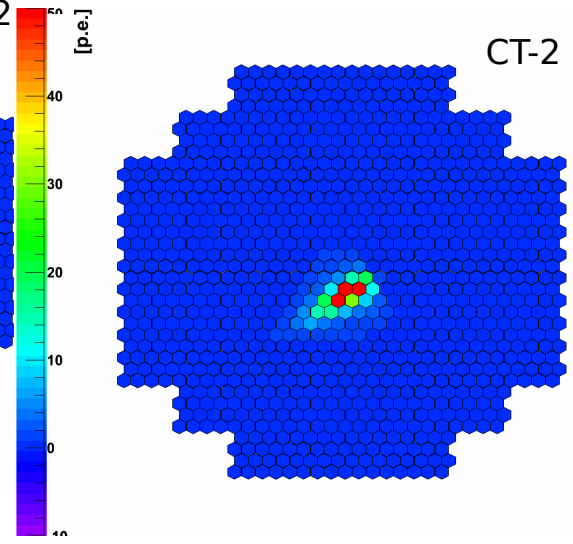


Figure 4.40: Predicted GRASP shower image after the fitting procedure for CT-2.

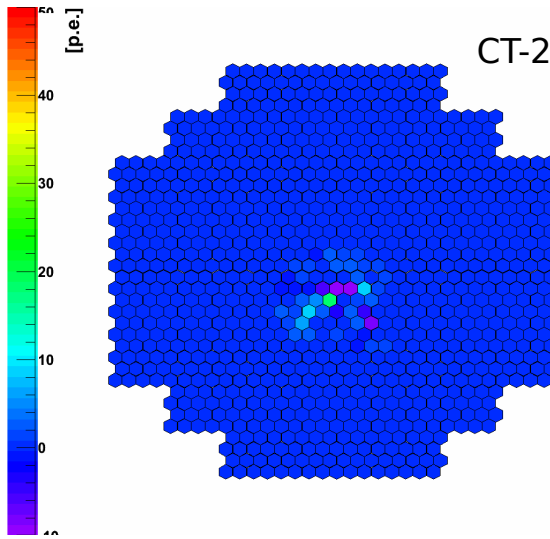


Figure 4.41: Residual image calculated by subtracting the simulated MC shower event image from the predicted shower image of the GRASP method.

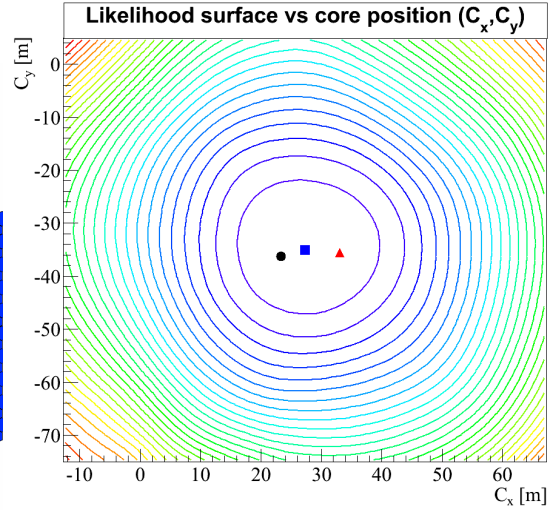


Figure 4.42: Two-dimensional projection of the likelihood surface with three position markers for the Hillas reconstructed core position (red triangle), the MC simulated core position (black circle) and the fitted GRASP core position (blue square).

4.6 γ -Hadron Separation

The Hillas based γ -hadron separation was already described in section 3.4.3. The basis for the background rejection deployed in this work is the multivariate analysis technique described in section 3.4.4. To that end new parameters from the GRASP method were used and combined with some of the parameters from the Hillas based reconstruction. This will be explained in detail in the following subsections.

4.6.1 Fit Parameters

In addition to the first fit described in section 4.4.2 a second fit was done for each shower image alone. The direction of the γ -ray like event was used to fix the zero point of the coordinate system defined in Fig. 4.32. From this the Moyal peak p , length l and a scaling factor k was fitted directly to each shower image in the camera of every participating telescope. The scaling factor k scales the width of the shower image. For a γ -ray event this scaling factor k is expected to be narrowly distributed around unity. For a hadronic event on the other hand, large deviations are expected with regard to the broader shower development. This means that eq. (4.18) is adjusted as follows:

$$\frac{\rho(u, v)}{dudv} = L_{\text{Moyal}}(u; p, l, n) \times \frac{k \cdot T_{\text{Lorentz}}(u, w)}{\pi((k \cdot T_{\text{Lorentz}}(u, w))^2 + v^2)} \text{ [p.e./degrees}^2\text{]} \quad (4.26)$$

The normalisation for this second fit was done in the following way:

$$\hat{\rho}(u, v) = I \cdot \frac{\bar{\rho}(u_c, v_c)}{\int_{\text{Camera}} \rho(u, v)} \quad (4.27)$$

where I is the total image amplitude of the shower image in the camera. In principle this second fit could be used in the framework of the Hillas method alone, by using Hillas reconstructed direction and impact parameter. This, however, has not been done yet and could be a subject for future studies. Throughout this work the second fit is only performed if the first fit for the shower reconstruction succeeded, see below for justification.

There are several parameters which yield a potential for γ -hadron separation.

- Moyal peak p from the second fit, which describes the shower maximum
- Moyal length l from the second fit
- Lorentz width scale k
- Difference of Moyal peak from first p_{firstfit} to second fit p_{secfit}
- Difference of Moyal length from first l_{firstfit} to second fit l_{secfit}
- X_{max} , calculated from Moyal peak and reconstructed impact distance, see section 4.2.2
- Convergence of the first fit to reconstruct shower parameters

Looking at the convergence of the first fit to reconstruct shower parameters for MC simulated data and real data containing only hadronic background events (Off-Data), the following table 4.3 can be given.

	MC simulated γ -ray data	Off-Data
Total number of events	871080 (870799)	1.747×10^7 (4.202×10^6)
Number of not converged events	23166 (54635)	0.224×10^7 (560628)
Fraction [%]	2.7 (6.2)	12.8 (13.3)

Table 4.3: Number of MC simulated γ -ray data and Off-Data for which the first fit to reconstruct shower parameters did not converge compared to the total number of events. It is shown for data at 0° zenith and at 55° zenith in brackets.

By looking at table 4.3 it becomes clear that a cut on the convergence of the first fit to reconstruct shower parameters can additionally reject hadronic background especially for sources with a low signal over background ratio. For a given data set this basically means that, when the GRASP shower reconstruction fit fails, the event will be discarded from the analysis.

4. GRASP - GAMMA RAY AIR SHOWER PARAMETERISATION

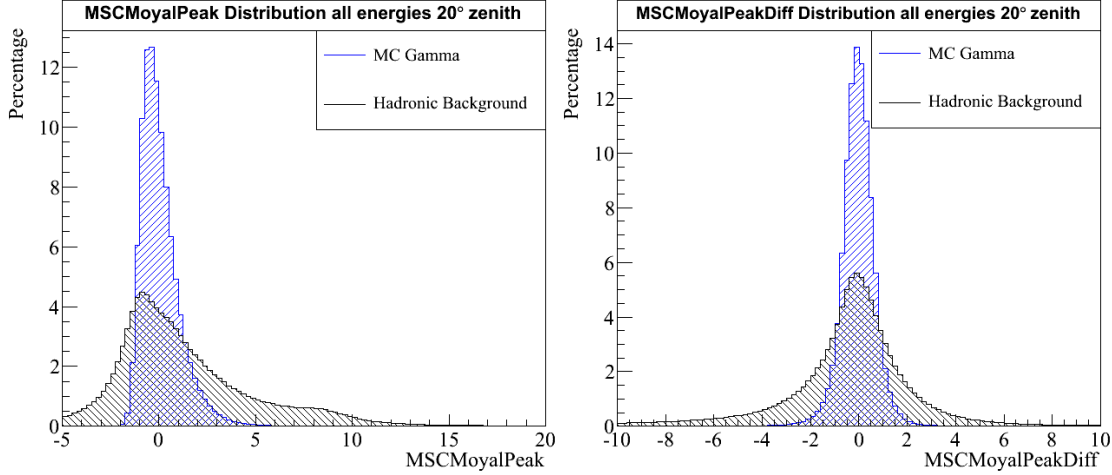


Figure 4.43: Right: MSC Moyal peak distribution for MC γ in blue and hadronic background in black in percent of the total number of events at 20° zenith. Right: MSC Moyal peak difference distribution for MC γ in blue and hadronic background in black in percent of the total number of events at 20° zenith.

Since the other parameters can be calculated for each participating telescope they will be mean scaled in the same manner as for the Hillas MSCW and MSCL in section 3.4.3. In this way the multiplicity of the air shower event is naturally incorporated and the training of boosted decision trees later can be handled more easily. It should be noted, however, that some of these parameters are highly correlated, depending on the energy band defined in section 4.6.2. The major advantages of boosted decision trees are that it treats non-linear correlations and is robust against weak variables. This justifies the above step of introducing many more new parameters that might not turn out to help in improving the γ -hadron separation. The mean scaled Moyal peak distribution for MC γ -rays and hadronic background for all energies at 20° zenith is shown in Fig. 4.43 on the left and the mean scaled Moyal peak difference distribution on the right. Both parameters show for MC γ -ray data a narrow distribution centred at zero with a smaller RMS than for hadronic background, which will yield the potential for γ -hadron separation. The next parameter is the mean scaled Moyal length and is shown in Fig. 4.44 on the top left and the mean scaled Moyal length difference on the top right. The last parameters are the Lorentz width scaling factor k and the reconstructed shower maximum X_{max} which are shown at the bottom left and right of Fig. 4.44. All of these parameters show a more or less good potential for γ -hadron separation and will

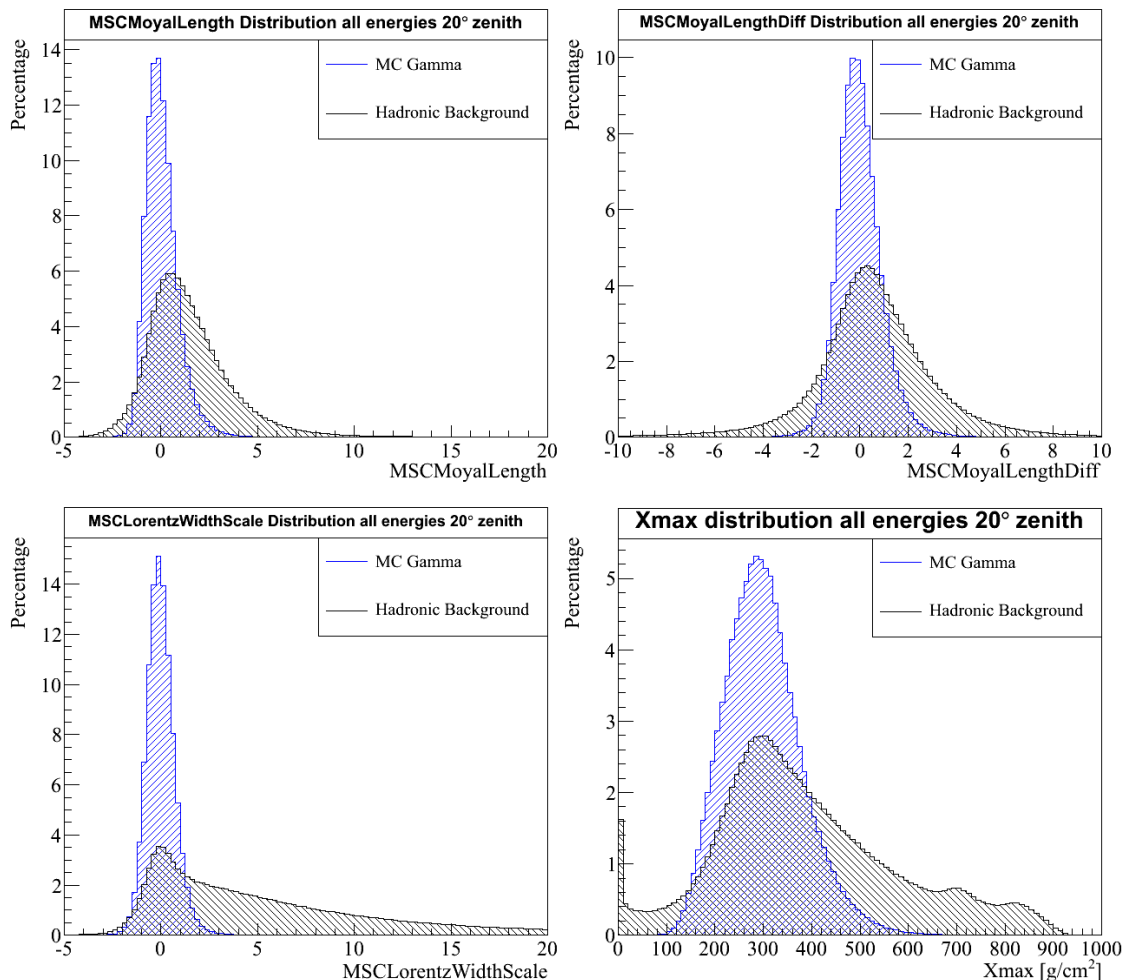


Figure 4.44: MSC parameter distribution for MC γ in blue and hadronic background in black in percent of the total number of events at 20° zenith

be used later in the training of the boosted decision trees. In order to have a better understanding of how the parameter distributions change as a function of energy or zenith, the mean and RMS of these distributions can be calculated. Fig. 4.45 shows the mean and RMS of the Moyal peak distribution as a function of energy on the left and for the Moyal peak difference distribution on the right. All the other parameters are shown in Fig. 4.46. The mean and RMS of the MC γ -ray data show only a small increase with increasing energy. In the case of an ideal γ -hadron separation parameter the mean would significantly deviate for the two different distributions and a small RMS would prevent an overlap. The figures, on the other hand, clearly show a some-

4. GRASP - GAMMA RAY AIR SHOWER PARAMETERISATION

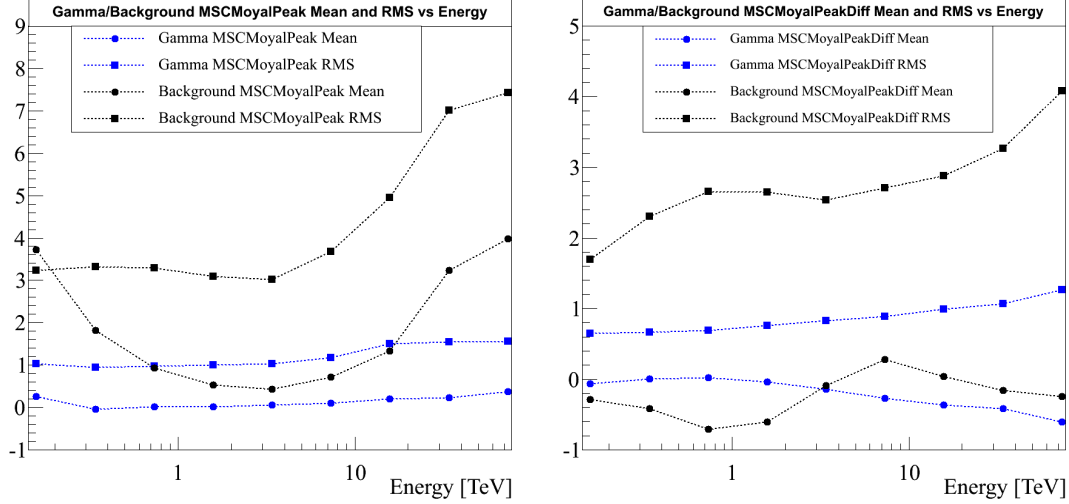


Figure 4.45: Mean (circle) and RMS (square) of the MSC parameter distributions as a function of energy for MC γ in blue and hadronic background in black.

what large RMS and for some energies a large difference in the mean. The large RMS is favorable, should the means of both distributions be close together. All of this ensures the possibility of γ -hadron separation.

In the same manner the variation of the mean and RMS of these parameters can be shown as a function of the zenith angle in Fig. 4.47. From these it can be seen that the mean and RMS for the MC γ -rays are quite stable with increasing zenith angle. On the other hand the mean for hadronic background for almost all the parameters is increasing with zenith angle. The parameter distribution for MC γ -rays and hadronic background build the samples in the training of the BDTs. In addition to all the new parameters obtained by the GRASP method, all Hillas based parameters for the previous multivariate analysis described in section 3.4.4 are incorporated as well. These parameters are the Hillas MSCW, MSCL, MSCWO, MSCLO and dE/E . The distribution of these parameters for hadronic background and MC γ -rays can be found in [Ohm et al., 2009]. Furthermore the shower maximum X_{max} is calculated from the Moyal peak p and impact distance d using the relation $h_{max} \approx d/p$ and is averaged over each participating telescope. The averaged height of shower maximum \bar{h}_{max} can then be converted to a thickness using the atmospheric profile.

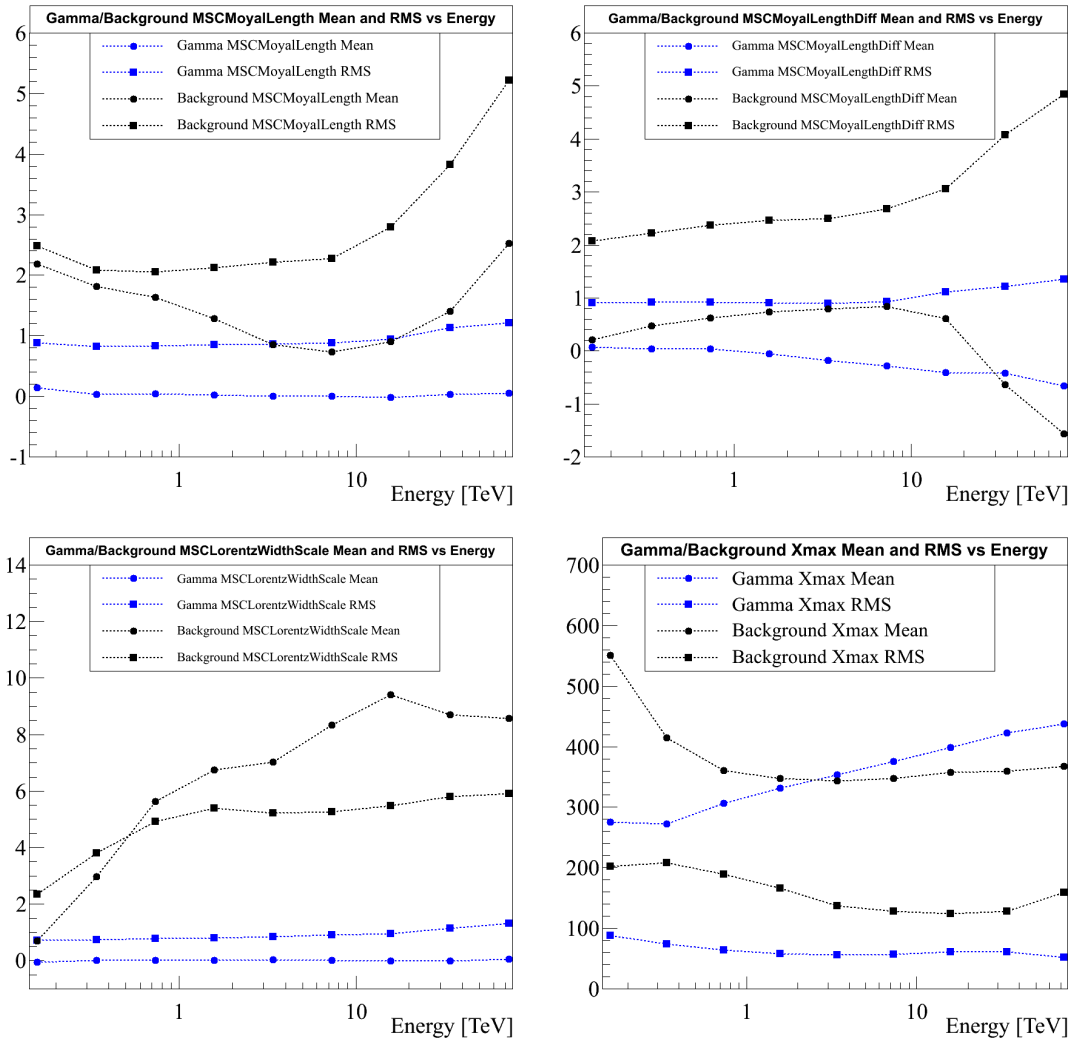


Figure 4.46: Mean (circle) and RMS (square) of the MSC parameter distributions as a function of energy for MC γ in blue and hadronic background in black.

4. GRASP - GAMMA RAY AIR SHOWER PARAMETERISATION

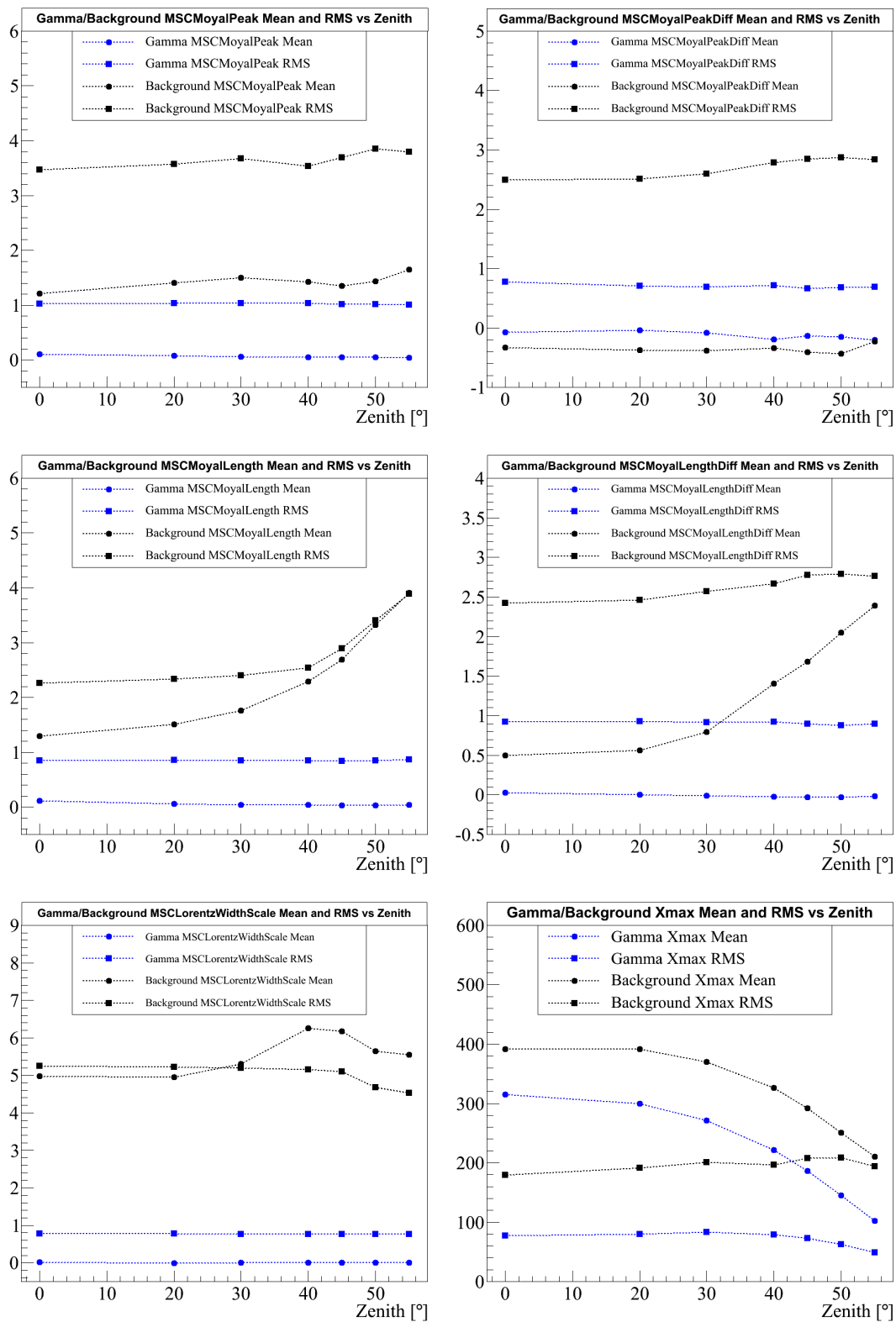


Figure 4.47: Mean (circle) and RMS (square) of the MSC Moyal peak distributions as a function of the zenith angle for MC γ in blue and hadronic background in black.

4.6.2 Multivariate analysis with BDTs

The general principle of boosted decision trees are explained in section 3.4.4. Following the same principle as described in [Ohm et al., 2009] the training is done in seven zenith bands of $\text{Zenith}_{\text{bands}} = \{0, 20, 30, 40, 45, 50, 55\}$ and six energy bands of $E_{\text{bands}} = \{0.1-0.3, 0.3-0.5, 0.5-1, 1-2, 2-5, 5-100\}$ TeV. In each of those training bands the sample of MC γ -ray and hadronic background data are separated in a test and training sample, where checks are performed on the test sample after the training procedure. The parameters for the training are kept the same as described in [Ohm et al., 2009] with the exception of the number of splits per tree which was increased to 150 since the number of parameters increased as well. The training sample contains only events passing the preselection cuts defined in section 3.4.3 as well as the loose preselection cut on MSCW and MSCL described in section 4.4.2. After the training procedure for each zenith and energy band the importance of each variable can be calculated as the rate of occurrence of a splitting variable during the training procedure, weighted by the squared separation-gain and the number of events in the corresponding nodes, see also [Breiman et al., 1984].

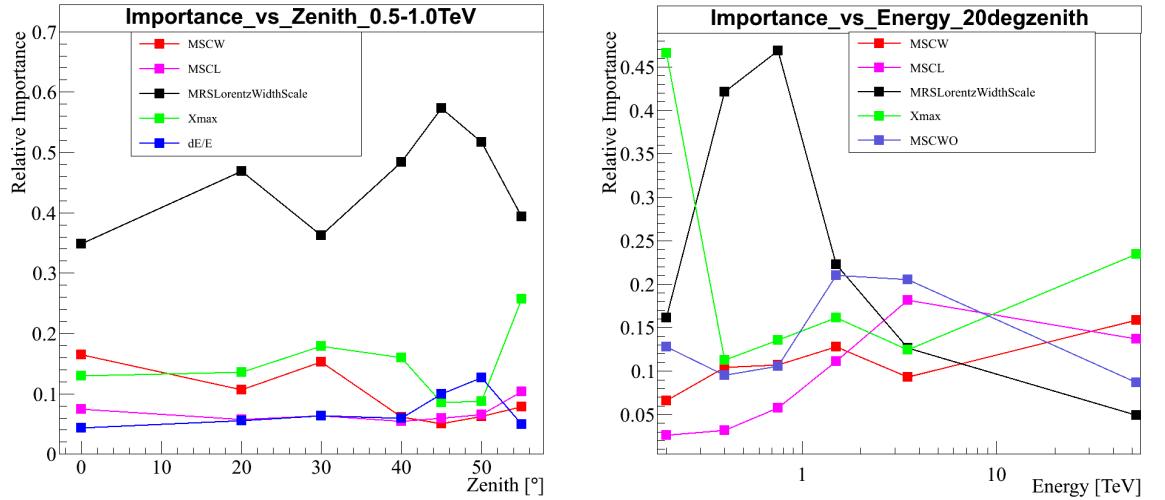


Figure 4.48: Relative importance of the top five most important variables as a function of the energy at 20° zenith (left) and as a function of the zenith angle for the energy band 0.5 TeV - 1 TeV (right).

4. GRASP - GAMMA RAY AIR SHOWER PARAMETERISATION

Fig. 4.48 shows the importance of the top five most important variables among the ten. It can be seen that in the energy range of 0.5 TeV to 1 TeV the Lorentz width scaling factor is the most important variable in all zenith bands (left). On the other hand the importance of this variable declines as a function of energy and the Hillas MSCW and MSCWO becomes more important. This behaviour might be an indication of the readout window which truncates shower images at higher energies, see also section 4.7.1.

4.7 Performance

4.7.1 Accuracy of Direction and Energy Reconstruction

A measure of the telescope direction reconstruction accuracy is the angular resolution. The angular resolution is obtained from the so called θ^2 -distribution. Here θ^2 is the squared angular difference between the reconstructed direction and the true direction of MC γ -ray simulations for a point source with *sim_telarray*. The energy spectrum of all MC γ -ray simulations is $\propto E^{-2}$. The θ^2 -distribution is illustrated for simulations with a zenith angle of 20° in Fig. 4.49. The following figures are obtained after background rejection, see section 4.6.

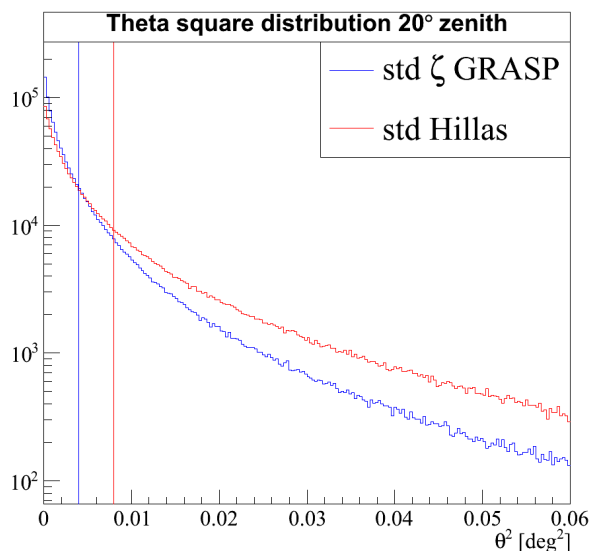


Figure 4.49: θ^2 distribution for MC γ -ray simulations at 20° zenith. Simulations for both azimuth angles of 0° and 180° are used. The blue line corresponds to the standard ζ GRASP and the red line to the standard Hillas method.

The angular resolution is defined as the 68 % containment radius, which is the radius in which 68 % of all the events fall. For GRASP the theta square value at which this happens is $\theta_{\text{GRASP},68}^2 \approx 0.0044$ and is shown as the blue vertical line in Fig. 4.49. This corresponds to an angular resolution of $\theta_{\text{GRASP},68} \approx 0.066^\circ$. For the Hillas reconstruction the theta square value is $\theta_{\text{HILLAS},68}^2 \approx 0.0077$ and is also shown in Fig. 4.49 as the red vertical line. This corresponds to an angular resolution of $\theta_{\text{HILLAS},68} \approx 0.088^\circ$. The relative improvement over the Hillas based reconstruction for

4. GRASP - GAMMA RAY AIR SHOWER PARAMETERISATION

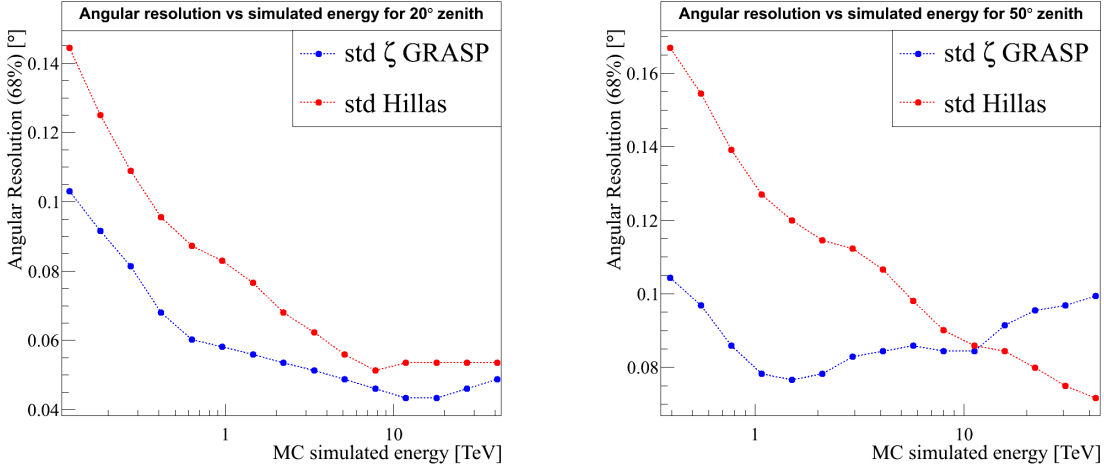


Figure 4.50: Angular resolution as a function of MC simulated energy for 20° zenith on the left and for 50° zenith on the right. Simulations for both azimuth angles of 0° and 180° are used. The blue circles are for the standard ζ GRASP and the red circles are for the standard Hillas method.

a zenith angle of 20° is therefore about 25%. The calculated angular resolution can also be shown as a function of MC simulated energy in Fig. 4.50. The left figure shows the angular resolution for MC data at 20° zenith and the right for 50° zenith. From this it can be seen that at 50° zenith angle the GRASP method performs not as well as the Hillas reconstruction above some 10 TeV. This is due to the fact that in this method no electronic simulations of the H.E.S.S. cameras were incorporated. As mentioned in section 3.2.2 the readout window for the cameras is a fixed window of about 16 ns around the trigger signal. For air showers with high enough energies (around 10 TeV) this leads to a truncation effect. A future improvement for this method would be to implement this readout window in the framework of GRASP which would affect the shape parameterisation lookups in section 4.3.2. This can also be illustrated when classifying the simulated events in two regimes of reconstructed impact distances, see Fig. 4.51. The first regime consists of relatively close events with a reconstructed impact distance smaller than 300 meters and the second with a reconstructed impact distance higher than 300 meters. It can be clearly seen that for showers with an impact distance larger than 300 meters the truncation effect due to the fixed readout window becomes increasingly severe.

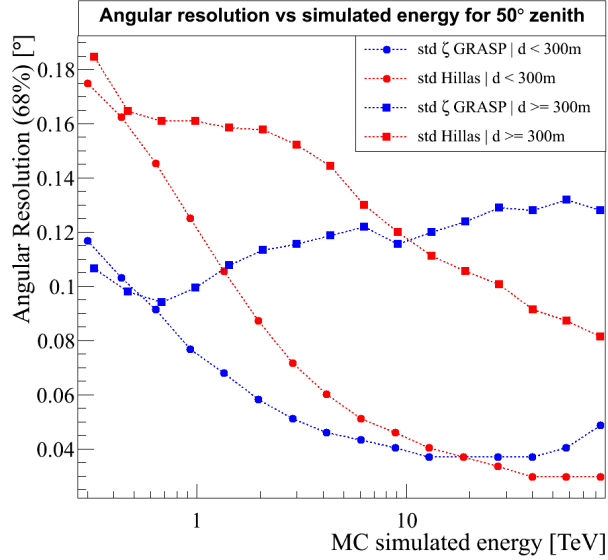


Figure 4.51: Angular resolution as a function of MC simulated energy at 50° zenith for events with a reconstructed impact distance of $d < 300\text{m}$ (circles) and $d \geq 300\text{m}$ (squares). Simulations for both azimuth angles of 0° and 180° are used.

The reason for that is that at larger impact distances the Cherenkov photons emitted at lower altitudes need more time to reach the telescope and are therefore more affected by the readout or integration window. The effect of the readout window takes its toll at energies greater than about 10 TeV especially for zenith angles greater than some 30° . However, since the spectral index (see eq. (1.1)) of the energy spectrum of most of the H.E.S.S. sources is between 2 and 3 there are about a factor of 100-1000 times less events at 10 TeV than at 1 TeV. Fig. 4.52 demonstrates the evolution of the angular resolution with zenith angle. Here all the events at all energies were used to calculate the angular resolution. It shows that, regardless of the worsening in angular resolution at higher energies, the improvement is about 27-33% at zenith angles greater than 10° . The zenith angle of 0° shows only an improvement of 20%.

4. GRASP - GAMMA RAY AIR SHOWER PARAMETERISATION

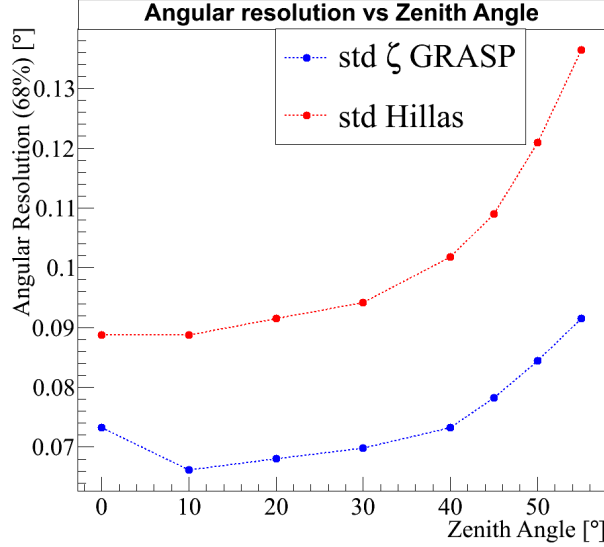


Figure 4.52: Angular resolution as a function of the zenith angle for a MC simulated γ -ray point source combining both observation azimuth of 0° and 180° . The blue circles are for the standard ζ GRASP and the red circles are for the standard Hillas method.

In order to quantify the accuracy of the reconstructed γ -ray energy, the energy resolution and energy bias can be calculated as a function of the simulated energy. By looking at the fractional deviation of the reconstructed γ -ray energy from the simulated energy defined as $(E_{\text{GRASP}} - E_{\text{Simulated}})/E_{\text{Simulated}}$ a distribution as a function of simulated energy can be created. The mean and RMS of this distribution is the aforementioned energy bias and energy resolution respectively. For 20° zenith angle this is shown in Fig. 4.53 and for 50° zenith angle in Fig. 4.54. The energy resolution in both cases shown here, as well as for the other zenith angles is improved. For the GRASP method it can be seen from the energy bias curves that the safe energy threshold stays about the same with regards to the Hillas reconstruction. The large bias for the low energy events stems from the fact that for the std reconstruction a minimum total image intensity of 60 p.e. is used, which selects lower energy showers with large upwards fluctuations in intensity. The energy bias stays for a long range in simulated energy inside 5-7 %. The safe energy threshold is usually defined where the energy bias becomes greater than 10 % ([Aharonian et al., 2006a]). It has to be noted, however, that a θ^2 -cut at the 80 % containment radius was used to produce these plots in order to remove badly reconstructed events in the tail of the θ^2 distribution.

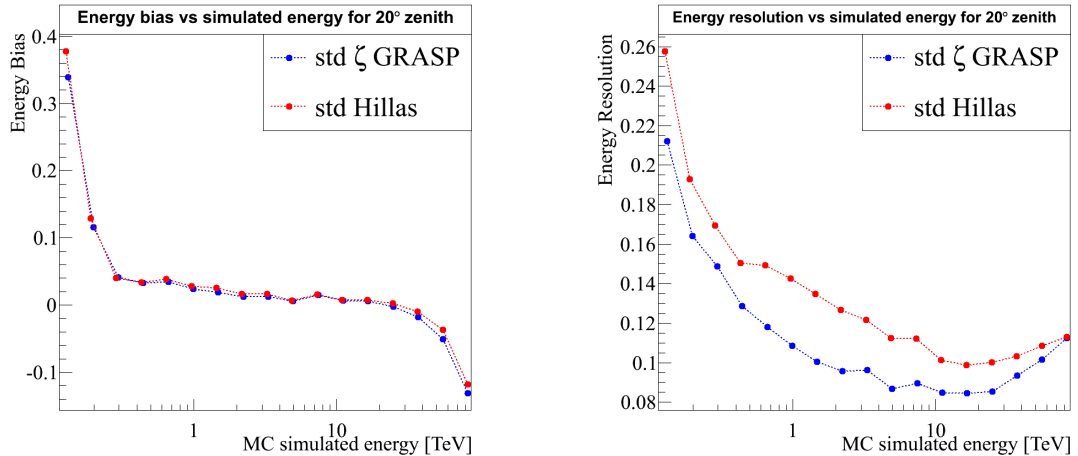


Figure 4.53: Energy bias as a function of the simulated MC energy on the left for 20° zenith. Simulations for both azimuth angles of 0° and 180° are used. The right figure shows the energy resolution as a function of the simulated MC energy for the same zenith angle. Only events were taken that were reconstructed inside the 80% containment radius to get rid of poorly reconstructed events in the tail of the θ^2 distribution. Additionally background rejection cuts were used.

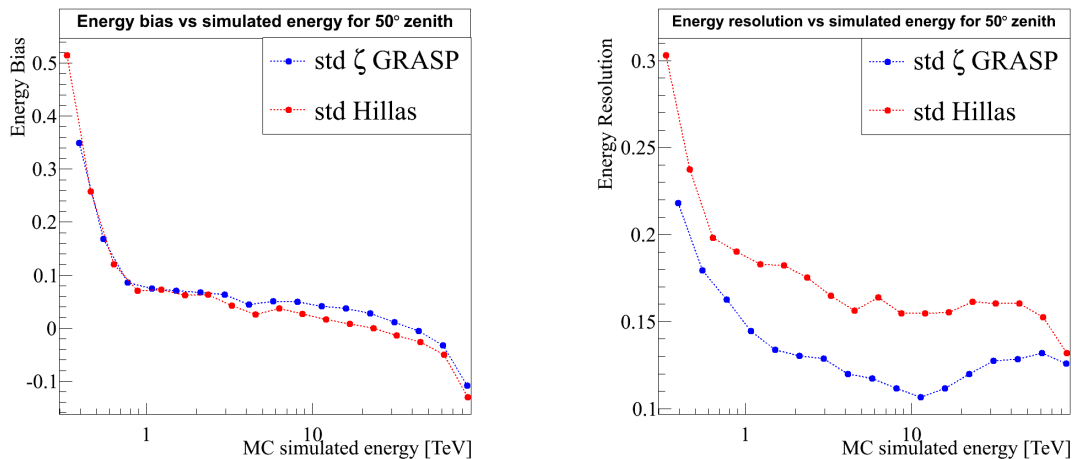


Figure 4.54: Energy bias as a function of the simulated MC energy on the left for 50° zenith. Simulations for both azimuth angles of 0° and 180° are used. The right figure shows the energy resolution as a function of the simulated MC energy for the same zenith angle. Only events were taken that were reconstructed inside the 80% containment radius to get rid of poorly reconstructed events in the tail of the θ^2 distribution. Additionally background rejection cuts were used.

4. GRASP - GAMMA RAY AIR SHOWER PARAMETERISATION

Additionally background rejection cuts were used. Another check is to see how well the height of the first interaction can be reconstructed, which can be used in the future to separate γ -rays from electron induced air showers. To that end Fig. 4.55 shows the resolution (error bars) and bias (triangles) as a function of the MC simulated energy.

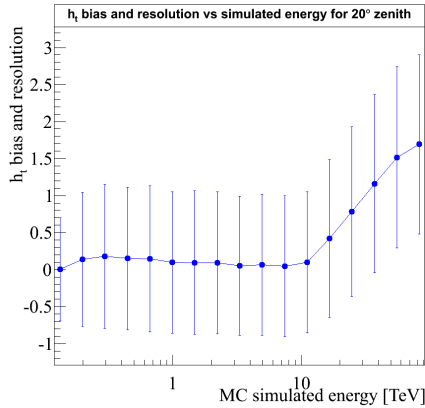


Figure 4.55: Resolution (error bars) and bias (triangles) for the height of the first interaction as a function of the MC simulated energy at 20° zenith.

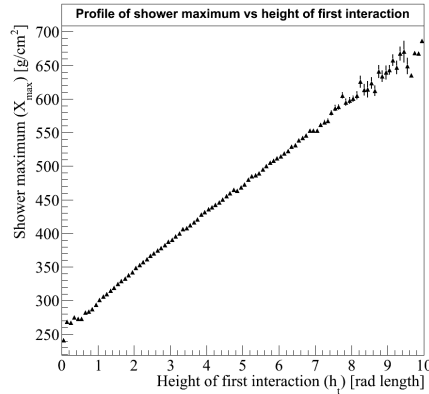


Figure 4.56: Profile of the shower maximum as a function of the height of the first interaction at 20° zenith. The error bars are computed as the standard error of the mean from the distribution inside each bin.

The mean and bias are obtained from a fit of a Gaussian to the distribution of $(h_{t_{\text{GRASP}}} - h_{t_{\text{Simulated}}})/h_{t_{\text{Simulated}}}$ in a few energy bands. It has to be noted that the distribution has a long tail towards values greater than one, which means the height of the first interaction is sometimes overestimated. The Gaussian fit was done in the range of ± 2 RMS of the distribution. This represents a conservative estimate on the resolution but as it can be seen the bias stays below a few percent up to an energy of about 10 TeV. The reconstructed shower maximum from the fitted Moyal peak can be compared to the fitted height of the first interaction. Fig. 4.56 shows this and a clear correlation between these two can be seen.

4.7.2 Test of Direction Reconstruction on a strong point-like Source

In order to test the improvement of the direction reconstruction on a real VHE γ -ray source only sources with a high signal over background ratio can be reliably used without optimising the Hillas γ -hadron separation cuts before. To that end the flare data of the blazar-type Active Galactic Nucleus (AGN) PKS 2155–304 was analyzed. PKS 2155–304 (redshift $z = 0.116$) is a well-known VHE (>100 GeV) γ -ray emitter, see [Aharonian et al., 2005a]. In July 2006 there was an outburst that produced an average flux of $I(>200 \text{ GeV}) = (1.72 \pm 0.05_{\text{stat}} \pm 0.34_{\text{syst}}) \times 10^{-9} \text{ cm}^{-2} \text{ s}^{-1}$, corresponding to ~ 7 times the flux observed from the Crab Nebula, see [Aharonian et al., 2007]. In total there were three observation runs taken in the early hours of July 28, 2006 (MJD 53944). After standard H.E.S.S. data-quality selection criteria the exposure yielded 1.32 h live time at a mean zenith angle of 13° . Using the standard Hillas based reconstruction and the GRASP reconstruction an analysis was done yielding a number of excess events as a function of the squared angular distance of the reconstructed event position to the observation position. This is shown for both analysis methods in Fig. 4.57.

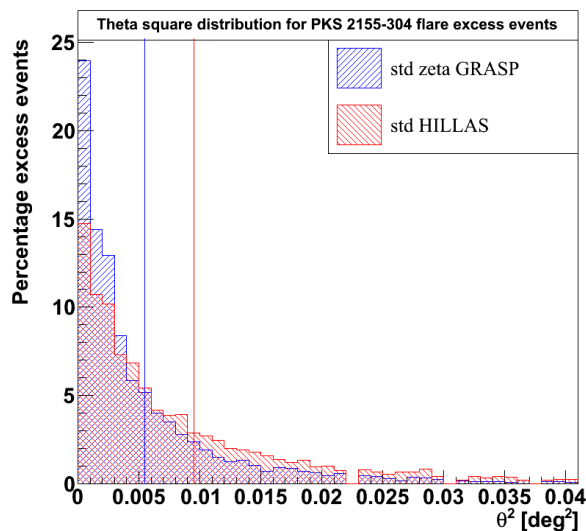


Figure 4.57: θ^2 distribution for PKS 2155-304 flare excess events, blue for std ζ GRASP and red for std Hillas analysis.

The blue vertical line corresponds to the 68% containment radius for GRASP and the red vertical line for the Hillas based reconstruction. They correspond to an angular

4. GRASP - GAMMA RAY AIR SHOWER PARAMETERISATION

resolution of about $\theta_{\text{GRASP},68} \approx 0.074^\circ$ and $\theta_{\text{Hillas},68} \approx 0.097^\circ$, which results in an improvement of about 24%.

4.7.3 Test of Background Rejection on a few Sources

In the following section the performance of the BDT background rejection will be shown for three different source types with different signal over background ratios. As illustrated in section 4.6.1, the more or less pronounced energy- and zenith dependence of the input parameters of the BDT leads to a zenith- and energy-dependent classification. This means that, depending on the observational conditions, a fixed cut on ζ would lead to different γ -ray selection efficiencies, which can be circumvented by assigning a γ -ray efficiency for every possible ζ cut value. By cutting on this γ -ray selection efficiency ϵ_γ only one cut value has to be defined, which can then be translated into a ζ value depending on the zenith angle and energy band the event falls into. As already described in section 3.4.3 the standard cuts are optimised for strong and steep spectrum sources. The parameters optimised in the Hillas analysis to obtain the maximum detection significance are the MSCW, MSCL, size and θ^2 . However, for the BDT method the mean scaled shape parameters are substituted with the γ -ray selection efficiency ϵ_γ . In this work the minimum size cut was chosen to be the same as for the standard ζ Hillas analysis, meaning 60 photo-electrons. The selection cuts for the standard configuration for GRASP and Hillas ζ BDT analysis is compared in table 4.4.

Configuration	ϵ_γ	θ^2 [°]	size [p.e.]
std ζ Hillas	0.84	0.0125	60
std ζ GRASP	0.9	0.007	60

Table 4.4: Selection cuts for the standard ζ configuration for GRASP. As a comparison the values for the Hillas ζ BDT analysis are shown as well, see [Ohm et al., 2009]

From this table it can be clearly seen that the θ^2 value is significantly reduced, which is an immediate result of the improved angular resolution of the GRASP method. In order to test the performance of the background rejection three source types are chosen and analyzed with the selection cuts defined in table 4.4 and using the reflected background estimation method described in section 3.4.5. The first source is the signal-dominated source Crab Nebula which is located at a distance of about 2 kpc, with an

age of 950 years, see also [Aharonian et al., 2006a] for more details. A signal-dominated source is a source with a large signal over background ratio (S/B). A new analysis with a data set of about 49 hours is shown in table 4.5.

Configuration	N_{on}	$\alpha \cdot N_{\text{off}}$	Excess γ	σ	S/B
std Hillas	15754	1611	14143	191	8.8
std ζ Hillas	15614	1197	14417	205	12
std ζ GRASP	16067	399	15668	259	39

Table 4.5: Comparison of the Hillas standard BDT analysis with the GRASP BDT analysis for the Crab Nebula.

As already mentioned and seen from this table, the Crab Nebula is a signal-dominated source, which means that cutting at a higher γ -efficiency leads automatically to an increase in significance. However, the ratio of the expected number of background events in the signal region $\alpha \cdot N_{\text{off}}$ between std ζ Hillas and std ζ GRASP yields a background rejection improvement of about 3. It should be noted that the standard cuts are optimised for a source with a spectral index of the Crab Nebula. The second source is an example of a background dominated source to better assess the improvement in background rejection. To that end the source NGC 253 is chosen, which is a starburst galaxy located at a distance of 2.6 to 3.9 Mpc and is one of the closest spiral galaxies outside the Local Group [Acero et al., 2009]. The analysis of about 155 hours of data is summarised in table 4.6.

Configuration	N_{on}	$\alpha \cdot N_{\text{off}}$	Excess γ	σ	S/B
std Hillas	7103	6853	250	2.9	0.04
std ζ Hillas	3346	3080	266	4.5	0.09
std ζ GRASP	2214	1876	338	7.3	0.18

Table 4.6: Comparison of the Hillas standard BDT analysis with the GRASP BDT analysis for the starburst galaxy NGC 253.

By looking at the ratio between the background events $\alpha \cdot N_{\text{off}}$ of the standard ζ Hillas analysis, and the standard ζ GRASP analysis it becomes clear that the background rejection is improved by a factor of about 1.6. However, the excess γ ray signal is also higher by a factor of 1.3 for the standard ζ GRASP analysis. The third and last source is HESS J1745-290, which is the Galactic centre region in the Milkyway and harbours

4. GRASP - GAMMA RAY AIR SHOWER PARAMETERISATION

the supermassive black hole Sgr A* and a number of supernova remnants. [Aharonian et al., 2004b]. This source has a signal over background ratio in the order of unity and the analysis of about 110 hours of data yields:

Configuration	N_{on}	$\alpha \cdot N_{\text{off}}$	Excess γ	σ	S/B
std Hillas	8887	5068	3819	45	0.8
std ζ Hillas	6217	2667	3550	54.1	1.3
std ζ GRASP	5661	1842	3819	66.5	2.1

Table 4.7: Comparison of the Hillas standard BDT analysis with the GRASP BDT analysis for the galactic centre region source HESS J1745-290

For this source the improvement in background rejection is of the order of 1.5 compared to the standard ζ Hillas analysis. The spectral index of the energy spectrum is about 2.2 and therefore softer than the spectral index of the Crab Nebula. The impact of the spectral index of a source on the background rejection and therefore on the performance of the BDT method could be further investigated in the future.

In order to further quantify the improvement in γ -hadron separation of the standard ζ GRASP method over the standard Hillas analysis a quality factor can be calculated, see:

$$Q = \frac{\epsilon_{\gamma}}{\sqrt{\epsilon_{CR}}} \text{ where } \epsilon_{\gamma} = \frac{\bar{N}_{\gamma}}{N_{\gamma}} \text{ and } \epsilon_{CR} = \frac{\bar{N}_{CR}}{N_{CR}} \quad (4.28)$$

Here \bar{N}_{γ} and \bar{N}_{CR} are the number of events passing the application of the γ -ray selection cuts defined in table 4.4. Furthermore N_{γ} and N_{CR} is the number of events without or before applying this selection criteria. With this definition it is now possible to calculate two different ratios that assess the background rejection improvement of the standard ζ GRASP method over the standard Hillas and standard ζ Hillas method. These are the ratios $Q_{\text{std } \zeta \text{ GRASP}}/Q_{\text{std Hillas}}$ and $Q_{\text{std } \zeta \text{ GRASP}}/Q_{\text{std } \zeta \text{ Hillas}}$ respectively. Fig. 4.58 shows this ratio as a function of zenith angle on the left and as a function of energy on the right. Another important quantity is the sensitivity for point-like sources. To that end the optimised standard ζ cuts are subsequently applied to MC γ -ray and Off-data. The sensitivity is the observation time required for a detection of a point-like VHE γ -ray source with a signal of 5σ above background and a flux between 0.1% and 10% of the flux of the Crab Nebula, assuming a power law in reconstructed

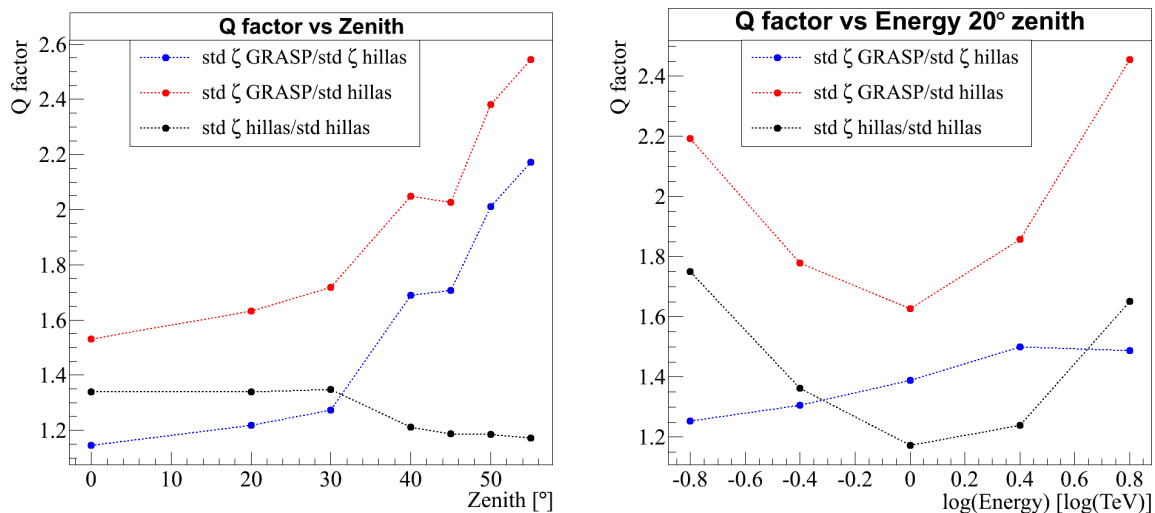


Figure 4.58: Q factor (for definition see text) versus zenith angle on the left and reconstructed energy on the right.

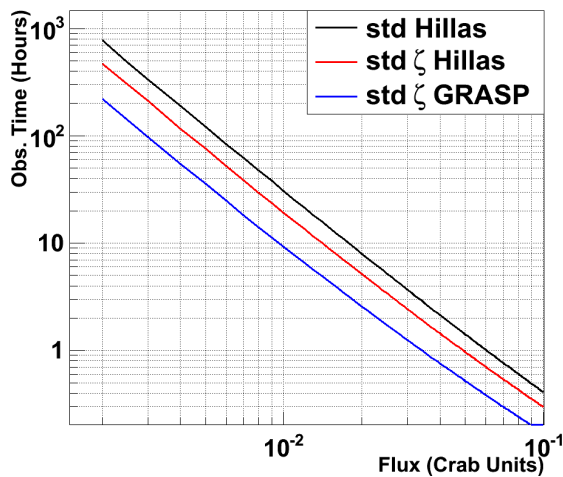


Figure 4.59: Observation time required for a detection of a point-like VHE γ -ray source with a signal of 5σ above background and a flux between 0.1% and 10% of the flux of the Crab Nebula, assuming a power law in reconstructed energy with a spectral index of 2.63. Shown are three curves, one for each analysis method with std Hillas in black, standard ζ Hillas in red and standard ζ GRASP in blue.

4. GRASP - GAMMA RAY AIR SHOWER PARAMETERISATION

energy with a spectral index of 2.63 [Aharonian et al., 2006a].

From Fig. 4.59 it can be seen that the sensitivity is significantly improved for the standard ζ GRASP analysis. The following table 4.8 shows the observation time required for a source with 1% flux of the Crab Nebula:

Configuration	Observation time required [hr]	Improvement [%]
std Hillas	30.7	0
std ζ Hillas	19.2	37
std ζ GRASP	9.3	70

Table 4.8: Comparison of the required observation time for a source with 1% flux of the Crab Nebula with a signal of 5σ above background.

Compared to the standard Hillas analysis the observation time required for a source with 1% flux of the Crab Nebula is reduced by about 70%. In order to quantify the improvement in sensitivity coming from the improved angular resolution and the enhanced γ -hadron separation 18 hrs of data of the blazar-type AGN PKS 2155–304 is analysed. Only observation runs are chosen with a zenith angle around 20° and that have included four telescopes. Table 4.9 summarises the result for the standard Hillas and standard ζ GRASP analysis method.

Configuration	N_{on}	$\alpha \cdot N_{\text{off}}$	Excess γ	σ	S/B
std Hillas	6137	1091	5046	96.6	4.6
std ζ GRASP	6414	377	6037	139.6	17

Table 4.9: Comparison of the Hillas standard analysis with the GRASP BDT analysis for AGN 2155–304

The point spread function (PSF) is obtained from the data by fitting a triple exponential function defined as,

$$PSF(\theta^2) = A \left(\exp(-\theta^2/2\sigma_1^2) + B \exp(-\theta^2/2\sigma_2^2) + C \exp(-\theta^2/2\sigma_3^2) \right) \quad (4.29)$$

to the theta square distribution of the excess events. Here A , B and C are normalisation coefficients. The PSF for both analysis methods is shown in Fig. 4.60. The blue and red line correspond to the PSF function for the standard Hillas and standard ζ GRASP method respectively. The black line corresponds to the background level and

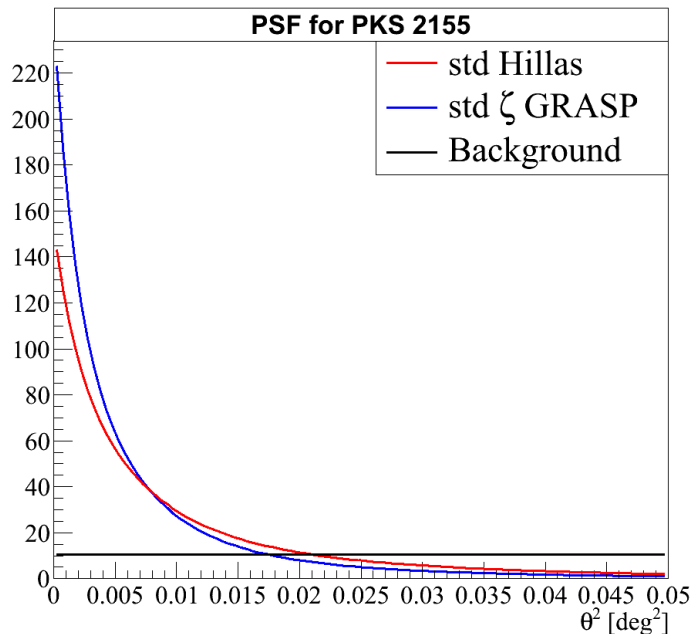


Figure 4.60: PSF functions for the AGN for PKS 2155–304 obtained from the data by fitting a triple exponential to the theta square distribution of the excess events. In blue for std ζ GRASP and in red for std Hillas. The black line corresponds to the background level for the std Hillas analysis assuming a signal over background ratio of 4.6.

is calculated from the PSF function of the standard Hillas analysis by demanding that the signal over background ratio inside the ON-region (defined by $\theta^2 = 0.0125$) is equal to 4.6. The normalisation parameter A for the PSF function of the standard ζ GRASP method (see eq. (4.29)) is then rescaled by a factor s defined by:

$$s = \frac{\int_0^{\theta_{\text{Hillas}}^2} \text{PSF}_{\text{Hillas}}(\theta^2) d\theta^2}{\int_0^{\theta_{\text{GRASP}}^2} \text{PSF}_{\text{GRASP}}(\theta^2) d\theta^2} \quad (4.30)$$

where θ_{Hillas}^2 and θ_{GRASP}^2 are the respective θ^2 sizes of the ON-regions, see Table 4.4.

4. GRASP - GAMMA RAY AIR SHOWER PARAMETERISATION

The signal over background ratio expected from the sole improvement of the PSF can be quantified by:

$$S/B = \frac{\int_0^{\theta_{\text{GRASP}}^2} \text{PSF}_{\text{GRASP}}(\theta^2) d\theta^2 - \int_0^{\theta_{\text{GRASP}}^2} \text{Backg}(\theta^2) d\theta^2}{\int_0^{\theta_{\text{GRASP}}^2} \text{Backg}(\theta^2) d\theta^2} \quad (4.31)$$

where Backg stands for the flat background shown as the black line in Fig. 4.60. This yields a signal over background ratio of ≈ 9.1 and is expected to come only from the improvement of the PSF. Comparing this with the value obtained from the dedicated analysis in Table 4.9 ($S/B \approx 17$) shows that about half of the improvement in sensitivity is expected to come from the enhanced γ -hadron discrimination.

4.7.4 Comparison of the Effective Area and Energy Spectrum

The effective collection area is the area on the ground in which the H.E.S.S. telescope array is sensitive to triggers from air showers. It depends on several parameters which can be expressed in the following:

$$A_{\text{eff}}(E, \phi, \theta, \psi) = 2\pi \int_0^{\infty} P(E, \phi, \theta, \psi, r) r dr \quad (4.32)$$

where E is the energy of the incoming particle, ϕ is the azimuth angle, θ the zenith angle and ψ is the position in the field of view of the telescopes, see also section 3.4.5. Furthermore r is the radial distance of the centre of the H.E.S.S. telescope array to the impact point of the shower core. The probability that a γ -ray shower is detected and passes the selection criterion for γ -ray like events is given by $P(E, \phi, \theta, \psi, r)$. It is calculated using MC γ -rays, by building the ratio of how many events are passing all event selection cuts to the total number of simulated γ -rays in a certain energy band ΔE . At some distance greater than a maximum radius r_{max} the effective area is negligibly small which leads to the following simplification:

$$A_{\text{eff}}(E, \phi, \theta, \psi) = 2\pi^2 r_{\text{max}}^2 \frac{N_{\text{cuts}}(\Delta E, \phi, \theta, \psi)}{N_{\text{tot}}(\Delta E, \phi, \theta, \psi)} \quad (4.33)$$

Fig. 4.61 shows a comparison of the effective area for standard ζ GRASP method in blue and for the standard ζ Hillas method in red. It is produced from MC γ -rays at

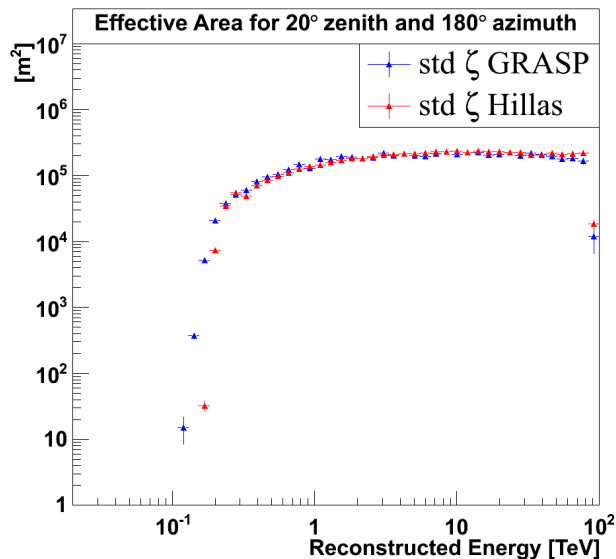


Figure 4.61: Effective Area for MC γ -ray simulations of a point source with a zenith angle of 20° , at an azimuth of 180° , at 0.5° offset using only events that triggered 4 telescopes. Blue triangles are for std ζ GRASP and red triangles for std ζ Hillas.

20° zenith, 180° azimuth, 0.5° offset in the field of view and with an energy spectral index of 2. Since the size cut is the same for both methods the increased effective detection area at smaller energies using the GRASP method comes from the increased γ -ray efficiency cut as well as the improved energy reconstruction.

The differential energy spectrum, or differential flux $F(E)$ of a source is defined as the number of excess photons N_γ (see eq. (3.21)) detected from the source per unit area and time, and can be expressed by:

$$F(E) = \frac{1}{t_{\text{lifetime}} \cdot A_{\text{eff}}(E, \phi, \theta, \psi)} \frac{dN_\gamma}{dE} \quad (4.34)$$

where A_{eff} is the effective collection area of the instrument defined above and t_{lifetime} the live time of the observation. The live time is defined as the total observation time corrected for the time in which the telescope system was not sensitive to triggers from the sky. For further details see [Hoppe, 2008]. As a test of the energy spectrum reconstruction and therefore the effective area, a new analysis with a data set of about 49 hours of the Crab Nebula was performed. In the original analysis in [Aharonian et al., 2006a] using the Hillas standard analysis with a total live time of 21 hours the fit of a power law function to the data yields $\Gamma = 2.63 \pm 0.02_{\text{stat}} \pm 0.09_{\text{sys}}$ and a differential

4. GRASP - GAMMA RAY AIR SHOWER PARAMETERISATION

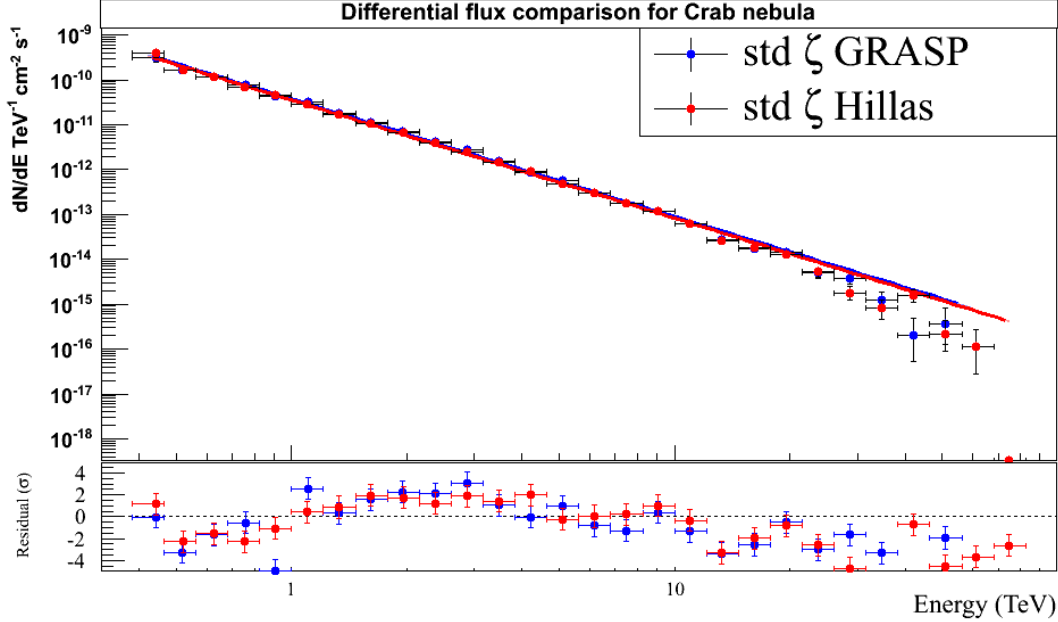


Figure 4.62: Differential flux spectrum for the Crab Nebula for std ζ GRASP (blue circles) and std ζ Hillas (red circles). The blue and red line correspond to a power law fit to the data respectively.

flux normalisation at 1 TeV of $I_0 = (3.45 \pm 0.05_{\text{stat}} \pm 0.69_{\text{sys}}) \times 10^{-11} \text{cm}^{-2} \text{s}^{-1} \text{TeV}^{-1}$. The new analysis with the standard ζ GRASP method is shown in Fig. 4.62 as the blue points and compared to a standard ζ Hillas analysis as the red points. They show a nice agreement with each other. The fit of a power law function in the case of the standard ζ GRASP method and the standard ζ Hillas method is compared in table 4.10. Within statistical and systematic errors the energy spectral index as well as the differential flux normalisation at 1 TeV show a nice agreement with each other.

Configuration	Spectral Index Γ	Differential flux (1 TeV) $10^{-11} \text{cm}^{-2} \text{s}^{-1} \text{TeV}^{-1}$	Integral Flux ($> 1 \text{TeV}$) $10^{-11} \text{cm}^{-2} \text{s}^{-1}$
std ζ Hillas	$2.63 \pm 0.01_{\text{stat}} \pm 0.09_{\text{sys}}$	$3.54 \pm 0.04_{\text{stat}} \pm 0.71_{\text{sys}}$	$2.17 \pm 0.04_{\text{stat}} \pm 0.43_{\text{sys}}$
std ζ GRASP	$2.62 \pm 0.01_{\text{stat}} \pm 0.09_{\text{sys}}$	$3.77 \pm 0.04_{\text{stat}} \pm 0.76_{\text{sys}}$	$2.33 \pm 0.04_{\text{stat}} \pm 0.47_{\text{sys}}$

Table 4.10: Comparison of the results of a power-law fit to the data using the configurations standard ζ GRASP and standard ζ Hillas for the Crab Nebula.

The biggest contribution to the systematic errors are the atmospheric model used in the Monte Carlo simulations, γ -ray selection cuts and Run-by-run variability due to variations in the atmosphere, see [Aharonian et al., 2006a]. The total estimated systematic error on the flux is 20% and the uncertainty in the spectral slope is estimated to be 0.09.

4.8 Galactic Plane Survey Map

Using the standard ζ GRASP method a galactic plane survey map can be produced using a data set of about 2673 hrs. Fig. 4.63 shows the significance survey map with a correlation radius of 0.07° with labels for sources that have a peak significance greater than 8 sigma.

4. GRASP - GAMMA RAY AIR SHOWER PARAMETERISATION

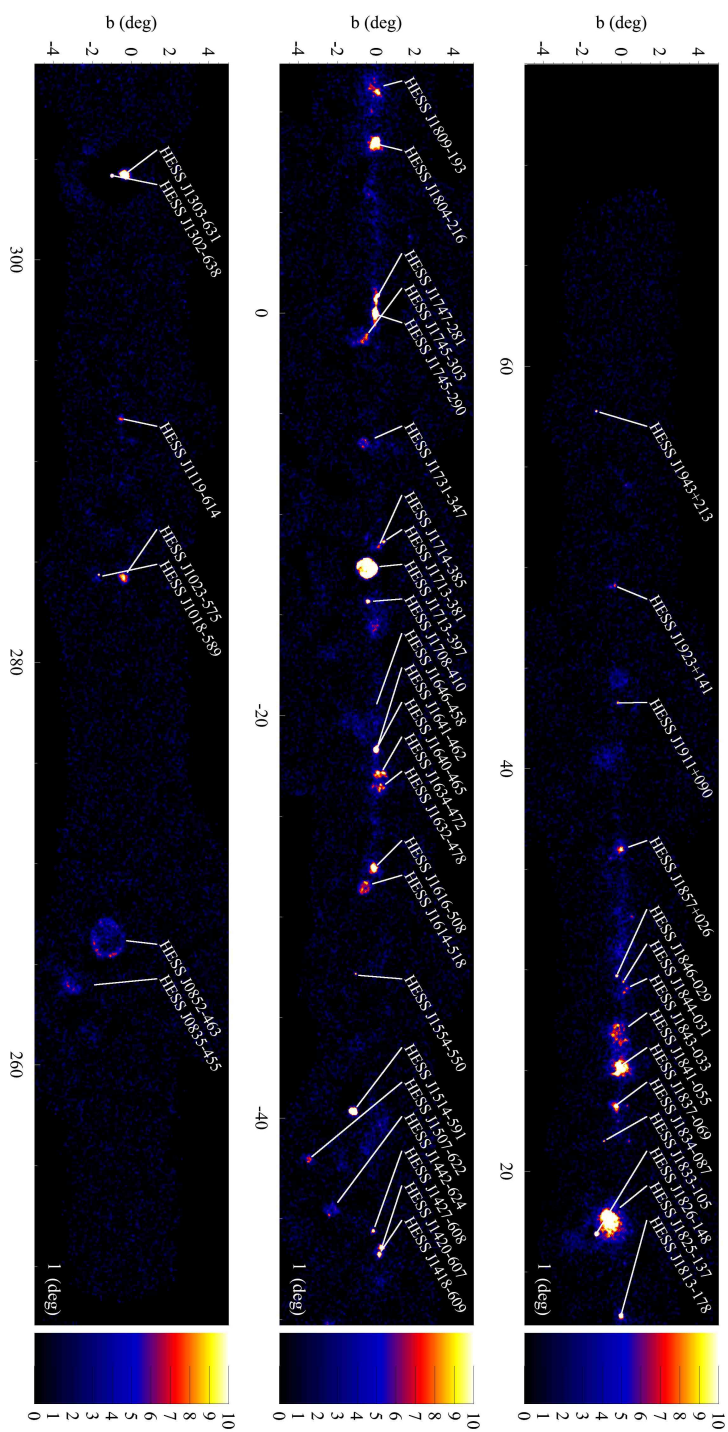


Figure 4.63: H.E.S.S. Galactic Plane Survey significance map produced with std ζ GRASP.

Chapter 5

CR Propagation and Pulsar Wind Nebulae

5.1 Introduction

Many experiments on balloons and in space have extensively measured the spectra of cosmic ray hydrogen, helium, heavier nuclei, antiprotons, electrons and positrons, see for instance Fig. 1.2. The left side of Fig. 5.1 shows the cosmic ray electron spectrum measured by AMS-02¹. It is an illustration of the cosmic ray electron flux scaled by the energy cubed, the latter so that features can be seen in the otherwise very steep spectrum. Between roughly 10 GeV and 1 TeV it follows a power-law with an spectral index of $\Gamma \approx 3.3$. The right side of Fig. 5.1 shows the measured positron fraction as a function of the energy. At energies < 10 GeV, a decrease in the positron fraction with increasing energy is visible and a steady increase in the positron fraction from 10 to 250 GeV [Claudio et al., 2014]. The increase in the positron fraction can be explained e.g. by the three-dimensional spatial distribution of CR sources, together with the contributions from nearby sources such as the Geminga pulsar or the Vela SNR [Gaggero et al., 2014].

¹Alpha Magnetic Spectrometer, AMS-02, is a general purpose high energy particle physics detector and was installed on the International Space Station (ISS), on 19 May 2011

5. CR PROPAGATION AND PULSAR WIND NEBULAE

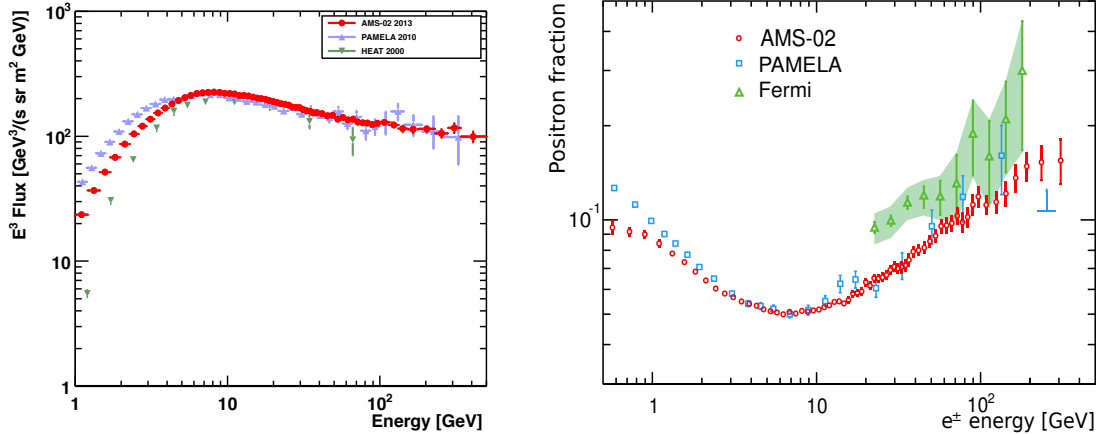


Figure 5.1: Right: The positron fraction measured by AMS-02 together with the most recent measurements from PAMELA and Fermi-LAT. Left: Electron energy spectrum measured by AMS-02 together with the most recent measurements from PAMELA and HEAT. Taken from [Claudio et al., 2014].

By looking at the energy budget of typical accelerators in our galaxy, one finds supernova explosions to be the most likely sources for CRs below an energy of ~ 1 PeV. The energy output of a typical supernova explosion is of the order 10^{51} erg with a rate of about 3 per century. From the confinement time of cosmic rays, the volume of the Milky Way as well as the locally measured CR density of 1 eV/cm^3 , about 10 % of the total supernova explosion needs to go into the acceleration of particles. A necessary condition is to contain the particles while they are accelerated to a maximum energy. The Larmor- or gyroradius is the radius of the circular motion of a charged particle in the presence of a magnetic field and is defined by:

$$R_g = \frac{pc}{eZB_{\perp}} \quad (5.1)$$

where p/Z is the rigidity and B_{\perp} is the magnetic field perpendicular to the momentum of the charged particle. In a diffusion process the mean squared distance over which the particle changes direction (scattered) can in general be expressed by $\langle d^2 \rangle \sim D(E)t$, where $D(E)$ is the energy dependent diffusion coefficient. If the charged particles scatter on inhomogeneities of the magnetic field, the diffusion coefficient will typically be larger or comparable to the gyroradius $D(E) \gtrsim R_g$ [Bellini and Ludhova, 2012]. In order to get an estimate of the maximal energy to which cosmic rays can be accelerated

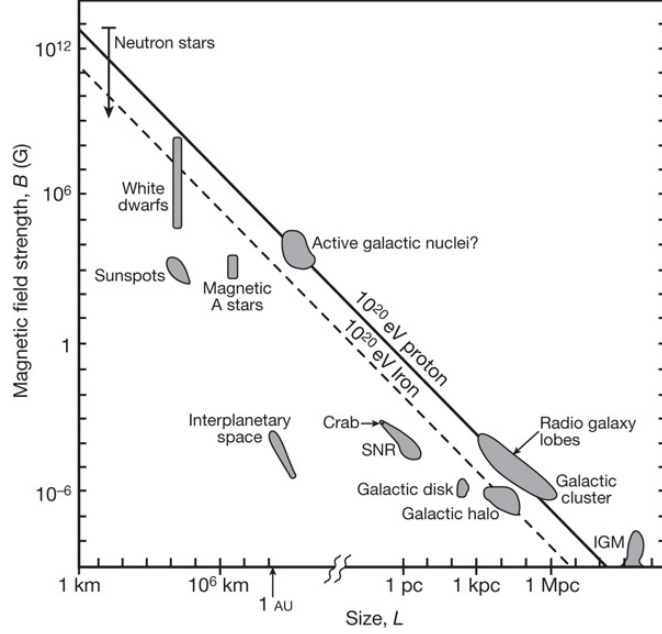


Figure 5.2: The so called Hillas plot shows the potential cosmic ray accelerators where on the x axis the size L (corresponds to R in the text) and on the y axis the magnetic field strength in units of gauss is shown. Taken from [Bauleo and Martino, 2009]

in shocks the following comparison is made. The time scale at which diffusion and convection length scales become comparable in a shock with velocity v_s and a size R_s can be expressed by:

$$\begin{aligned}
 d^2 &\sim D(E)t \sim (v_s t)^2 \Rightarrow t \sim \frac{D(E)}{v_s^2} \\
 \Rightarrow d &\sim \frac{D(E)}{v_s} < R_s \\
 \Rightarrow \frac{R_g}{v_s} &\lesssim R_s \\
 \Rightarrow E_{\max} &\lesssim eZBR_s v_s
 \end{aligned} \tag{5.2}$$

Here eZ is the charge of the particle and B the magnetic field. This is also called the Hillas criterion [Hillas, 1984]. The so called Hillas plot represents astrophysical objects which are potential cosmic ray accelerators and is shown in Fig. 5.2. It shows the magnetic field strength B as a function of the size linear extension R of the accelerator. This figure clearly illustrates that the more compact the accelerator, the stronger the magnetic field needs to be in order to accelerate the particles up to the maximum

energy. The most predominant source class seen with H.E.S.S. is that of the e^-e^+ -Nebula formed around a pulsar, the so called pulsar wind nebula (PWN).

5.2 Theory of Pulsars and Pulsar Wind Nebulae

5.2.1 Pulsars

Pulsars are highly magnetised and fast spinning neutron stars. In general they are formed from a massive ($M > 8M_\odot$) progenitor star as a result of the gravitational collapse of the iron core. From observations their typical masses have been determined to be on the order of $1.3-1.4 M_\odot$. Once the nuclear fusion inside the progenitor star stops, the radiation pressure from inside ceases and the whole star collapses under its own gravitation. The degeneracy pressure of the fermions will eventually counterbalance the gravitational collapse leading to a stable core. Furthermore the inverse β -decay via the reaction $p + e^- \rightarrow n + \nu_e$ transforms most of the matter into neutrons, which gives the star the name neutron star. The whole star is compressed to a compact object with a diameter of the order $\sim 10\text{km}$. Additionally the collapse increases the rotation speed of the star because of angular momentum conservation. The typical pulsar period is in the order of tens to hundreds of milliseconds and magnetic field strengths are around 10^{12} to 10^{13} gauss. These high magnetic fields result from the conservation of magnetic flux which leads to an increase in the magnetic field when the star collapses in on itself. An estimate of the surface magnetic field strength B_S can be derived from the observation of the rotation period P and its time derivative \dot{P} . For magnetic dipole radiation, the surface magnetic field B_S is given by [Lorimer and Kramer, 2004]:

$$B_S = \sqrt{\frac{3c^3}{8\pi^2 R^6 \sin^2 \psi} P \dot{P}} \quad (5.3)$$

where R is the radius of the pulsar. The magnetic axis of a pulsar is inclined by an angle ψ with respect to its rotational axis, giving rise to a pulsed emission when the beam of radiation sweeps through the line of sight towards the pulsar.

The rotational energy dissipates with time leading to an increase in its period P . The rotational energy is given by:

$$E_{rot} = \frac{I\omega^2}{2} = \frac{2\pi^2 I}{P^2} \quad (5.4)$$

5.2 Theory of Pulsars and Pulsar Wind Nebulae

with $\omega = 2\pi/P$ and I as the moment of inertia. The power of the pulsar, also called the spin-down luminosity \dot{E} is then defined as:

$$\dot{E} = -\frac{dE_{rot}}{dt} = I\omega\dot{\omega} = 4\pi^2 I \frac{\dot{P}}{P^3} \quad (5.5)$$

Values of \dot{E} for the observed pulsar population range from $\approx 5 \times 10^{38}$ erg/s for the Crab pulsar, down to 3×10^{28} erg/s for the slowest known pulsar PSR J2144-3933, see also [Manchester et al., 2005].

The pulsar's spin-down period P or frequency ω can be described by:

$$\dot{\omega} = -k\omega^n \quad (5.6)$$

where k is a constant and n the so called braking index, see [Gaensler and Slane, 2006]. The braking index of a pulsar can directly be calculated if the second derivative of the period can be measured, because it follows:

$$n = \frac{\omega\ddot{\omega}}{\dot{\omega}^2} = 2 - \frac{P\ddot{P}}{\dot{P}^2} \quad (5.7)$$

The value of the braking index provides information about the energy loss mechanisms which leads to a decrease in the pulsar period. In the case where the magnetic axis is misaligned with respect to the rotational axis the process is called magnetic braking. Fig. 5.3 shows the schematic model for this scenario. For a magnetic dipole with a moment of $|\vec{m}|$, the radiation power is equal to:

$$P_{rad} = \dot{E}_{dipole} = \frac{2}{3c^3}\omega^4|\vec{m}|^2\sin^2\psi \quad (5.8)$$

Comparing this with eq. (5.5) and assuming that the loss of rotational energy is entirely converted into magnetic dipole radiation it follows:

$$\dot{\omega} = -\left(\frac{2|\vec{m}|^2\sin^2\psi}{3c^3I}\right)\omega^3 = -k\omega^3 \quad (5.9)$$

This means a braking index of $n = 3$ corresponds to a spin-down via pure magnetic dipole radiation. The braking index is only measured for a few pulsars and is i.e. $n = 1.4 \pm 0.2$ for the Vela pulsar [Lyne et al., 1996] or $n = 2.839 \pm 0.003$ for PSR B1509-58 [Livingstone et al., 2005]. For these examples the braking index clearly deviates from what would be expected for pure magnetic dipole radiation. One possible explanation is, that the spin-down energy loss from the pulsar originates not only from electromagnetic

5. CR PROPAGATION AND PULSAR WIND NEBULAE

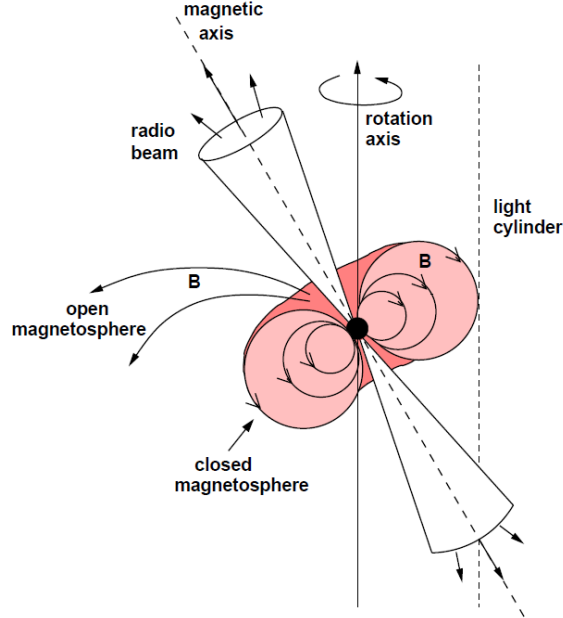


Figure 5.3: Schematic view of a pulsar. In a general case the rotation axis and magnetic axis are misaligned. The pulsar can be detected if the radio beam sweeps across the Earth. Taken from [Carrigan, 2007]

radiation, but has also a contribution from particle outflows.

Assuming $n \neq 1$ and $\dot{n} = 0$ the age of the system is [Manchester and Taylor, 1977]:

$$\tau = \frac{P}{(n-1)\dot{P}} \left(1 - \left(\frac{P_0}{P} \right)^{n-1} \right) \quad (5.10)$$

where P_0 is the initial period of the pulsar. Assuming $n = 3$ and $P_0 \ll P$ a characteristic age of the pulsar can be defined:

$$\tau \simeq \tau_c = \frac{P}{2\dot{P}} \quad (5.11)$$

It should be noted that this formula overestimates the true age when P_0 is not much smaller than P . For example, the pulsar PSR J1400–6325 has a characteristic age of $\tau_c \approx 12.7$ kyrs, however, multiwavelength observations suggest an age smaller than a few thousand years [Renaud et al., 2010].

Due to the small rotation periods and the high magnetic fields, very large electrical fields are induced at the pulsar surface. These in turn generate forces which create

5.2 Theory of Pulsars and Pulsar Wind Nebulae

a plasma in the surroundings of the pulsar, which is also called the magnetosphere. The maximal distance between the pulsar surface and co-rotating particles is called the light cylinder, defined by $r_L = c/\omega$. In most regions, the magnetic field lines are equipotentials and therefore charges move along those lines without accelerating. However, there are some regions where charges are accelerated along field lines which in turn emit γ radiation by inverse Compton (IC), synchrotron and curvature radiation. This pulsed emission from the magnetosphere only extends to some 10 GeV and then cuts off sharply due to the production of electron-positron pairs in the magnetic fields. These secondary electrons or positrons get accelerated themselves and form a pair cascade at these locations in the pulsar's magnetosphere. Three regions are typically considered for these locations: the polar cap region [Daugherty and Harding, 1982], slot gap region [Muslimov and Harding, 2004] and the outer gap region [Hirotani, 2008].

5. CR PROPAGATION AND PULSAR WIND NEBULAE

5.2.2 PWN

The relativistic cascade of charged particles can stream along open field lines and therefore leave the magnetosphere of the pulsar. This creates a relativistic wind outside the pulsar's magnetosphere (unshocked wind). From this region, no synchrotron emission is expected to be emitted, since the magnetic field is frozen into the plasma, which means that the particle outflow moves together with the magnetic field. However, IC emission is expected due to the interaction between the unshocked wind and low-energy photons. A shock is formed at a typical distance of R_s (shock radius) where the ram pressure of the unshocked wind is balanced by the internal pressure of the PWN. This shock radius is given by [Gaensler and Slane, 2006]

$$R_s = \sqrt{\frac{\dot{E}}{4\pi\omega c P_{\text{PWN}}}} \quad (5.12)$$

where ω is the equivalent filling factor for an isotropic wind and P_{PWN} is the total pressure in the interior of the shocked nebula. The actual PWN is formed from the flow of particles away from the termination shock. There, particles can be accelerated to ultra-relativistic energies. This acceleration is thought to happen in diffusive shock acceleration, see e.g. [Bell, 1978]. In a spherically symmetric case the radius R_{PWN} of the PWN's forward shock at time t , with E_{SN} and M_{ej} being the kinetic energy and ejected mass respectively, can be given by:

$$R_{\text{PWN}} \approx 1.1 \text{pc} \left(\frac{\dot{E}_0}{10^{38} \text{ erg s}^{-1}} \right)^{1/5} \left(\frac{E_{\text{SN}}}{10^{51} \text{ erg}} \right)^{3/10} \left(\frac{M_{\text{ej}}}{10 M_{\odot}} \right)^{-1/2} \left(\frac{t}{10^3 \text{ years}} \right)^{6/5} \quad (5.13)$$

Emission from this region can be observed at many different wavelength regimes and extends to distances in the order of 10 pc. This can be compared to a typical radius of the termination shock of 0.1 pc.

A sketch of the different components of a PWN and the type of expected emission from each region is shown in Fig. 5.4. The emission spectrum of a PWN shows an almost flat shape at radio wavelengths. It can be described by a power-law as $F_{\nu} \sim \nu^{-\alpha}$, with α typically between 0. and 0.3. At X-ray wavelengths the spectrum considerably steepens with an index between approximately 1.5 and 2.5. Due to the effect of synchrotron cooling of the lepton population, a harder spectrum is observed close to R_s and a steeper spectrum further out, which results in a smaller extension

Radiation from a **Pulsar-wind-nebula** complex

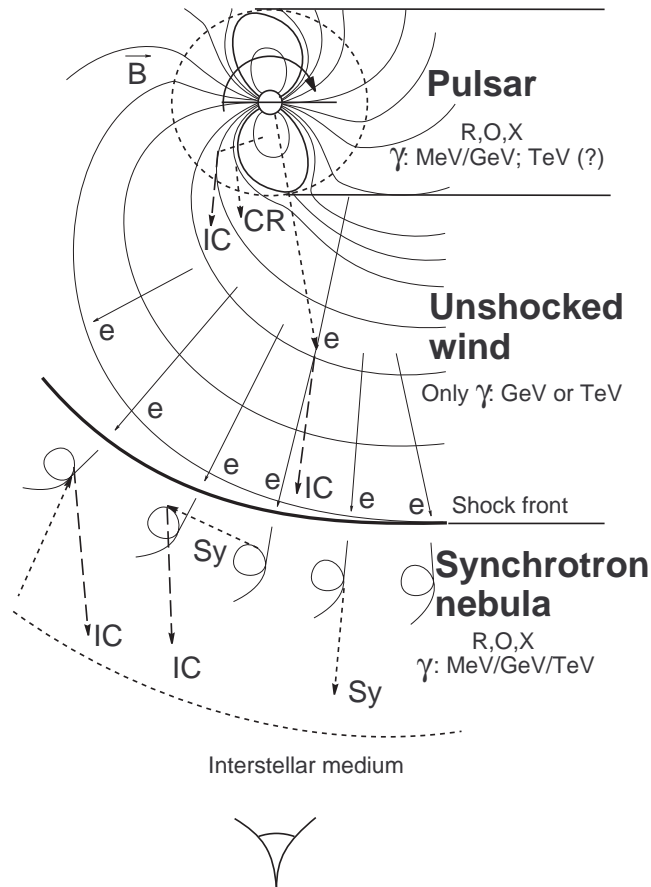


Figure 5.4: Sketch of the different regions and radiation mechanisms of nonthermal emission. Pulsar: the region within the light cylinder where the magnetospheric pulsed radiation from radio to γ -rays is produced. Unshocked wind: the part of the wind of cold relativistic plasma close to the light cylinder which effectively emits GeV and TeV γ -rays through the IC mechanism. Synchrotron nebula: the surrounding synchrotron nebula which emits broad-band electromagnetic radiation from radio to TeV γ -rays through the synchrotron and IC channels. Taken from [Aharonian and Bogovalov, 2003]

5. CR PROPAGATION AND PULSAR WIND NEBULAE

of the synchrotron nebula with increasing energy. In the γ -ray regime the detected emission is most likely due to IC emission that is produced in the up-scattering of background photons by the accelerated leptons. The typical spectrum in the TeV energy range can be described by a power-law spectrum ($\sim E^{-\Gamma}$) with an index $\Gamma \sim 2$.

5.2.3 Supernova Remnant

Since a pulsar is formed in a supernova (SN) explosion, the star and its PWN are surrounded by an expanding supernova remnant (SNR). The typical kinetic energy released in a SN explosion is of the order $E_{\text{SN}} \sim 10^{51}$ erg with several solar masses of stellar ejecta M_{ej} . This ejecta has a range of velocities depending also on the type of the supernova explosion. A characteristic initial explosion velocity $(2E_{\text{SN}}/M_{\text{ej}})^{1/2}$ is of the order 10^4 km s $^{-1}$ for a Type Ia and 5000 km s $^{-1}$ for a core-collapse event [Reynolds, 2008]. This is higher than the expected sound speeds of order $1 - 10$ km s $^{-1}$ in the surrounding interstellar medium (ISM) and consequently a shock front is formed ahead of the expelled material (blast wave). Asymmetry in the supernova explosion give the pulsar a velocity of typically about $400 - 500$ km s $^{-1}$, see [Gaensler and Slane, 2006]. This means that the pulsar gradually moves away from the center of the SNR. Behind the blast wave, the ejecta initially expands almost freely and cools adiabatically to very low temperatures. The blast wave heats the ambient medium which in turn exerts a pressure back onto the expanding shell. This triggers the formation of a reverse shock that is traveling inwards. Adiabatic losses dominate from ~ 1000 years after the supernova explosion until the PWN collides with the reverse shock. The SNR enters the Sedov-Taylor phase when the swept-up mass by the SNR shell roughly equals the initial ejecta mass. After typically a few thousand years the reverse shock collides with the outer edge of the PWN. After the collision it shocks the swept-up ejecta surrounding the PWN, but not the PWN itself because the sound speed inside the PWN is significantly higher than the velocity of the reverse shock [Gelfand et al., 2009]. Because the PWN is no longer in an almost pressureless environment the velocity of the PWN decreases significantly. Beginning typically ~ 6000 years after the supernova explosion the high-pressure ejecta downstream of the reverse shock will compress the PWN and will lead to a series of contractions and re-expansions that continue until the SNR enters the radiative phase of its evolution [Gelfand et al., 2009]. For a high space velocity of

the pulsar itself, it is possible that the PWN will be stripped of its pulsar during its re-expansion.

5.3 Anisotropic Diffusion

The diffusion of CRs in the galaxy is governed by scattering on inhomogeneities in the Galactic magnetic field (GMF). Since the scale of these inhomogeneities is comparable to the Larmor radius R_g of CR, their propagation in the GMF resembles a random walk and is therefore well described by the diffusion approximation. The GMF has a turbulent component which varies on scales between $l_{\min} \lesssim 1$ AU and $l_{\max} \sim 200$ pc [Giacinti et al., 2012]. If the diffusion of CRs is assumed to be isotropic, valid if they propagate distances $l \gtrsim l_{\max}$, the CRs with a given energy E after a time t are distributed roughly homogeneously within a distance of $R_d(E) \approx \sqrt{6D(E)t}$. The energy density in CRs from supernova explosions can then be estimated by $n_{\text{CR}}(E) \sim \eta E_{\text{SN}}/R_d(E)^3$, where η is the fraction of the supernova explosion energy E_{SN} converted into accelerated particles. However, CR diffusion becomes anisotropic even for an isotropic random magnetic field and can lead to a filamentary structure of the CR density around young sources [Giacinti et al., 2012]. Responsible for these anisotropies are turbulent field modes with variation scales $1/k$ much larger than the Larmor radius of CRs ($1/k \gg R_g$) which mimic a regular field. Furthermore, if the intensity of the turbulent field δB on scales comparable with the Larmor radius is significantly smaller than the mean large scale field B_0 ($\delta B/B_0 \ll 1$), CR diffusion becomes also anisotropic [Casse et al., 2002]. If particles diffuse along a magnetic flux tube characterised by a very long coherence length, after a time t the particle will have diffused up to a distance of $R_d \approx \sqrt{2D_{\parallel}t}$ [Nava and Gabici, 2012]. Here D_{\parallel} is the diffusion coefficient along the magnetic tube with $D_{\parallel} \gg D_{\perp}$ and the transverse distribution of the CRs will be equal to the radius of the SNR shock R_{sh} at the time of their escape ($\approx 1 - 10$ pc). The CR density in the flux tube will therefore be proportional to $n_{\text{CR}} \sim (R_d^{-1}R_{\text{sh}}^{-2})$. This means that for one-dimensional diffusion the cosmic ray density will differ by a factor $\approx (R_d/R_{\text{sh}})^2$ compared to the cosmic ray density in the isotropic case.

5. CR PROPAGATION AND PULSAR WIND NEBULAE

Chapter 6

Complex Source MSH 15-5-2

In this section the PWN MSH 15-5-2, discovered in 1961 is investigated. The abbreviation "MSH" stands for the radio catalog composed by Mills, Slee and Hill [Mills et al., 1961]. The source has a right ascension (RA) coordinate of 15, and a declination (DEC) coordinate of -50. The fourth number is an ordinal number from the catalog and does not stand for any coordinate information. The name MSH 15-5-2 refers to the whole supernova remnant (SNR), which is also known as G320.4-1.2, and simultaneously to the pulsar wind nebula inside. The system is powered by the pulsar PSR B1509-58, which supplies energy via its spin-down losses.

6.1 Radio and X-ray Measurements

MSH 15-5-2 was first discovered at X-ray energies by [Seward and Harnden, 1982]. They measured a pulsar period of 150 ms and derived a spin-down luminosity of $5 \times 10^{37} \text{erg s}^{-1}$ and a characteristic age of 1600 years. Not long after the discovery the pulsar was also detected at radio wavelengths by [Manchester et al., 1982]. The position¹ of PSR B1509-58 was determined by [Gaensler et al., 1999] to have a right ascension of $\alpha = 15\text{h}13\text{m}55\text{s}.61 \pm 0\text{s}.02$ and a declination of $\delta = 59^\circ 08' 08''.67 \pm 0.''26$. They also suggest the association between the radio shell, the wind nebula and the pulsar. Using HI absorption measurements the distance is estimated at 5.2 ± 1.4 kpc [Gaensler et al., 1999], which is consistent with the value of 4.2 ± 0.6 kpc derived from the dispersion measurement [Cordes and Lazio, 2002]. A combined image from radio

¹Specified by the Julian epoch (J2000)

6. COMPLEX SOURCE MSH 15-5-2

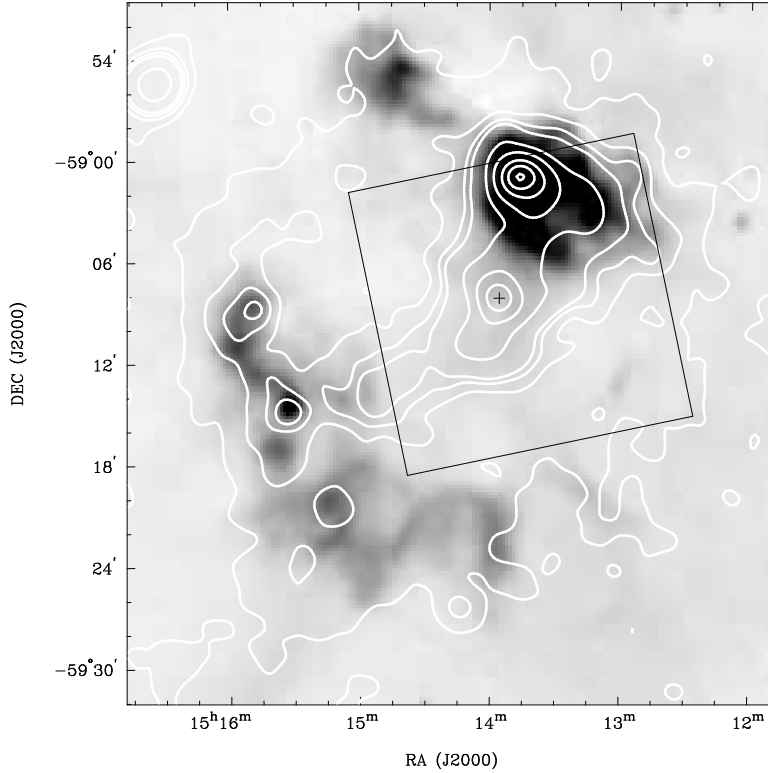


Figure 6.1: View of MSH15-52 at radio and X-ray wavelengths. The grey scale corresponds to the 843MHz MOST radio data [Whiteoak and Green, 1996] and the white contours are smoothed ROSAT PSPC data from [Trussoni et al., 1996]. The position of the pulsar PSR B1509-58 is marked with a cross (+) and the black box illustrates the field of view of the Chandra ACIS-I camera. Taken from [Gaensler et al., 2002]

data (grey scale) of the Molonglo Galactic Plane Survey (MGPS) at 843 MHz with the Molonglo Observatory Synthesis Telescope (MOST) [Whiteoak and Green, 1996] and X-ray observations of ROSAT in the energy range from 0.6 – 2.1 keV (white contours) from [Trussoni et al., 1996] can be seen in Fig. 6.1. From the radio data a partial shell is visible in the southeast of the pulsar PSR B1509-58 and a bright component to the northwest, which coincides with the nebula RCW 89. The $H\alpha$ emission nebula RCW 89 was discovered by [Rodgers et al., 1960]. Since the X-ray contours are predominant at this position as well, two possible scenarios have been proposed for the energy source of the thermal nebula: the supernova blast wave and the pulsar jet [Manchester, 1987].

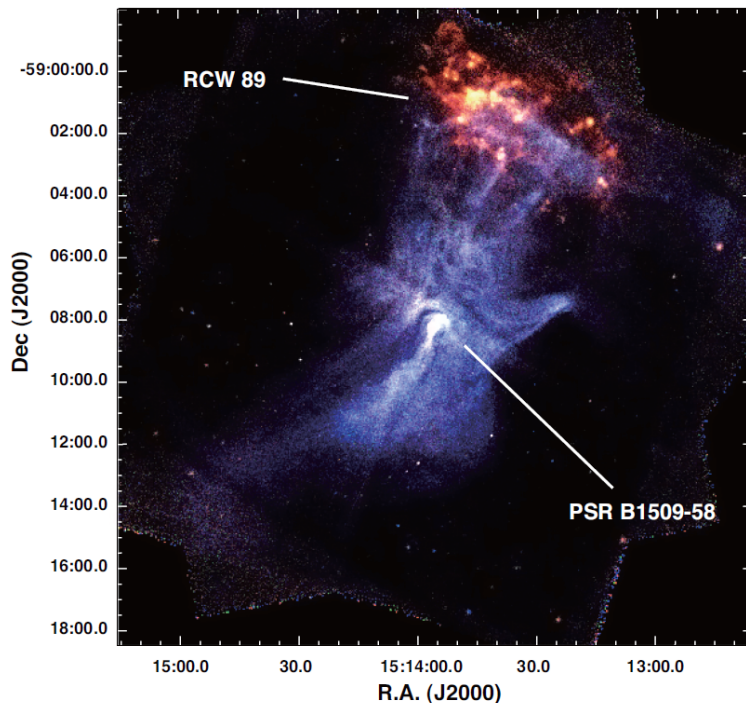


Figure 6.2: Image of MSH 15-5-2 accompanied by PSR B1509-58 with 190 ks exposure taken by Chandra. The colors correspond to the energy bands 0.4–1.5 keV (Red), 1.5–2.0 keV (Green), and 2.0–8.0 keV (Blue). It shows labels for the pulsar PSR B1509-58 and the H α emission nebula RCW 89. Taken from [Yatsu, 2008]

The analysis of ASCA¹ data [Tamura et al., 1996] showed that in the RCW 89 region thermal emission with prominent line features is dominant. The analysis of the thermal X-ray spectra showed that its energy content was consistent with being powered by the pulsar through the jet. This, however, needs to be reconsidered since Chandra has revealed that the energy content is smaller by 2 orders of magnitude than that deduced from the ASCA observations. An analysis of the data set from Chandra observations was conducted by [Yatsu et al., 2009], who used a total exposure of 190 ks in their study of the vicinity of PSR B1509-58. An overview image of MSH 15-5-2 using the Chandra data set is shown in Fig 6.2. Because of the proximity of RCW 89 to MSH 15-5-2, it has been considered to be a contact point of the jet and the surrounding SNR [Yatsu et al., 2005].

¹Advanced Satellite for Cosmology and Astrophysics

6.2 Previous γ -ray Measurements

H.E.S.S.

MSH 15-5-2 was detected in VHE γ -rays with H.E.S.S. in 2005 [Aharonian et al., 2005b]. The observations used in the analysis were made between March and June 2004. Only data with good atmospheric conditions were selected yielding a total live time of 22.1 hours at a mean zenith angle of 37° . The analysis shows an excess with a significance of about 25σ detected within the region of radius 0.14° centered at the pulsar position with the standard Hillas point source analysis, see Fig. 6.3. It should be noted, however, that only γ -ray candidates with an image size greater than 400 p.e. were selected, which reduces the angular resolution to about 0.07° . On the other hand this cut also raises the energy threshold to about 900 GeV. The map is convolved with a Gaussian of $\sigma = 0.04^\circ$ in order to smooth out statistical fluctuations. The energy spectrum reconstruction was obtained from excess events within a circle with a radius of 0.3° . The data is consistent with a power law up to ~ 40 TeV with a spectral index of $\Gamma = 2.27 \pm 0.03_{\text{stat}} \pm 0.20_{\text{sys}}$ and a differential flux at 1 TeV of $(5.7 \pm 0.2_{\text{stat}} \pm 1.4_{\text{sys}}) \times 10^{-12} \text{ TeV}^{-1} \text{ cm}^{-2} \text{ s}^{-1}$. In order to extract the intrinsic size, the unsmoothed excess map was fitted with a two-dimensional Gaussian model. The results are shown in table 6.1.

Pos Ra (J2000)	Pos Dec (J2000)	Minor Axis [$^\circ$]	Major Axis [$^\circ$]	Angle [$^\circ$]
$15\text{h}14\text{m}7\text{s} \pm 21\text{s}$	$-59^\circ 9' 27'' \pm 11''$	0.038 ± 0.008	0.107 ± 0.012	131 ± 13

Table 6.1: Previous fit results for a model including one two-dimensional Gaussian for MSH 15-5-2, [Aharonian et al., 2005b]. The angle is measured from the declination axis pointing North to East.

Fermi-LAT

A few years later in 2010, high-energy emission in the GeV energy regime from the PWN was detected with the Fermi-LAT instrument [Abdo et al., 2010]. Above a few GeV there is extended γ -ray emission which is spatially coincident with the PWN seen at X-ray and TeV energies. The nebular spectrum in the energy range of 1 – 100 GeV can be well described by a power law with a spectral index of $(1.57 \pm 0.17_{\text{stat}} \pm 0.13_{\text{sys}})$

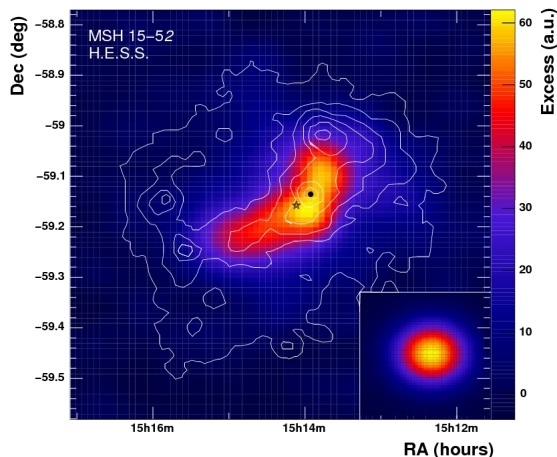


Figure 6.3: Image of MSH 15-5-2 in the very high energy regime with H.E.S.S.. Smoothed excess map, overlaid with white contour lines from X-ray measurements by ROSAT [Trussoni et al., 1996]. The black point and black star lie at the pulsar position and at the excess centroid, respectively. The right-bottom inset shows the identically smoothed PSF. Taken from [Aharonian et al., 2005b]

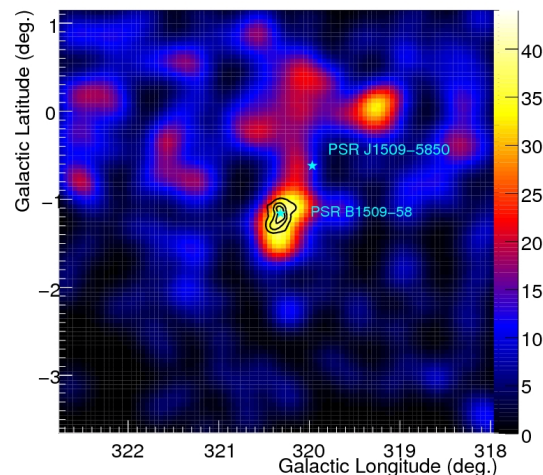


Figure 6.4: Image of MSH 15-5-2 in the high energy regime with Fermi-LAT. Smoothed count map above 10 GeV, overlaid with H.E.S.S. significance contours from [Aharonian et al., 2005b]. The map is smoothed with a Gaussian of $\sigma = 0.15^\circ$. The positions of the pulsars PSR J1509-5850 and PSR B1509-58 are marked by blue stars. Taken from [Abdo et al., 2010]

and a flux above 1 GeV of $(2.91 \pm 0.79_{\text{stat}} \pm 1.35_{\text{sys}}) \times 10^{-9} \text{ cm}^{-2} \text{ s}^{-1}$. Fig. 6.4 shows a smoothed Fermi-LAT count map above 10 GeV, overlaid with H.E.S.S. significance contours from [Aharonian et al., 2005b]. Because of the better angular resolution and the non-contamination from the Galactic diffuse emission, morphological studies were performed above 6.4 GeV. The best fits are obtained with either a uniform disk model with an extension of $0.25^\circ \pm 0.05^\circ$ or with a one-dimensional Gaussian model with an extension of $0.15^\circ \pm 0.02^\circ$. For both type of models the fit positions are within uncertainties compatible with each other. The Gaussian model results in a best-fit position of $\alpha = 15\text{h}14\text{m}02.58\text{s}$ and $\delta = -59^\circ 14' 54.9''$, see [Abdo et al., 2010].

6.3 Analysis using GRASP

Looking at the image of MSH 15-5-2 taken by Chandra Fig. 6.2 a complex X-ray morphology can be seen. The improved angular resolution of GRASP makes this an ideal case for studying the morphology in VHE γ -rays. A new analysis using standard ζ GRASP on an extended data set with a total live time of 95.7 hours (also with a mean zenith angle of 37°) shows an excess with a significance of about 41σ within the region of radius 0.14° centered at the pulsar position. Due to the improvement in the direction reconstruction the angular resolution is comparable to the one used in the previous analysis (0.07°) while the energy threshold of about 320 GeV, compared to the previous 900 GeV, is considerably lower. Fig. 6.5 shows the smoothed excess map, where the green contours are the smoothed ROSAT PSPC data [Trussoni et al., 1996].

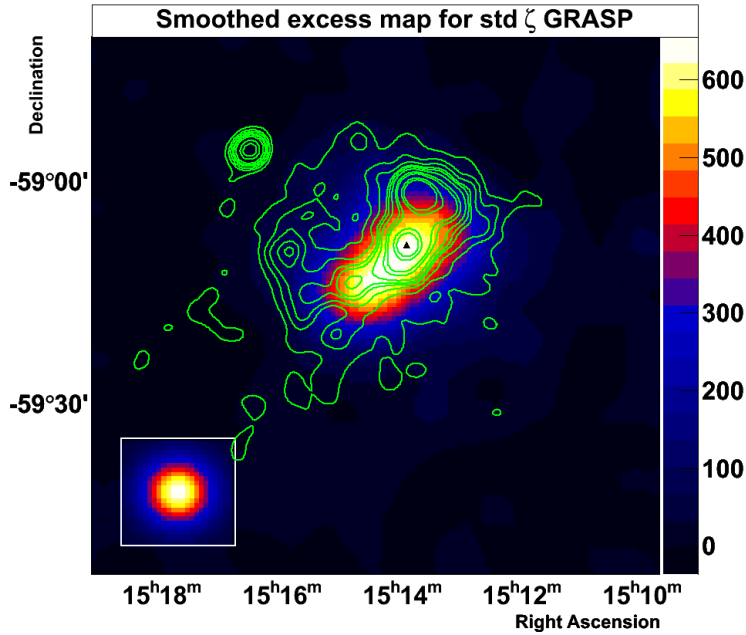


Figure 6.5: Smoothed excess map of MSH 15-5-2 using std ζ GRASP. Reanalysis used 41.8 hours of live time on the source. The map is convolved with a Gaussian of $\sigma = 0.04^\circ$ in order to smooth out statistical fluctuations. The green contours are obtained from the smoothed ROSAT PSPC data [Trussoni et al., 1996]. The left-bottom inset shows the identically smoothed PSF for GRASP.

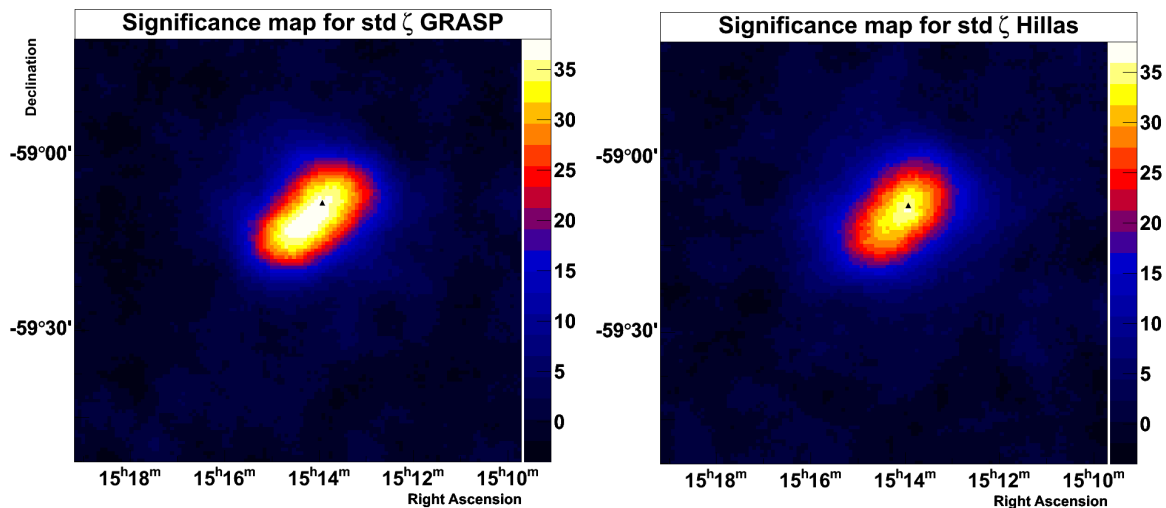


Figure 6.6: Significance map of MSH 15-5-2 for std ζ GRASP on the left and for std ζ Hillas on the right. Both maps have the same scale and are produced with a correlation radius of 0.07° . The black triangle marks the position of the pulsar.

An analysis of the same data set with the standard ζ Hillas method is performed and a significance map is shown in Fig. 6.6 on the right. This can be compared to the significance map of the standard ζ GRASP method illustrated in Fig. 6.6 on the left. It appears that using GRASP the emission seems to be more elongated towards the south-east of the pulsar.

6.3.1 Morphology of MSH 15-5-2

Fit of one two-dimensional Gaussian

Using the On-Off Likelihood fit, the On map can be fitted to a model prediction for different types of models. The model is convolved with the PSF and the background from the data is added. The result of a fit of one two-dimensional (2D) Gaussian and the residuals are shown in Fig. 6.7. The corresponding fit parameters are summarized in table 6.2.

6. COMPLEX SOURCE MSH 15-5-2

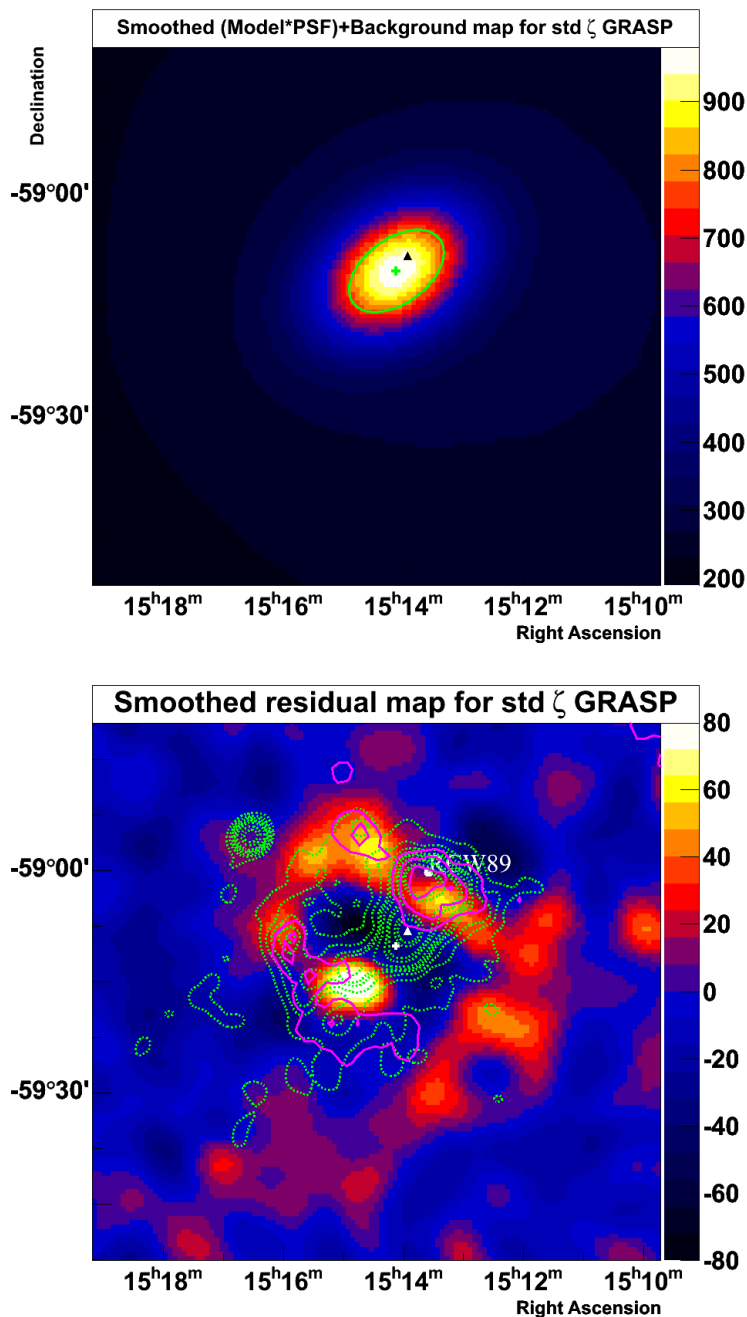


Figure 6.7: Top: Smoothed model map of one 2D Gaussian as a result of an On-Off Likelihood fit to MSH 15-5-2. The green cross and line shows the position and the ellipse of the fit result respectively. The black triangle marks the position of the pulsar. Bottom: Smoothed residual map for the result shown on the top. Both maps are smoothed with a Gaussian of $\sigma = 0.04^\circ$. The white cross shows the best fit position and the white circle the position of the H α emission nebula RCW 89. The green dashed contours are obtained from the smoothed ROSAT PSPC data [Trussoni et al., 1996] and the pink solid contours are obtained from MOST radio data [Whiteoak and Green, 1996]

Pos Ra (J2000)	Pos Dec (J2000)	Minor Axis [$^{\circ}$]	Major Axis [$^{\circ}$]	Angle [$^{\circ}$]
$15^{\text{h}}14^{\text{m}}7.13\text{s} \pm 1.21\text{s}$	$-59^{\circ}10'10.2'' \pm 8.7''$	0.071 ± 0.003	0.117 ± 0.003	129.4 ± 2.3

Table 6.2: Fit results for a model including one 2D Gaussian for MSH 15-5-2. The angle is measured from the declination axis pointing North to East.

Fit of two 2D Gaussians

The residuals clearly show that only one 2D Gaussian does not describe the complex morphology very well. Therefore, the model is extended by another 2D Gaussian and the fit is repeated. From Fig. 6.8 it becomes clear that this significantly improves the agreement between the assumed model of MSH 15-5-2 and the measured morphology. A log likelihood ratio test (LRT) justifies the inclusion of another 2D Gaussian.

$$\text{LRT} = -2 \times \ln \left(\frac{\text{likelihood for one 2D Gaussian}}{\text{likelihood for two 2D Gaussian}} \right) \approx 82.54 \quad (6.1)$$

The probability distribution is approximately a chi-squared distribution with 6 degrees of freedom. Calculating the one sided p -Value from the cumulative distribution function (CDF) for a chi-squared distribution with 6 degrees of freedom results in $p \approx 3.1 \times 10^{-17}$. This can be converted into significance, defined as the number of standard deviations σ at which a Gaussian random variable of zero mean would give a one-sided tail area equal to the same p -Value.

$$p = \int_{\sigma}^{\infty} \frac{1}{\sqrt{2\pi}} \exp\left(\frac{-x^2}{2}\right) = 1 - \Phi(\sigma) \quad (6.2)$$

where $\Phi(\sigma)$ is the cumulative distribution function for the normal distribution. Through the inverse CDF function Φ^{-1} the significance can be calculated to be about 8.4σ . This indicates that a model of two 2D Gaussians is highly favoured over just one 2D Gaussian. The fitted parameters for a model including two 2D Gaussians are summarized in table 6.3.

6. COMPLEX SOURCE MSH 15-5-2

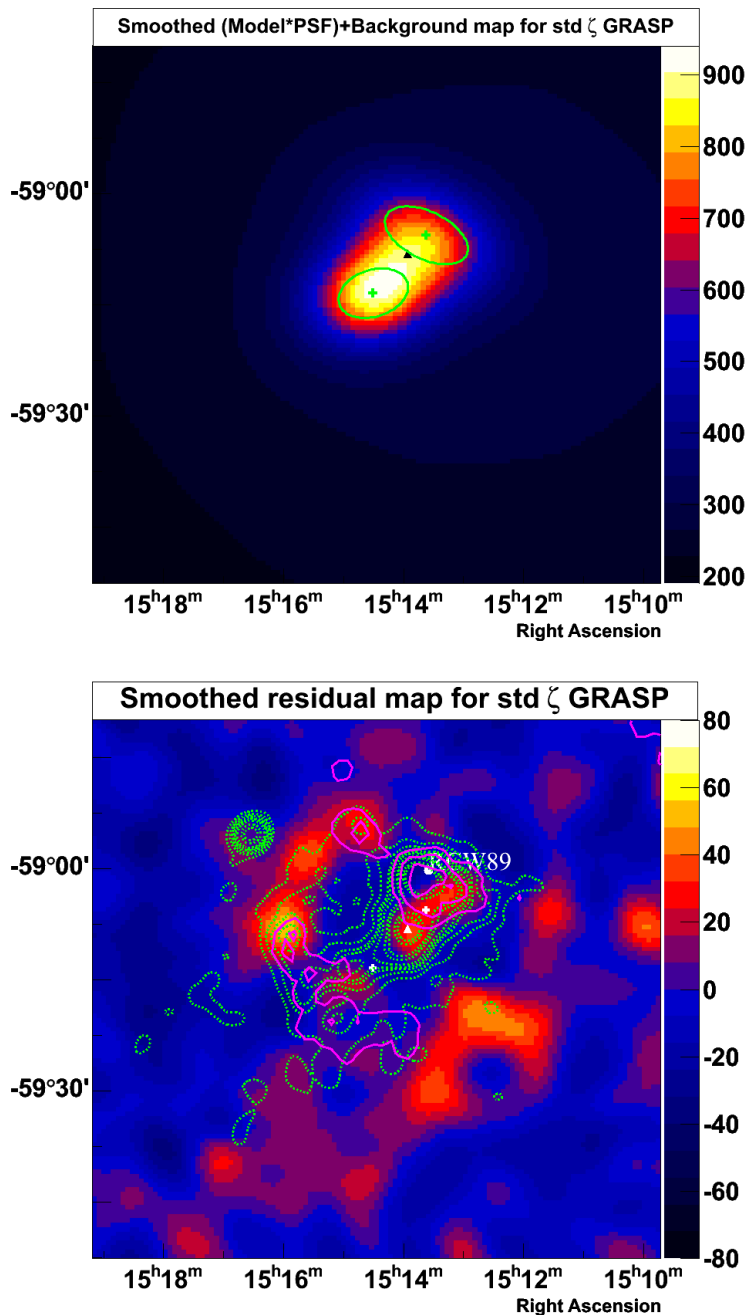


Figure 6.8: Top: Smoothed model map of two 2D Gaussians as a result of a On-Off Likelihood fit to MSH 15-5-2. The green crosses and lines show the positions and the ellipses of the fit result respectively. The black triangle marks the position of the pulsar. Bottom: Smoothed residual map for the result shown on the top. Both maps are smoothed with a Gaussian of $\sigma = 0.04^\circ$. The white crosses show the best fit positions and the white circle the position of the H α emission nebula RCW 89. The green dashed contours are obtained from the smoothed ROSAT PSPC data [Trussoni et al., 1996] and the pink solid contours are obtained from MOST radio data [Whiteoak and Green, 1996]

6.3 Analysis using GRASP

Pos Ra (J2000)	Pos Dec (J2000)	Minor Axis [$^{\circ}$]	Major Axis [$^{\circ}$]	Angle [$^{\circ}$]
$15\text{h}14\text{m}30.29\text{s} \pm 3.65\text{s}$	$-59^{\circ}13'25.68'' \pm 24.12''$	0.077 ± 0.006	0.052 ± 0.006	20.1 ± 7.8
$15\text{h}13\text{m}37.32\text{s} \pm 2.91\text{s}$	$-59^{\circ}5'37.32'' \pm 30.24''$	0.053 ± 0.007	0.097 ± 0.006	61.9 ± 4.9

Table 6.3: Fit results for a model including two 2D Gaussians for MSH 15-5-2. The angle is measured from the declination axis pointing North to East.

Fit of two 2D Gaussians plus point-like source

From the residual map of a model including two 2D Gaussians in Fig. 6.8 it can be seen that there still seems to be an indication of an excess at a position overlapping with a part of the SNR-shell as seen in radio (pink contours) from the MGPS-2 at 843 MHz, see also section 6.1. In order to try to include this emission at this point, a point-source model is added to the model of two 2D Gaussians. Table 6.4 shows the results of a fit of a model including two 2D Gaussians plus a point-like source. Comparing table 6.3 and 6.4, the positions and extensions for the two 2D Gaussians are within errors consistent with each other. A log-likelihood ratio test comparing a model including two 2D Gaussians plus a point-like source compared to a model with only two 2D Gaussians is favored by about 3.8σ . It should be noted that this does not show an association of the emission from this point with the shell of the SNR by itself. Fig. 6.9 shows the model map at the top and the residual map at the bottom.

Pos Ra (J2000)	Pos Dec (J2000)	Minor Axis [$^{\circ}$]	Major Axis [$^{\circ}$]	Angle [$^{\circ}$]
$15\text{h}14\text{m}29.45\text{s} \pm 8.93\text{s}$	$-59^{\circ}13'26.4'' \pm 1'8.1''$	0.075 ± 0.016	0.049 ± 0.005	26.9 ± 17.6
$15\text{h}13\text{m}36.91\text{s} \pm 5.57\text{s}$	$-59^{\circ}5'40.2'' \pm 1'11.28''$	0.053 ± 0.015	0.097 ± 0.017	60.2 ± 7.9
$15\text{h}15\text{m}56.88\text{s} \pm 4.15\text{s}$	$-59^{\circ}7'32.16'' \pm 47.52''$	—	—	—

Table 6.4: Fit results for a model including two 2D Gaussians plus a point-like source for MSH 15-5-2. The angle is measured from the declination axis pointing North to East.

6. COMPLEX SOURCE MSH 15-5-2

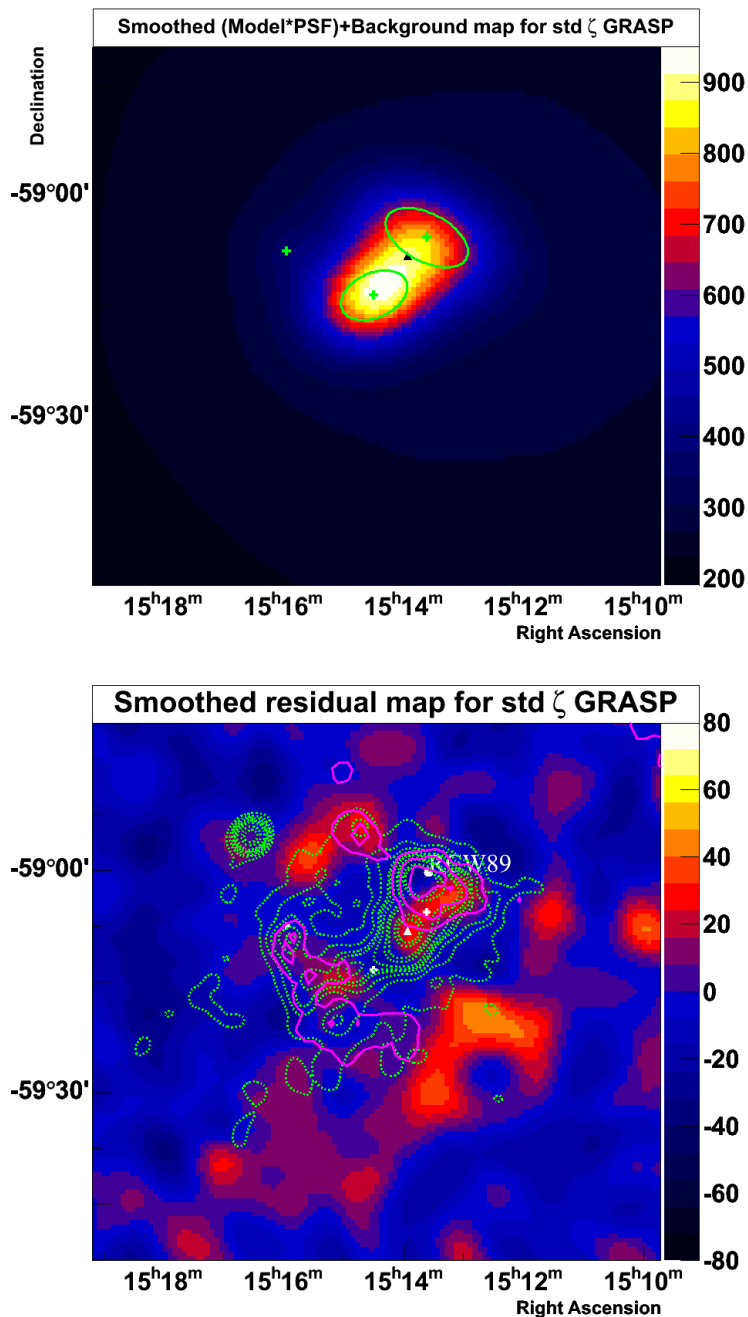


Figure 6.9: Top: Smoothed model map of two 2D Gaussians plus a point-like source as a result of an On-Off Likelihood fit to MSH 15-5-2. The green crosses and lines show the position and the ellipses of the fit result respectively. The black triangle marks the position of the pulsar. Bottom: Smoothed residual map for the result shown on the top. Both maps are smoothed with a Gaussian of $\sigma = 0.04^\circ$. The white crosses show the best fit positions and the white circle the position of the H α emission nebula RCW 89. The green dashed contours are obtained from the smoothed ROSAT PSPC data [Trussoni et al., 1996] and the pink solid contours are obtained from MOST radio data [Whiteoak and Green, 1996]

Fit of three 2D Gaussians

A more general approach is the inclusion of another 2D Gaussian, resulting in a model consisting of three 2D Gaussians. The result of the fit together with the residuals is shown in Fig. 6.10. The LRT-test shows that three 2D Gaussians are favored over two 2D Gaussians by 4.2σ . Table 6.5 shows the results of the fit of three 2D Gaussians.

Pos Ra (J2000)	Pos Dec (J2000)	Minor Axis [$^{\circ}$]	Major Axis [$^{\circ}$]	Angle [$^{\circ}$]
$15\text{h}14\text{m}18.58\text{s} \pm 4.99\text{s}$	$-59^{\circ}11'56.04'' \pm 38.88''$	0.099 ± 0.009	0.039 ± 0.005	41.2 ± 3.1
$15\text{h}13\text{m}38.09\text{s} \pm 3.72\text{s}$	$-59^{\circ}4'54.12'' \pm 27.72''$	0.047 ± 0.007	0.116 ± 0.013	62.1 ± 3.8
$15\text{h}14\text{m}30.05\text{s} \pm 9.84\text{s}$	$-59^{\circ}14'12.48'' \pm 38.16''$	0.038 ± 0.012	0.15 ± 0.03	66.9 ± 3.4

Table 6.5: Fit results for a model including three 2D Gaussians for MSH 15-5-2. The angle is measured from the declination axis pointing North to East.

6. COMPLEX SOURCE MSH 15-5-2

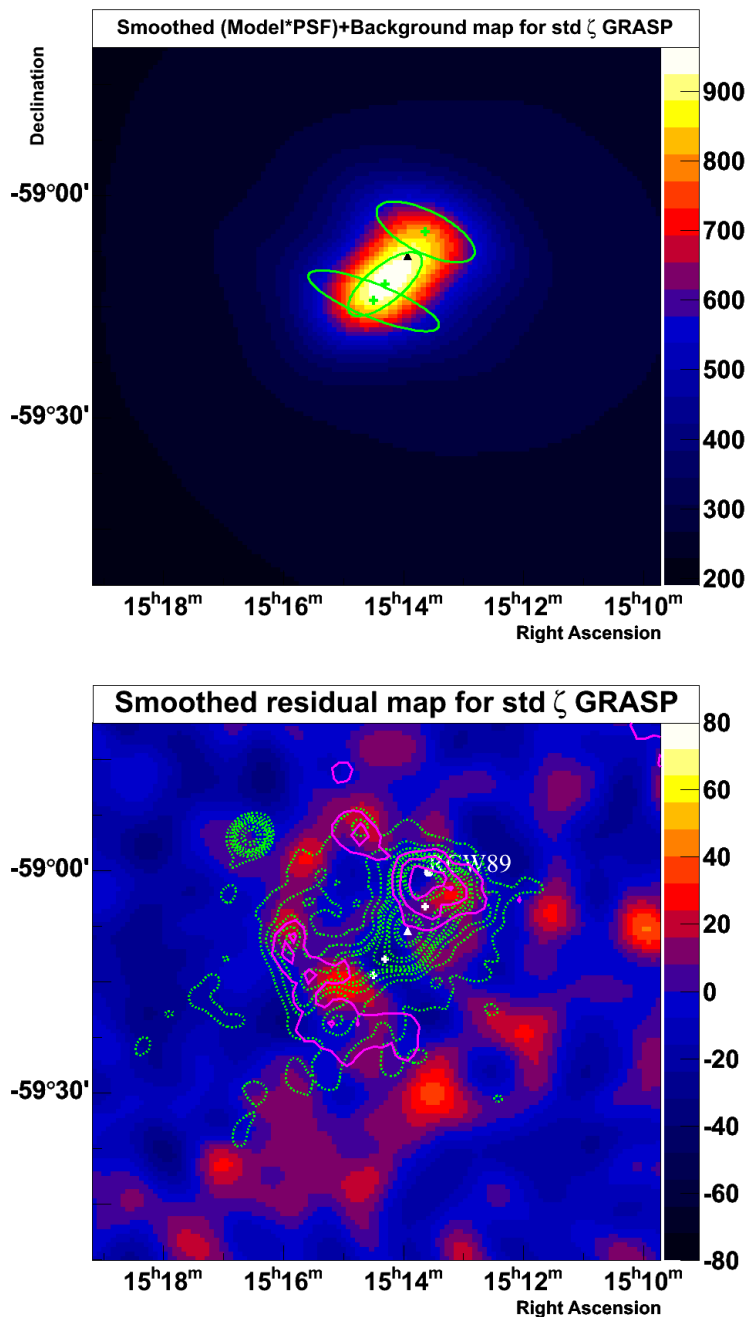


Figure 6.10: Top: Smoothed model map of three 2D Gaussians as a result of an On-Off Likelihood fit to MSH 15-5-2. The green crosses and lines show the positions and the ellipses of the fit result respectively. The black triangle marks the position of the pulsar. Bottom: Smoothed residual map for the result shown on the top. Both maps are smoothed with a Gaussian of $\sigma = 0.04^\circ$. The white crosses show the best fit positions and the white circle the position of the H α emission nebula RCW 89. The green dashed contours are obtained from the smoothed ROSAT PSPC data [Trussoni et al., 1996] and the pink solid contours are obtained from MOST radio data [Whiteoak and Green, 1996]

Energy dependent morphology

The first direct evidence, in VHE γ -rays, of an energy dependent morphology was found for the PWN HESS J1825–137, which was attributed both to IC and synchrotron cooling of the continuously accelerated electrons [Aharonian et al., 2006b]. In order to check for energy dependent morphology for MSH 15-5-2, the data set with a total live time of 95.7 hours was analysed and divided in five reconstructed energy ranges. The first energy range is from 0.3 to 0.5 TeV, the second from 0.5 to 1.5 TeV, the third from 1.5 to 3 TeV, the fourth from 3 to 5 TeV and the fifth from 5 to 100 TeV. It should be noted that the energy threshold is about 320 GeV and the highest energy bin with significant excess is around 35 TeV, see Fig. 6.15. For each of these energy ranges a significance map is produced using the Ring background method (see section 3.4.5), shown in Fig. 6.11. There seems to be an indication of energy dependent morphology, especially for the energy ranges of 0.3 to 0.5 TeV and 3 to 5 TeV. However, it is peculiar that for the energy range of 0.3 to 0.5 TeV, where the angular resolution is worse than in all the other energy ranges, there seems to be an indication of two separate areas of emission. On the other hand the background rejection in this energy range is significantly improved over the traditional Hillas based analysis. A model fit of one 2D Gaussian is performed and the results are shown in Fig. 6.12. The fitted position for the 2D Gaussian is also shown as a black cross in Fig. 6.11. The results show no significant energy dependent morphology, although the last two points for the highest energy range of the minor and major axis seem to suggest a decrease in extension. However, a model with one 2D Gaussian does not adequately describe the complex source morphology.

6. COMPLEX SOURCE MSH 15-5-2

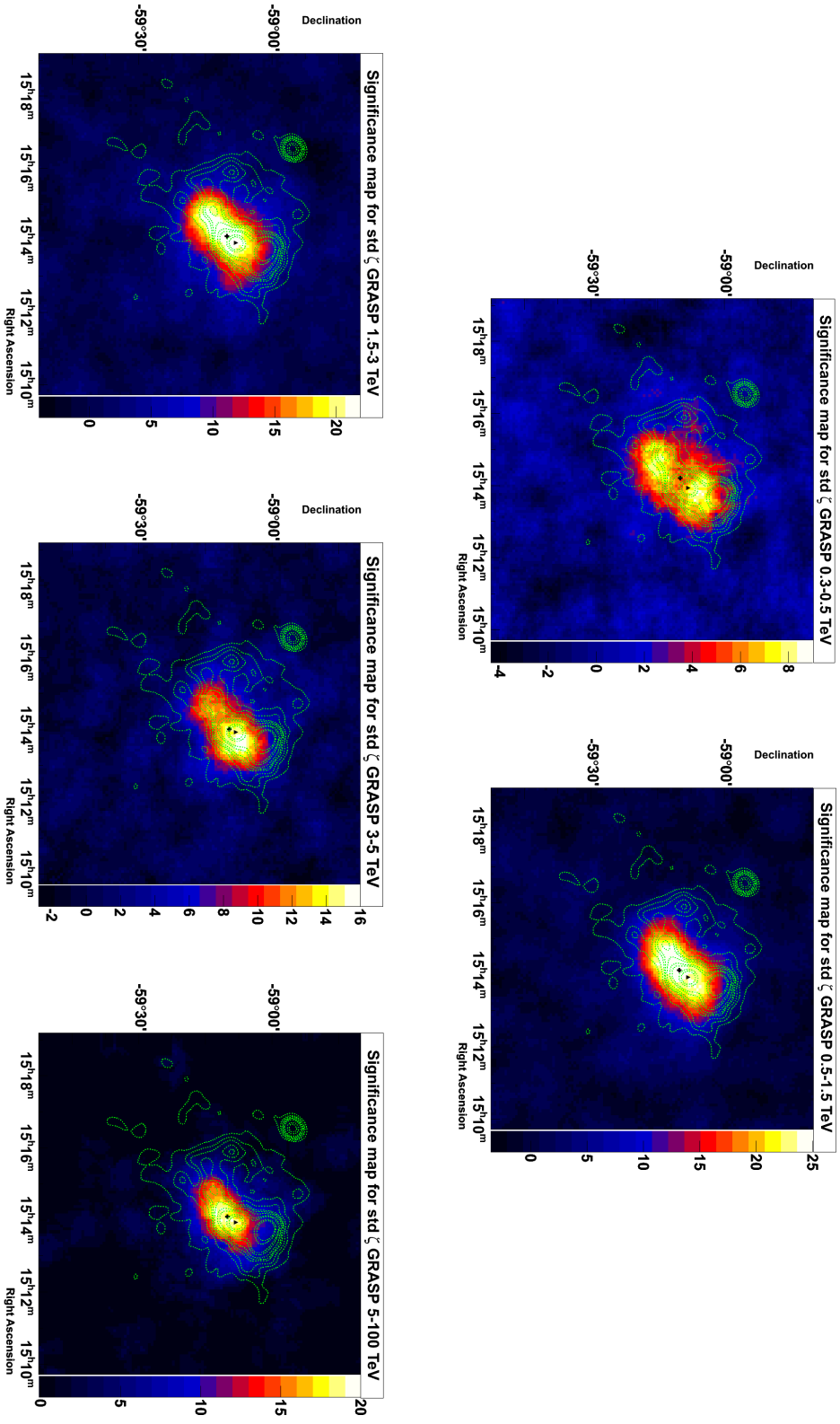


Figure 6.11: Significance maps (correlation radius of 0.07°) for MSH 15-5-2 in energy ranges. The black cross shows the position of the fit of one 2D Gaussian and the black triangle marks the position of the pulsar.

6.3 Analysis using GRASP

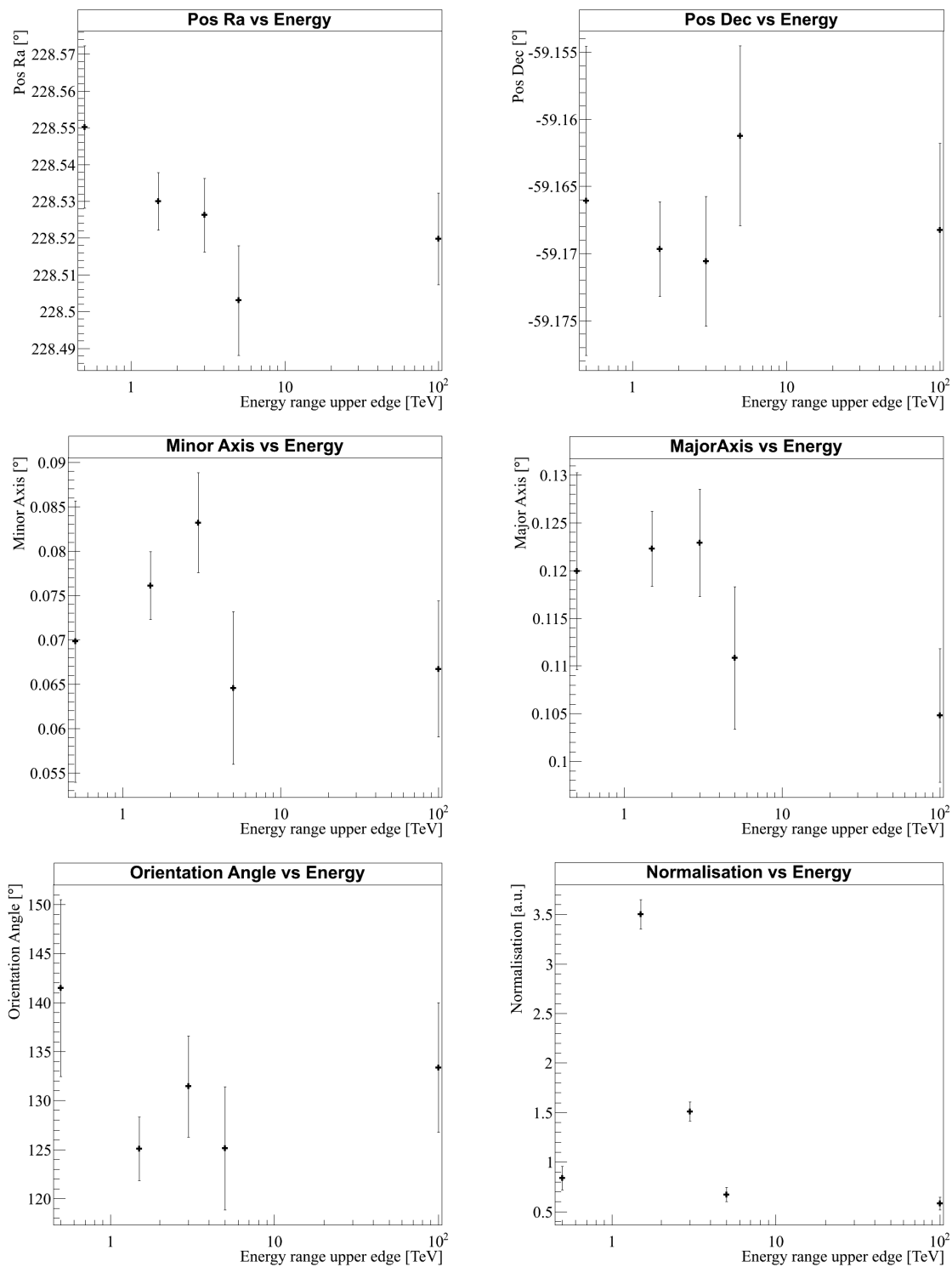


Figure 6.12: Energy dependent parameter results for a fit of one 2D Gaussians.

6. COMPLEX SOURCE MSH 15-5-2

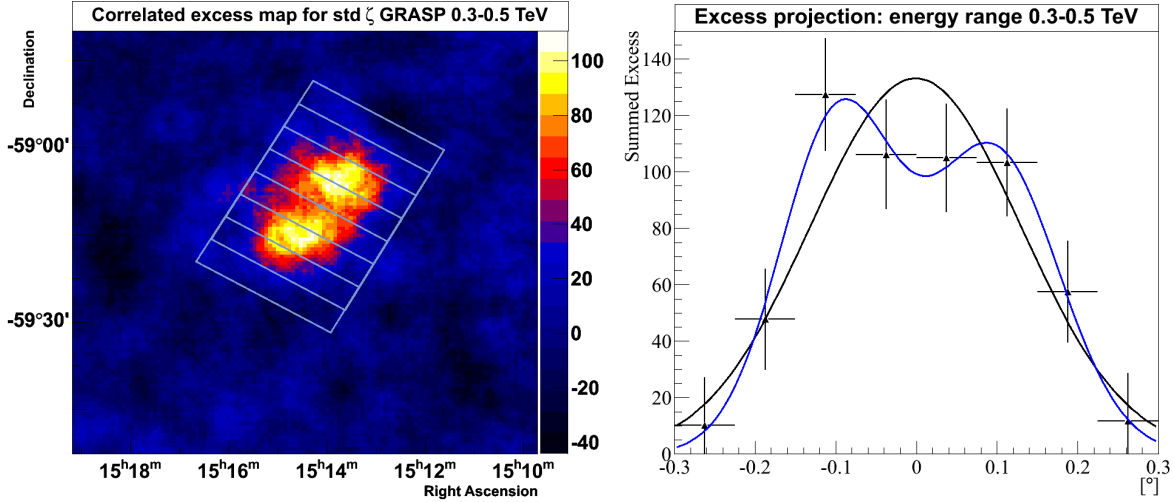


Figure 6.13: Left: Correlated excess map (correlation radius of 0.07°) for the energy range of $0.3 - 0.5$ TeV, overlaid with a sketch of the slices. Right: Summed up excess for the slices together with a fit of one and two Gaussians, illustrated as the black and blue curve respectively.

In order to investigate the significance of the two areas of emission, the excess map for each energy range is projected inside slices onto an axis along the major axis of the source. This procedure is illustrated in Fig. 6.13 on the left side, where a blue box around the PWN is shown. In each of the slices the excess is summed up and shown on the right side of Fig. 6.13, together with a fit of one and two Gaussians, illustrated as the black and blue curve respectively. The width of the slices is chosen to match the angular resolution of 0.07° . A log-likelihood ratio test favours the two Gaussians with a significance of almost 3σ . The same procedure is done in the other energy ranges as well. The result of a fit of one and two Gaussians to the projections of the excess is illustrated in Fig. 6.14. For the energy range from $0.5-1.5$ TeV and $1.5-3$ TeV the LRT-test favors the model of two Gaussians at the level of 4 and 3σ respectively. In the higher energy ranges the two Gaussians show no significant preference over only one Gaussian model. This further shows a complex underlying source morphology and also explains why a model including two 2D Gaussians are highly favoured over only one 2D Gaussian.

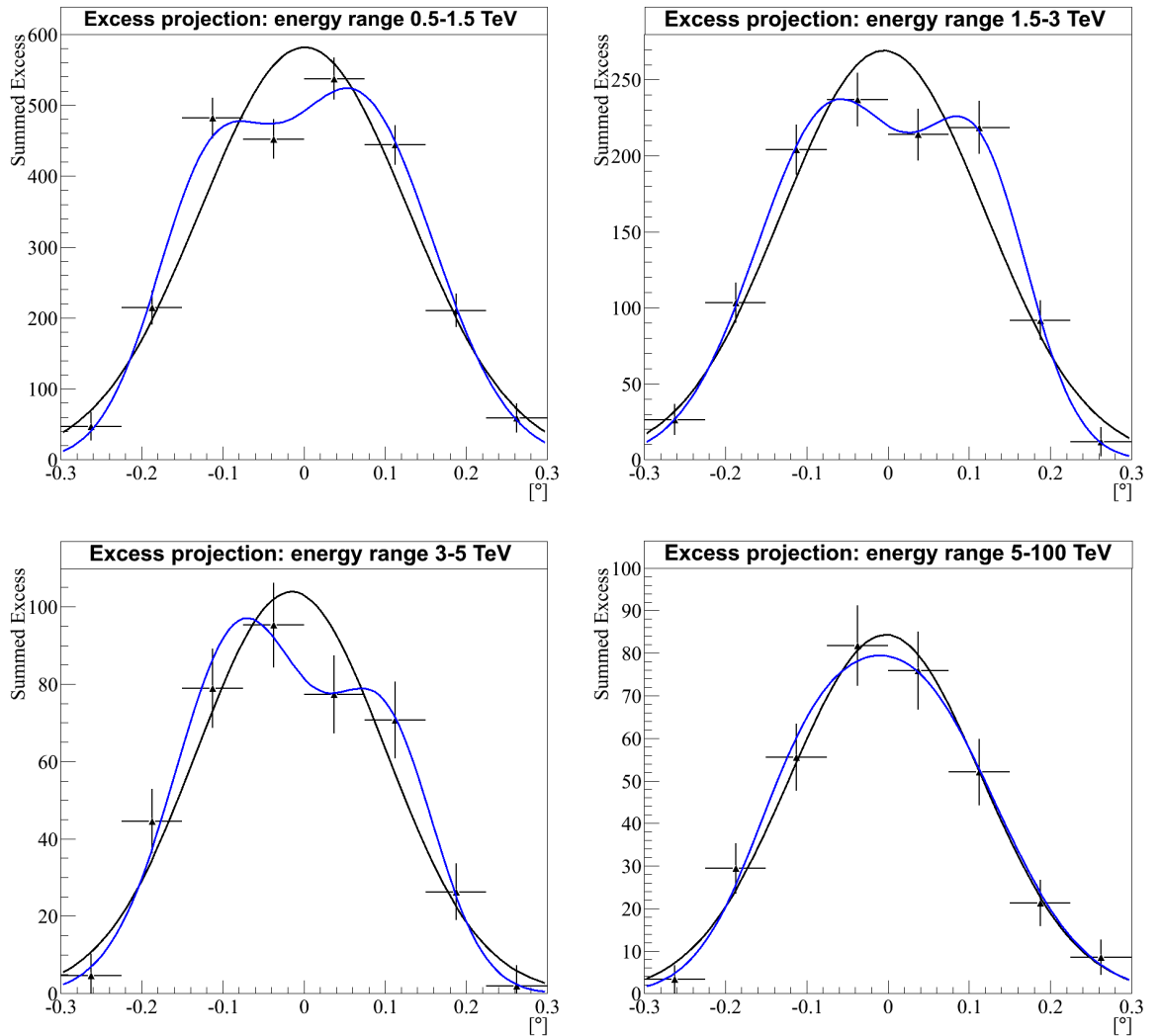


Figure 6.14: Summed up excess for the slices, in the other energy ranges, together with a fit of one and two Gaussians, illustrated as the black and blue curve respectively.

6.3.2 Energy Spectrum of MSH 15-5-2

Whole Source

The energy spectrum reconstruction was done similar to the previous analysis, using only excess events inside a circle with a radius of 0.3° centred on the best fit position shown in table 6.2 and indicated by the green cross in Fig. 6.7 (top). Table 6.6 shows the results of a fit of a power law model ($\propto (E/E_0)^{-\Gamma}$) and an exponential cut-off power law model ($\propto (E/E_0)^{-\Gamma} \exp(-E/E_{\text{cut}})$) to the data. The spectral index as well as the differential flux at 1 TeV show a nice agreement with the original published results, see section 6.2. The log-likelihood ratio test between the two models shows an indication of an exponential cut-off behaviour at an energy of about 17 TeV at the 3σ level. The cut-off energy could reflect a cut-off in the primary electron spectrum or the beginning of the Klein-Nishina regime (PUT reference from joachim).

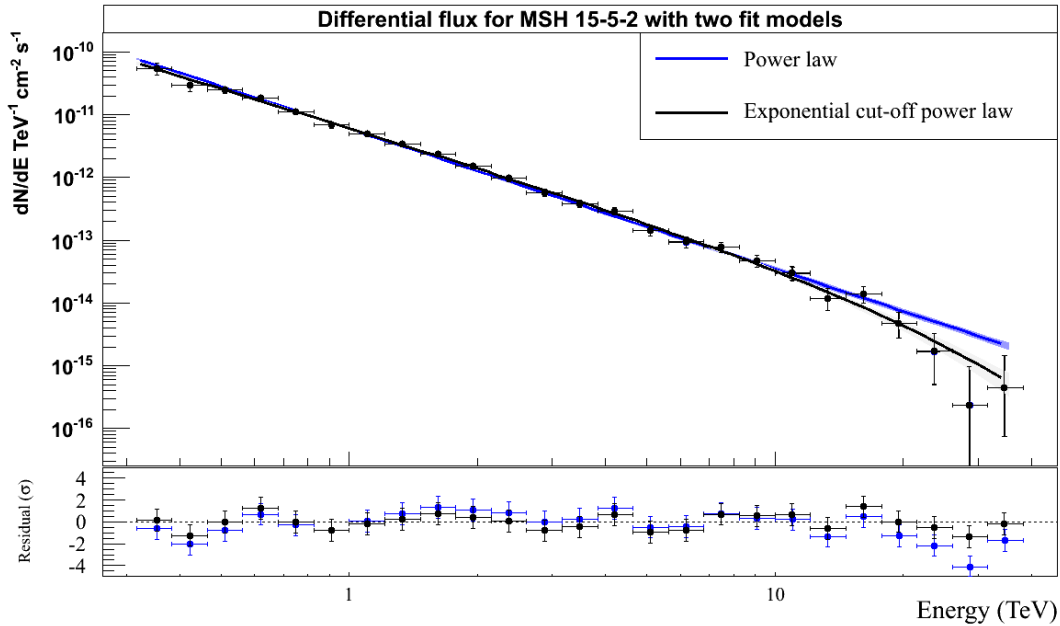


Figure 6.15: Differential flux spectrum for MSH 15-5-2 for std ζ GRASP (black circles). The data points were fit with two models, a power law (blue) and an exponential cut-off power law (black). The extraction region is a circle with a radius of 0.3° centred on the best fit position.

Parameter	Power law	Exponential cut-off power law
Spectral Index Γ	$2.24 \pm 0.03_{\text{stat}} \pm 0.09_{\text{sys}}$	$2.05 \pm 0.06_{\text{stat}} \pm 0.09_{\text{sys}}$
E_{cut}	–	$17.1 \pm 4.8_{\text{stat}}$
Differential flux (1 TeV) $10^{-12} \text{ cm}^{-2}\text{s}^{-1}\text{TeV}^{-1}$	$5.99 \pm 0.19_{\text{stat}} \pm 1.19_{\text{sys}}$	$6.44 \pm 0.24_{\text{stat}} \pm 1.29_{\text{sys}}$
Integral Flux (> 1 TeV) $10^{-12} \text{ cm}^{-2}\text{s}^{-1}$	$4.79 \pm 0.22_{\text{stat}} \pm 0.96_{\text{sys}}$	$5.01 \pm 0.16_{\text{stat}} \pm 1.01_{\text{sys}}$
$-2 \times (\text{log-likelihood value})$	-32.699	-22.642

Table 6.6: Comparison of two model results of a power-law and an exponential cut-off power law fit to the energy spectrum using standard ζ GRASP for MSH 15-5-2. Only excess events inside a circle with a radius of 0.3° are used in the energy reconstruction.

Spatially Resolved Spectral Analysis

Fig. 6.11 and Fig. 6.12 might suggest that the extension of the PWN decreases as a function of energy. A way to test this hypothesis is to perform a spatially resolved spectral analysis to search for a change in photon index across the source. This procedure could successfully show an increase of the photon index for larger distances from the pulsar position of HESS J1825–137 [Aharonian et al., 2006b]. Fig. 6.16 shows again the excess map along with wedges going radially outwards from the pulsar position. The spectral extraction region was divided into two parts, the first being comprised of three wedges along the north-east direction and is shown in Fig. 6.16 in green. The second consists of four wedges along the south-west direction in blue. The radii of the wedges increase in steps of 0.07° and inside every wedge the energy spectrum is determined and fitted with a power-law. The energy spectrum is obtained in the range from 300 GeV to 10 TeV and is shown for the north-east direction in Fig. 6.18 at the top and for the south-west direction at the bottom. The resulting spectral index from a fit of a power-law as a function of radial distance is shown in Fig. 6.17 on the top along the north-east direction and on the bottom along the south-west direction. The analysis was repeated with wedges increasing in steps of 0.1° and yield for the south-west direction comparable results. Along the north-west direction the increased size of the wedges limited the statistics in the third wedge and no indication of spectral steepening could be found.

6. COMPLEX SOURCE MSH 15-5-2

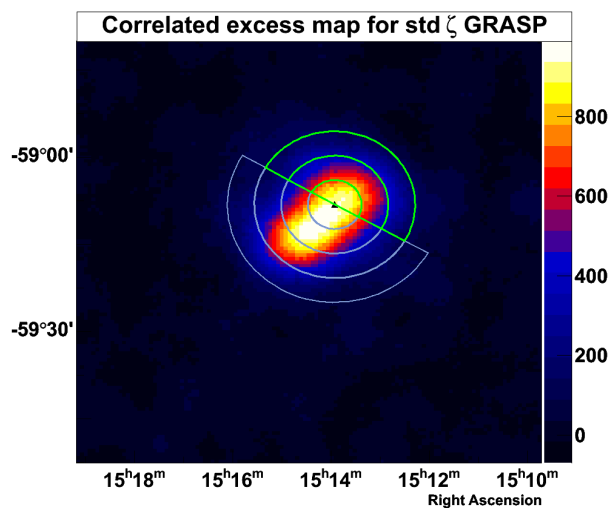


Figure 6.16: Correlated excess map (correlation radius of 0.07°), overlaid with a sketch of the wedges. There are three wedges going along the north-east direction in green and four wedges along the south-west direction in blue. The black triangle marks the position of the pulsar.

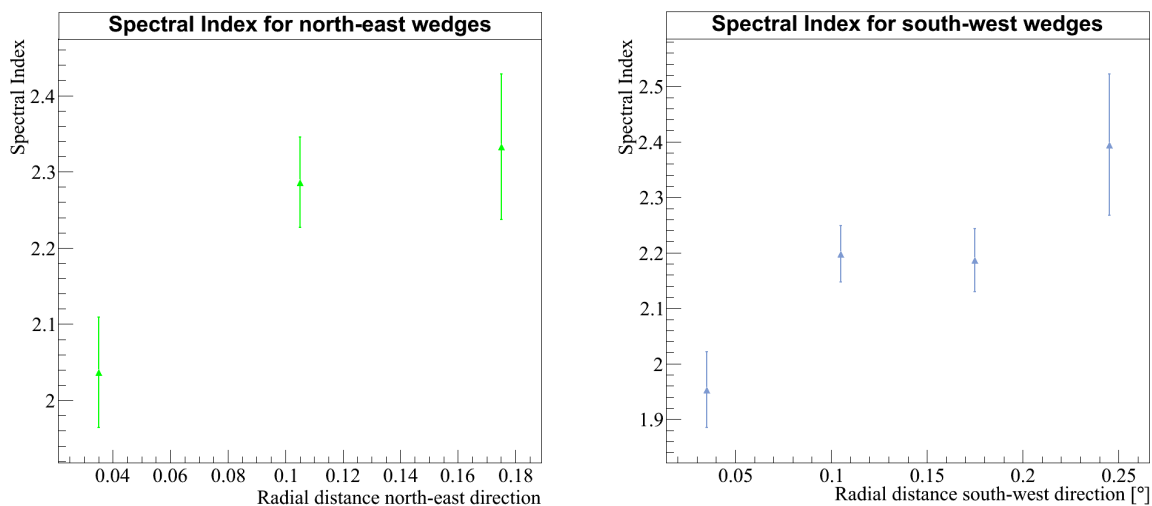


Figure 6.17: Top: Spectral Index of a power-law fit as a function of the radial distance along the north-east direction. Bottom: Spectral Index of a power-law fit as a function of the radial distance along the south-west direction.

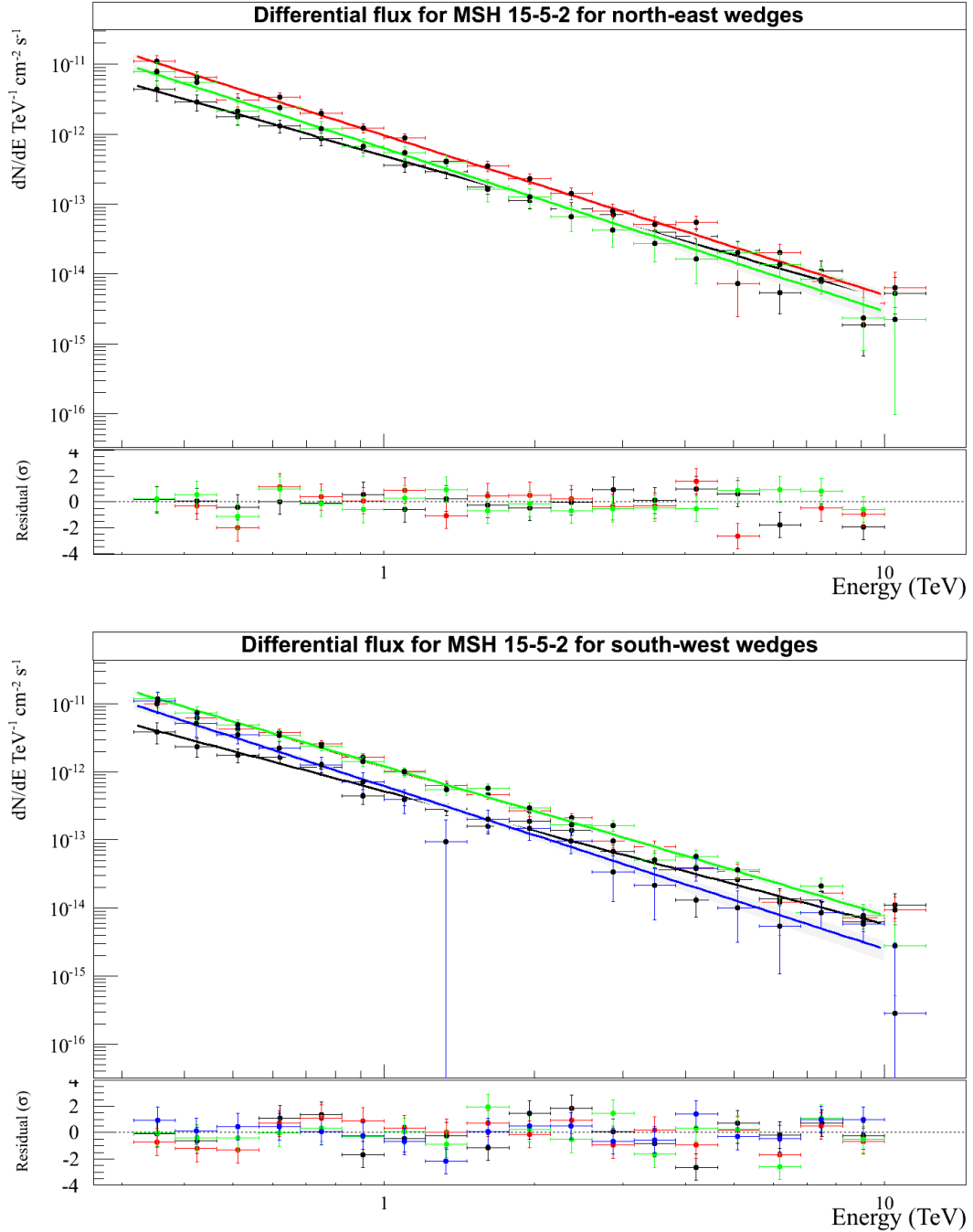


Figure 6.18: Top: MSH 15-5-2 differential energy spectrum for a spatially resolved spectral analysis in the north-east direction. Bottom: MSH 15-5-2 differential energy spectrum for a spatially resolved spectral analysis in the south-west direction. The color represents the wedge number going radially outwards (1:black, 2: red, 3: green, 4: blue).

6.3.3 Upper Limit on SNR Explosion Energy

Because of the location of the H α emission nebula RCW 89, it has been considered to be a contact point of the jet and the surrounding SNR [Yatsu et al., 2005]. Using an upper limit on the γ -ray flux at the position of the H α emission nebula RCW 89 and assuming an hadronic process, the cosmic ray density can be calculated. For example Fig. 6.8 shows the position marker of RCW 89 as a white circle. In order to get an upper limit on the γ -ray flux coming from the interaction of the PWN with this gas cloud, the following procedure was conducted:

- Using the best-fit parameters for one 2D Gaussian alone, another fit of one 2D Gaussian plus a point-like source at the position of RCW 89 is performed.
- The parameters Pos Ra, Pos Dec, Minor Axis, Major Axis and Angle of the 2D Gaussian were fixed to the values given in table 6.2
- The position of the point-like source was fixed to the position of RCW 89
- Only the two normalisation parameters from the 2D Gaussian and the point-like model are left free

From the best-fit model parameters an artificial excess map can be produced for each model, yielding a total integrated excess of 5688 for the 2D Gaussian model. Let $N_{\text{point-like}}$ be the fitted normalisation of the point-like model and $\sigma_{N_{\text{point-like}}}$ its 1- σ error. By scaling the artificial excess map of the point-like model with a factor s defined by

$$s = \frac{N_{\text{point-like}} + 3 \times \sigma_{N_{\text{point-like}}}}{N_{\text{point-like}}} \quad (6.3)$$

an integrated excess of 187 is obtained. The ratio of the two integrated excesses multiplied by the integral flux above 1 TeV for MSH 15-5-2 yields a 3σ upper limit of:

$$\begin{aligned} \frac{dF_{ul}}{dAdt} &\leq \frac{187}{5688} \times (4.79 \pm 0.22_{\text{stat}} \pm 0.96_{\text{sys}}) \times 10^{-12} \text{cm}^{-2} \text{s}^{-1} \\ &\approx (0.157 \pm 0.007_{\text{stat}} \pm 0.032_{\text{sys}}) \times 10^{-12} \text{cm}^{-2} \text{s}^{-1} \end{aligned} \quad (6.4)$$

For a differential flux at an energy E , assuming a power-law, it can be written:

$$\frac{dF(E)}{dAdEdt} = \Phi(E_0) \left(\frac{E}{E_0} \right)^{-\Gamma} \quad (6.5)$$

This can be translated into an energy density of γ -rays inside the cloud RCW 89.

$$\begin{aligned}
 \int_{E_{\min}}^{\infty} E \cdot \frac{dF(E)}{dAdtdE} dE &= \Phi(E_0) \int_{E_{\min}}^{\infty} E \cdot \left(\frac{E}{E_0}\right)^{-\Gamma} dE \\
 &= \Phi(E_0) \frac{E_{\min}^2}{\Gamma - 2} \left(\frac{E}{E_0}\right)^{-\Gamma} \\
 &= \frac{dF(> E_{\min})}{dAdt} \frac{E_{\min}^2}{\Gamma - 2}
 \end{aligned} \tag{6.6}$$

where $\Gamma \neq 2$. The γ -ray flux from a SNR due to neutral pion decay can be expressed by [Gabici, 2012]:

$$\frac{dF(> E_{\min})}{dAdt} \frac{E_{\min}^2}{\Gamma - 2} \approx \frac{W_{\text{CR}} c_{p \rightarrow \gamma}}{\tau_{pp} (4\pi d^2)} \tag{6.7}$$

where $c_{p \rightarrow \gamma} \approx 0.1$ is the average fraction of the proton energy transferred to the γ -ray photon, $\tau_{pp} \approx 6 \times 10^7 \left(\frac{n}{1 \text{ cm}^{-3}}\right)^{-1}$ is the energy loss time due to proton-proton interactions in years and d is the distance to the SNR. The total energy in cosmic rays from the SNR is W_{CR} . Combining eq. (6.7) with eq. (6.6) it follows:

$$W_{\text{CR}} \approx \frac{dF(> E_{\min})}{dAdt} \frac{E_{\min}^2}{\Gamma - 2} \cdot \tau_{pp} \frac{4\pi d^2}{c_{p \rightarrow \gamma}} \tag{6.8}$$

With $E_{\min} = 1 \text{ TeV}$, $d \approx 5.2 \pm 1.4 \text{ kpc}$, $n \approx 15 \text{ cm}^{-3}$ [Dubner et al., 2002] and the integral flux upper limit in eq. (6.4) a 3σ upper limit on the total energy in cosmic rays can be calculated to be:

$$W_{\text{CR}} \lesssim (2.37 \pm 1.41) \times 10^{48} \text{ TeV} \tag{6.9}$$

With an assumed mass of $1700 M_{\odot}$ for RCW 89, the energy density of cosmic rays due to proton-proton interactions becomes:

$$n_{\text{CR}} = \frac{W_{\text{CR}}}{V} \lesssim (24.7 \pm 14.6) \text{ eV/cm}^3 \tag{6.10}$$

If RCW 89 consists of the ejecta from the supernova associated with the central pulsar, the ejecta must have traveled at least $\approx 7.5 \text{ pc}$ from the SNR center [Yatsu et al., 2005]. Assuming one-dimensional diffusion the energy density in cosmic rays can be estimated by (see section 5.3):

$$n_{\text{CR}}(E) \sim \frac{\Omega}{4\pi} \eta \frac{E_{\text{SN}}}{R_d(E) R_{\text{sh}}^2} \tag{6.11}$$

6. COMPLEX SOURCE MSH 15-5-2

where Ω is the solid angle corresponding to the distance and size of RCW 89. With a size of about $10'$ and a distance of ≈ 7.5 pc, the solid angle becomes $\Omega \approx 1.86$. An estimation on the supernova explosion energy E_{SN} , assuming $\eta \approx 0.1$, $D_{\parallel} \approx 10^{28}$ cm²/s, $t \approx 1600 \pm 100$ years and $R_{sh} \approx 7.5$ pc can be given by:

$$E_{SN} \lesssim \frac{4\pi n_{CR} R_{sh}^2 \sqrt{2tD_{\parallel}}}{\Omega \eta} \quad (6.12)$$

$$\approx (4.6 \pm 2.7) \times 10^{49} \text{ erg} \quad (6.13)$$

In the isotropic case the supernova explosion energy is increased to $\approx (4.5 \pm 2.7) \times 10^{50}$ erg.

6.4 Discussion

This section outlines the conclusions from the results obtained in the analysis of MSH 15-5-2.

Morphology

A new analysis with an extended data set for MSH 15-5-2 reveals a complex morphology. It has been shown that a model including two 2D Gaussians are preferred over a model including only one 2D Gaussian by about 8σ . These two 2D Gaussians are well aligned in comparison with the X-ray map from ROSAT PSPC data, see Fig. 6.8. The residual image for this model indicates a leftover excess at the position coincident with the expected SNR shell seen in radio. However, it is difficult to conclude that this emission is indeed associated with the SNR shell. The inclusion of a third 2D Gaussian is favoured over a model including only two 2D Gaussians at the 4σ level. This indicates that the morphology of MSH 15-5-2 might not be adequately described with a model including two 2D Gaussians.

An analysis of the morphology in energy bands indicates that there seems to be two separate areas of emission in the lowest energy band from 0.3 – 0.5 TeV. One of these areas is located to the north-west of the pulsar and the other one to the south-east. An association with the relativistic outflows (jets) from the pulsar seen in X-rays might be possible, but needs further investigation. The results from this analysis show an indication of two separated sources of VHE γ -ray emission at the 3-4 σ level below 3 TeV.

Energy spectrum

The spectrum of MSH 15-5-2, see Fig. 6.15, shows a possible indication of an exponential cut-off at about 17 TeV. Depending on the composition of the radiation fields in the region, the cut-off could either result from an intrinsic cut-off in the electron spectrum or due to the onset of the Klein-Nishina regime in the presence of an IR radiation field. Assuming the former, a cut-off at about 17 TeV would lead to a cut-off in the electron spectrum at approximately 74 TeV, considering inverse Compton scattering of the CMB photons [de Jager and Djannati-Atai, 2009]. The synchrotron cooling time is given by the expression [Hinton and Hofmann, 2009]:

$$\tau_{\text{yr}} = 1.3 \times 10^7 B_{\mu\text{G}}^{-2} E_{\text{TeV}}^{-1} \quad (6.14)$$

Assuming $\tau_{\text{yr}} = 1600 \pm 100$ years and $E_{\text{TeV}} = 17 \pm 5$ TeV, the magnetic field can be estimated at $\approx (21.7 \pm 3.3)\mu\text{G}$. The magnetic field in the jet was estimated by [Yatsu et al., 2005] to be about $38\mu\text{G}$ and $25\mu\text{G}$ for the north and south jet respectively. Furthermore, a dynamical model for the PWN describing the multiband observed emission by [Fang and Zhang, 2010] yield a magnetic field strength inside the PWN of $19.3\mu\text{G}$. Modeling performed by [Torres et al., 2014] yield a similar result for the magnetic field of the order of $20 - 25\mu\text{G}$.

A spatially resolved spectral analysis shows an indication of energy dependent morphology, especially in the south-east direction. Spectral variation with distance from the pulsar could result from energy loss of particles during their propagation from e.g., synchrotron and inverse Compton (IC) losses. Assuming isotropic distributions of electrons and target photons, a power law distribution of electrons $N_e(E) \sim E^{-\Gamma_e}$ will generate IC and synchrotron spectra of index $\Gamma_\gamma = (\Gamma_e + 1)/2$. In the Klein-Nishina regime the γ -ray spectrum steepens and the spectral index will be given by $\Gamma_\gamma = \Gamma_e + 1$. On the other hand a variation of the shape of the injection spectrum with the age of the pulsar can also account for the spatial variation of the spectrum. In case of continuous injection over time from the pulsar, assuming synchrotron losses or IC losses in the Thomson regime dominate, the electron energy distribution will exhibit a spectral break, with index Γ_e increasing by one unit [Kardashev, 1962]. This will cause a break with an index change $\Delta\Gamma = 0.5$ in the IC and synchrotron spectrum, which approximately matches the observed variation between the inner and outer regions.

6. COMPLEX SOURCE MSH 15-5-2

However, due to the large uncertainties on the spectral index points it is hard to draw definitive conclusions.

RCW 89

Assuming anisotropic diffusion, the supernova explosion energy has been estimated at $(5.7 \pm 3.3) \times 10^{49}$ erg, which is lower than the typical supernova explosion energy of 10^{51} erg. However, this was estimated from the integral γ -ray flux above 1 TeV, which corresponds to protons with an energy above some 10 TeV. The missing fraction to the total energy in cosmic ray protons coming from protons with an energy below 10 TeV can be estimated. Assuming a proton spectrum with a spectral index of $\Gamma_p \approx 2.1$, this will increase the total energy in cosmic ray protons by a factor of ≈ 3.5 and therefore also the supernova explosion energy. Furthermore, according to [Gaensler et al., 1999] the SNR shell is still expanding in the cavity with a low ambient density and therefore produces no observable emission. This might also explain the lower value for the obtained supernova explosion energy since it is obtained assuming that the shell is already in contact with RCW 89.

Chapter 7

Summary and Conclusions

In this work a γ -ray air shower event reconstruction algorithm is developed. The basic concept is to use the Monte Carlo air shower simulation software CORSIKA to parameterise the angular Cherenkov photon distribution with suitable analytical functions. These functions, in turn, depend on air shower parameters like the impact distance of the incident γ -ray to the telescope or the height of the first interaction in the atmosphere. From this Gamma Ray Air Shower Parameterisation (GRASP) an expected two-dimensional image can be obtained. Applying a fit of the observed pixel amplitudes to the ones obtained from this expected image reconstructs observable shower parameters. These are the direction of the γ -ray, its energy, height of first interaction and the core position on the ground. Depending on the zenith angle of observation, the reconstruction improves the angular resolution by 20-30% with respect to traditional image moment analysis methods. Furthermore, the energy resolution is improved by 5-30% depending on the energy and zenith angle of the incident γ -ray. The GRASP method provides several new classifying variables to differentiate γ -ray induced air showers from hadronic ones. The most important variables are the scaling factor of the Lorentz width of the shower image and the peak intensity corresponding to the height of the shower maximum. With these new parameters and with parameters obtained from the traditional Hillas method a new training of a multivariate BDT is performed. In combination with this MVA-based background rejection method the sensitivity can be significantly improved by about 70 % over the standard Hillas reconstruction. The improvement in sensitivity stems in almost equal parts from the improved angular resolution and the enhanced γ -hadron discrimination. Furthermore, an increased sensitivity

7. SUMMARY AND CONCLUSIONS

is essential in detecting new VHE γ -ray sources or for an accurate description of the morphology of complex sources. Future improvements of this method could be:

- Implementation of the electronic readout window into the framework of GRASP to better describe showers at large energies and large zenith angles.
- Investigation of the validity of a Moyal function, to describe the longitudinal angular Cherenkov photon distribution, for air shower events with an impact distance to the telescope smaller than ≈ 50 m, see section 4.5.

In the last part of this work the newly developed GRASP method combined with the multivariate BDT is utilised in the analysis of the PWN MSH 15-5-2. In X-ray it shows a complex morphology, showing the pulsar wind nebula, a south jet extending to the south-west and a north jet in the direction of the synchrotron nebula coincident with the $H\alpha$ nebula RCW 89 to the north-east. From the radio data a partial shell is visible in the south-east of the pulsar PSR B1509-58. The improved sensitivity of the GRASP method makes this an ideal case for studies of the morphology in VHE γ -rays. A new analysis of a data set with a total live time of 95.7 hours in the entire energy range ($\approx 0.32 - 35$ TeV) shows an excess with a significance of about 41σ within the region of radius 0.14° centered at the pulsar position. An investigation of the morphology shows that a model including two 2D asymmetric Gaussians is favored over a model with only one 2D Gaussian by about 8σ . These two 2D Gaussians are well aligned in comparison with the X-ray map from ROSAT PSPC data, see Fig. 6.8. The residual image for this model indicates a leftover excess at the position coincident with the expected SNR shell seen in radio. However, it is difficult to conclude that this emission is indeed associated with the SNR shell. The inclusion of a third 2D Gaussian is favoured over a model including only two 2D Gaussian at the 4σ level. This indicates that the morphology of MSH 15-5-2 might not even be adequately described with a model including only two 2D Gaussians.

An analysis of the morphology in energy bands indicates that there seems to be two separate areas of emission in the lowest energy band from $0.3 - 0.5$ TeV. One of these areas is located to the north-west of the pulsar and the other one to the south-east. An association with the relativistic outflows (jets) from the pulsar seen in X-rays might be possible, but needs further investigations. The results from this analysis show an indication of two separated sources of VHE γ -ray emission at the $3-4 \sigma$ level below 3

TeV. This shows that even in VHE γ -ray the morphology seems to be quite complex and needs to be further investigated. This could for example be done with the production of a new set of hard γ -ray selection cuts for the GRASP method. While this would lead to an increase in energy threshold, the angular resolution would be expected to be even lower than 0.07° .

The reconstructed energy spectrum shows an indication of an exponential cut-off at an energy of about 17 TeV at the 3σ level. Depending on the composition of the radiation fields in the region, the cut-off could either result from an intrinsic cut-off in the electron spectrum or due to the onset of the Klein-Nishina regime in the presence of an IR radiation field. Assuming the former, a cut-off at about 17 TeV would lead to a cut-off in the electron spectrum at approximately 74 TeV. From this, a magnetic field strength of $\approx (21.7 \pm 3.3)\mu\text{G}$ can be estimated, which seems to be consistent with estimations done by [Yatsu et al., 2005] for the north and south jets. Furthermore, a dynamical model for the PWN describing the multiband observed emission by [Fang and Zhang, 2010], as well as by [Torres et al., 2014] yield compatible results for the magnetic field strength inside the PWN.

A spatially resolved spectral study is performed, which shows an indication of a steepening of the γ -ray spectrum away from the position of the energetic pulsar PSR B1509–58. However, the large uncertainties on the spectral index points makes it hard to draw a definitive conclusion. For the future Cherenkov Telescope Array (CTA) MSH 15-5-2 will be a most interesting object to study and is presumably be able to confirm the indication for energy dependant morphology.

Using an 3σ upper limit on the γ -ray flux at the position of the $\text{H}\alpha$ emission nebula RCW 89 an upper limit on the supernova explosion energy assuming a hadronic process is calculated. Depending on the assumption of the diffusion symmetry it is shown to be about one or two orders of magnitude below the canonical value of 10^{51} erg. However, the supernova explosion energy was estimated from the integral γ -ray flux above 1 TeV, which corresponds to protons with an energy above some 10 TeV. The missing fraction to the total energy in cosmic ray protons coming from protons with an energy below 10 TeV can be estimated. Assuming a proton spectrum with a spectral index of $\Gamma_p \approx 2.1$, this will increase the total energy in cosmic ray protons by a factor of ≈ 3.5 and therefore also the supernova explosion energy. Furthermore, according to [Gaensler et al., 1999] the SNR shell is still expanding in the cavity with a low ambient density

7. SUMMARY AND CONCLUSIONS

and produces therefore no observable emission. This might also explain the lower value for the obtained supernova explosion energy since it is obtained assuming that the shell is already in contact with RCW 89.

References

- A. A. Abdo et al. Detection of the Energetic Pulsar PSR B1509-58 and its Pulsar Wind Nebula in MSH 15-52 Using the Fermi-Large Area Telescope. *The Astrophysical Journal*, (Volume 714, Issue 1):927–936, 2010. 128, 129
- F. Acero et al. Detection of Gamma Rays from a Starburst Galaxy. *Science*, (Volume 326, no. 5956):1080–1082, 2009. 103
- Aharonian et al. Calibration of cameras of the H.E.S.S. detector. *Astroparticle Physics*, (Volume 22), 2004a. 27, 30
- Aharonian et al. Very high energy gamma rays from the direction of Sagittarius A*. *Astronomy and Astrophysics*, (Volume 425, no. 1):L13–L17, 2004b. 104
- Aharonian et al. H.E.S.S. observations of PKS 2155-304. *Astronomy and Astrophysics*, (Volume 403, Number 3):865–875, 2005a. 101
- Aharonian et al. Observations of the Crab nebula with HESS. *Astronomy and Astrophysics*, (Volume 457):899–915, 2006a. 24, 98, 103, 106, 109, 111
- Aharonian et al. An Exceptional Very High Energy Gamma-Ray Flare of PKS 2155-304. *Astrophysical Journal*, (Volume 664, Number 2), 2007. 101
- F. Aharonian et al. Discovery of extended VHE gamma-ray emission from the asymmetric pulsar wind nebula in MSH 15-52 with HESS. *Astronomy and Astrophysics*, (Volume 435, Issue 1):17–20, 2005b. 128, 129
- F. Aharonian et al. Energy dependent γ -ray morphology in the pulsar wind nebula HESS J1825-137. *Astronomy and Astrophysics*, (Volume 460, Number 2):365–374, 2006b. 139, 145

REFERENCES

- F. A. Aharonian and S. V. Bogovalov. Exploring physics of rotation powered pulsars with sub-10 GeV imaging atmospheric Cherenkov telescopes. *New Astronomy*, (Volume 8, Issue 2):85–103, 2003. 121
- G. Aielli et al. Proton-air cross section measurement with the ARGO-YBJ cosmic ray experiment. *Physical Review D*, (Volume 80, Issue 9), 2009. 12
- A. Balzer et al. The H.E.S.S. central data acquisition system. *Astroparticle Physics*, (Volume 54):67–80, 2014. 25
- A. Barrau et al. The CAT imaging telescope for very-high-energy gamma-ray astronomy. *Nuclear Instruments and Methods in Physics Research*, (Volume 416, Issue 2-3): 278–292, 1998. 3
- Bauleo and Martino. The dawn of the particle astronomy era in ultra-high-energy cosmic rays. *Nature*, (Volume 458):847–851, 2009. 115
- Y. Becherini and M. Punch. Performance of HESS-II in multi-telescope mode with a multi-variate analysis. *AIP Conference Proceedings*, (Volume 1505):741–744, 2012. 22
- A. R. Bell. The acceleration of cosmic rays in shock fronts. *Monthly Notices of the Royal Astronomical Society*, (Volume 182):147–156, 1978. 120
- G. Bellini and L. Ludhova. *Neutrino Physics and Astrophysics*. IOS Press, Amsterdam, NL, 2012. 114
- Berge et al. Background modelling in very-high-energy γ -ray astronomy. *Astronomy and Astrophysics*, (Volume 466):1219–1229, 2007. 42, 43
- K. Bernloehr. CTA simulations with CORSIKA sim_telarray. *AIP Conference Proceedings*, (Volume 1085, Issue 1), 2008. 81
- K. Bernloehr et al. The optical system of the H.E.S.S. imaging atmospheric Cherenkov telescopes, Part I: layout and components of the system. *Astroparticle Physics*, (Volume 20), 2003. 21
- K. Bernloehr et al. Monte Carlo design studies for the Cherenkov Telescope Array. *Astroparticle Physics*, (Volume 43):171–188, 2012. 23

REFERENCES

- H. Bethe and W Heitler. On the Stopping of Fast Particles and on the Creation of Positive Electrons. *Proc. R. Soc. Lond. A*, (Volume 146, no. 856), 1934. 11
- P.M.S. Blackett. Proceedings of the International Conference on the Emission Spectra of the Night Sky and Aurorae, held under the auspices of the Gassiot Committee of the Royal Society, London. *Physical Society*, pages 34–35, 1948. 1
- L. Breiman, J. Friedman, R. Olshen, and C. Stone. *Classification and Regression Trees*. Wadsworth and Brooks, Monterey, CA, 1984. 41, 93
- Rene Brun and Fons Rademakers. ROOT - An object oriented data analysis framework. *New Computing Techniques in Physics Research V*, (Volume 389):81–86, 1997. 78
- S Carrigan. Pulsar Wind Nebulae with H.E.S.S.: Establishing a Connection between high-power Pulsars and very-high-energy gamma-ray Sources. *Dissertation Ruprecht-Karls-Universität, Heidelberg, Germany*, 2007. 118
- F. Casse et al. Transport of cosmic rays in chaotic magnetic fields. *Physical Review D*, (Volume 65), 2002. 123
- C. Claudio et al. The cosmic ray electron and positron spectra measured by AMS-02. *arXiv:1402.0437*, 2014. 113, 114
- J. M. Cordes and T. J. W. Lazio. NE2001.I. A New Model for the Galactic Distribution of Free Electrons and its Fluctuations. *arXiv:astro-ph/0207156*, 2002. 125
- J. K. Daugherty and A. K. Harding. Electromagnetic cascades in pulsars. *Astrophysical Journal, Part 1*, (Volume 252, Issue 6582):337–347, 1982. 119
- Davies and Cotton. *J. Solar Energy Sci. and Eng.*, 1, 16, 1957. 21
- Ocker C. de Jager and Arache Djannati-Atai. Implications of HESS Observations of Pulsar Wind Nebulae. *Astrophysics and Space Science Library, Springer Berlin Heidelberg*, (Volume 357), 2009. 151
- Mathieu de Naurois. Analysis methods for Atmospheric Cerenkov Telescopes. *arXiv:astro-ph/0607247*, 2006. 17

REFERENCES

- Mathieu de Naurois and Loic Rolland. A high performance likelihood reconstruction of gamma-rays for Imaging Atmospheric Cherenkov Telescopes. *arXiv:0907.2610*, 2009. 77, 78
- G. M. Dubner et al. The Interstellar Medium around the Supernova Remnant G320.4-1.2. *The Astronomical Journal*, (Volume 123), 2002. 149
- R.D. Evans. *The atomic nucleus*. McGraw-Hill, New York, 1955. 6
- J. Fang and L. Zhang. Multiband Emission from Pulsar Wind Nebulae: A Possible Injection Spectrum. *arXiv:1003.1656*, 2010. 151, 155
- G. G. Fazio et al. A Search for Discrete Sources of Cosmic Gamma Rays of Energies Near 2×10^{12} eV. *Astrophysical Journal*, (Volume 154), 1968. 2
- E. J. Fenyves, S. N. Balog, N. R. Davis, D. J. Suson, and Todor Stanev. Electromagnetic component of 10^{14} - 10^{16} eV air showers. *Physical Review D*, 37:649–656, 1988. 58
- Stefano Gabici. Cosmic rays and molecular clouds. *arXiv:1208.4979*, 2012. 149
- Gaensler and Slane. The Evolution and Structure of Pulsar Wind Nebulae. *Annual Review of Astronomy and Astrophysics*, (Volume 44):17–47, 2006. 117, 120, 122
- B. M. Gaensler et al. SNR G320.4-01.2 and PSR B1509-58: new radio observations of a complex interacting system. *Monthly Notices of the Royal Astronomical Society*, (Volume 305, Issue 3):724–736, 1999. 125, 152, 155
- B. M. Gaensler et al. Chandra Imaging of the X-Ray Nebula Powered by Pulsar B1509-58. *The Astrophysical Journal*, (Volume 569, Issue 2):878–893, 2002. 126
- D. Gaggero et al. PAMELA and AMS-02 e^+ and e^- spectra are reproduced by three-dimensional cosmic-ray modeling. *Physical Review D*, (Volume 89, Issue 8), 2014. 113
- W. Galbraith and J.V. Jelley. Light Pulses from the Night Sky associated with Cosmic Rays. *Nature*, (171):349–350, 1953. 1, 2
- W. Galbraith and J.V. Jelley. Light-pulses from the night sky and Cherenkov radiation. *Journal of Atmospheric and Terrestrial Physics*, (Volume 6):250–252, 1955. 1

REFERENCES

- J. D. Gelfand et al. A Dynamical Model for the Evolution of a Pulsar Wind Nebula Inside a Nonradiative Supernova Remnant. *The Astrophysical Journal*, (Volume 703, Issue 2):2051–2067, 2009. 122
- G. Giacinti et al. Filamentary Diffusion of Cosmic Rays on Small Scales. *Physical Review Letters*, (Volume 108), 2012. 123
- K. Greisen. The extensive air showers. *Progress in Cosmic Ray Physics* 3, 1956. 8
- K. Greisen. Cosmic Ray Showers. *Annual Review of Nuclear Science*, (Volume 10): 63–108, 1960. 8
- D. Heck et al. <http://www.wik.fzk.de/corsika/physicsdescription/corsikaphys.html>. *Report FZKA 6019, Forschungszentrum Karlsruhe*, 1998. 47
- W. Heitler. *The Quantum Theory of Radiation*. Oxford University Press, London, 1954. 7
- A. Hillas. Cerenkov light images of EAS produced by primary gamma. *In NASA. Goddard Space Flight Center 19th Intern. Cosmic Ray Conf.*, (Volume 3):445–448, 1985. 4, 34
- A. M. Hillas. The Origin of Ultra-High-Energy Cosmic Rays. *Annual Review of Astronomy and Astrophysics*, (Volume 22):425–444, 1984. 115
- J. A. Hinton and W. Hofmann. Teraelectronvolt Astronomy. *Annual Review of Astronomy and Astrophysics*, (Volume 47):523–565, 2009. 151
- K. Hirotani. Outer-Gap versus Slot-Gap Models for Pulsar High-Energy Emissions: The Case of the Crab Pulsar. *The Astrophysical Journal*, (Volume 688, Issue 1): 25–28, 2008. 119
- S. Hoppe. Emitters of VHE γ -radiation as revealed by the H.E.S.S. Galactic plane survey. *PhD Thesis, Ruprecht-Karls Universität, Heidelberg, Germany*, 2008. 109
- Kamata and Nishimura. The Lateral and the Angular Structure Functions of Electron Showers. *Progress of Theoretical Physics Supplement*, (Volume 6):93–155, 1958. 8

REFERENCES

- N. S. Kardashev. Nonstationarity of Spectra of Young Sources of Nonthermal Radio Emission. *Soviet Astronomy*, (Volume 6), 1962. 151
- R. C. Lamb et al. Observations of TeV photons at the Whipple Observatory. *High energy gamma-ray astronomy; Proceedings of the International Conference*, pages 47–64, 1990. 3
- S. Le Bohec et al. A new analysis method for very high definition Imaging Atmospheric Cherenkov Telescopes as applied to the CAT telescope. *Nucl. Instrum. Meth.*, (Volume 416):425–437, 1998. 77
- T. Li and Y. Ma. Analysis methods for results in gamma-ray astronomy. *Astrophysical Journal*, (Volume 272):317–324, 1983. 42
- Livingstone et al. 21 Years of Timing PSR B1509-58. *Astrophysical Journal*, (Volume 619, Issue 2), 2005. 117
- D. Lorimer and M. Kramer. *Handbook of Pulsar Astronomy*. Cambridge University Press, Cambridge, UK, 2004. 116
- A. G. Lyne et al. Discovery of the Inner Ring around PSR B1509-58. *Nature*, (Volume 381, Issue 6582):497–498, 1996. 117
- R. N. Manchester. The radio structure of supernova remnants. *Astronomy and Astrophysics*, (Volume 171):205–215, 1987. 126
- R. N. Manchester et al. Discovery of radio pulsations from the X-ray pulsar in the supernova remnant G320.4-1.2. *Astrophysical Journal, Part 2 - Letters to the Editor*, (Volume 262):31–33, 1982. 125
- R. N. Manchester et al. The Australia Telescope National Facility Pulsar Catalogue. *The Astronomical Journal*, (Volume 129, Issue 4):1993–2006, 2005. 117
- R.N. Manchester and J.H. Taylor. *Pulsars (A Series of books in astronomy and astrophysics)*. Freeman WH, San Francisco, 1977. 118
- J. Matthews. A Heitler model of extensive air showers. *Astroparticle Physics*, (Volume 22, Issue 5-6):387–397, 2004. 14

-
- B. Y. Mills, O. B. Slee, and E. R. Hill. A Catalogue of Radio Sources between Declinations -50° and -80° . *Australian Journal of Physics*, (Volume 14):497, 1961. 125
- R. Mirzoyan et al. The first telescope of the HEGRA air Cherenkov imaging telescope array. *Nuclear Instruments and Methods in Physics Research*, (Volume 351, Issue 2-3):513–526, 1994. 3
- Alex G. Muslimov and Alice K. Harding. High-Altitude Particle Acceleration and Radiation in Pulsar Slot Gaps. *The Astrophysical Journal*, (Volume 606, Issue 2): 1143–1153, 2004. 119
- L. Nava and S. Gabici. Anisotropic CR diffusion and γ -ray production close to supernova remnants, with an application to W28. *arXiv:1211.1668*, 2012. 123
- Nishimura. Handbuch der Physik, Siegfried Flügge. *Springer*, 1967. 8
- S. Ohm et al. Gamma-Hadron Separation in Very-High-Energy γ -ray astronomy using a multivariate analysis method. *Astroparticle Physics*, (Volume 31), 2009. 39, 40, 41, 90, 93, 102
- M. Renaud et al. Discovery of a Highly Energetic Pulsar Associated with IGR J14003-6326 in the Young Uncataloged Galactic Supernova Remnant G310.6-1.6. *The Astrophysical Journal*, (Volume 716, Issue 1):663–670, 2010. 118
- S. P. Reynolds. Supernova Remnants at High Energy. *Annual Review of Astronomy and Astrophysics*, (Volume 46):89–126, 2008. 122
- A. W. Rodgers et al. A catalogue of H α -emission regions in the southern Milky Way. *Monthly Notices of the Royal Astronomical Society*, (Volume 121):103, 1960. 126
- B. Rossi. *High-Energy Particles*. Prentice-Hall, New York, 1952. 8
- Stefan Schlenker. Simulation Study of the H.E.S.S. Single Telescope Trigger Rate. *Diploma thesis at the Humboldt-University in Berlin*, 2001. 24
- F. D. Seward and Jr. Harnden, F. R. A new, fast X-ray pulsar in the supernova remnant MSH 15-52. *Astrophysical Journal, Part 2 - Letters to the Editor*, (Volume 256):45–47, 1982. 125

REFERENCES

- K. Tamura et al. Evidence for a Pulsar Jet Producing a Hot Nebula in the Supernova Remnant MSH 15-52. *Publications of the Astronomical Society of Japan*, (Volume 48):33–36, 1996. 127
- D. F. Torres et al. Time-dependent modeling of TeV-detected, young pulsar wind nebulae. *arXiv:1402.5485*, 2014. 151, 155
- E. Trussoni et al. ROSAT PSPC observations of the supernova remnant MSH 15-52. *Astronomy and Astrophysics*, (Volume 306):581, 1996. 126, 129, 130, 132, 134, 136, 138
- Y Tsai. Pair production and bremsstrahlung of charged leptons. *Reviews of Modern Physics*, (Volume 46), 1974. 6
- P. Vincent et al. Performance of the H.E.S.S. cameras. *The 28th International Cosmic Ray Conference*, 2003. 23
- B. M. Vladimirov et al. Cerenkov Gamma-telescope GT-48 of the Crimean Astrophysical Observatory of the USSR Academy of Sciences. *Very High Energy Gamma Ray Astronomy, Proceedings of the International Workshop*, 1989. 3
- Heinrich J. Voelk and Konrad Bernloehr. Imaging very high energy gamma-ray telescopes. *Experimental Astronomy August 2009*, (Volume 25, Issue 1-3):173–191, 2009. 15
- T. C. Weekes et al. Observation of TeV gamma rays from the Crab nebula using the atmospheric Cerenkov imaging technique. *Astrophysical Journal*, (Volume 342):379–395, 1989. 2
- J. B. Z. Whiteoak and A. J. Green. The MOST supernova remnant catalogue (MSC). *Astronomy and Astrophysics Supplement*, (Volume 118):329–380, 1996. 126, 132, 134, 136, 138
- Y. Yatsu. A Study of Pulsar wind nebulae with Chandra. *PhD Thesis, Tokyo Institute of Technology*, 2008. 127
- Y. Yatsu et al. Chandra Observation of the Interaction between the Hot Plasma Nebula RCW 89 and the Pulsar Jet of PSR B1509-58. *The Astrophysical Journal*, (Volume 631, Issue 1):312–319, 2005. 127, 148, 149, 151, 155

REFERENCES

- Y. Yatsu et al. Discovery of the Inner Ring around PSR B1509-58. *Publications of the Astronomical Society of Japan*, (Volume 61):129–135, 2009. 127

Danksagung

An dieser Stelle möchte ich mich bei allen bedanken, die auf unterschiedlichster Art und Weise zum Gelingen dieser Arbeit beigetragen haben. Mein besonderer Dank gilt:

- Professor Werner Hofmann, möchte ich für das interessante Thema meiner Arbeit danken und dass er mir ermöglicht hat bei H.E.S.S. mitzuarbeiten.
- Professor Stefan Wagner dafür, dass er das Koreferat übernommen hat.
- Henning Gast, dafür dass ich jederzeit zu Dir kommen konnte um Dich mit Fragen zu löchern und dass du selbst nach deinem Umzug nach Achen noch Zeit hattest mir gute Ratschläge zu geben.
- Francois Brun, Dan Parsons und Vincent Marandon dafür dass ihr euch immer Zeit genommen habt, selbst dann wenn ihr selbst nur wenig hattet. Vorallem Dan und Vincent nochmal im speziellen für die zahlreichen Diskussionen und die hilfreichen Kommentare beim Zusammenschreiben.
- Stefan Ohm, dafür dass Du Dir immer die Zeit genommen hast um meine zahlreichen Fragen über TMVA zu beantworten.
- All den anderen Mitgliedern der H.E.S.S. Gruppe für eine schöne Zeit und eine angenehme Arbeitsatmosphäre.
- Joachim Hahn, ich schätze mich glücklich dass Du mein Freund bist und bin froh mit Dir zusammen das Physikstudium bestritten zu haben.
- Der gesamten D&D Gruppe für die vielen Stunden Spass beim Würfeln.

- Margarete Sigmann, für einen sehr inspirierenden Kalender, die vielen tollen Ausflüge und die kulinarischen Köstlichkeiten.
- Meinen Eltern, Frank und Irmgard sowie meinem Bruder Matthias, dafür dass ihr mich in all meinen Lebensphasen unterstützt habt. Insbesondere möchte ich mich bei Euch bedanken, dass Ihr mir immer zur Seite standet, denn ohne euch hätte ich es bestimmt nicht bis zur Promotion geschafft. Ich könnte mich nicht glücklicher schätzen euch als Eltern und Bruder zu haben.

Zum Schluß möchte ich noch meiner Hanna danken. Die tollen Reisen an den Bodensee, nach Schottland, ins Elsass und Florida waren ein echtes Highlight. Ich könnte mir keinen Tag mehr ohne Dich vorstellen und bin so froh, dass das Schicksal uns zusammengeführt hat. Danke dass Du immer für mich da bist. Du bist die Liebe meines Lebens.

So eine Arbeit wird eigentlich nie fertig, man muss sie für fertig erklären, wenn man nach Zeit und Umständen das Möglichste getan hat.

(J.W. von Goethe)

Nicht das Beginnen wird belohnt, sondern einzig und allein das Durchhalten.

(K. von Siena)